

University College London

# Computational studies of the adsorption of hydrazine on Cu surfaces

Thesis submitted for the degree of Doctor of Philosophy (PhD) by

**Saeedeh Sarabadani Tafreshi**

Supervised by

**Prof. Nora H. de Leeuw**

University College London

Department of Chemistry

July 2015

## **Declaration**

I, Saeedeh Sarabadani Tafreshi confirm that the work presented in this thesis is my own. Where information has been derived from other sources, I confirm that this has been indicated in the thesis.

Sign: \_\_\_\_\_

Date: \_\_\_\_\_

# Abstract

This thesis presents a comprehensive computational study of the molecular and dissociative adsorption of hydrazine ( $\text{N}_2\text{H}_4$ ) on low-index perfect and defective copper surfaces, using the density functional theory calculations with long-range dispersion correction (DFT-D2).

Firstly, we have studied the adsorption of hydrazine on low-index planar copper surfaces, where (111) is found to be the most stable surface, whilst (110) surface is the least stable. DFT-D2 calculations with a correction for the van der Waals interactions result in significant enhancement of molecule-substrate binding.

Secondly, DFT-D2 has been used to simulate the interaction of hydrazine with low-index defect-containing copper surfaces. We have studied three types of defects at the surfaces: monoatomic steps, Cu-adatoms and vacancies, where our calculations show that the adsorption energy increases as the coordination of the adsorption sites decreases, with the strongest adsorption energy found on the stepped (110) surface.

Thirdly, we have investigated the arrangement of multiple hydrazine molecules upon adsorption onto the Cu(111) surface, showing that the main contributors to the assembly of the hydrazine layers are the binding interactions between the adsorbates and the substrate and the organisation of the  $\text{N}_2\text{H}_4$  monolayers is primarily due to the long-range interactions.

Furthermore, we have simulated the dissociative adsorption of hydrazine on the planar and stepped Cu(111) surfaces. We found that hydrazine prefers to form  $\text{NH}_2$  via N–N bond decoupling, where the  $\text{NH}_2$  molecule reacts fairly easily with

co-adsorbed  $\text{NH}_2$  to form  $\text{NH}_3$ , as well as with  $\text{N}_2\text{H}_x$  ( $x=1-4$ ) by subtracting hydrogen to produce  $\text{NH}_3$  and  $\text{N}_2$  molecules.

Finally, we have constructed a microkinetic model to develop our understanding of the catalytic process of  $\text{N}_2\text{H}_4$  dissociation on the planar  $\text{Cu}(111)$  surfaces. The temperature programmed reaction and batch reactor simulations were simulated, showing that the  $\text{NH}_3$  and  $\text{N}_2$  are the dominant gaseous products, while  $\text{H}_2$  is the minor gaseous product.

# Table of contents

<b>Declaration</b> .....	<b>2</b>
<b>Abstract</b> .....	<b>3</b>
<b>Table of contents</b> .....	<b>5</b>
<b>Acknowledgment</b> .....	<b>10</b>
<b>List of publications</b> .....	<b>11</b>
<b>List of conference presentations</b> .....	<b>12</b>
<b>List of figures</b> .....	<b>13</b>
<b>List of tables</b> .....	<b>21</b>
<b>Chapter 1: Introduction</b> .....	<b>25</b>
<b>Abstract</b> .....	<b>25</b>
<b>1.1. Copper Nanoparticles</b> .....	<b>26</b>
1.1.1. Synthesis of copper nanoparticles.....	28
1.1.1.1. Chemical synthesis from reverse micelles .....	29
<b>1.2. Copper nanoparticles for direct hydrazine fuel cell</b> .....	<b>32</b>
<b>1.3. Adsorption of hydrazine on metal surfaces</b> .....	<b>36</b>
<b>1.4. Dissociative adsorption of hydrazine on metal surfaces</b> .....	<b>37</b>
<b>1.5. Overview of the thesis</b> .....	<b>41</b>
<b>Chapter 2: Computational methods</b> .....	<b>43</b>
<b>Abstract</b> .....	<b>43</b>
<b>2.1. Schrödinger equation</b> .....	<b>44</b>
<b>2.2. Density functional theory</b> .....	<b>46</b>
2.2.1. The Hohenberg-Kohn theorems.....	46
2.2.2. The Kohn-Sham Theory .....	47
2.2.3. Exchange correlation functionals: LDA and GGA.....	48
<b>2.3. Dispersion correction (DFT-D2)</b> .....	<b>50</b>
<b>2.4. Basis sets</b> .....	<b>51</b>
2.4.1. Periodicity and plane-wave basis sets.....	52
<b>2.5. Pseudopotentials</b> .....	<b>53</b>

<b>2.6. Geometry optimization .....</b>	<b>54</b>
<b>2.7. Analysis of systems .....</b>	<b>55</b>
2.7.1. Transition state.....	55
2.7.2. Vibrational frequencies.....	56
2.7.3. Density of states.....	57
2.7.4. Bader charge analysis .....	57
<b>2.8. Catalysis .....</b>	<b>58</b>
<b>2.9. Microkinetic simulation.....</b>	<b>59</b>
2.9.1. Rate equations.....	60
2.9.2. Reaction mechanisms .....	61
2.9.3. Transition state theory (TST).....	63
2.9.4. Partition function .....	63
2.9.4.1. Translational partition function .....	65
2.9.4.2. Rotational partition function .....	65
2.9.4.3. Vibrational partition function.....	66
2.9.4.4. Electronic and nuclear partition function .....	67
2.9.5. Adsorption processes .....	67
2.9.6. Reaction processes.....	69
2.9.7. Desorption processes .....	69
<b>Chapter 3: Adsorption of hydrazine on the perfect low-index Cu surfaces .....</b>	<b>71</b>
<b>Abstract.....</b>	<b>71</b>
<b>3.1. Introduction.....</b>	<b>72</b>
<b>3.2. Computational methods .....</b>	<b>74</b>
<b>3.3. Results and discussions.....</b>	<b>76</b>
3.3.1. Surface properties .....	76
3.3.2. Hydrazine molecule .....	77
3.3.3. Adsorption of N <sub>2</sub> H <sub>4</sub> at the perfect Cu(111) .....	78
3.3.4. Adsorption of N <sub>2</sub> H <sub>4</sub> at the perfect Cu(100) .....	80
3.3.5. Adsorption of N <sub>2</sub> H <sub>4</sub> at the perfect Cu(110) .....	81
<b>3.4. Conclusions .....</b>	<b>83</b>
<b>Chapter 4: Adsorption of hydrazine on the defective low-index Cu surfaces ....</b>	<b>85</b>

<b>Abstract</b> .....	<b>85</b>
<b>4.1. Introduction</b> .....	<b>86</b>
<b>4.2. Computational methods</b> .....	<b>86</b>
<b>4.3. Results and discussions</b> .....	<b>88</b>
4.3.1. Surface Properties .....	88
4.3.2. Adatom diffusion .....	91
4.3.3. N <sub>2</sub> H <sub>4</sub> adsorption at the Cu(111) surfaces.....	95
4.3.3.1. Adsorption at the stepped (111) .....	95
4.3.3.2. Adsorption at the adatoms on (111) .....	97
4.3.3.3. Adsorption at the vacancies on (111).....	99
4.3.4. N <sub>2</sub> H <sub>4</sub> adsorption at the Cu(100) surfaces.....	100
4.3.4.1. Adsorption at the stepped (100) .....	100
4.3.4.2. Adsorption at the adatoms on (100) .....	102
4.3.4.3. Adsorption at the vacancies on (100).....	104
4.3.5. N <sub>2</sub> H <sub>4</sub> adsorption at the Cu(110) surfaces.....	105
4.3.5.1. Adsorption at the stepped (110) .....	105
4.3.5.2. Adsorption at the adatoms on (110) .....	107
4.3.5.3. Adsorption at the vacancies on (110).....	109
4.3.6. Electronic structure analysis .....	111
4.3.6.1. Calculation of core level binding energy shifts.....	111
4.3.6.2. Morphology .....	114
4.3.6.3. Density of states .....	116
4.3.6.4. Charge density analysis .....	118
4.3.6.5. Coordination Number .....	122
<b>4.4. Conclusions</b> .....	<b>124</b>
<b>Chapter 5: Hydrazine network on the Cu(111) surface</b> .....	<b>126</b>
<b>Abstract</b> .....	<b>126</b>
<b>5.1. Introduction</b> .....	<b>127</b>
<b>5.2. Computational methods</b> .....	<b>128</b>
<b>5.3. Results and discussions</b> .....	<b>130</b>
5.3.1. Adsorption Structures of hydrazine molecules on Cu(111).....	131
5.3.2. Electronic structure characterization .....	138

5.3.3.	Temperature programmed desorption.....	143
<b>5.4.</b>	<b>Conclusions .....</b>	<b>146</b>

**Chapter 6: Hydrazine decomposition mechanism on the planar and stepped Cu(111) surfaces .....** **148**

<b>Abstract.....</b>	<b>148</b>
----------------------	------------

<b>6.1. Introduction.....</b>	<b>149</b>
-------------------------------	------------

<b>6.2. Computational methods .....</b>	<b>152</b>
---	------------

<b>6.3. Results .....</b>	<b>154</b>
---------------------------	------------

6.3.1.	Adsorption on the planar and stepped Cu(111) .....	157
--------	--	-----

6.3.2.	$N_2H_x$ (x=1-4) decomposition pathways on the planar and stepped Cu(111) surface .....	160
--------	---	-----

6.3.2.1.	$N_2H_4$ dissociation and dehydrogenation.....	160
----------	--	-----

6.3.2.2.	$N_2H_3$ dissociation and dehydrogenation.....	162
----------	--	-----

6.3.2.3.	$N_2H_2$ dissociation and dehydrogenation.....	167
----------	--	-----

6.3.2.4.	NNH dissociation and dehydrogenation.....	169
----------	---	-----

6.3.2.5.	$N_2$ dissociation.....	169
----------	-------------------------	-----

6.3.2.6.	$NH_x$ (x=1-3) dehydrogenation.....	171
----------	-------------------------------------	-----

6.3.2.7.	H–H coupling .....	172
----------	--------------------	-----

6.3.2.8.	Inter-molecular dehydrogenation pathways .....	173
----------	--	-----

6.3.2.8.1.	$N_2H_x$ (x=1–4) dehydrogenation by $NH_2$ .....	174
------------	--	-----

6.3.2.8.2.	Interaction of $NH_2$ molecules .....	175
------------	---------------------------------------	-----

<b>6.4. Discussions .....</b>	<b>178</b>
-------------------------------	------------

<b>6.5. Conclusions .....</b>	<b>184</b>
-------------------------------	------------

**Chapter 7: Microkinetic simulation of hydrazine dissociation on the Cu(111) surface .....** **185**

<b>Abstract.....</b>	<b>185</b>
----------------------	------------

<b>7.1. Introduction.....</b>	<b>186</b>
-------------------------------	------------

<b>7.2. Computational methods .....</b>	<b>188</b>
---	------------

<b>7.3. Results and discussions .....</b>	<b>192</b>
---	------------

7.3.1.	Temperature programmed reaction simulation.....	194
--------	---	-----

7.3.2.	Batch reactor simulation .....	202
--------	--------------------------------	-----

<b>7.4. Conclusions .....</b>	<b>208</b>
<b>Chapter 8: Conclusions and future works .....</b>	<b>210</b>
<b>Appendix .....</b>	<b>214</b>
<b>References .....</b>	<b>221</b>

# Acknowledgment

First and above all, I praise the Almighty God for His grace, care, protection and providing me this opportunity and granting me the capability to proceed my PhD studies successfully.

Secondly, my heartfelt acknowledgement goes to my supervisor, Professor Nora de Leeuw, my esteemed promoter, for accepting me as a PhD student, her warm encouragement, thoughtful guidance and insightful directions and supporting me and my family throughout the last four years.

Special acknowledgement should also go to Dr. Alberto Roldan for his excellent advice and invaluable help and guidance during my PhD studies.

I also would like to express my thanks to Dr. Zhimei Du for her valuable help during the first stage of my PhD studies.

I also thank University College London for funding my studies through the Overseas Research Scholarship and Industrial Doctorate Centre for Molecular Modelling & Material Science for studentship.

I also acknowledge the use of the computer clusters including HECToR, ARCHER, IRIDIS and Legion supercomputers, as well as Huygens and IB-server clusters, in the completion of this work.

I warmly thank and appreciate my parents and my parents-in-law in Iran for their spiritual support in all aspects of my life. I also would like to thank my brothers, sisters, and brothers and sisters-in-law, for their assistance in numerous ways.

I dedicate this thesis to my family; my lovely sweet sons, Amir Mohammad, for his great patience and understanding during my PhD and Amir Hosein, in the hope that when he arrives he will continue to challenge what science teaches us and my lovely husband, Hamid Reza, without whose support and encouragement I could not have finished this work.

# List of publications

The work described in this thesis has been published in the following papers:

1. **S. S. Tafreshi**, A. Roldan, N. Y. Dzade, N. H. de Leeuw: “Adsorption of Hydrazine on the Perfect and Defective Copper (111) Surface: A Dispersion-Corrected DFT Study.” *Surf Sci*, 622, 1-8 (2014).
2. **S. S. Tafreshi**, A. Roldan, N. H. de Leeuw: “Density Functional Theory Study of the Adsorption of Hydrazine on the Perfect and Defective Copper (100), (110), and (111) Surfaces”. *J. Phys. Chem. C*, 118(45), 26103-26114 (2014).
3. **S. S. Tafreshi**, A. Roldan, N. H. de Leeuw: “Hydrazine Network on Cu(111) Surface: A Density Functional Theory Approach”. *Surf Sci*, 637-638, 140-148 (2015).
4. **S. S. Tafreshi**, A. Roldan, N. H. de Leeuw: “Density Functional Theory Calculations of the Hydrazine Decomposition Mechanism on the Planar and Stepped Cu(111) Surfaces”. *Phys. Chem. Chem. Phys.*, 17, 21533-21546 (2015).
5. **S. S. Tafreshi**, A. Roldan, N. H. de Leeuw: “Microkinetic Simulation of Hydrazine Dissociation on the Cu(111) Surface”. *J.Catal.* (2015), submitted.

# List of conference presentations

The work described in this thesis has been presented at the following conferences:

1. **S. S. Tafreshi**, A. Roldan, N. H. de Leeuw: “A density functional theory investigation of the decomposition mechanism of hydrazine on Cu(111)”, *15<sup>th</sup> International Conference on Theoretical Aspects of Catalysis (ICTAC-15)*, UCL, London, UK, June 30 - July 4, 2014.
2. **S. S. Tafreshi**, A. Roldan, N. H. de Leeuw: “Theoretical simulation of hydrazine dissociation on Cu(111) from density functional calculations”, *RSC Solid-state Group Easter Meeting 2014: Solid-state chemistry and renewable energy*, Royal society international center in Chichley, Milton Keynes, UK, 14-16 April 2014.
3. **S. S. Tafreshi**, A. Roldan, N. H. de Leeuw: “Molecular and dissociative adsorption of hydrazine on the perfect and defective low-index copper surfaces: A density functional theory approach with Van der Waals corrections”, *8<sup>th</sup> International Conference on Surfaces, Coating and Nanostructures Materials (NAMOSMAT)*, Granada, Spain, 22-25 September 2013.
4. **S. S. Tafreshi**, A. Roldan, N. H. de Leeuw: “Application of hydrazine on the perfect and defective low-index copper surfaces: A dispersion-corrected DFT study”, *Theory meets experiment workshop: Organic molecules on Inorganic surfaces*, Department of Chemistry, UCL, London, UK, 24<sup>th</sup> June 2013.

## List of figures

<b>Figure 1.1.</b> Reverse micelle. Reproduced with permission from (Pileni, 2003). .....	29
<b>Figure 1.2.</b> Representation of the stable nuclei for the formation of copper nanoparticles. Reproduced with permission from (Salzemann <i>et al.</i> , 2004b). .....	30
<b>Figure 1.3.</b> Schematic illustration of the growth mechanism of (A) cubic and (B) elongated (C) trigonal lamellar copper nanocrystals in reverse micelles synthesis. Reproduced with permission from (Salzemann <i>et al.</i> , 2004b).....	31
<b>Figure 1.4.</b> General description of a room-temperature hydrazine/air direct-liquid fuel cell (DLFC), based on the use of nanostructured copper electrodes. Reproduced with permission from (Granot <i>et al.</i> , 2012). .....	35
<b>Figure 1.5.</b> Hydrazine conformations: gauche, trans and eclipsed.....	37
<b>Figure 3.1.</b> Surface structures (top-view) of the perfect (a) Cu(111), (b) Cu(100) and (c) Cu(110) and cells used in the calculations (all distances in Å). .....	77
<b>Figure 3.2.</b> Representation of the N <sub>2</sub> H <sub>4</sub> conformations, from left to right: gauche, trans and eclipsed. ....	78
<b>Figure 3.3.</b> The three lowest-energy configurations for adsorption of N <sub>2</sub> H <sub>4</sub> on the perfect Cu(111) surface. Adsorption energies are in parenthesis. ....	79
<b>Figure 3.4.</b> Surface geometry of the lowest-energy configurations for adsorption of N <sub>2</sub> H <sub>4</sub> on the perfect Cu(100) surface. (Adsorption energies are given in parenthesis). .....	80
<b>Figure 3.5.</b> The lowest-energy configurations for adsorption of N <sub>2</sub> H <sub>4</sub> on the perfect Cu(110) surface. (Adsorption energies are given in parenthesis). .....	83
<b>Figure 4.1.</b> Side view of simulation cells used in the calculations of stepped surfaces where the low-coordinated copper atoms are shaded darker: (a) Cu(111); (b) Cu(100), and (c) Cu(110).....	88

<b>Figure 4.2.</b> The surface geometry (top-view) of different sites for adatom (a) (111) and (b) (100) as well as (c) (110) surfaces. Copper adatoms are shaded darker. A vacancy defect on each surface is also shown. S-bridge and L-bridge indicate the short and long bridges sites on the (110) surface respectively.....	89
<b>Figure 4.3.</b> Diffusion processes of an adatom via hopping on (a) Cu(100), (b) Cu(110) and (c) Cu(111).....	93
<b>Figure 4.4.</b> Schematic illustration of initial adsorption configurations where N <sub>2</sub> H <sub>4</sub> was placed at different sites on the step and terraces of the stepped Cu(111) surface. ....	95
<b>Figure 4.5.</b> The three lowest-energy configurations for adsorption of N <sub>2</sub> H <sub>4</sub> on the stepped Cu(111) surface. Adsorption energies are given in parenthesis. ....	96
<b>Figure 4.6.</b> The lowest-energy configurations of adsorption of N <sub>2</sub> H <sub>4</sub> on fcc-adatom Cu(111) surface.....	98
<b>Figure 4.7.</b> The lowest-energy configurations for adsorption of N <sub>2</sub> H <sub>4</sub> on vacant Cu(111) surface.....	100
<b>Figure 4.8.</b> The lowest-energy configurations for adsorption of N <sub>2</sub> H <sub>4</sub> on the stepped Cu(100) surface. (Adsorption energies are given in parenthesis).....	102
<b>Figure 4.9.</b> Surface geometry of the lowest-energy configurations for adsorption of N <sub>2</sub> H <sub>4</sub> on the adatom Cu(100) surface. (Adsorption energies are given in parenthesis). ....	104
<b>Figure 4.10.</b> The lowest-energy configurations for adsorption of N <sub>2</sub> H <sub>4</sub> on the Cu(100) vacancy surface. (Adsorption energies are given in parenthesis).....	105
<b>Figure 4.11.</b> The lowest-energy configurations of adsorption of N <sub>2</sub> H <sub>4</sub> on the stepped Cu(110) surface. (Adsorption energies are given in parenthesis).....	107
<b>Figure 4.12.</b> The lowest-energy configurations for adsorption of N <sub>2</sub> H <sub>4</sub> on the adatom Cu (110) surface. (Adsorption energies are given in parenthesis).....	109

<b>Figure 4.13.</b> The lowest-energy configurations for adsorption of $N_2H_4$ on the Cu(110) vacancy surface. (Adsorption energies are given in parenthesis).....	110
<b>Figure 4.14.</b> Core-level binding energy shifts ( $E_{CLS}$ ) for N(1s) of $N_2H_4$ in the strongest adsorption structures on the perfect, stepped, adatom and vacancy Cu(111) surfaces.....	113
<b>Figure 4.15.</b> Calculated crystal morphology of copper before hydrazine adsorption: (a) perfect, adatom and vacancy, (b) step crystals; and after hydrazine adsorption: (c) perfect, adatom and vacancy, (d) step crystals.....	115
<b>Figure 4.16.</b> Site-projected electronic LDOS of the lowest-energy adsorbed structures on each perfect and defective (111) surface for nitrogen p-band. N(1) is the nitrogen closest to the surface and N(2) is the second nitrogen atom of $N_2H_4$ .....	117
<b>Figure 4.17.</b> Site-projected electronic LDOS of the lowest-energy adsorbed structures on each perfect and defective (100) surface for nitrogen p-band. N(1) is the nitrogen closest to the surface and N(2) is the second nitrogen atom of $N_2H_4$ .....	117
<b>Figure 4.18.</b> Site-projected electronic LDOS of the lowest-energy adsorbed structures on each perfect and defective (110) surface for nitrogen p-band. N(1) is the nitrogen closest to the surface and N(2) is the second nitrogen atom of $N_2H_4$ .....	118
<b>Figure 4.19.</b> Induced charge density presentation of the adsorption of $N_2H_4$ molecule on (a) perfect, (b) adatom, (c) step and (d) vacant Cu(111) surfaces by an isosurface of $\pm 0.02 e/\text{\AA}^3$ , where yellow and blue denote lost and gain of electron density. Low-coordinated atoms are shown in red.....	119
<b>Figure 4.20.</b> Induced charge density presentation of the adsorption of $N_2H_4$ molecule on (a) perfect, (b) adatom, (c) step and (d) vacant Cu(100) surfaces by an isosurface of $\pm 0.02 e/\text{\AA}^3$ , where yellow and blue denote lost and gain of electron density. Low-coordinated atoms are shown in red.....	119
<b>Figure 4.21.</b> Induced charge density presentation of the adsorption of $N_2H_4$ molecule on (a) perfect, (b) adatom, (c) step and (d) vacant Cu(110) surfaces by an isosurface of $\pm 0.02 e/\text{\AA}^3$ , where yellow and blue denote lost and gain of electron density. Low-coordinated atoms are shown in red.....	120

**Figure 4.22.** (a) adsorption energy per N interaction, (b) d-band centre of interacting Cu atoms as a function of coordination number (CN) of interacting Cu atoms, for the lowest-energy adsorption structures on the perfect and defective Cu(111), (100) and (110) surfaces, except on the adatom (100) and vacancy surfaces, where we used the second lowest-energy adsorption structures (see text). The linear trend-lines in the plots fit the equation (a)  $y = -0.09x - 1.71$ ,  $R^2 = 0.84$  and (b)  $y = 0.0605x - 1.0648$ ,  $R^2 = 0.68$ . ..... 124

**Figure 5.1.** Top and side views of the lowest-energy  $N_2H_4$  adsorption configurations of (1), single  $N_2H_4$  molecule adsorption, and 2(A), 2(B) and 2(C) configurations for two molecules on the Cu(111) surface. The hydrogen-bond distances are indicated and labelled in Å. (N = blue, H = white, Cu = orange). ..... 133

**Figure 5.2.** Assembly of hydrazine configurations 3(A), 3(B) and 3(C) for three molecules on the Cu(111) surface. The hydrogen-bond distances are indicated and labelled in Å. (N = blue, H = white, Cu = orange). ..... 135

**Figure 5.3.** Self-assembly of hydrazine for four, five, six and nine molecules on the Cu(111) surface. The hydrogen-bond distances are indicated and labelled in Å. (N = blue, H = white, Cu = orange). ..... 137

**Figure 5.4.** Top and side views of the charge density difference induced by deposition of 5 and 9 hydrazine molecules on Cu(111). The isosurface was set to  $\pm 0.02 e/\text{Å}^3$ , where yellow and blue denote loss and gain of electron density respectively. ..... 139

**Figure 5.5.** Simulated STM images of the hydrazine network with a) 5 and b) 9 hydrazine molecules at a simulated bias of -1.5 V. Insets show enlargement of the STM images. Densities and tip distances are also indicated. (N = blue, H = white). ..... 140

**Figure 5.6.** The average PDOS of N and H atoms of trans and gauche conformations of  $N_2H_4$  corresponding to  $[N_2H_4]_5$  cluster in (a) and (b); and the full coverage  $[N_2H_4]_9$  cluster in (c) and (d) on the Cu(111) surface.  $E = 0$  eV corresponds to the Fermi level. ..... 141

<b>Figure 5.7.</b> Adsorption ( $E_{ads}$ ), binding ( $E_{bind}$ ) and cohesion ( $E_{cohe}$ ) energies of the lowest-energy adsorption structures as a function of the number of hydrazine molecules.....	142
<b>Figure 5.8.</b> Surface energy ( $\gamma$ ) of the Cu(111) surface for the lowest-energy adsorption structures as a function of the number of molecules. The linear trend-lines in the plots fit the equation $y = -0.0779x + 1.9534$ , $R^2 = 0.99$ .....	143
<b>Figure 5.9.</b> Simulated TPD curves for $N_2H_4$ desorption from Cu(111) surface for a reaction time of 1 s and heating rate of 1 K/min at different initial coverages.....	146
<b>Figure 6.1.</b> The simulation cells and surface geometry of different sites used in the calculations of (a) perfect (top view) and (b) stepped (side view) surfaces. Note that low-coordinated atoms in the stepped surface are shaded darker.....	155
<b>Figure 6.2.</b> Representation of the $N_2H_4$ conformations, from left to right: gauche, trans and eclipsed.....	155
<b>Figure 6.3.</b> Surface geometries of the most preferred adsorption configurations of the various intermediates on the flat (top-view) and stepped (side-view) Cu(111) surfaces with their N–N and N–H bond distances in Å.....	156
<b>Figure 6.4.</b> Schematic representation of the initial, transition and final states for $N_2H_4$ dissociation pathways on the flat (top-view) and stepped (side-view) Cu(111) surfaces via (a) N–N, (b) N–H breaking. Bond lengths are given in Å.....	162
<b>Figure 6.5.</b> Schematic representation of the initial, transition and final states for $N_2H_3$ dissociation pathways on the flat (top-view) and stepped (side-view) Cu(111) surfaces via (a) N–N, (b) and (c) N–H breaking. Bond lengths are given in Å.....	166
<b>Figure 6.6.</b> Schematic representation of the initial, transition and final states for $NNH_2$ dissociation pathways on the flat (top-view) and stepped (side-view) Cu(111) surfaces via (a) N–N, and (b) N–H breaking. Bond lengths are given in Å.....	167
<b>Figure 6.7.</b> Schematic representation of the initial, transition and final states for $NH_2NH$ dissociation pathways on the flat (top-view) and stepped (side-view) Cu(111) surfaces via (a) N–N, and (b) N–H breaking. Bond lengths are given in Å.....	168

- Figure 6.8.** Schematic representation of the initial, transition and final states for NNH dissociation pathways on the flat (top-view) and stepped (side-view) Cu(111) surfaces via (a) N–N, (b) N–H breaking. Bond lengths are given in Å..... 170
- Figure 6.9.** Schematic representation of the initial, transition and final states for N<sub>2</sub> dissociation pathways on the flat (top-view) and stepped (side-view) Cu(111) surfaces. Bond lengths are given in Å..... 170
- Figure 6.10.** Schematic representation of the initial, transition and final states for (a) NH<sub>3</sub>, (b) NH<sub>2</sub> and (c) NH dehydrogenation pathways on the flat (top-view) and stepped (side-view) Cu(111) surfaces. Bond lengths are given in Å..... 172
- Figure 6.11.** Schematic representation of the initial, transition and final states for H–H coupling pathways on the flat (top-view) and stepped (side-view) Cu(111) surfaces. Bond lengths are given in Å..... 173
- Figure 6.12.** Schematic representation of the initial, transition and final states for dehydrogenation pathways on the flat (top-view) and stepped (side-view) Cu(111) via NH<sub>2</sub> attacking to (a) N<sub>2</sub>H<sub>4</sub>, (b) and (c) N<sub>2</sub>H<sub>3</sub>, (d) NNH<sub>2</sub>, (e) NHNH and (f) NNH. Bond lengths are given in Å..... 177
- Figure 6.13.** Schematic representation of the initial, transition and final states for dehydrogenation pathway via NH<sub>2</sub> attacking NH<sub>2</sub> on the flat (top-view) and stepped (side-view) Cu(111) surfaces. Bond lengths are given in Å..... 177
- Figure 6.14.** Reaction profiles for dissociation of N<sub>2</sub>H<sub>4</sub> via intra-molecular dehydrogenation mechanism on the flat (---) and stepped (—) Cu(111) surfaces. Energies are relative to the energy of the gas-phase hydrazine (in eV). Note that we have considered the diffusion of intermediates to their most stable adsorption sites on the surface as a barrier-less pathway..... 181
- Figure 6.15.** Reaction profiles for dissociation of N<sub>2</sub>H<sub>4</sub> via N–N bond breaking and subsequent dehydrogenation pathways on the flat (---) and stepped (—) Cu(111) surfaces. Energies are relative to the energy of the gas-phase hydrazine (in eV). Note that we have considered the diffusion of intermediates to their most stable adsorption sites on the surface as a barrier-less pathway..... 182

<b>Figure 6.16.</b> Reaction profiles for dissociation of $N_2H_4$ via inter-molecular dehydrogenation via $NH_2$ on the flat (---) and stepped (—) Cu(111) surfaces. Energies are relative to the energy of the gas-phase hydrazine (in eV). Note that we have considered the diffusion of inter-mediates to their most stable adsorption sites on the surface as a barrier-less pathway.....	183
<b>Figure 7.1.</b> Calculated thermodynamic properties of $NH_3$ in the gas phase compared with the NIST database (Chase <i>et al.</i> , 1998).....	191
<b>Figure 7.2.</b> Calculated thermodynamic properties of $N_2$ and $H_2$ in the gas phase compared with NIST database (Chase <i>et al.</i> , 1998).....	192
<b>Figure 7.3.</b> Calculated reaction rate constants ( $k$ ) as a function of temperature ( $T$ ) for reactions of, (a) $N_2H_x$ ( $x=1-4$ ) dehydrogenation, (b) $N_2H_x$ ( $x=1-4$ ) N–N decoupling, (c) $NH_x$ ( $x=1-3$ ) dehydrogenation and, (d) interaction of $NH_2$ with $N_2H_x$ ( $x=1-4$ ) mechanisms.....	194
<b>Figure 7.4.</b> Simulated TPR spectra for $N_2H_4$ , $NH_3$ , $N_2$ and $H_2$ desorption from Cu(111) surface starting from adsorbed $N_2H_4$ at different initial coverages at a reaction time of 1s with a 1K/min heating rate.....	197
<b>Figure 7.5.</b> (a) The partial pressure of desorbed $N_2H_4$ , $NH_3$ , $N_2$ and $H_2$ gases and (b) surface coverage of $N_2H_4$ , $N_2H_3$ and $NH$ as a function of temperature with an initial $N_2H_4$ full coverage in the TPR simulation at a reaction time of 1s with a 1K/min heating rate.....	199
<b>Figure 7.6.</b> Simulated TPR curves for $N_2H_4$ , $NH_3$ , $N_2$ and $H_2$ desorption from Cu(111) surface starting from an initial $N_2H_4$ coverage of 1 ML (full coverage) at reaction time of 1s for different heating rates.....	200
<b>Figure 7.7.</b> $N_2H_4$ , $NH_3$ , $N_2$ and $H_2$ evolution from Cu(111) surface as a function of temperature for an initial $N_2H_4$ coverage of 1 ML (full coverage) in the TPR simulation at reaction time of 1s for different heating rates.....	201
<b>Figure 7.8.</b> $N_2H_4$ , $NH_3$ , $N_2$ and $H_2$ evolution from Cu(111) surface as a function of temperature and time for an initial $N_2H_4$ pressure of 6 Pa with a 1K/min heating rate in the batch reactor simulation.....	204

**Figure 7.9.** The surface coverage of (a)  $\text{N}_2\text{H}_4$  and  $\text{N}_2\text{H}_3$ , (b)  $\text{NH}_3$ , H and NH as a function of temperature with an initial  $\text{N}_2\text{H}_4$  pressure of 6 Pa, in the batch reactor simulation at a reaction time of 1s with a 1K/min heating rate. .... 204

**Figure 7.10.**  $\text{N}_2\text{H}_4$  conversion and  $\text{NH}_3$ ,  $\text{N}_2$  and  $\text{H}_2$  selectivities as a function of (a) initial  $\text{N}_2\text{H}_4$  pressure at 350 K, (b) temperature with an initial  $\text{N}_2\text{H}_4$  pressure of 6 Pa in the batch reactor simulation at a reaction time of 1s with a 1K/min heating rate. .... 207

## List of tables

<b>Table 3.1.</b> Surface energies of the perfect (111), (100) and (110) copper surfaces. .	77
<b>Table 3.2.</b> Geometries and adsorption energies ( $E_{ads}$ ) of relaxed $N_2H_4$ adsorbed structures on the perfect Cu(111) surface. The angle between the N–N bond and the surface plane is $\Theta$ ; the N–N bond length in gas phase is 1.44 Å. (Bold numbers indicate a non-bonding nitrogen atom). .....	79
<b>Table 3.3.</b> Geometries and adsorption energies ( $E_{ads}$ ) of the relaxed $N_2H_4$ adsorbed structures on the perfect Cu(100) surface. The angle between the N–N bond and the surface plane is $\Theta$ , the N–N bond length in the gas phase is 1.44 Å. (Bold numbers indicate a non-bonding nitrogen atom). .....	81
<b>Table 3.4.</b> Geometries and adsorption energies ( $E_{ads}$ ) of the relaxed $N_2H_4$ adsorbed structures on the perfect Cu(110) surface. The angle between the N–N bond and the surface plane is $\Theta$ , the N–N bond length in the gas phase is 1.44 Å. (Bold numbers indicate a non-bonding nitrogen atom.) .....	82
<b>Table 4.1.</b> Formation energies of Cu-adatom and vacancy on the Cu(111), (100) and (110) surfaces. ....	90
<b>Table 4.2.</b> Surface energies of the perfect and defective (111), (100) and (110) copper surfaces.....	91
<b>Table 4.3.</b> Activation energies, pre-exponential factors ( $D_0$ ) and diffusion coefficients ( $D$ ) of adatom diffusion on Cu(100), (110) and (111). The results in this table are for the moves in <b>Figure 4.3</b> For comparison, the corresponding values from other references are also reported. ....	94
<b>Table 4.4.</b> Geometries and adsorption energies ( $E_{ads}$ ) of the relaxed $N_2H_4$ adsorbed structures on the stepped Cu(111) surface. The angle between the N–N bond and the surface plane is $\Theta$ , the N–N bond length in the gas phase is 1.44 Å. (Bold numbers indicate a non-bonding nitrogen atom). .....	97
<b>Table 4.5.</b> Geometries and adsorption energies for the relaxed $N_2H_4$ adsorbed structures on the fcc-adatom Cu (111) surface. The angle between the N–N bond and	

the surface plane is  $\Theta$ , the N–N bond length in the gas phase is 1.44 Å. (Bold numbers indicate a nitrogen atom is bound to the adatom). ..... 98

**Table 4.6.** Geometries and adsorption energies for the lowest-energy N<sub>2</sub>H<sub>4</sub> adsorbed structures on the vacant Cu(111) surface. The angle between the N–N bond and the surface plane is  $\Theta$ , the N–N bond length in the gas phase is 1.44 Å. (Bold numbers indicate a non-bonding nitrogen atom). ..... 100

**Table 4.7.** Geometries and adsorption energies ( $E_{ads}$ ) of the relaxed N<sub>2</sub>H<sub>4</sub> adsorbed structures on the stepped Cu(100) surface. The angle between the N–N bond and the surface plane is  $\Theta$ , the N–N bond length in the gas phase is 1.44 Å. (Bold numbers indicate a non-bonding nitrogen atom). ..... 101

**Table 4.8.** Geometries and adsorption energies ( $E_{ads}$ ) of the relaxed N<sub>2</sub>H<sub>4</sub> adsorbed structures on the adatom Cu(100) surface. The angle between the N–N bond and the surface plane is  $\Theta$ , the N–N bond length in the gas phase is 1.44 Å. (Bold numbers indicate a nitrogen atom is bound to the adatom). ..... 103

**Table 4.9.** Geometries and adsorption energies ( $E_{ads}$ ) of the relaxed N<sub>2</sub>H<sub>4</sub> adsorbed structures on the Cu(100) vacancy surface. The angle between the N–N bond and the surface plane is  $\Theta$ , the N–N bond length in the gas phase is 1.44 Å. (Bold numbers indicate a non-bonding nitrogen atom.) ..... 105

**Table 4.10.** Geometries and adsorption energies ( $E_{ads}$ ) of the relaxed N<sub>2</sub>H<sub>4</sub> adsorbed structures on the stepped Cu(110) surface. The angle between the N–N bond and the surface plane is  $\Theta$ , the N–N bond length in the gas phase is 1.44 Å. (Bold numbers indicate a non-bonding nitrogen atom.) ..... 106

**Table 4.11.** Geometries and adsorption energies ( $E_{ads}$ ) of the relaxed N<sub>2</sub>H<sub>4</sub> adsorbed structures on the adatom Cu(110) surface. The angle between the N–N bond and the surface plane is  $\Theta$ , the N–N bond length in the gas phase is 1.44 Å. (Bold numbers indicate a nitrogen atom is bound to the adatom). ..... 108

**Table 4.12.** Geometries and adsorption energies ( $E_{ads}$ ) of the relaxed N<sub>2</sub>H<sub>4</sub> adsorbed structures on the Cu(110) vacancy surface. The angle between the N–N bond and the surface plane is  $\Theta$ , the N–N bond length in the gas phase is 1.44 Å. (Bold numbers indicate a non-bonding nitrogen atom). ..... 110

<b>Table 4.13.</b> Core-level binding energy shifts ( $E_{CLS}$ ) for both N(1s) for atoms of $N_2H_4$ on the strongest adsorption structures on the perfect, stepped, adatom and vacant Cu(111) surfaces. ....	113
<b>Table 4.14.</b> Atomic charges of adsorbed hydrazine and the interacting surface Cu atoms on different Cu(111) surfaces. The atomic charges of gas-phase hydrazine are also reported. ....	121
<b>Table 4.15.</b> Atomic charges of adsorbed hydrazine and the interacting surface Cu atoms on different Cu(100) surfaces. The atomic charges of gas-phase hydrazine are also reported. ....	121
<b>Table 4.16.</b> Atomic charges of adsorbed hydrazine and the interacting surface Cu atoms on different Cu(110) surfaces. The atomic charges of gas-phase hydrazine are also reported. ....	122
<b>Table 5.1.</b> Distances ( $d$ ) and charge transfer ( $CT$ ) between the surface and the cluster on the most-stable structures with one, two and three $N_2H_4$ molecules on the Cu(111). The distances between the interacting Cu atoms and the N atoms of each $N_2H_4$ molecule are reported. ....	133
<b>Table 5.2.</b> Adsorption ( $E_{ads}$ ), binding ( $E_{bind}$ ) and cohesion ( $E_{cohe}$ ) energies. Long-range interaction energy contributions to these energies are also reported with vdW superscript. ....	135
<b>Table 5.3.</b> Calculated pre-exponential factors ( $A_0$ ) and desorption rate constants ( $k$ ) for $N_2H_4$ from Cu(111) at 150 and 300 K are reported. ....	145
<b>Table 6.1.</b> Adsorption energies ( $E_{ads}$ ) and average geometric parameters of the most favourable adsorption structures of different $N_2H_4$ decomposition intermediates on the flat and stepped Cu(111) surface. Adsorption energies are relative to the gas-phase hydrazine; bold numbers show the adsorption energies relative to the species in their gas-phase: $NH_3$ , $N_2$ and $H_2$ . ....	155
<b>Table 6.2.</b> Calculated reaction ( $E_r$ ) and barrier ( $E_a$ ) energies for the forward and reverse reaction pathways considered. Note that (*) indicates adsorbed state. The $E_r$	

of the adsorption and desorption processes are the corresponding  $E_{ads}$  which for each species were calculated relative to them in the gas-phase. .... 164

**Table 7.1.** Relative errors (in %) of the calculated thermodynamic properties of  $\text{NH}_3$ ,  $\text{N}_2$  and  $\text{H}_2$  in the gas phase compared with the NIST database (Chase *et al.*, 1998). .... 192

**Table 7.2.** Calculated ZPE corrected reaction ( $E_r^{ZPE}$ ) and barrier ( $E_a^{ZPE}$ ) energies for the reaction pathways considered. The pre-exponential factors ( $A_0$ ) and reaction rate constants ( $k$ ) at 300 and 650 K are also included. The  $E_r^{ZPE}$  of the adsorption and desorption processes are the corresponding  $E_{ads}^{ZPE}$  and  $E_{des}^{ZPE}$  which for each species were calculated relative to them in the gas-phase. Note that “\*” and (X\*) indicate a free site and the adsorbed specie on the surface respectively. The units of  $A_0$  and  $k$  for first order and second order reactions are  $\text{s}^{-1}$  and  $\text{ML}^{-1}\text{s}^{-1}$  respectively. .... 195

**Table 7.3.** Calculated sticking coefficients ( $S_0$ ) of  $\text{N}_2\text{H}_4$ ,  $\text{NH}_3$ ,  $\text{N}_2$  and  $\text{H}_2$  adsorption on Cu(111) surface at 300 and 650 K. Note that “\*” and (X\*) indicate a free site and the adsorbed species on the surface, respectively. .... 197

**Table 7.4.** Percentage of composition of gaseous products throughout the hydrazine decomposition on Cu(111) surface from an initial  $\text{N}_2\text{H}_4$  full coverage in the TPR simulation at a reaction time of 1s with a 1K/min heating rate at different temperatures in comparison with experimental reports (Alhaydari *et al.*, 1985)..... 202

# *Chapter 1: Introduction*

## **Abstract**

The copper–hydrazine system has attracted considerable attention due to its numerous applications in diverse fields *e.g.* in the production of metallic copper nanoparticles using hydrazine as a reducing agent and in the room-temperature hydrazine/air direct-liquid fuel cells based on the use of nanostructured copper electrodes. This Chapter describes the aims and objectives of our research enclosed in a literature survey of different applications of the copper–hydrazine system and well documented areas of research, where both experimental studies and modelling investigations have been conducted. It also includes the aims and overview of the subsequent Chapters.

## 1.1. Copper Nanoparticles

Over the last two decades, metallic nanoparticles smaller than 100 nm (Fahlman, 2007) have received much attention due to their applications in a wide range of areas including catalysis, magnetics, optoelectronics, electronic materials, biological identification, environmental detection and monitoring (Heath, 1999; Matsui, 2005; Liu, 2006). This wide applicability is in part due to their position between isolated atoms and extended solids as well as their surface properties, since they are composed almost entirely of surfaces and the surface-bulk ratio becomes important. Generating specific nanoparticles with defined properties which are influenced by their shape and size (Lisiecki and Pileni, 1993; Salzemann *et al.*, 2004a; Germain *et al.*, 2005; Kooij and Poelsema, 2006; Salzemann *et al.*, 2006; El-Sayed, 2004) depends on several parameters such as temperature, pressure and synthesis techniques (Tanori and Pileni, 1995; Tanori and Pileni, 1997; Pileni, 2001; Filankembo *et al.*, 2003; Kitchens *et al.*, 2003; Salzemann *et al.*, 2004b; Lisiecki and Pileni, 1993; Wei *et al.*, 2010).

Over the past few years, copper nanoparticles have considerable industrial significance due to their catalytic behaviour and optical properties, high thermal and electrical conductivity and durability, at a much lower cost than other metals such as silver and gold (Jones, 1996; Huang *et al.*, 1997; Tilaki *et al.*, 2007). Previous works identified numerous applications of copper nanoparticles which some of them have been highlighted here.

Copper nanoparticles are used in catalysis due to their high activities and selectivities in various chemical processes such as methanol synthesis (Herman *et al.*, 1979; Shen *et al.*, 2005), steam reforming (Kobayashi *et al.*, 1981; Matter *et al.*, 2004; Kniep *et*

*al.*, 2005), conversion of heavy petroleum (Dhas *et al.*, 1998), dehydrogenation of alcohols (Fridman and Davydov, 2000; Marchi *et al.*, 1996), transformation of alcohols into aldehydes (Ron *et al.*, 1998), solar energy harvesting (Liu *et al.*, 2008), ester hydrogenolysis (Brands *et al.*, 1999; Vandescheur *et al.*, 1994), isomerization of chlorolefines (Rostovshchikova *et al.*, 2005), reduction of NO<sub>x</sub> (Chary *et al.*, 2004; Diaz *et al.*, 1999; Bennici and Gervasini, 2006), oxidation of CO and hydrocarbons (Park and Ledford, 1998; Tang *et al.*, 2005), oxidation of alkanethiols (Chen *et al.*, 2002), oxidation of phenol with molecular oxygen (Vitulli *et al.*, 2002) and coupling of epoxyalkylhalids (Rieke *et al.*, 1989).

Metal nanoparticles such as silver, gold and copper are found to have antibacterial activity (Wei *et al.*, 2010). The antimicrobial effect of nanoparticles is due to their size and the high surface-to-volume ratio enabling them to interact closely with bacterial membranes (Morones *et al.*, 2005). The antibacterial effects of gold (Cui *et al.*, 2012) and silver (Morones *et al.*, 2005; Baker *et al.*, 2005; Sondi and Salopek-Sondi, 2004) nanoparticles have been reported. There are a few studies about the antifungal and bacteriostatic properties of copper nanoparticles (Yoon *et al.*, 2007; Cioffi *et al.*, 2005; Ramyadevi *et al.*, 2012; Chatterjee *et al.*, 2012). The antimicrobial characteristics of silver and copper nanoparticles against *Escherichia* and *Bacillus subtilis* have been reported, where the copper nanoparticles showed superior antibacterial activity compared to the silver nanoparticles (Yoon *et al.*, 2007; Ruparelia *et al.*, 2008). The antimicrobial activity of copper nanoparticles against *E.coli* and *Staphylococcus* species is also reported (Ren *et al.*, 2009; Ruparelia *et al.*, 2008). Antibacterial effects of copper nanoparticles find applications in various fields such as the manufacture of medical equipment and in material for food processing (Anyagogu *et al.*, 2008).

Copper nanoparticles can also be used as the active anode material in solid oxide fuel cells (Park *et al.*, 2000; Gorte *et al.*, 2000). They play an important role in the preparation of lubricants (Zhou *et al.*, 2006), composite materials (Su *et al.*, 2007) and in enhancing the thermal conductivity of fluids (Eastman *et al.*, 2001).

### **1.1.1. Synthesis of copper nanoparticles**

The synthesis of copper nanoparticles (Cu-NPs) is a significant challenge because of their rapid oxidation in air or aqueous solution (Datta *et al.*, 2010). However, there are many methods for the production of copper nanoparticles, including thermal reduction (Dhas *et al.*, 1998), vapour deposition (Ponce and Klabunde, 2005), flame spray (Athanassiou *et al.*, 2006), laser irradiation (Yeh *et al.*, 1999),  $\gamma$ -irradiation (Joshi *et al.*, 1998), sono-electrochemical process (Haas *et al.*, 2006), chemical reduction (Chen *et al.*, 2006; Athawale *et al.*, 2005; Chatterjee *et al.*, 2012; Kruk *et al.*, 2015; Ziegler *et al.*, 2001), solvated metal atom dispersion technique (SMAD) (Vitulli *et al.*, 2002; Davis and Klabunde, 1982; Ponce and Klabunde, 2005), the polyol process (Park *et al.*, 2007; Zhao *et al.*, 2004; Ramyadevi *et al.*, 2012), reduction in micro-emulsions and reverse micelles (Haram *et al.*, 1996; Lisiecki *et al.*, 1995; Lisiecki, 2005; Salzemann *et al.*, 2004b), etc.

Controlling the size and shape of nanoparticles is a real challenge in the field of nanotechnology (Pileni, 2003). One particular factor during synthesis is the variation in the concentration of reducing agents like hydrazine ( $N_2H_4$ ), which has been shown to have significant effects in the distribution of copper particle shapes and sizes (Filankembo *et al.*, 2003; Salzemann *et al.*, 2004b). Literature, *e.g.* in reverse micelle-based synthesis, has achieved much in the way of controlling the size and

shape of copper nanoparticles (Salzemann *et al.*, 2004b; Lisiecki, 2005) which has been expanded in the next section.

#### 1.1.1.1. Chemical synthesis from reverse micelles

There are a number of studies about the production of nanoparticles from colloidal systems with controlling size and shape (Lisiecki, 2005; Tanori and Pileni, 1995; Tanori and Pileni, 1997; Pileni, 2001; Filankembo *et al.*, 2003; Lisiecki, 2004; Salzemann *et al.*, 2004b; Kitchens *et al.*, 2003; Lisiecki *et al.*, 1995). Salzemann *et al.* (Salzemann *et al.*, 2004b) discovered the effect of concentration of reducing agent such as hydrazine ( $N_2H_4$ ) on the shape and size of copper nanoparticles using chemical reduction of copper ions in mixed reverse micelles.

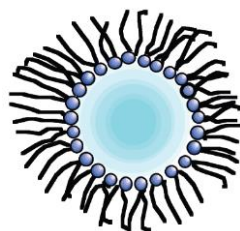


**Figure 1.1.** Reverse micelle. Reproduced with permission from (Pileni, 2003).

In a mixture of water and oil, surfactant molecules tend to emulsify the oil as micelles. Surfactants, which are molecules with a polar hydrophilic head and a hydrophobic hydrocarbon chain, form water-in-oil droplets called reverse micelles, **Figure 1.1.** The surfactant most used is sodium di(2-ethylhexyl) sulfosuccinate, usually called  $Na(AOT)$ . The choice of solvent affects the interaction between micelles. Experimental methods found that isooctane is a suitable solvent for the synthesis of controlled nanoparticles. The ratio of water to surfactant concentration  $w = [H_2O]/[Na(AOT)]$  determines the reverse micelle size. Spherical water droplets at low water content become cylindrical as the water content increases. With a

further increase in water, the cylinders become interconnected. Controlling the structure of micellar system is a useful tool in shape control of nanoparticles (Tanori and Pileni, 1995). Lisiecki (Lisiecki, 2005) summarises the key parameters which enable the size control of spherical nanoparticles produced in spherical reverse micelles as the degree of hydration of the reactants, the dynamic character of the micelles, the capping with the surfactant, and the reducing agent concentration.

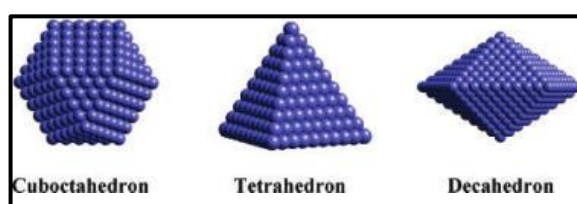


**Figure 1.2.** Representation of the stable nuclei for the formation of copper nanoparticles. Reproduced with permission from (Salzemann *et al.*, 2004b).

A great deal of work has been done with copper(II) bis (2-ethylhexyl) sulfosuccinate,  $Cu(AOT)_2$  as the copper source (Salzemann *et al.*, 2004b). A mixture of  $Cu(AOT)_2$  and  $Na(AOT)$  solubilized in iso-octane forms spherical reverse micelles. The ratio  $R$ ,  $R = [N_2H_4]/[Cu(AOT)_2]$  is defined for the concentration of reducing agent relative to that of the copper precursor. At low concentration of reducing agent, nanocrystals are mostly spherical with very small amounts of triangular and elongated nanocrystals. At higher concentrations, highly faceted, larger, and more crystalline shapes such as triangles, cubes and elongated forms are observed. For copper, the stable nuclei are cuboctahedral, tetrahedral, and decahedral, shown in **Figure 1.2**, which then grow to cube, trigonal lamellar and elongated shapes during nanocrystal growth in the large excess of reducing agent. The cuboctahedral nucleus shown in **Figure 1.3.A**, having surfaces made with  $\{100\}$  and  $\{111\}$  facets, can be grown into cubes of copper nanocrystals (Filankembo *et al.*, 2003; Filankembo and Pileni, 2000)

which are characterized by only  $\{100\}$  facets (Salzemann *et al.*, 2004b). This occurs by the specific growth of  $\{111\}$  facets of the cuboctahedral nucleus (**Figure 1.3.A**). This behaviour is explained by the selective adsorption of present capping agent in the reaction mixture like *AOT* on  $\{100\}$  facets, which prevents the growth of  $\{100\}$  facets resulting in cubes with  $\{100\}$  facets as the dominant surface of the Cu nanocrystal.

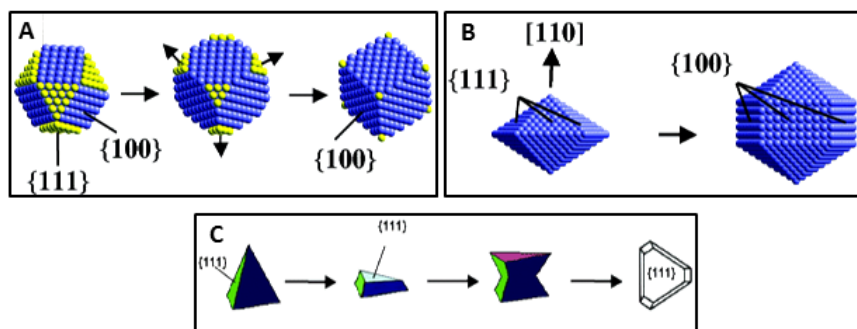


**Figure 1.3.** Schematic illustration of the growth mechanism of (A) cubic and (B) elongated (C) trigonal lamellar copper nanocrystals in reverse micelles synthesis. Reproduced with permission from (Salzemann *et al.*, 2004b).

The decahedral precursor shown in **Figure 1.3.B**, is formed of five deformed tetrahedra bound by  $\{111\}$  planes which are twinned and share a single edge. The elongation along the  $[110]$  direction, the 5-fold axis, exposes  $\{100\}$  surfaces on the sides of the elongated nanocrystal (Salzemann *et al.*, 2004b) (**Figure 1.3.B**). Such a formation is again explained by the preferential growth of the  $\{111\}$  facets compared to the growth of the  $\{100\}$  facets.

Flat triangles (**Figure 1.3.C**) known as trigonal lamellar particles, are also formed from tetrahedra but they are truncated on the  $\{111\}$  plane and then twinned by reflection at this surface, producing a stable nucleus (Salzemann *et al.*, 2004b).

The effect of addition of certain salts, including chloride and bromide ions, on surfactant (*AOT*) capping was also investigated. Chloride anions adsorb more efficiently on the {100} facets of the truncated decahedron than *AOT* molecules resulting in the production of longer elongated particles and giving a method of controlling the length of the metal particle. By adding bromide ions, elongated particles sizes do not change drastically, but the growth of cubic nanoparticles is promoted by selective adsorption.

Similarly, the presence of hydrazine as a reducing agent in the production of nanoparticles is expected to affect the morphology via important interactions at the surface by altering both the nucleation and growth rate of the particles. Although the reverse micelles synthesis work has achieved much in the control of the size and shape of copper nanoparticles, further experimental or computational investigations are needed to enable greater understanding of the processes occurring during nucleation and growth.

## **1.2. Copper nanoparticles for direct hydrazine fuel cell**

A fuel cell (FC) is an electrochemical device that converts the chemical energy of fuels directly into electrical energy. Due to their high efficiency, they are considered as the mostly used power source of next generation with applications from mobile devices to automobiles and space ships. There are several types of fuel cell which have been developed over the last four decades (Miley *et al.*, 2007; Minh, 1993; Springer *et al.*, 1991; Carrette *et al.*, 2000; Parsons and Vandernoot, 1988; Yamamoto, 2000; Demirci, 2007). One of those are proton exchange membrane fuel cells (PEMFCs) based on using hydrogen under high pressure as fuel, which are suitable as a power source for vehicles, mobile electric appliances, space and military

applications, because they do not affect air, health and environment by emission of toxic substances and carbon dioxide. However, the high-density storage of hydrogen problem has limited the widespread use of this type of fuel cell. It is therefore desirable to use a liquid fuel with high energy density that has improved ease of handling.

Direct fuel cell systems, where fuel is directly supplied to the fuel cell are beneficial for vehicles and mobile electric appliances (Waidhas *et al.*, 1996). The direct methanol fuel cell (DMFC) is a promising candidate of the direct fuel cell system (Ren *et al.*, 1996; Dyer, 2002). However, they still have a number of drawbacks, including severe poisoning of the anode catalyst by reaction intermediates such as CO, which causes a low cell voltage and requires a high loading amount of expensive catalysts like platinum. Thus, there is a need for more research to develop stable and low-cost efficient non-platinum catalysts (Serov and Kwak, 2009a; Serov *et al.*, 2007; Serov *et al.*, 2008; Serov and Kwak, 2009b; Serov *et al.*, 2009; Serov *et al.*, 2010). In addition, methanol crossover from anode to cathode through the electrolyte membrane significantly reduces the fuel cell performance and durability (Wang *et al.*, 1996; Kauranen and Skou, 1996). Therefore, investigations of new types of liquid-fed fuel cells are necessary to enable practical applications for instance, hydrazine ( $N_2H_4$ ), as a fuel for fuel cells has been studied since the 1970s (Tamura and Kahara, 1976; Andrew *et al.*, 1972). The reasons for considering hydrazine as an ideal fuel are:

- It does not exhaust environmentally loading materials such as  $CO_2$ , reducing the overall emission of greenhouse gases.

- It is a carbon free molecule leading to zero production of species like CO that may poison the electro-catalysts.
- It has high theoretical electromotive force at 1.56 V (Blomen and Mugerwa, 1993), leading to high power density.
- Hydrazine with hydrogen content of 12.5 wt% is a good source for on board hydrogen generation in PEMFCs, *e.g.* in space vehicles or satellites (Zheng *et al.*, 2005; Schmidt, 2001; Pakdehi *et al.*, 2014).

The total reaction of hydrazine electro-oxidation can be written as:



From the hydrolysis of hydrazine-water solutions, the hydrazonium cation is produced according to the equation (1.2);



According to equations (1.3) and (1.4), the oxidation of hydrazine on the anode is possible in both acidic and alkaline solutions;



The cathodic reaction is shown as follows;



There are some studies using less expensive metals *e.g.* Ag, Pd and Cu in direct hydrazine fuel cells (DHFCs) (Gao *et al.*, 2007; Yi *et al.*, 2008; Yang *et al.*, 2008; Ye

*et al.*, 2008; Dong *et al.*, 2008; Tan *et al.*, 2009; Chen *et al.*, 2009; Shen *et al.*, 2009; Karim-Nezhad *et al.*, 2009). Copper, due to its low cost and high conductivity, is a good catalyst for this purpose. Granot *et al.* fabricated a hydrazine/air direct liquid fuel cell using nanostructured copper anodes and showed that the fuel cell has high electrical efficiency for long periods (Granot *et al.*, 2012). The fuel cell was constructed with a Cu/hydrazine anode, combined with a commercial air cathode coated by a protective layer of polyvinyl alcohol (PVA), and polyethylene glycol (PEG), shown in **Figure 1.4**. The  $\text{OH}^-$  ions formed at the cathodic side (electro-reduction of oxygen), are transferred through the protective layer and are consumed at the anodic side (electro-oxidation of hydrazine), shown in **Figure 1.4**.

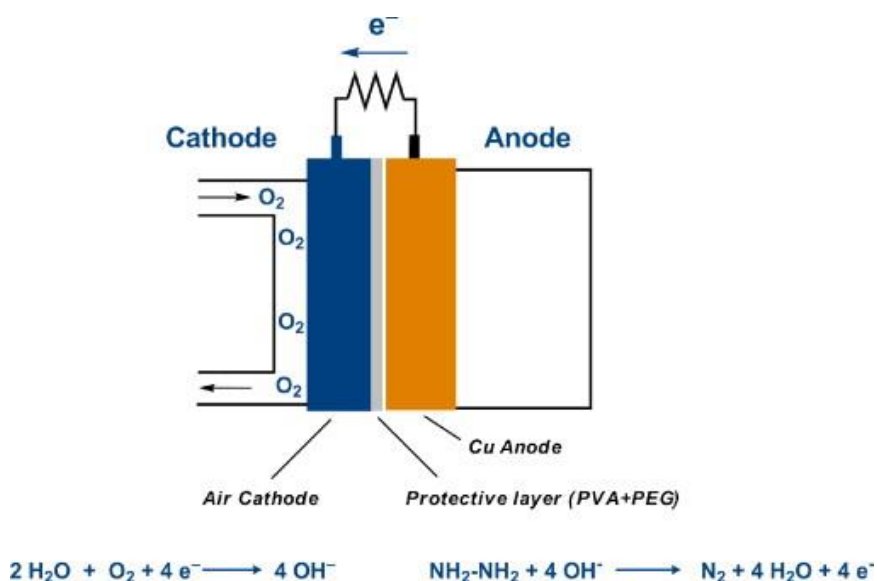


**Figure 1.4.** General description of a room-temperature hydrazine/air direct-liquid fuel cell (DLFC), based on the use of nanostructured copper electrodes. Reproduced with permission from (Granot *et al.*, 2012).

There is a need for more computational and experimental investigations to understand what is happening on the Cu electrode of the hydrazine/air direct liquid fuel cell and be able to know more about the mechanism of hydrazine interaction

with the Cu surfaces such as determining the rate-limiting step and the effects of inclusion of defects on the Cu surfaces.

### 1.3. Adsorption of hydrazine on metal surfaces

To understand more about the interaction of hydrazine with metal surfaces, it is interesting to know how hydrazine adsorbs on them. Hydrazine can take various structural conformations due to its ability of taking its  $\text{NH}_2$  group to rotate internally around its N–N axis (Kasuya and Kojima, 1963). As a result of this rotation, hydrazine has three conformations; gauche, trans and eclipsed as shown in **Figure 1.5**. Most studies regarding different hydrazine conformations, reported that the gauche is the most stable configuration in the gas-phase (Williams *et al.*, 1981; Chungphillips and Jebber, 1995; Riggs and Radom, 1986). Experimental works relating to hydrazine adsorption on Fe(111) (Grunze, 1979) and Pt(111) (Alberas *et al.*, 1992) showed that hydrazine is adsorbed in its eclipsed-conformation. Furthermore, theoretical studies on Ir(111) (Zhang *et al.*, 2011) and Pd(111) (Zhou *et al.*, 2011) confirmed hydrazine adsorption in its eclipsed-conformation. However other theoretical works showed that hydrazine is adsorbed in its gauche-conformation, such as adsorption on Cu(111), Cu(110), Cu(100) (Daff *et al.*, 2009) and Fe(211) (McKay *et al.*, 2011). A preference for adsorption in the trans-configuration is observed on Pt(111) (Agusta *et al.*, 2011), Ni(100) (Agusta *et al.*, 2010) and Ni(111) (Agusta and Kasai, 2012).

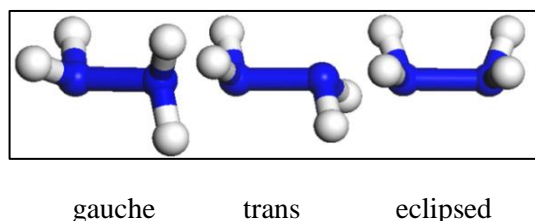


**Figure 1.5.** Hydrazine conformations: gauche, trans and eclipsed.

## 1.4. Dissociative adsorption of hydrazine on metal surfaces

Understanding of the mechanism of the decomposition of hydrazine on metal surfaces is of interest owing to its applications in different fields. First of all, although hydrazine is a toxic substance, its decomposition products are N<sub>2</sub>, H<sub>2</sub> and NH<sub>3</sub>, which are non-poisonous and CO-free (Zheng *et al.*, 2005). Furthermore, it has application in ammonia synthesis (Block and Schulzek.G, 1973; Grunze, 1979). In addition, hydrazine as a substance with hydrogen content of 12.5 wt % is a good hydrogen source for PEMFCs and since it is liquid at a temperature range from 2°C to 114°C is ideal for portable applications, *e.g.* in space vehicles or satellites (Zheng *et al.*, 2005; Schmidt, 2001; Pakdehi *et al.*, 2014). The decomposition of hydrazine is also applied in monopropellant thrusters to control and adjust the orbits and altitudes of spacecrafts and satellites (Mary *et al.*, 1999; Schmidt, 2001). This is possible due to the production of larger volumes of N<sub>2</sub>, H<sub>2</sub> and NH<sub>3</sub> gases from decomposition of a relatively small volume of liquid hydrazine. The most important catalyst used for this reaction is Ir/Al<sub>2</sub>O<sub>3</sub> with a high loading of the iridium (20 – 40 %) (Mary *et al.*, 1999; Balcon *et al.*, 2000; Schmidt, 2001; Contour and Pannetie.G, 1972). However, due to the high price and limited resources of iridium, scientists are seeking to develop new, cheaper, active and readily available alternative catalysts for N<sub>2</sub>H<sub>4</sub> decomposition.

We aim to investigate the catalytic activity of Cu towards  $N_2H_4$  decomposition at a molecular level to better understand the thermodynamics and kinetics of every elementary step. Experimental studies revealed that the adsorption of  $N_2H_4$  on copper at lower temperatures is likely to be reversible and non-dissociative up to  $\sim 300$  K, above which the hydrazine decomposes and generates the gaseous products,  $NH_3$ ,  $N_2$  and  $H_2$  (Matloob and Roberts, 1977; Alhaydari *et al.*, 1985).

There are two typical reactions for hydrazine decomposition, equations (1.6) and (1.7) (Contour and Pannetie.G, 1972; Maurel and Menezo, 1978; Tong *et al.*, 2010);

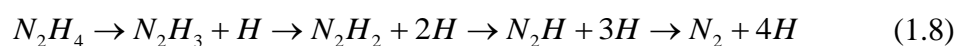


The competition between these two reactions depends on the catalyst and reaction conditions such as temperature and pressure (Grunze, 1979).

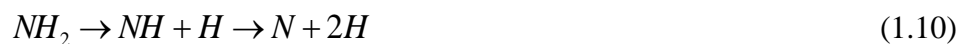
Despite a number of theoretical and experimental studies on hydrazine decomposition (Alberas *et al.*, 1992; Huang *et al.*, 1993; Gland *et al.*, 1985; Dopheide *et al.*, 1991; Grunze, 1979; Johnson and Roberts, 1980; Wood and Wise, 1975a; Volter and Lietz, 1969; Cosser and Tompkins, 1971b; Bu *et al.*, 1992; Prasad and Gland, 1991c), the mechanism is not completely clear and is still controversial.

There are mainly two possible paths for hydrazine decompositions:

- i) Step by step elimination of H atoms leading to the formation of  $N_2$  and  $H_2$  which is observed for the decomposition of hydrazine on Ni(100) (Huang *et al.*, 1993) and Pt(111) (Alberas *et al.*, 1992);



- ii) N–N bond of hydrazine breaks first, then each NH<sub>2</sub> fragment dehydrogenates and forms N<sub>2</sub> and H<sub>2</sub> molecules;



This mechanism is observed on Fe(111) (Grunze, 1979), Ni(111) (Gland *et al.*, 1985), Pd(100) (Dopheide *et al.*, 1991), polycrystalline aluminium (Johnson and Roberts, 1980), polycrystalline iridium foil (Wood and Wise, 1975a) and transition metals (Cr, Mn, Fe, W, Re and Os) (Volter and Lietz, 1969; Cosser and Tompkins, 1971b).

Some surfaces prefer path (i) at low temperatures, while at high temperatures, path (ii) seems to take place *e.g.* on Si(111) (Bu *et al.*, 1992), Rh(111) (Wagner and Schmidt, 1991) and polycrystalline rhodium surfaces (Prasad and Gland, 1991c). Both paths are likely to take place on Ru(001) (Rauscher *et al.*, 1993).

Also, NH<sub>2</sub> molecules produced via path (ii) can be hydrogenated to yield NH<sub>3</sub> molecules (Grunze, 1979; Volter and Lietz, 1969; Wagner and Schmidt, 1991; Falconer and Wise, 1976);



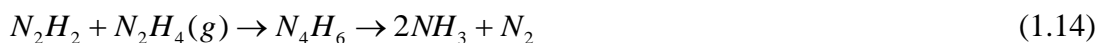
In addition to these pathways, there are other mechanisms on surfaces such as Rh(111) (Wagner and Schmidt, 1991) at low temperatures where proton transfer in hydrazine produces NH<sub>3</sub>;



Production of  $\text{NH}_3$  can take place via the hydrogenation of hydrazine on Pt(111) (Alberas *et al.*, 1992), polycrystalline aluminium (Johnson and Roberts, 1980) and tungsten film (Cosser and Tompkins, 1971b);



Also, reaction between the adsorbed  $\text{N}_2\text{H}_2$  intermediate and  $\text{N}_2\text{H}_4$  in the gas phase produces  $\text{N}_2$  and  $\text{NH}_3$  molecules (Wood and Wise, 1975a);



DFT studies of hydrazine decomposition on the Ir(111) surface suggest the formation of two  $\text{NH}_2$  radicals via N–N bond breaking and the reaction of the newly formed  $\text{NH}_2$  with a hydrazine molecule or  $\text{N}_2\text{H}_x$  ( $x=1-3$ ) species. The capture of H atoms leads to the formation of  $\text{N}_2$  and  $\text{NH}_3$  products (Zhang *et al.*, 2011).

Also, the study of the dissociative chemisorption of hydrazine on the Fe(211) surface (McKay *et al.*, 2011) showed that dehydrogenation and nitrogen decoupling are competitive routes for hydrazine decomposition, while  $\text{NH}_2$  and N adatoms are the dominant surface products at low-to-moderate temperatures. However, adsorbed molecular  $\text{N}_2$  will not be produced by the dehydrogenation of  $\text{N}_2\text{H}_x$ , but must be formed from N adatoms or via some multi-hydrazine coupling mechanism.

Daff *et al.* (Daff and de Leeuw, 2012) reported that the thermodynamics of dissociative adsorption via the breaking of the hydrazine N–N bond shows that this bonding mode is strongly favoured over molecular adsorption both on the planar surface and on the adatom of Cu surfaces.

## 1.5. Overview of the thesis

In this thesis, we have used computational methods based on DFT that have been applied to copper metal based systems with the aim of understanding the interaction between hydrazine and copper at the molecular level.

This Chapter contains a survey of relevant literature about the different applications of the copper-hydrazine system that form the major motivation behind this project. A summary of prior relevant and similar modelling and experimental studies were reported. Chapter 2 describes theoretical and practical information about the methodology employed in this work, namely Density Functional Theory (DFT).

Chapter 3 provides details of the adsorption of a single  $\text{N}_2\text{H}_4$  molecule on the perfect low-index copper surfaces and the effect of inclusion of long-range interactions has been shown.

Chapter 4 gives a theoretical insight into the interaction of a single  $\text{N}_2\text{H}_4$  with defect-containing Cu surfaces to shed light on the effect of inclusion of low-coordinated sites on the adsorption process. Chapter 5 includes the results of the simulation of  $\text{N}_2\text{H}_4$  networks on Cu(111) to provide insight into the interplay between lateral adsorbate-adsorbate and vertical adsorbate-substrate interactions.

Chapter 6 presents the results of simulation of  $\text{N}_2\text{H}_4$  decomposition on the planar and stepped Cu(111) surfaces in order to find the favoured decomposition mechanism from thermodynamic and kinetic points of view. We have also investigated the effect of the step on the  $\text{N}_2\text{H}_4$  decomposition. Finally, in Chapter 7, the microkinetic simulation of  $\text{N}_2\text{H}_4$  decomposition were carried out to develop our understanding of the catalytic process of  $\text{N}_2\text{H}_4$  dissociation on the planar Cu(111) surfaces.

A summary that discusses the results and an outline of possible future works concludes this thesis in Chapter 8.

## *Chapter 2: Computational methods*

### **Abstract**

In this Chapter we discuss the methods and theory behind the simulations that have been employed throughout the research presented in this thesis. Density functional theory (DFT) has been chosen as an accurate technique that can provide electronic structure information about the systems under consideration. Within this framework, the Vienna Ab-initio Simulation Package (VASP) has been used throughout this thesis.

## 2.1. Schrödinger equation

The time-independent Schrödinger equation (Schrodinger, 1926), as the key equation of quantum mechanics, for a system of  $M$  nuclei and  $N$  electrons, described respectively by the coordinates  $R \equiv R_1, \dots, R_M$  and  $r \equiv r_1, \dots, r_N$  has the general form:

$$\hat{H}\Psi(r, R) = E\Psi(r, R) \quad (2.1)$$

Where  $\hat{H}$  is the Hamiltonian operator and  $\Psi(r, R)$  is the wave function and eigenstates of the Hamiltonian where each of them has an associated eigenvalue,  $E$ , a real number representing the energy and satisfies the eigenvalue equation. A more complete description of the Hamiltonian is:

$$\hat{H} = \hat{T}_e + \hat{T}_N + \hat{V}_{eN} + \hat{V}_{ee} + \hat{V}_{NN} \quad (2.2)$$

Where  $\hat{T}_e$  and  $\hat{T}_N$  are the kinetic energy operators of electron and nuclei respectively:

$$\hat{T}_e = -\sum_{i=1}^N \frac{1}{2} \nabla_i^2 \quad (2.3)$$

$$\hat{T}_N = -\sum_{I=1}^M \frac{1}{2M_I} \nabla_I^2 \quad (2.4)$$

Where  $M_I$  represents the ratio of the mass of nucleus  $I$  to the mass of an electron.

The Laplace operator ( $\nabla^2$ ) is the second derivative with respect to the spatial coordinates of the electron or nucleus.

$\hat{V}_{eN}$ ,  $\hat{V}_{ee}$  and  $\hat{V}_{NN}$  are the potential energy operators of attractive electron-nucleus, repulsive electron-electron, and nucleus-nucleus interactions:

$$\hat{V}_{eN} = -\sum_{i=1}^N \sum_{I=1}^M \frac{Z_I}{r_{iI}} \quad (2.5)$$

$$\hat{V}_{ee} = \sum_{i=1}^N \sum_{j>i}^N \frac{1}{r_{ij}} \quad (2.6)$$

$$\hat{V}_{NN} = \sum_{I=1}^M \sum_{J>I}^M \frac{Z_I Z_J}{R_{IJ}} \quad (2.7)$$

The above equations are given in atomic units, where  $r_{ij}$ ,  $r_{iI}$  and  $R_{IJ}$  are the  $i^{\text{th}}$ - $j^{\text{th}}$  electrons,  $i^{\text{th}}$  electron- $I^{\text{th}}$  nucleus and  $I^{\text{th}}$ - $J^{\text{th}}$  nuclei distances respectively.  $Z_I$  and  $Z_J$  are the atomic numbers of nuclei  $I$  and  $J$ .

The exact solution to this Schrödinger equation for many-body problems which involves dealing with a system of  $N$  electrons and  $M$  nuclei is impossible and a series of approximations are necessary to help simplify the problem.

One such approximation is the Born-Oppenheimer which is based on the fact that the nuclei are much heavier than the electrons (Born and Oppenheimer, 1927). It is therefore possible to assume that electrons move faster than nuclei and treat nuclei as being stationary in relation to the moving electrons. Within this approximation, the Hamiltonian in the Schrödinger equation is simplified by neglecting the kinetic term  $\hat{T}_N$ , and considering the repulsion  $\hat{V}_{NN}$  as a constant. The simplified equation is the electronic Hamiltonian:

$$\hat{H}_{el} \equiv \hat{T}_e + \hat{V}_{eN} + \hat{V}_{ee} \quad (2.8)$$

The many-body electron problem involves evaluation of the two-body coulomb interactions and exchange correlation in the third term which needs further approximations. Density functional theory (DFT) provides enormous simplifications for this problem.

## 2.2. Density functional theory

Density functional theory (DFT) solves the Schrödinger equation where the basic variable used is the ground-state electron density rather than N-electron wave functions. Fundamental to this theory, which is the most widely used method in the context of solid state simulation, are the Hohenberg-Kohn theorems (Hohenberg and Kohn, 1964) and Kohn-Sham equations (Kohn and Sham, 1965).

### 2.2.1. The Hohenberg-Kohn theorems

The first approach for solving many-body electron problem of Schrodinger equation was postulated by Hohenberg and Kohn (Hohenberg and Kohn, 1964). The two theorems can be formulated as follow:

- The first states that the external potential due to the nuclei,  $V_{ext}(r)$ , felt by an arbitrary number of electrons is uniquely determined by the ground state electron density,  $n_0(r)$ . It therefore follows that all the properties of a physical system can be calculated if the electron density is known.
- Second theorem states that for any external potential,  $V_{ext}(r)$ , there is a functional for the energy  $E[n(r)]$  of an electronic system. The ground state energy of a system for a given external potential is the global minimum of this functional and the electron density which gives the minimum value of the

functional must be the electron density in the ground state  $n_0(r)$ . Thus the total energy functional can be written as follows:

$$E[n(r)] = \int V_{ext}(r)n(r)dr + F[n(r)] \quad (2.9)$$

The functional  $F[n(r)]$ , is the electronic part of the Hamiltonian and contains the kinetic energy of electrons as well as electron-electron repulsion, exchange and correlation energies.

The Schrödinger equation can be rewritten now as a function of the electron density,  $[n(r)]$ :

$$\hat{T}[n(r)] + \hat{V}_{ee}[n(r)] + \hat{V}_{ext}[n(r)]\psi = E[n(r)]\psi \quad (2.10)$$

Despite all the above demonstrations, there is still the problem of calculating the electron-electron repulsion term of the above equation and thus no practical way of determining the ground state density of the system. This issue was solved by Kohn and Sham (Kohn and Sham, 1965).

### 2.2.2. The Kohn-Sham Theory

Kohn and Sham developed the approach of early density functional theory by assuming that the many-body electronic wave function acts in a same way as a fictitious single-particle non-interacting wave functions which are called Kohn-Sham (KS) one-electron orbitals  $\psi_i$  and defined as follows:

$$n(r) = \sum_{i=1}^N |\psi_i|^2 \quad (2.11)$$

The Kohn-Sham equation is therefore used to find the one-electron orbitals that minimize the equation of energy:

$$\hat{H}^{KS}\psi_i = \varepsilon_i^{KS}\psi_i \quad (2.12)$$

Thus the Kohn-Sham Hamiltonian,  $\hat{H}^{KS}$ , acting on each electron is:

$$\hat{H}^{KS} = -\frac{1}{2}\nabla_i^2 - \sum_{A=1}^M \frac{Z_A}{|r-R_A|} + \frac{1}{2} \int \frac{n(r')}{|r-r'|} dr' + V_{xc}(r) \quad (2.13)$$

Where the first term represents the kinetic energy of the non-interacting system, the second term represents the external potential from nuclei ( $A$ ) felt by the electron, where there is a distance of  $r-R_A$  between the electron and nuclei, the third term represents the coulombic repulsion between the particular electronic density with the other electrons in the system and the last term represents the exchange-correlation potential which is equal  $\frac{\delta E_{xc}[n(r)]}{\delta n(r)}$ .  $E_{xc}[n(r)]$  is the exchange-correlation energy

which accounts for the differences between interacting and non-interacting systems and, as it is unknown, approximations must be made to describe this term.

### 2.2.3. Exchange correlation functionals: LDA and GGA

The exchange-correlation term  $E_{xc}[n(r)]$  consists of a correction to the one-particle kinetic energy and coulombic repulsion. It is the difference between the energy obtained from the non-interacting system and the exact energy from the real system. The exchange-correlation term also includes a correction for electron self-interaction where an electron has coulombic interaction with itself.

Two of the most commonly used approximations for calculation of exchange-correlation functional are local density approximation (LDA) and generalised gradient approximation (GGA).

In the LDA, the exchange-correlation energy at point  $r$  is determined using only the electron density,  $n(r)$ , at that point, and not dependent on the density at other points. In this approximation, the exchange-correlation of a real system behaves locally as a uniform, homogeneous electron gas of the same system. The LDA exchange-correlation energy has the form:

$$E_{xc}^{LDA}[n(r)] = \int n(r) \varepsilon_{xc}^{\text{hom}}[n(r)] dr \quad (2.14)$$

Where  $\varepsilon_{xc}^{\text{hom}}$  is the exchange-correlation energy per particle of a uniform electron gas. The LDA works well for the systems where the density remains almost constant over the space like metals. Although the LDA is good at calculating of geometries, vibrational frequencies and charge densities, it has a tendency to overestimate binding energies.

An obvious approach to improve the LDA is to include the gradient of the electronic density,  $|\nabla n(r)|$ , as an independent variable leading to GGA exchange-correlation approximation which introduces non-local effects on the functional:

$$E_{xc}^{GGA}[n(r)] = \int n(r) \varepsilon_{xc}^{LDA}[n(r), \nabla n(r)] dr \quad (2.15)$$

This functional considers fast varying changes in the electron density, which are not accounted for by LDA, resulting in better geometries, vibrational frequencies, charge densities and binding energies than LDA. The most common GGA functionals are

Perdew, Burke and Ernzerhof (PBE) (Perdew *et al.*, 1996), and Perdew and Wang (PW91) (Perdew and Wang, 1992).

### 2.3. Dispersion correction (DFT-D2)

Standard DFT fails to describe properly the weak, non-local, long-range dispersion forces, which may be occurring within the system. The most common form of dispersion correction for DFT is the Grimme method known as DFT-D2 (Grimme, 2004; Grimme, 2006). It leads to a more accurate geometry and structural energy, with a minimal increase in computational cost. Compared to the other dispersion correction methods, DFT-D2 requires fewer fitted parameters and is less empirical. In this scheme, an extra energy term ( $E_{disp}$ ) is added to the conventional Kohn-Sham DFT energy ( $E_{KS-DFT}$ ):

$$E_{DFT-D2} = E_{KS-DFT} + E_{disp} \quad (2.16)$$

Where

$$E_{disp} = -S_6 \sum_{i=1}^{N-1} \sum_{j=i+1}^N \frac{C_6^{ij}}{R_{ij}^6} f_{damp} R(ij) \quad (2.17)$$

Where  $N$  is the number of atoms in system,  $C_6^{ij}$  is the dispersion coefficient for the atom pair  $ij$  and is proportional to atomic polarizabilities and ionization energies,  $S_6$  is a global scaling factor that depends on the DFT functional used, and  $R_{ij}$  represents the distance between atoms  $i$  and  $j$ . A damping function,  $f_{damp}$ , must be used in order to avoid double counting for small interatomic distances, as follows:

$$f_{damp}(R_{ij}) = \frac{1}{1 + e^{-d(R_{ij}/R_{vdW}-1)}} \quad (2.18)$$

Where  $d$  is the damping parameter and  $R_{vdW}$  is the sum of the atomic van der Waals radii of the atoms  $i$  and  $j$ .

## 2.4. Basis sets

Basis sets are one of the approximations used in all quantum mechanical calculations, which enable molecular orbitals to be described by linear combination of atomic orbitals (LCAO):

$$\psi_i = \sum_{k=1}^n c_{ki} \phi_k \quad (2.19)$$

Where  $\psi_i$  is the  $i^{\text{th}}$  molecular orbital,  $c_{ki}$  are the coefficients for linear combination,  $\phi_k$  is the  $k^{\text{th}}$  atomic orbital, and  $n$  is the number of atomic orbitals. The solution of Kohn-Sham equation is based on the one-electron orbitals, which are also called basis functions, and often corresponds to the atomic orbitals in the equation above. The main objective is to find the best set of coefficients for which the energy of system is a minimum:

$$\frac{\partial E}{\partial c_{ki}} = 0 \quad (2.20)$$

In order to have an accurate solution, we need to have an infinite number of basis functions, which is impossible, because more basis functions means more computational cost, therefore a right balance between accuracy and cost is required. The basis sets used in quantum chemistry calculations include localized atomic

orbitals and plane-waves basis sets. The atomic orbitals centre on each atom within molecules in the localized basis set, while plane-waves do not depend on the position of the atoms and are completely delocalized. Basis set superposition error (BSSE) is the main problem of using localized basis sets where there is an overlap between basis sets when two particles approach each other. The plane-wave basis sets were used in this thesis through the vienna ab-initio simulation package (VASP).

### 2.4.1. Periodicity and plane-wave basis sets

For simulation of a bulk solid material with many atoms, symmetry elements can help us to simplify the system by simulating a unit-cell of the solid that can be repeated in three dimensions. When a periodic system is being treated, Bloch's theorem (Bloch, 1928) can be used where the wave function of an electron can be written as product of a periodic cell and a wavelike part:

$$\Psi_{i,k}(r) = f_{i,k}(r)e^{ik \cdot r} \quad (2.21)$$

Where  $f_{i,k}(r)$  has the periodic character of the cell and may be expanded in terms of a Fourier series:

$$f_{i,k}(r) = \sum_G c_{i,k,G} e^{iG \cdot r} \quad (2.22)$$

Where  $G$  is the reciprocal lattice vector and  $c$  represents the plane-wave expansion coefficients. The wave function of electron may therefore be written as a sum of plane-waves by substituting equation (2.22) in (2.21):

$$\Psi_{i,k}(r) = \sum_G c_{i,k+G} e^{i(k+G) \cdot r} \quad (2.23)$$

In principle, an infinite number of plane-waves in the equation above are needed. However it is impossible and as plane-waves with high kinetic energy are less important, we introduce only those plane-waves with kinetic energies less than certain cut-off in order to have a finite basis set that sufficiently converges the total energy calculation:

$$\frac{\hbar(k + G)^2}{2m} < E_{cutoff} \quad (2.24)$$

In order to solve Kohn-Sham equation and find the ground state density, an integral over all  $\mathbf{k}$ -point is required in the first Brillouin zone which is the primitive cell in reciprocal space. Since the electron wave-functions will be almost the same for the  $\mathbf{k}$ -points that are close to each other, we can consider a single  $\mathbf{k}$ -point over a region of reciprocal space and replace the integral with a finite sum over distinct  $\mathbf{k}$ -points. A very popular scheme to define these  $\mathbf{k}$ -points is Monkhorst-Pack method (Monkhorst and Pack, 1976) which is an equally-spaced mesh to sample the Brillouin zone.

There is still one problem with using plane-waves basis set, where both core and valence electrons need to be treated increasing computational cost. The pseudopotential approximation reduces this problem by treating only valence electrons.

## 2.5. Pseudopotentials

It is known that very internal electrons do not significantly contribute to chemical bonding and the majority of physical properties of solids depend on the valence electrons. Hence, the core electrons can be considered as being frozen and the

coulomb potential of the core electrons and nucleus may be replaced with a pseudopotential acting on a set of pseudo-wave-functions of valence electrons, resulting in fewer plane-waves reducing the computational cost significantly.

Different kind of pseudopotentials are available, such as non-conserving (Hamann *et al.*, 1979) and ultrasoft pseudopotentials (Vanderbilt, 1990). Among the most used pseudopotential methods, the projector augmented-wave (PAW) method (Blochl, 1994; Kresse and Joubert, 1999) produces more accurate results than other pseudopotentials, because even it is a frozen-core method, it has access to the full all-electron wave-function, meaning that PAW describes core electrons with a frozen nodal structure and valence electrons by an all-electron wave-function.

## 2.6. Geometry optimization

In order to determine the optimized geometry, a minimization of energy is needed. The conjugate gradients method is one of the several algorithms used to find the minimum of a function with several variables (Gill *et al.*, 1981). In our calculations using VASP, the conjugate gradients method is used. It works by calculating the energy and its derivative with respect to nuclei coordinates, the latter of which is described as the force on the ions by Hellmann-Feynman theorem (Hellmann, 1937; Feynman, 1939). In this method, the first step to find the minimum energy takes place opposite the direction of the largest gradient of energy, *i.e.* the direction for which E decreases the fastest. Each direction is obtained from:

$$d_k = \Delta E_k + \gamma_k d_{k-1} \tag{2.25}$$

Where the direction  $d_k$ , starting from point  $r_k$ , is computed from the gradient at the point of previous direction of  $d_{k-1}$  and  $\gamma_k$  is given by:

$$\gamma_k = \frac{\Delta E_k \cdot \Delta E_k}{\Delta E_{k-1} \cdot \Delta E_{k-1}} \quad (2.26)$$

As the equations above show, the idea of this method is that each direction is chosen from the information from all the previous (conjugate) directions.

## 2.7. Analysis of systems

In this section we provide the methodologies derived from DFT that we have used to characterize some properties of the systems under investigation.

### 2.7.1. Transition state

A transition state (saddle point) is the state on the minimum energy path (MEP) that has the highest energy along the reaction coordinate. Knowing the energy of the transition state helps us to calculate the activation energy barrier.

Many different methods have been developed for calculating the MEP and saddle points. A combination of two varieties of the nudged elastic band (NEB) method (Mills and Jonsson, 1994; Mills *et al.*, 1995) and the improved dimer method (IDM) (Heyden *et al.*, 2005) were used in this thesis.

The NEB method finds saddle points between known initial and final states. The method works by optimizing a number of intermediate images between reactants and products. There is a spring interaction between adjacent images of the path to keep continuity of the band like an elastic band. The optimization of the images takes

place decreasing the forces on their atoms leading to the minimum energy on the path.

The IDM is the modified version of the original dimer method proposed by Henkelman and Jónsson (Henkelman and Jonsson, 1999) which has been implemented in VASP. The method works by specifying only one initial state and its dimer axis.

In this thesis, we have used the NEB method only for finding the images between initial and final states and then for those two images, which are closest to the saddle point, the IDM method was used to find the optimised saddle point. The transition state was further verified by a single imaginary frequency associated with the reaction coordinate. The activation energy barrier ( $E_a$ ) was defined as the energy difference between the saddle point and the initial state.

### **2.7.2. Vibrational frequencies**

In any steady state, the forces or first derivatives of the potential energy are zero and the second derivatives are positive. Since vibrational frequencies are related directly with the second derivatives of the potential, they are all real at a minimum, whereas there is one imaginary frequency for a transition state, related with the reaction coordination.

In VASP, each ion is allowed to move in the direction of each Cartesian coordinate and then the second derivatives of a potential are calculated from the energy gradients variation in these displacements leading to the Hessian matrix (matrix of the second derivative of the energy with respect to the atomic positions). The vibrational frequencies are determined by the eigenvalues of the Hessian matrix.

### 2.7.3. Density of states

The density of states (DOS) describes the number of states at each energy level, which are available for occupation by electrons. A high DOS means that there are many states available to be occupied at that energy level and zero DOS means that no states are available for occupation at that energy level. In solid systems with a large number of atoms, the energy levels are so close to each other that continuous bands are formed. There are two characteristic bands, the valence band, which contains the highest-in-energy occupied states and is below the Fermi level ( $E_F$ ), and the conduction band which includes unoccupied states and is above the Fermi level. The projected DOS, PDOS, can be projected onto atomic orbitals to study the states involved in chemical bonds. Changes in the position and intensity of the interacting bands can help us to understand charge transfers and interaction characters in the adsorption systems.

### 2.7.4. Bader charge analysis

Decomposition of the electronic density of a material into separate atoms indicates charge transfer process and thus enlightens the characterization of the bonding character between an adsorbate and a substrate. The bader charge analysis method is based on a useful method of dividing molecules into atoms, called the theory of atoms in molecules (AIM), this in turn originates from the electronic charge density (Bader *et al.*, 1987). The electron density is divided into subsystems, which are separated by zero-flux surfaces. A zero flux surface is a 2-D surface on which the charge density is a minimum perpendicular to the surface. The volume enclosed by this surface is termed the Bader basin, inside of which the electron density is summed in order to find the atomic charge.

## 2.8. Catalysis

Catalysis is the process in which the rate of a chemical reaction is increased by a chemical substance called a catalyst. A catalyst offers an alternative, energetically favourable mechanism to the reaction by forming bonds with the reacting molecules. It is not consumed during the reaction and detaches unaltered from the products to be available for the next reaction.

Catalytic effectiveness is determined by two parameters: conversion and selectivity. The conversion is defined as the amount of reactant converted to the amount of reactant fed, *i.e.*,

$$X_A = \frac{F_{A0} - F_A}{F_{A0}} \quad (2.27)$$

Where,  $F_{A0}$  is the initial amount of reactant and  $F_A$  is the amount of reactant present in the reaction system.

The selectivity is the amount of formed desired product compared with the amount of converted reactant, *i.e.*,

$$S_P = \frac{F_P}{F_{A0} - F_A} * \frac{\nu_A}{\nu_P} \quad (2.28)$$

Where  $F_P$  is the amount of product present in the reaction system,  $\nu_A$  and  $\nu_P$  are the stoichiometric coefficients of the reactant and product, respectively.

Conversion and selectivity can be reported as dimensionless numbers ranging from 0 to 1 or 0 to 100 %.

There are three sub-disciplines in catalysis depending on the number and types of systems phases: homogeneous, bio-catalysis and heterogeneous.

In homogeneous catalysis both the catalyst and reactants are in the same phase, usually in the gas phase or liquid phase. Enzymes are nature's catalysts, which are highly specific and efficient as large proteins have very shape-specific active site to guide reactant molecules. In heterogeneous catalysis, the reactants and products are in different phase than the catalyst, which is usually in the solid phase. Since heterogeneous catalysts are the workhorses of the chemical and petrochemical industries, there are lots of efforts in the research of surface science towards the understanding of heterogeneous catalysis. The principal advantage of heterogeneous systems is that it is easy to separate the final products from the catalysts. One example of this is the Haber-Bosch process (Appl, 2000), where  $N_2$  and  $H_2$  react to yield  $NH_3$  on metallic iron, or the Fischer-Tropsch reaction (Kaneko *et al.*, 2000), where  $H_2$  and CO react to yield methanol or other hydrocarbons on some metallic oxides.

## 2.9. Microkinetic simulation

Kinetics studies provide the framework for describing the rate of a chemical reaction and enable us to find a reaction mechanism that describes how the molecules react to the final product. It also allows us to calculate the rate of reaction as a function of concentration, pressures and temperatures. Hence kinetics provides us with the tools to link the microscopic world of reacting molecules to the macroscopic world of industrial reaction engineering. Obviously, kinetics is a key discipline for catalysis (Chorkendorff and Niemantsverdriet, 2007).

Kinetics describes the behaviour of large ensembles of molecules during a reaction where the energies and coordinates of all reacting molecules are important. It therefore considers all the elementary steps of the process. How to deal with the kinetics of processes with more than one elementary step depends on the sort of reactor employed.

There are two types of reactor, namely the flow and batch reactor. The flow reactor is typically used in large-scale industrial processes. Reactants are continuously fed into the reactor at a constant rate, and products appear at the outlet, also at a constant rate. Such reactors are said to operate under steady state conditions, implying that both the rates of reaction and concentrations become independent of time (unless the rate of reaction oscillates around its steady state value). The batch reactor is generally used in the production of fine chemicals. At the start of the process the reactor is filled with reactants, which gradually convert into products. As a consequence, the rate of reaction and the concentrations of all participants in the reaction vary with the time. In the current work, batch reactor is used where it behaves as a well stirred tank reactor, such that all participants are well mixed and concentration gradients do not occur.

### 2.9.1. Rate equations

The rate of a reaction is defined as the rate of reactants disappearance, or the rate of products formation. For a reaction between molecules  $A$  and  $B$  as reactants and molecules  $C$  and  $D$  as products, the reaction equation is:



Where  $k^+$  and  $k^-$  are forward and backward rate constants, respectively, and  $\nu_a, \nu_b, \nu_c$  and  $\nu_d$  are stoichiometric coefficients. The rate of equation,  $r$ , is therefore defined as:

$$r = -\frac{1}{\nu_a} \frac{d[A]}{dt} = -\frac{1}{\nu_b} \frac{d[B]}{dt} = \frac{1}{\nu_c} \frac{d[C]}{dt} = \frac{1}{\nu_d} \frac{d[D]}{dt} \quad (2.30)$$

Where  $[X]$  is the concentration of component  $X$ . If the reaction occurs in the gas phase, we may replace the concentrations by partial pressures.

A reaction is elementary if it occurs in a single step that cannot be divided into further sub-steps. If there is an elementary step such as equation (2.29), the rate can be written as:

$$r = k^+ [A]^{\nu_a} [B]^{\nu_b} - k^- [C]^{\nu_c} [D]^{\nu_d} = r^+ - r^- \quad (2.31)$$

The temperature dependence of rate constant is given by Arrhenius equation:

$$k(T) = A_0 e^{-E_a/k_B T} \quad (2.32)$$

Where  $A_0$  is the pre-exponential factor,  $E_a$  is the activation energy and  $k_B$  is the Boltzman's constant.

### 2.9.2. Reaction mechanisms

In heterogeneous catalysis, a catalyst is considered as a collection of active sites (denoted by  $*$ ) on the surface, where all sites are equivalent. The fraction of occupied sites by the species  $A$  is shown by  $\theta_A$ . Since the total number of sites is constant, the fraction of unoccupied sites available for reaction,  $\theta_*$ , is given via:

$$\theta_* = 1 - \sum_{i=1}^n \theta_i \quad (2.33)$$

Where  $q_i$  represents the coverage of the intermediates present in the reaction system.

Catalytic processes include a number of elementary steps which may be difficult to be identified. From computational results, we can know the elementary steps from which we are able to derive rate equation for such processes. To solve the kinetics for a catalytic reaction as a set of elementary steps, as follow,



We need the differential equations describing the coverage and pressure of all species in the reaction:

$$\frac{dP_{A_2}}{dt} = -k_1 P_{A_2} \theta_*^4 + k_2 \theta_{A_2} \quad (2.36)$$

$$\frac{d\theta_{A_2}}{dt} = k_1 P_{A_2} \theta_*^4 - k_2 \theta_{A_2} - k_3 \theta_{A_2} + k_4 \theta_A^2 \quad (2.37)$$

$$\frac{d\theta_A}{dt} = 2k_3 \theta_{A_2} - 2k_4 \theta_A^2 \quad (2.38)$$

$$\theta_* = 1 - 4\theta_{A_2} - 2\theta_A \quad (2.39)$$

Although these equations can be solved numerically by a computer without any approximation, the rate constants must be calculated and there are many reaction rate theories which are capable of predicting the value of kinetics parameters.

### 2.9.3. Transition state theory (TST)

Transition state theory is a theory for the rate of a reaction, developed independently by Eyring (Eyring, 1935) and also Evans and Polanyi (Evans and Polanyi, 1935), which provides a basis for the Arrhenius equation, equation (2.32), to be able to interpret the meaning of a pre-exponential factor. TST considers the transition state as an activated complex at the top of the energy potential surface between reactants and products. The reaction event is described by the reaction coordinate, which is usually a vibration. If the reaction is the dissociation of a bond, then the reaction coordinate is the stretching vibration between the two atoms. According to the TST, the rate constant ( $k$ ) of each surface elementary step may be computed via the equation 2.40 that bears great resemblance to the Arrhenius equation;

$$k = A_0 \exp\left(\frac{-\Delta E^\ddagger}{k_B T}\right) = \frac{k_B T}{h} \frac{Q^\ddagger}{Q} \exp\left(\frac{-\Delta E^\ddagger}{k_B T}\right) \quad (2.40)$$

Where  $\Delta E^\ddagger$  is the reaction activation energy and;  $Q$  and  $Q^\ddagger$  are the partition functions of reactants and transition states, respectively. Therefore, to use TST we need the partition functions that follow from the Boltzmann distribution. Hence, these partition functions are introduced in the following section.

### 2.9.4. Partition function

According to the Boltzmann distribution, there is a large ensemble of particles with energy levels  $\varepsilon_i$ , with  $i = 0, 1, 2, \dots, N$ , the chance  $P_i$  to find the system at a temperature  $T$  in a state with energy  $\varepsilon_i$ , is derived by:

$$P_i = \frac{e^{-\varepsilon_i/k_B T}}{\sum_{i=0}^{\infty} e^{-\varepsilon_i/k_B T}} \quad (2.41)$$

The summation of states is called partition function, as follows;

$$q = \sum_{i=0}^{\infty} g_i e^{-\varepsilon_i/k_B T} \quad (2.42)$$

Where,  $g_i$  is the degeneracy factor to ensure that all states are taken into account even if they have the same energy. Important properties of a system such as entropy ( $S$ ), specific heat at constant pressure ( $C_p$ ), enthalpy ( $H$ ) and free Gibbs energy ( $G$ ) can be calculated straightforwardly from the partition function:

$$S = k_B \ln Q + k_B T \left( \frac{\partial \ln Q}{\partial T} \right)_V \quad (2.43)$$

$$C_p = T \left( \frac{\partial^2 \ln Q}{\partial T^2} \right)_p \quad (2.44)$$

$$H = E_{DFT} + E_{(S=0, T=0, ZPE)} + \int_0^T C_p \partial T \quad (2.45)$$

$$G = H - TS \quad (2.46)$$

Where, we consider the global partition function as the product of the partition functions:

$$Q = q_{translational} \cdot q_{rotational} \cdot q_{vibrational} \cdot q_{electronic} \cdot q_{nuclear} \quad (2.47)$$

**2.9.4.1. Translational partition function**

The coordinates available for a particle of mass  $m$  moving in one dimension  $x$  over a line of length  $l$ , can be divided into small cells with size  $h$ , the Planck's constant. The partition function of translation is calculated by integration over phase space in  $x$  and particle momentum,  $p_x = m v_x$ :

$$q_{trans} = l \frac{(2\pi m k_B T)^{\frac{1}{2}}}{h} \quad (2.48)$$

For a particle moving over an area  $A$  on a surface, the translational partition function obtained via:

$$q_{trans}^{2D} = A \frac{2\pi m k_B T}{h^2} \quad (2.49)$$

And for a particle moving in a box with volume  $V$ :

$$q_{trans}^{3D} = V \frac{(2\pi m k_B T)^{\frac{3}{2}}}{h^3} \quad (2.50)$$

**2.9.4.2. Rotational partition function**

The rotational partition function is calculated from the rotational energy:

$$\varepsilon_J = \frac{h^2 J(J+1)}{8\pi^2 I} \quad (2.51)$$

Where  $J$  is the rotational quantum number, and  $I$  is the moment of inertia:

$$I = \mu r^2 \quad (2.52)$$

With  $\mu$  the reduced mass and  $r$  the atoms distance to the centre of mass. Rotational energy leads to the rotational partition function, which for linear molecules is calculated by:

$$q_{rot}^{linear} = \frac{1}{\sigma} \frac{8\pi^2 I k_B T}{h^2} \quad (2.53)$$

The symmetry factor,  $\sigma$ , can be estimated directly from the symmetry of the molecule, *i.e.* it is 2 for a homonuclear linear molecule.

The rotational partition function for a non-linear molecule is calculated via:

$$q_{rot}^{nonlinear} = \frac{1}{\sigma} \left( \frac{8\pi^2 k_B T}{h^2} \right)^{3/2} \sqrt{\pi I_a I_b I_c} \quad (2.54)$$

Where  $I_a, I_b, I_c$  are the moments of inertia along the three principal axes:

$$I_a = \sum_i^N m_i (b_i^2 + c_i^2) \quad (2.55)$$

$$I_b = \sum_i^N m_i (a_i^2 + c_i^2) \quad (2.56)$$

$$I_c = \sum_i^N m_i (a_i^2 + b_i^2) \quad (2.57)$$

Where, each atom ( $i$ ) in the molecule has a distance to new axis ( $a_i, b_i$  and  $c_i$ ).

#### 2.9.4.3. Vibrational partition function

The vibrational energy in the harmonic oscillator approximation of a vibration with frequency  $\nu$  from the bottom of the iso-surface potential is obtained by:

$$\varepsilon_i = \left(i + \frac{1}{2}\right) h \nu \quad (2.58)$$

Then the vibrational partition function relative to this energy is calculated via:

$$q_{vib} = \prod_i \frac{e^{-\frac{1}{2}h\nu_i/k_B T}}{1 - e^{-h\nu_i/k_B T}} \quad (2.59)$$

If the energy is corrected by the energy of the lowest occupied state, zero point energy (ZPE), the partition function is thus calculated via:

$$q_{vib} = \prod_i \frac{1}{1 - e^{-h\nu_i/k_B T}} \quad (2.60)$$

#### 2.9.4.4. Electronic and nuclear partition function

The electronic partition functions can be considered as the electronic ground state of the molecule since the energy separation between excited states is usually very large compared with  $k_B T$ .

The nuclear partition function does not usually contribute to the partition function and can therefore be taken as unity.

Once the  $Q$  (equation 2.47) is available, the  $G$  (equation 2.46) is known as a function of temperature for each elementary step and we can construct a microkinetic model to describe the overall reaction. We need to set a rate expression for each reaction mechanism: adsorption, reaction and desorption.

#### 2.9.5. Adsorption processes

There are two types of adsorption, direct and indirect; the direct adsorption implies that the molecule lands immediately at its final adsorption site and stays at the point of impact as an adsorbed species while in indirect adsorption, the molecule adsorbs via a physisorbed precursor and after some time in this state, it finds a free site to

bond to the surface (Chorkendorff and Niemantsverdriet, 2007). We have considered the direct adsorption for molecules through the microkinetic simulation in this thesis.

For describing the adsorption process, we need to consider the rate of collision between gas and surface which is estimated using the classical Hertz-Knudsen equation (Laidler, 1987):

$$r_{coll-surf} = \frac{P_i}{\sqrt{2\pi m_i k_B T}} \quad (2.61)$$

Using this equation we obtain the total number of collisions in time interval  $\Delta t$  on the surface of area  $A$  as a function of molecule pressure ( $P_i$ ).

In general, since the molecules must have a specific orientation, or hit a specific site on the surface in order to adsorb, an efficient coefficient called the sticking coefficient,  $S$ , is needed, which is a measure of the fraction of incident molecules which adsorb upon the surface. TST offers a description of the sticking coefficient, equation (2.62), which considers the temperature dependency of  $S$  where a free molecule moves perpendicular to the surface towards transition state (TS) where it is then anchored and its translation and rotation are frustrated. Hence, its partition function includes only vibration,  $q_{vib}^{TS}$ , derived by equation (2.59), from which the reaction coordinate, perpendicular to the surface, has been excluded.

$$S_0(T) = \frac{q_{vib}^{TS}}{q_{trans}^{2D} q_{rot}^{gas} q_{vib}^{gas}} \exp\left(-\frac{\Delta E}{k_B T}\right) \quad (2.62)$$

The  $q_{trans}^{2D}$  is the 2D-translational partition function for the free molecule derived by equation (2.49), where the third frustrated translational mode vanishes since it is the reaction coordinate. The rotational partition function for a free molecule,  $q_{rot}^{gas}$ , is

calculated using equations (2.53) or (2.54) depending on its symmetry. The vibrational partition function in the gas phase,  $q_{vib}^{gas}$ , is also calculated by using the equation (2.59) for the  $3N_i - 6$  and  $3N_i - 5$  vibrational degrees of freedom of a non-linear and linear molecule in the gas phase respectively, where  $N_i$  is the number of atoms in the molecule.

The rate of adsorption on a surface is therefore calculated via:

$$r_{ads,i} = \frac{A}{\sqrt{2\pi m_i k_B T}} P_i \theta^* S_0(T) \quad (2.63)$$

Where,  $A$  is the effective area of catalyst and  $\theta^*$  is the coverage of free sites.

### 2.9.6. Reaction processes

The rate constant for each surface elementary step is computed using the TST:

$$k_{react} = \frac{k_B T}{h} \frac{Q_{TS}}{Q_{IS}} \exp\left(\frac{-\Delta E^\ddagger}{k_B T}\right) = \frac{k_B T}{h} \frac{q_{vib}^{TS}}{q_{vib}} \exp\left(\frac{-\Delta E^\ddagger}{k_B T}\right) \quad (2.64)$$

Where,  $\Delta E^\ddagger$  is the reaction activation energy. The translations and rotations of the adsorbed species are frustrated on the surface and therefore we considered only vibrational modes (Chorkendorff and Niemantsverdriet, 2007).

### 2.9.7. Desorption processes

The desorption process is the end of the catalytic cycle and forms the basis of temperature programmed desorption (TPD) which is a powerful tool to determine the

activation energies and pre-exponential factors of desorption. The rate constant for desorption process is computed using the TST:

$$k_{des} = \frac{k_B T}{h} \frac{Q_{TS}}{Q_{IS}} \exp\left(\frac{-\Delta E^{des}}{k_B T}\right) = \frac{k_B T}{h} \frac{q_{vib}^{TS}}{q_{vib}} \exp\left(\frac{-\Delta E^{des}}{k_B T}\right) \quad (2.65)$$

Where  $\Delta E^{des}$  is the desorption energy. The partition function  $Q_{IS}$  includes only the vibrational frequencies of the adsorbed species on the surface, while  $Q_{TS}$  is the partition function for the transition state, which we have considered as in direct adsorption and includes only vibration,  $q_{vib}^{TS}$ , from which the reaction coordinate has been excluded.

## ***Chapter 3: Adsorption of hydrazine on the perfect low-index Cu surfaces***

### **Abstract**

In this Chapter we discuss the results for the adsorption of hydrazine ( $\text{N}_2\text{H}_4$ ) on low-index copper surfaces using density functional theory calculations with a correction for the long-range interactions (DFT-D2). We have modelled the perfect Cu(111), (100) and (110) surfaces, which are found in the experimentally produced structures of copper nanoparticles (Salzemann *et al.*, 2004b). The (111) is the most stable surface with the weakest adsorption of hydrazine, while the (110) surface is the least stable and hence more reactive surface with the highest adsorption energy, where the hydrazine bridges along the short-bridge. We found that inclusion of the dispersion correction results in significant enhancement of molecule-substrate binding, thereby increasing the adsorption energy. This strong adsorption results in a bridging adsorption geometry for hydrazine, with a rotation around the N–N bond where the torsional angle changes from a gauche towards an eclipsed conformer to help the molecule to bridge through both nitrogen atoms, in agreement with experimental evidence.

### 3.1. Introduction

Over the last two decades, nanoparticles smaller than 100 nm (Fahlman, 2007) have received much attention due to their applications in a wide range of areas including catalysis, magnetics, optoelectronics, electronic materials, biological identification, environmental detection and monitoring (Heath, 1999; Matsui, 2005; Liu, 2006). This wide applicability is in part due to their position between isolated atoms and extended solids as well as their surface properties, since they are composed almost entirely of surfaces. The formation of copper nanoparticles with specific properties, which are influenced by their shape and size (Lisiecki and Pileni, 1993; Salzemann *et al.*, 2004a; Germain *et al.*, 2005; Kooij and Poelsema, 2006; Salzemann *et al.*, 2006; El-Sayed, 2004), is of interest in the design of materials for particular applications.

Generating specific nanoparticles with defined morphologies depends on several parameters such as temperature, pressure and synthesis devices. One particular factor during synthesis is the variation in the concentration of reducing agents like hydrazine ( $\text{N}_2\text{H}_4$ ), which experiment has shown results in significant changes in the distribution of copper particle shapes and sizes (Filankembo *et al.*, 2003; Salzemann *et al.*, 2004b). Although experimental work, *e.g.* in reverse micelle-based synthesis, has achieved much in the way of controlling the size and shape of copper nanoparticles (Lisiecki, 2005), the underlying processes are still not fully understood and molecular-level information would help to generate tailored particles more efficiently.

More generally,  $\text{N}_2\text{H}_4$  itself has applications in fuel cells, for example in direct hydrazine fuel cells using proton exchange membranes and room-temperature hydrazine/air direct-liquid fuel cells based on the use of nanostructured copper

electrodes (Andrew *et al.*, 1972; Granot *et al.*, 2012; Yamada *et al.*, 2003). The copper-hydrazine interface is thus of importance in a number of applications and in order to produce copper particles with specific properties or improve copper electrodes for more efficient fuel cells, we need to gain fundamental understanding of the interactions between  $\text{N}_2\text{H}_4$  and Cu surfaces.

Computational techniques based on the density functional theory (DFT) have become an important tool for unravelling the interactions between adsorbates and surfaces. We have carried out first-principles calculations of the interaction of  $\text{N}_2\text{H}_4$  with the Cu(111), (100) and (110) surfaces, which are found experimentally (Salzemann *et al.*, 2004b). Compared to the (111), different surface geometries such as less close-packed atomic arrangements, low-coordinated surface atoms and longer Cu–Cu distances, may modify the way the molecule is accommodated at the copper surface.

Daff *et al.* (Daff *et al.*, 2009; Daff and de Leeuw, 2012) have previously investigated aspects of the copper-hydrazine system, but this earlier work did not include a correction for the dispersion contribution, and a comparison with the dispersion corrected calculations is therefore deemed valuable since the standard DFT calculations are not capable of describing the long-range interactions properly (Kohn and Sham, 1965; Hohenberg and Kohn, 1964). In this study, we have applied the DFT-D2 method by Grimme (Grimme, 2004; Grimme, 2006) which is a recent approach to include dispersive interactions, to characterize the interaction of hydrazine with the low-index Cu surfaces.

## 3.2. Computational methods

Density functional theory (DFT-D2) calculations including the long-range dispersion correction approach by Grimme (Grimme, 2004; Grimme, 2006) were employed to simulate the copper bulk and surface structures as well as the hydrazine adsorption. We have used the Vienna Ab-initio Simulation Package (VASP) (Kresse and Furthmuller, 1996b; Kresse and Furthmuller, 1996a; Kresse and Hafner, 1993; Kresse and Hafner, 1994), with the projector augmented wave (PAW) potentials and the generalized gradient approximation (GGA) based on the Perdew-Burke-Ernzerhof (PBE) exchange-correlation functional (Kresse and Joubert, 1999; Blochl, 1994; Perdew *et al.*, 1996). We have used the global scaling factor optimized for PBE, ( $s_6 = 0.75$ ) and a damping function to avoid near singularities for small distances; the total energy is therefore calculated as a function of the dispersion coefficient for each atom pair. The geometries of all stationary points were found with the conjugate gradient algorithm and considered converged when the force on each ion dropped below  $0.01 \text{ eV/\AA}$ , whereas the energy self-consistency of the electron density was set to  $10^{-5} \text{ eV}$ . The valence orbitals are calculated as linear combinations of plane waves, and the size of the basis set is determined by a cut-off energy of 600 eV, which gave bulk energies converged to within 0.001 eV/atom, whereas the core electrons are kept frozen during the calculations. Calculations were carried out using Monkhorst-Pack (Monkhorst and Pack, 1976) grids of  $11 \times 11 \times 11$   $\mathbf{k}$ -points for the bulk simulation. We obtained a lattice parameter of  $3.571 \text{ \AA}$  from the bulk optimisation of the fcc metal with an error of  $\sim 1.2 \%$  compared to the experimental value of  $3.614 \text{ \AA}$  (Strauman.Me and Yu, 1969). All the surfaces were created by cutting the geometry optimised bulk using METADISE (Watson *et al.*,

1996). The perfect Cu surfaces were modelled by four-layer slabs and each full simulation cell was grown into a  $3\times 3$  supercell for (111) with a  $3\times 3\times 1$   $\mathbf{k}$ -point grid, a  $2\times 2$  supercell for the (100) surface with a  $5\times 5\times 1$   $\mathbf{k}$ -point grid, and a  $3\times 2$  supercell for the (110) surface with a  $3\times 5\times 1$   $\mathbf{k}$ -point grid. Test calculations with a higher number of  $\mathbf{k}$ -points led to an energy difference smaller than 0.01 eV per cell. The surface areas then correspond to a hydrazine coverage ( $\theta_{N_2H_4}$ ) of 0.03, 0.125 and 0.083 ML on the (111), (100) and (110) respectively, where ML is defined as the number of molecules divided by the number of Cu atoms at the surface. At these coverages, the closest  $NH_2-NH_2$  distances for neighbouring hydrazine molecules are 13.56, 5.91 and 8.84 Å on the (111), (100) and (110), respectively, precluding lateral interactions between molecules in adjacent unit cells. During the geometry optimisations, we allowed the adsorbate molecule and three top surface layers to relax, while the rest of the atoms in the slab were fixed at their bulk lattice positions. This set-up, where one side of the slab is kept fixed, ensures the explicit geometry optimisation of a realistic number of surface layers, whilst still retaining a reasonably sized slab, which made it feasible to investigate a large number of initial adsorption geometries. In addition, a vacuum of 20 Å was included between the slabs to avoid perpendicular interactions. Different slab and vacuum thicknesses were tested until convergence within 0.01 eV per cell achieved. Although the copper surfaces do not contain intrinsic dipoles, adsorption of the hydrazine molecule on one side of the slab gives rise to a dipole perpendicular to the surface and we have therefore employed the dipole correction in VASP to aid convergence.

To characterize the surface stabilities of the various Cu surfaces, we have computed the surface energy ( $\gamma$ ) which is a measure of the thermodynamic stability of a given

surface; the smaller its value, the more stable the surface. We have calculated the relaxed surface energy ( $\gamma_r$ ) using equation (3.1), where  $E_{slab}^{relaxed}$  is the energy of the relaxed slab with one side fixed in the optimised bulk geometry,  $E_{slab}^{unrelaxed}$  is the total energy of the unrelaxed slab prior to surface geometry optimization,  $E_{bulk}$  is the energy of the primitive cell containing one Cu atom,  $n$  is the number of atoms in the slab and  $A$  is the surface area of one side of the slab.

$$g_r = \frac{E_{slab}^{relaxed} - nE_{bulk}}{A} - \frac{E_{slab}^{unrelaxed} - nE_{bulk}}{2A} \quad (3.1)$$

The adsorption energy ( $E_{ads}$ ) was calculated as the difference between the total energy of the optimised substrate-adsorbate system ( $E_{slab+N_2H_4}$ ) and the sum of the relaxed clean surface ( $E_{slab}$ ) and isolated  $N_2H_4$  in the gauche conformation ( $E_{N_2H_4}$ ), equation (3.2):

$$E_{ads} = E_{slab+N_2H_4} - (E_{slab} + E_{N_2H_4}) \quad (3.2)$$

### 3.3. Results and discussions

#### 3.3.1. Surface properties

We have created the perfect Cu(111), (100) and (110) surfaces (**Figure 3.1**). The (111) shows the close-packed plane of the fcc structure (**Figure 3.1.a**) and is the most stable copper surface (Daff *et al.*, 2009). The surface Cu atoms are located in a hexagonal lattice with a separation of 2.52 Å between nearest neighbour atoms. The (100) surface is a square lattice obtained by cleaving the face-centred bulk plane with a Cu–Cu distance of 2.52 Å (**Figure 3.1.b**), while the (110) surface has a rectangular

lattice and atoms are aligned with a distance of 2.52 Å between Cu atoms (short-bridge) and distance of 3.57 Å between elevated rows (long-bridge) (**Figure 3.1.c**).

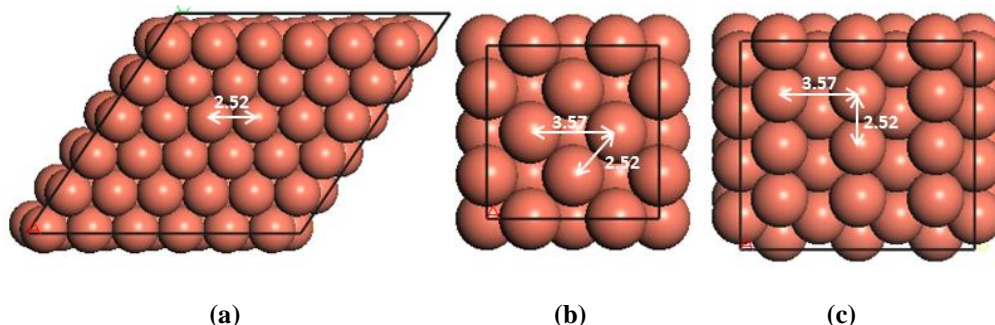


**Figure 3.1.** Surface structures (top-view) of the perfect (a) Cu(111), (b) Cu(100) and (c) Cu(110) and cells used in the calculations (all distances in Å).

**Table 3.1** summarizes the calculated surface energies of the low-index perfect copper surfaces. These surfaces show stabilities increasing from (110) < (100) < (111). The small discrepancies between our results and previous theoretical studies reported in **Table 3.1** are due to the variation in methods used.

**Table 3.1.** Surface energies of the perfect (111), (100) and (110) copper surfaces.

Surface	$\gamma_{(111)}$ ( $\text{Jm}^{-2}$ )	$\gamma_{(100)}$ ( $\text{Jm}^{-2}$ )	$\gamma_{(110)}$ ( $\text{Jm}^{-2}$ )
<b>This work</b>	1.97	2.08,	2.14,
<b>Other works</b>	1.96 <sup>A</sup>	2.09 <sup>A</sup>	2.237 <sup>B</sup>

<sup>A</sup> (Skriver and Rosengaard, 1992)

<sup>B</sup> (Vitos *et al.*, 1998)

### 3.3.2. Hydrazine molecule

The three major conformations of hydrazine in the gas phase: gauche, trans and eclipsed, are shown in **Figure 3.2**. The gauche conformer is the lowest-energy structure, with the trans and eclipsed conformations 0.13 and 0.36 eV higher in energy respectively. We have started our investigation by placing the different N<sub>2</sub>H<sub>4</sub> conformers in a number of initial configurations at a variety of positions on the

perfect Cu(111), (100) and (110) surfaces in order to identify the lowest energy system.

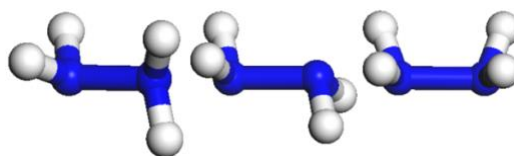


**Figure 3.2.** Representation of the N<sub>2</sub>H<sub>4</sub> conformations, from left to right: gauche, trans and eclipsed.

### 3.3.3. Adsorption of N<sub>2</sub>H<sub>4</sub> at the perfect Cu(111)

We have investigated a number of initial adsorbed hydrazine configurations to ensure as far as possible that the lowest-energy configuration is obtained rather than a local minimum. **Figure 3.3** shows the three lowest-energy adsorption configurations obtained on the perfect Cu(111) with structural and energetic details listed in **Table 3.2**. The preferred adsorption structures on the perfect Cu(111) surface are for N<sub>2</sub>H<sub>4</sub> in gauche or trans conformations, both releasing an  $E_{ads}$  of 0.85 eV/N<sub>2</sub>H<sub>4</sub>. Gauche N<sub>2</sub>H<sub>4</sub> bonds through both nitrogen atoms to the surface with Cu–N distances of 2.16 and 2.17 Å with the molecule almost parallel to the surface (0.3 °, **Figure 3.3.flat.111a**). The molecule rotates around the N–N bond, towards the eclipsed conformer with a torsional angle of 41.5 ° from the gauche conformer and the N–N bond distance is increased by 0.02 Å, whereas N<sub>2</sub>H<sub>4</sub> in the trans conformation has one N atom in a position slightly displaced from the atop site on a Cu atom where the molecule is at an angle of 26.2 ° to the surface (**Figure 3.3.flat.111b**).

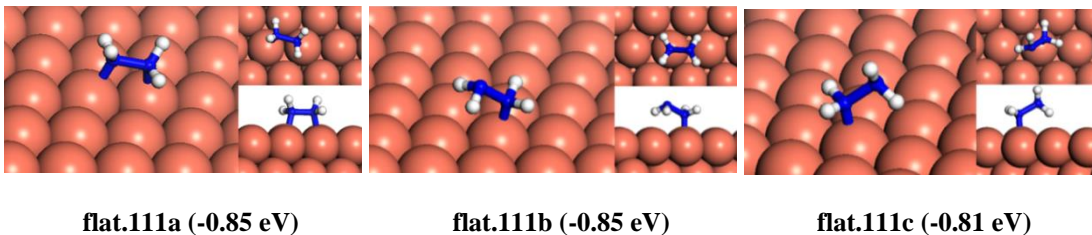


**Figure 3.3.** The three lowest-energy configurations for adsorption of  $N_2H_4$  on the perfect Cu(111) surface. Adsorption energies are in parenthesis.

**Table 3.2.** Geometries and adsorption energies ( $E_{ads}$ ) of relaxed  $N_2H_4$  adsorbed structures on the perfect Cu(111) surface. The angle between the N–N bond and the surface plane is  $\Theta$ ; the N–N bond length in gas phase is 1.44 Å. (Bold numbers indicate a non-bonding nitrogen atom).

Label	Geometry	$E_{ads}$ (eV/ $N_2H_4$ )	N–Cu (Å)	N–Cu (Å)	N–N (Å)	$\Theta$ (°)
<b>flat.111a</b>	bridge	-0.85	2.16	2.17	1.46	0.3
<b>flat.111b</b>	trans-atop	-0.85	2.07	<b>3.04</b>	1.47	26.2
<b>flat.111c</b>	gauche-atop	-0.81	2.09	<b>3.01</b>	1.44	29.4

Only marginally less favourable is the situation where  $N_2H_4$  is adsorbed in the gauche configuration releasing an energy of 0.81 eV/ $N_2H_4$ , with the N atom placed atop at a Cu–N distance of 2.09 Å and the molecule positioned at an angle of 29.4 ° to the surface (**Figure 3.3.flat.111c**).

Daff *et al.* (Daff *et al.*, 2009) obtained the lowest-energy configuration of hydrazine in the gauche conformation bound to only one Cu surface atom by using pure DFT. In that case, the  $N_2H_4$  adsorption energy is -0.42 eV/ $N_2H_4$  (Daff *et al.*, 2009), which is half of our calculated adsorption energy for the DFT-D2 calculation where the  $N_2H_4$  adsorbs to the surface through both N atoms. The higher coverage used by Daff *et al.* may also alter the adsorption structure, therefore we have calculated the adsorption structures on the same supercell size of Cu(111) to check the impact of  $\theta_{N_2H_4}$  on the results. We found that the molecule still adsorbs strongly to the surface, releasing even larger adsorption energy, 0.91 eV/ $N_2H_4$  with vdW contribution of -

0.58 eV/N<sub>2</sub>H<sub>4</sub>. The pure DFT adsorption energy is therefore only -0.33 eV/N<sub>2</sub>H<sub>4</sub> differing only 0.1 eV/N<sub>2</sub>H<sub>4</sub> with earlier reports (Daff *et al.*, 2009) due to the different functional used. The van der Waals contribution may modify even the nature of interaction as found in the flat adsorption of pyridine on the Cu(110) surface, where the nature of the adsorption process changed from physisorption ( $E_{ads} \sim -0.21$  eV) to chemisorption ( $E_{ads} \sim -0.61$  eV) (Atodiresei *et al.*, 2008), and a similar effect has been found in the self-assembly of molecules on Au surfaces (Irrera *et al.*, 2013b).

### 3.3.4. Adsorption of N<sub>2</sub>H<sub>4</sub> at the perfect Cu(100)

The lowest-energy structures for hydrazine adsorption on the perfect Cu(100) surface are represented in **Figure 3.4**, with structural and energetic details listed in **Table 3.3**.

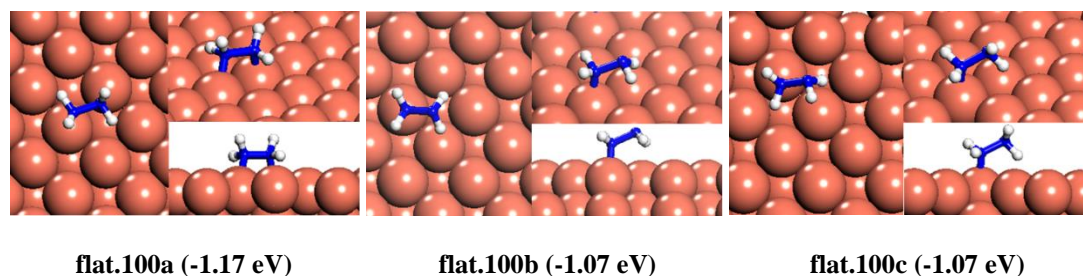


**Figure 3.4.** Surface geometry of the lowest-energy configurations for adsorption of N<sub>2</sub>H<sub>4</sub> on the perfect Cu(100) surface. (Adsorption energies are given in parenthesis).

In the most favourable configuration, the hydrazine molecule lies parallel to the surface, having rotated around the N–N bond towards the eclipsed conformer. It binds to the surface through both nitrogen atoms with Cu–N distances of 2.12 Å and releasing an adsorption energy of  $E_{ads} = 1.17$  eV/N<sub>2</sub>H<sub>4</sub> (**Figure 3.4.flat.100a**). Although the adsorption structure is similar to the one on the (111), the molecule adsorbs more strongly to the (100) by 0.32 eV/N<sub>2</sub>H<sub>4</sub>. In the most favourable structure for the adsorption of hydrazine on the perfect Cu(100) identified by Daff *et al.* using

pure DFT (Daff *et al.*, 2009), the molecule was in the gauche conformation and bound to only one Cu surface atom, releasing an adsorption energy of 0.57 eV/N<sub>2</sub>H<sub>4</sub> which is only half of our calculated adsorption energy, showing the importance of including the dispersion correction in DFT calculations of this type of systems.

The next two favoured structures were obtained from hydrazine in the trans and gauche conformations, aligned perpendicularly to the plane and placed atop a copper atom (**Figure 3.4.flat.100b, c**). Despite producing the same adsorption energies, the trans conformer is bound to the surface with a slightly shorter Cu–N distance of 2.06 Å compared to 2.09 Å for the gauche conformer.

**Table 3.3.** Geometries and adsorption energies ( $E_{ads}$ ) of the relaxed N<sub>2</sub>H<sub>4</sub> adsorbed structures on the perfect Cu(100) surface. The angle between the N–N bond and the surface plane is  $\Theta$ , the N–N bond length in the gas phase is 1.44 Å. (Bold numbers indicate a non-bonding nitrogen atom).

Label	Geometry	$E_{ads}$ (eV/N <sub>2</sub> H <sub>4</sub> )	N–Cu (Å)	N–Cu (Å)	N–N (Å)	$\Theta$ (°)
<b>flat.100a</b>	bridge	-1.17	2.12	2.12	1.45	0.20
<b>flat.100b</b>	trans-atop	-1.07	2.06	<b>3.05</b>	1.48	23.77
<b>flat.100c</b>	gauche-atop	-1.07	2.09	<b>3.01</b>	1.45	26.75

### 3.3.5. Adsorption of N<sub>2</sub>H<sub>4</sub> at the perfect Cu(110)

**Figure 3.5** and **Table 3.4** show the lowest-energy adsorption structures on the perfect Cu(110) surface. The strongest adsorption of all our calculations of the perfect (111), (100) and (110) surfaces occurred on the (110), releasing an adsorption energy of 1.34 eV/N<sub>2</sub>H<sub>4</sub> (**Figure 3.5.flat.110a**). This structure has the N<sub>2</sub>H<sub>4</sub> molecule lying along the short-bridge row, with Cu–N distances of 2.10 Å, in a conformation close to the gauche conformer with a torsion of about 22.5 ° towards the eclipsed conformation. In the most favourable adsorption geometry on the perfect (110),

obtained using pure DFT, the hydrazine binds to the surface through both nitrogen atoms along the short-bridge row, releasing a smaller energy of 0.82 eV/N<sub>2</sub>H<sub>4</sub> (Daff *et al.*, 2009).

**Table 3.4.** Geometries and adsorption energies ( $E_{ads}$ ) of the relaxed N<sub>2</sub>H<sub>4</sub> adsorbed structures on the perfect Cu(110) surface. The angle between the N–N bond and the surface plane is  $\Theta$ , the N–N bond length in the gas phase is 1.44 Å. (Bold numbers indicate a non-bonding nitrogen atom.)

Label	Geometry	$E_{ads}$ (eV/N <sub>2</sub> H <sub>4</sub> )	N–Cu (Å)	N–Cu (Å)	N–N (Å)	$\Theta$ (°)
<b>flat.110a</b>	short-bridge	-1.34	2.10	2.10	1.45	0.20
<b>flat.110b</b>	long-bridge	-1.32	2.15	2.15	1.45	0.20
<b>flat.110c</b>	gauche-atop	-1.10	2.06	<b>2.95</b>	1.45	18.75
<b>flat.110d</b>	gauche-atop	-1.09	2.05	<b>2.97</b>	1.45	39.94
<b>flat.110e</b>	trans-atop	-1.02	2.03	<b>3.04</b>	1.41	50.96

The geometry with N<sub>2</sub>H<sub>4</sub> along a long-bridge (**Figure 3.5.flat.110b**) is less stable, but the hydrazine still binds more strongly than on either the Cu(111) or (100) surfaces. The molecule remains parallel to the surface with a Cu–N distance of 2.15 Å, releasing an adsorption energy of 1.32 eV/N<sub>2</sub>H<sub>4</sub>. The optimisation from a structure with N<sub>2</sub>H<sub>4</sub> bridging two copper atoms across the diagonal of the rectangular lattice of the (110) yields a configuration with a single copper interaction, with an adsorption energy of -1.10 eV/N<sub>2</sub>H<sub>4</sub> and the molecule in the gauche conformation (**Figure 3.5.flat.110c**). We also found two weaker non-bridging adsorption structures, shown in **Figures 3.5.flat.110d** and **e**. The optimised structures from a perpendicular hydrazine in gauche and trans conformations release energies of 1.09 and 1.02 eV/N<sub>2</sub>H<sub>4</sub>, respectively, with the molecule remaining in its gauche or trans conformation, whereas the nitrogen is slightly displaced from the atop position on the copper atom.

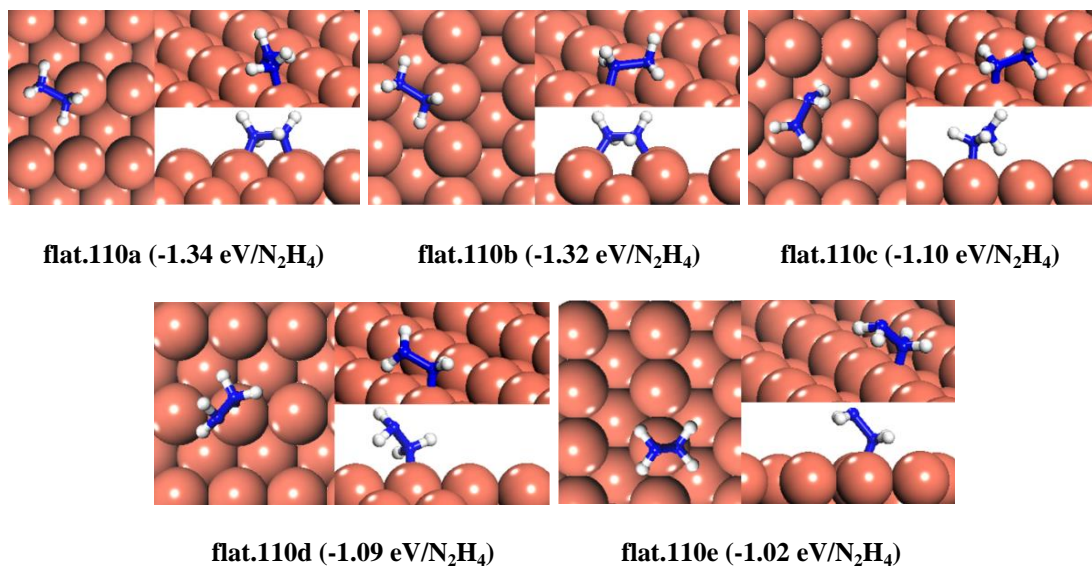


**Figure 3.5.** The lowest-energy configurations for adsorption of N<sub>2</sub>H<sub>4</sub> on the perfect Cu(110) surface. (Adsorption energies are given in parenthesis).

### 3.4. Conclusions

We have carried out a systematic study of N<sub>2</sub>H<sub>4</sub> adsorption on perfect low-index Cu surfaces using DFT level calculations with long-range interaction corrections. Our study has shown that the planar (111) surface offers the weakest adsorption to the molecule, while the largest adsorption energy is obtained on the least stable (110) surface, where bridging of hydrazine along the short-bridge is the preferred configuration. Our results, in comparison with previous study, indicate that the long-range interactions are important in determining the most favourable adsorption structures, which also lead to stronger bonds between Cu and N atoms inclining the molecule to the surface in bridging modes. This mode of adsorption is in agreement with that found by experiments (Matloob and Roberts, 1977; Alhaydari *et al.*, 1985), which suggests that a two-point attachment of the N–N of the N<sub>2</sub>H<sub>4</sub> molecule occurs on Cu surfaces. This bridging structure was also proposed by Alberas *et al.* (Alberas *et al.*, 1992) for hydrazine on Pt(111), based on XPS and high resolution electron energy loss spectroscopy (HREELS) measurements, and by Grunze (Grunze, 1979)

on Fe(111), based on photoelectron spectroscopy experiments. In this study, we have also used larger simulation cells to obtain lower  $\text{N}_2\text{H}_4$  coverages than previous work, which help to prevent interactions between the molecules in neighbouring cells and ensure that we calculate only the surface-adsorbate interactions of the isolated hydrazine molecule.

The electronic properties studies of the perfect low-index Cu surfaces are investigated in comparison with those of defective Cu surfaces in the next Chapter.

## ***Chapter 4: Adsorption of hydrazine on the defective low-index Cu surfaces***

### **Abstract**

In this Chapter we discuss the results of investigation of the adsorption of hydrazine on defect-containing copper (111), (100) and (110) surfaces by first-principles calculations. We have studied adsorption of hydrazine at three types of defects in the surfaces, *i.e.* monoatomic steps, Cu adatoms and Cu vacancies. Several low-energy adsorption structures for hydrazine on each defective surface have been identified and compared. Our calculations reveal that hydrazine bridges surface copper atoms, with the molecule twisted from the gauche towards an eclipsed conformation, except on the adatom (100) and vacancy-containing (100) and (110) surfaces, where it adsorbs through one nitrogen atom in gauche and trans conformations, respectively. The strongest adsorption energy is found on the stepped (110) surface, where hydrazine bridges between the copper atoms on the step edge and the terrace, as it stabilizes the low-coordinated copper atoms. Our results show that, although the (110) surface contains a number of low-coordinated atoms that enhance the surface-molecule interactions, the addition of defects on the more stable (111) and (100) surfaces provides sites that enable hydrazine binding to almost the same extent. The core-level binding shifts for the N(1s) states upon N<sub>2</sub>H<sub>4</sub> adsorption on Cu(111) surfaces have been calculated at DFT level to provide further insight into the N<sub>2</sub>H<sub>4</sub> adsorption process on the copper surfaces. This study also confirms general observations of surface adsorption trends in terms of d-band center and binding

energy as a function of coordination number, *i.e.* the stronger the molecular adsorption, the higher the d-band shifts at low-coordinated sites.

## 4.1. Introduction

The copper-hydrazine system has attracted significant attention due to the role of hydrazine in the production of metallic copper nanoparticles (Filankembo et al., 2003; Salzemann et al., 2004b; Lisiecki, 2005) and in the direct hydrazine fuel cell using nanostructured copper electrodes (Andrew et al., 1972; Granot et al., 2012; Yamada et al., 2003) (for the detailed description, please refer to Chapter 1).

Following our investigation of the adsorption of molecular hydrazine on perfect Cu surfaces in Chapter 2 and since computational studies have often focused on the ideal surfaces, whereas real surfaces are never perfect and chemical processes often occur at defective sites, we have carried out a comprehensive computational study based on DFT in this Chapter to obtain an atomistic understanding of the adsorption of N<sub>2</sub>H<sub>4</sub> at three defective Cu(111), (100) and (110) surfaces; surface steps, where the copper terraces are offset by one atomic layer from plane to plane, Cu adatoms and Cu vacancies. Low-coordinated atoms provide sites for stronger adsorption, especially to those molecules that have lone-pair electrons (Tang and Chen, 2007), which is shown by larger adsorption energies and shorter distances for the adsorbates bound at those sites.

## 4.2. Computational methods

All the calculations in this Chapter were done based on the density functional theory (DFT-D2) including the long-range dispersion correction approach by Grimme

(Grimme, 2004; Grimme, 2006) using the Vienna Ab-initio Simulation Package (VASP) (Kresse and Furthmuller, 1996b; Kresse and Furthmuller, 1996a; Kresse and Hafner, 1993; Kresse and Hafner, 1994). For the detailed methodology employed in this Chapter, please refer to the methodology of Chapter 3. The adatom and vacancy surfaces were represented by four-layer slabs and each full simulation cell was grown into a  $3 \times 3$  supercell for (111) with a  $3 \times 3 \times 1$   $\mathbf{k}$ -point grid, a  $2 \times 2$  supercell for the (100) surface with a  $5 \times 5 \times 1$   $\mathbf{k}$ -point grid, and a  $3 \times 2$  supercell for the (110) surface with a  $3 \times 5 \times 1$   $\mathbf{k}$ -point grid where we allowed the adsorbate molecule and three top surface layers to relax, while the rest of the atoms in the slab were fixed at their bulk lattice positions. The stepped surfaces were modelled by a  $3 \times 2$  supercell using a  $3 \times 5 \times 1$   $\mathbf{k}$ -point grid. The stepped (111) has five layers, while the stepped (100) and (110) have 6 layers. During the optimization the molecule and four top layers of Cu atoms of the stepped surfaces were allowed to relax. On the stepped surfaces, the hydrazine molecules are not interacting with their images in neighbouring cells either, as the shortest  $\text{NH}_2\text{--NH}_2$  distances are 8.81, 7.44 and 7.05 Å on the (111), (100) and (110) respectively.

The formation energy of a defect is the amount of energy required to create it. We have calculated the vacancy and adatom formation energies using equations (4.1) and (4.2) respectively;

$$E_{f,vac} = (E_{vac,r} + E_{bulk}) - E_{perfect,r} \quad (4.1)$$

$$E_{f,adatom} = E_{adatom,r} - (E_{bulk} + E_{perfect,r}) \quad (4.2)$$

Where  $E_{bulk}$  is the energy of the primitive cell containing one Cu atom,  $E_{vac,r}$  and  $E_{adatom,r}$  are the total energies of the relaxed slab with one side fixed in the optimised

bulk geometry, containing a vacancy and adatom at the relaxed site of the slab respectively, and  $E_{perfect,r}$  is the energy of the relaxed defect-free surface with one side fixed in the optimised bulk geometry.

The relaxed surface energy ( $\gamma_r$ ) and adsorption energy ( $E_{ads}$ ) were calculated using the equations (3.1) and (3.2) in Chapter 3.

### 4.3. Results and discussions

#### 4.3.1. Surface Properties

Since experimental surface structures are never perfect, we have created three defects on the surfaces: steps, adatoms and vacancies.

The stepped surfaces have been studied to investigate the presence of an extended edge of low-coordinated atoms on the surface stabilities and adsorption behaviour. Each unit cell (shown in **Figures 4.1.a-c**) in the stepped slab was offset by one atomic layer with respect to the next cell (de Leeuw *et al.*, 2000; de Leeuw and Nelson, 2003; de Leeuw *et al.*, 2004).

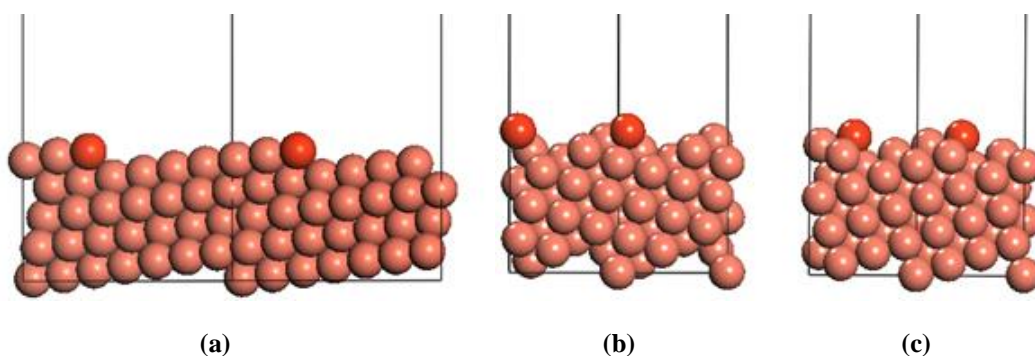


**Figure 4.1.** Side view of simulation cells used in the calculations of stepped surfaces where the low-coordinated copper atoms are shaded darker: (a) Cu(111); (b) Cu(100), and (c) Cu(110).

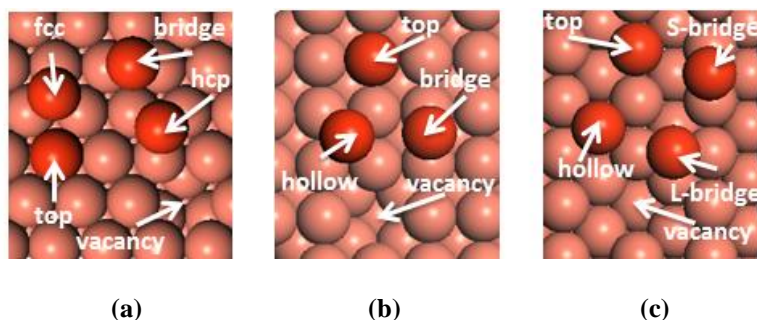


**Figure 4.2.** The surface geometry (top-view) of different sites for adatom (a) (111) and (b) (100) as well as (c) (110) surfaces. Copper adatoms are shaded darker. A vacancy defect on each surface is also shown. S-bridge and L-bridge indicate the short and long bridges sites on the (110) surface respectively.

One point defect on the surface that we have investigated, is a Cu atom added at different sites of the relaxed side of the slab (**Figures 4.2.a-c**). As **Figure 4.2** shows, we have studied three different adatom adsorption sites: hollow, bridge and top sites. During relaxation of the top and bridge adatom, we restricted its movement, allowing perpendicular movement to the surface only to keep it at these lateral positions. These calculations enabled us to obtain energies for these higher energy adatom positions, which could provide information on pathways for adatom diffusion across the copper surface (Yildirim *et al.*, 2006; Karimi *et al.*, 1995). Because of the uneven structure of the (110) surface, adatoms can bridge two different sites on the rows: between two copper surface atoms along either long or short edge, which are separated by 3.57 Å (long-bridge) or 2.52 Å (short-bridge) respectively (**Figure 4.2.c**). Finally, we have studied a surface vacancy, where one of the atoms in the top layer has been removed from the slab, also shown in **Figures 4.2.a-c**.

As shown by the formation energies in **Table 4.1**, the hollow site is the preferred place for the adatom on the Cu surfaces with formation energies of 0.54 and 0.30 eV on the (100) and (110) surfaces respectively, less endothermic than on the (111)

surface. Although formation of a vacancy is energetically less expensive than that of an adatom on the (100) by 0.06 eV, although less favourable by 0.05 eV on the (110), both are more likely to form than on the (111); This is due to the higher relative stability of the (111) surface and lower coordination to the adatom on the (111) than on the (100) and (110). Our results are in agreement with previous reports (Karimi *et al.*, 1995; Ereemeev *et al.*, 1997), where the adatom-hollow and vacancy formation energies on the (111) were larger than those on (100) and (110) surfaces.

**Table 4.2** summarizes the calculated surface energies of the low-index perfect and defective copper surfaces. The perfect surfaces show stabilities increasing from (110) < (100) < (111). As expected, the presence of defects affects the stabilities of the planes and the trend changes to (100) < (110) for the adatom and vacancies, although the (111) remains the most stable surface in all cases. The small discrepancies between our results and previous theoretical studies reported in **Table 4.2** are due to the variation in methods used.

**Table 4.1.** Formation energies of Cu-adatom and vacancy on the Cu(111), (100) and (110) surfaces.

Surface site	$E_f$ (eV), (111)	$E_f$ (eV), (100)	$E_f$ (eV), (110)
<b>hollow</b>	0.83 (fcc), 0.85 (hcp), 0.93 <sup>A</sup> , 0.97 <sup>B</sup>	0.54, 0.66 <sup>A</sup> , 0.71 <sup>B</sup>	0.30, 0.31 <sup>A</sup> , 0.31 <sup>B</sup>
<b>bridge</b>	1.01	1.01	0.50 (l-bridge), 1.37 (s-bridge)
<b>top</b>	1.19	1.37	1.68
<b>vacancy</b>	0.82, 0.72 <sup>A</sup>	0.48, 0.58 <sup>A</sup>	0.35, 0.29 <sup>A</sup>

<sup>A</sup> (Ereemeev *et al.*, 1997)

<sup>B</sup> (Karimi *et al.*, 1995)

**Table 4.2.** Surface energies of the perfect and defective (111), (100) and (110) copper surfaces.

Surface	$\gamma_{(111)}$ ( $\text{Jm}^{-2}$ )	$\gamma_{(100)}$ ( $\text{Jm}^{-2}$ )	$\gamma_{(110)}$ ( $\text{Jm}^{-2}$ )
<b>perfect</b>	1.97, 1.96 <sup>A</sup> , 1.952 <sup>B</sup>	2.08, 2.09 <sup>A</sup> , 2.166 <sup>B</sup>	2.14, 2.31 <sup>A</sup> , 2.237 <sup>B</sup>
<b>stepped</b>	2.10	2.45	2.58
<b>adatom (hollow)</b>	2.04	2.23	2.19
<b>adatom (bridge)</b>	2.05	2.37	2.22 (l-bridge ), 2.34 (s-bridge)
<b>adatom (top)</b>	2.06	2.48	2.39
<b>vacant</b>	2.04	2.21	2.19

<sup>A</sup> (Skriver and Rosengaard, 1992)<sup>B</sup> (Vitos *et al.*, 1998)

### 4.3.2. Adatom diffusion

The hopping mechanism for copper adatom self-diffusion, also called “bridge” by reference (Ayrault and Ehrlich, 1974), were calculated according to how adatoms migrate from one hollow site to an adjacent one by overcoming the saddle point of the potential energy barrier between them. The calculated activation energy barriers ( $E_a$ ) for the adatom hopping processes (A-D in **Figure 4.3**) across the (100), (110) and (111) surfaces are presented in **Table 4.3** and compared to the available theoretical and experimental values.

Our value of 0.46 eV for the direct hopping activation energy of a Cu adatom over a bridge on a Cu(100) surface (process A) is in good agreement with the results of previous theoretical studies (Karimi *et al.*, 1995; Yildirim *et al.*, 2006; Kurpick *et al.*, 1997). Due to the lower symmetry of the (110) surface, there are two different diffusion paths, across the close-packed rows, *i.e.* over the short-bridge site (process B) and parallel to the close-packed direction, *i.e.* over the long-bridge sites (process C). The energy barrier for hopping across the short-bridge (1.07 eV) is larger than that across the long-bridge (0.20 eV), which values are similar to those of earlier

works (Karimi *et al.*, 1995; Yildirim *et al.*, 2006; Montalenti and Ferrando, 1999). We found the activation energy for the adatom to diffuse over a bridge on a Cu(111) surface (process D) to be 0.17 eV, which is also in agreement with the experimental and theoretical observations (Jones *et al.*, 1990; Hansen *et al.*, 1991).

Based on the activation energies, we have calculated the diffusion coefficient ( $D$ ) at two temperatures (300 K and 600 K) according to the transition-state theory (Glasstone *et al.*, 1941), using equation (4.3) (Liu *et al.*, 1991; Kurpick, 2001);

$$D = D_0 \exp\left(\frac{-E_a}{k_B T}\right) \quad (4.3)$$

The pre-exponential factor,  $D_0$ , was calculated using equation (4.4), where we have neglected either the entropy or the vibrational contributions of the internal energy;

$$D_0 = \frac{k_B T}{h} \frac{nd^2}{2\alpha} \quad (4.4)$$

Where  $d$  is the jump distance to an adjacent site,  $\alpha$  is the dimensionality of the motion which is  $\alpha = 2$  for (100) and (111) surfaces and  $\alpha = 1$  for (110),  $n$  is the number of jump directions available to the adatom with  $n = 4$  for diffusion on (100) surfaces,  $n = 2$  for diffusion along or perpendicular to the rows on (110) surfaces and  $n = 3$  for diffusion on (111) planes,  $k_B$  is the Boltzman constant,  $T$  is the temperature,  $h$  is the Plank constant and  $E_a$  is the activation energy of each hopping process. The corresponding diffusion coefficients and pre-exponential factors are given in **Table 4.3**. Our calculated diffusion coefficients and pre-exponential factors are similar to those from previous works although the overestimations due to the omission of the vibrational energy contribution in our study become more noticeable as the

temperature increases, indicating that vibrational effects should be included in any complete description of the temperature-dependence of the diffusion coefficient (Kurpick *et al.*, 1997; Kurpick and Rahman, 1999).

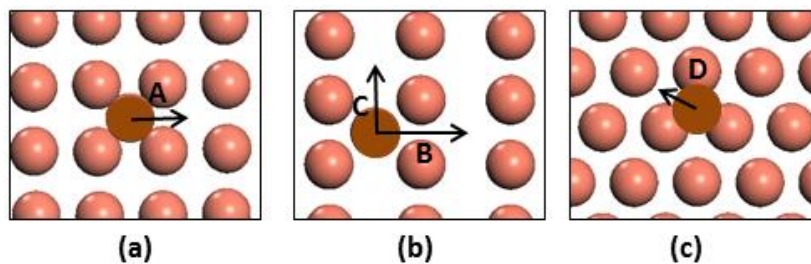


**Figure 4.3.** Diffusion processes of an adatom via hopping on (a) Cu(100), (b) Cu(110) and (c) Cu(111).

**Table 4.3.** Activation energies, pre-exponential factors ( $D_0$ ) and diffusion coefficients ( $D$ ) of adatom diffusion on Cu(100), (110) and (111). The results in this table are for the moves in **Figure 4.3** For comparison, the corresponding values from other references are also reported.

Process	$E_a$ (eV)	$D_0$ (cm <sup>2</sup> /s), 300 K	$D_0$ (cm <sup>2</sup> /s), 600 K	$D$ (cm <sup>2</sup> /s), 300 K	$D$ (cm <sup>2</sup> /s), 600 K
<b>A Cu(100)</b>	0.46	$3.97 \times 10^{-3}$	$7.94 \times 10^{-3}$	$7.61 \times 10^{-11}$	$1.10 \times 10^{-6}$
	0.48 <sup>A, B</sup>	$2.5 \times 10^{-3}$ <sup>E</sup>	$7.43 \times 10^{-4}$ <sup>C</sup>	$2.39 \times 10^{-12}$ <sup>C</sup>	$4.26 \times 10^{-8}$ <sup>C</sup>
	0.505 <sup>C</sup>	$1.2 \times 10^{-3}$ <sup>F</sup>			
	$0.39 \pm 0.06$ <sup>D</sup>	$5.2 \times 10^{-3}$ <sup>F</sup>			
		$7.29 \times 10^{-4}$ <sup>C</sup>			
		$8.7 \times 10^{-4}$ <sup>G</sup>			
<b>B Cu(110)</b>	1.07	$7.97 \times 10^{-3}$	$1.59 \times 10^{-2}$	$8.92 \times 10^{-21}$	$1.69 \times 10^{-11}$
	1.146 <sup>C</sup>	$9.97 \times 10^{-4}$ <sup>C</sup>	$1.1 \times 10^{-3}$ <sup>C</sup>	$5.57 \times 10^{-23}$ <sup>C</sup>	$2.4 \times 10^{-13}$ <sup>C</sup>
	1.15 <sup>A</sup>				
<b>C Cu(110)</b>	0.20	$3.97 \times 10^{-3}$	$7.94 \times 10^{-3}$	$1.75 \times 10^{-6}$	$1.67 \times 10^{-4}$
	0.23 <sup>C, H</sup>	$1.1 \times 10^{-3}$ <sup>E</sup>	$6.39 \times 10^{-4}$ <sup>C</sup>	$8.61 \times 10^{-8}$ <sup>C</sup>	$7.48 \times 10^{-6}$ <sup>C</sup>
	0.24 <sup>A</sup>	$8 \times 10^{-4}$ <sup>F</sup>			
		$4.4 \times 10^{-4}$ <sup>F</sup>			
		$6.29 \times 10^{-4}$ <sup>C</sup>			
<b>D Cu(111)</b>	0.17	$9.99 \times 10^{-4}$	$2 \times 10^{-3}$	$1.41 \times 10^{-6}$	$7.49 \times 10^{-5}$
	0.1-0.15 <sup>I, J</sup>	$3 \times 10^{-4}$ <sup>F</sup>			
		$4.6 \times 10^{-4}$ <sup>F</sup>			
		$1.2 \times 10^{-4}$ <sup>E</sup>			

<sup>A</sup> (Karimi *et al.*, 1995)

<sup>B</sup> (Kurpick *et al.*, 1997)

<sup>C</sup> (Yildirim *et al.*, 2006)

<sup>D</sup> (Breeman and Boerma, 1992)

<sup>E</sup> (Kurpick, 2001)

<sup>F</sup> (Liu *et al.*, 1991)

<sup>G</sup> (Kurpick and Rahman, 1999)

<sup>H</sup> (Yildirim *et al.*, 2006)

<sup>I</sup> (Jones *et al.*, 1990)

<sup>J</sup> (Hansen *et al.*, 1991)

### 4.3.3. $\text{N}_2\text{H}_4$ adsorption at the Cu(111) surfaces

#### 4.3.3.1. Adsorption at the stepped (111)

We have investigated the adsorption of various conformations and configurations of the  $\text{N}_2\text{H}_4$  molecule at different positions on the stepped Cu(111) surface. **Figure 4.4** shows a schematic illustration of the initial configurations where the molecule was placed either bridging across or atop Cu atoms on the step or in the vicinity on the surface. **Figure 4.5** shows the lowest-energy structures obtained after relaxation, whereas the adsorption energies and other structural parameters are summarized in **Table 4.4**. It can be seen that the adsorption configurations where  $\text{N}_2\text{H}_4$  interacts with the low-coordinated step atoms leads to adsorption energies that are much larger than on the terrace.

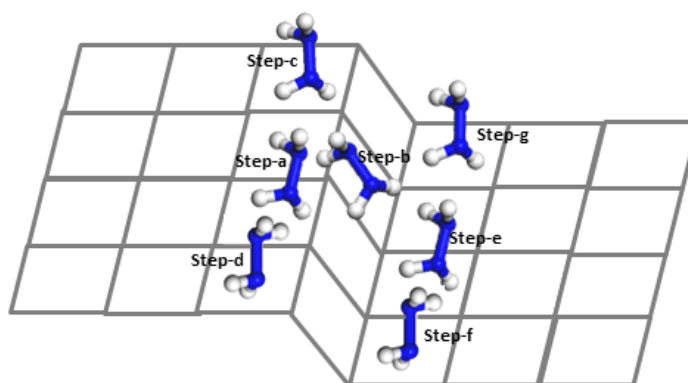


**Figure 4.4.** Schematic illustration of initial adsorption configurations where  $\text{N}_2\text{H}_4$  was placed at different sites on the step and terraces of the stepped Cu(111) surface.

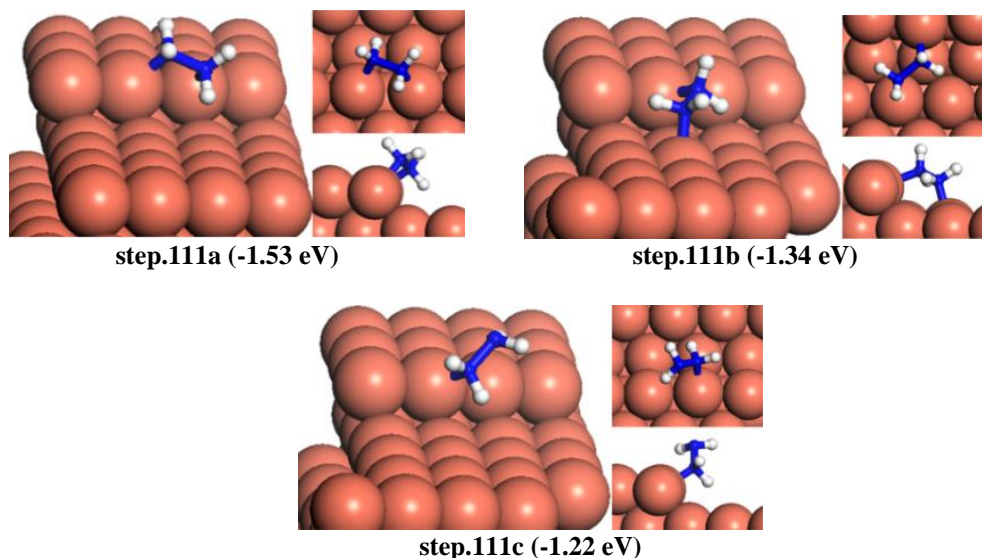


**Figure 4.5.** The three lowest-energy configurations for adsorption of  $\text{N}_2\text{H}_4$  on the stepped Cu(111) surface. Adsorption energies are given in parenthesis.

The lowest-energy structure (**Figure 4.5.step.111a**), with  $E_{ads}$  of  $-1.53 \text{ eV}/\text{N}_2\text{H}_4$ , was found by optimising the initial conformation where the molecule in its gauche conformation bridges two Cu atoms on the step edge with resulting Cu–N distances of 2.12 and 2.09 Å. The molecule rotates around its N–N bond and has a torsional angle of  $59.0^\circ$  relative to the eclipsed conformer. We have found that hydrazine can also bridge between two atoms, one on the step and another on the terrace with adsorption energy of  $-1.34 \text{ eV}/\text{N}_2\text{H}_4$  (**Figure 4.5.step.111b**). A local minimum energy structure is found when the gauche  $\text{N}_2\text{H}_4$  is adsorbed through one N atom atop of a step edge Cu atom at a distance of 2.07 Å, the molecule is inclined towards the terrace, releasing an  $E_{ads}$  of  $1.22 \text{ eV}/\text{N}_2\text{H}_4$  (**Figure 4.5.step.111c**). In addition, we have studied configurations where the molecule is placed in the step vicinity. As shown in **Table 4.4**, the adsorption energies decrease as  $\text{N}_2\text{H}_4$  adsorbs away from the step edge.

**Table 4.4.** Geometries and adsorption energies ( $E_{ads}$ ) of the relaxed  $N_2H_4$  adsorbed structures on the stepped Cu(111) surface. The angle between the N–N bond and the surface plane is  $\Theta$ , the N–N bond length in the gas phase is 1.44 Å. (Bold numbers indicate a non-bonding nitrogen atom).

Label	Geometry	$E_{ads}$ (eV/ $N_2H_4$ )	N–Cu (Å)	N–Cu (Å)	N–N (Å)	$\Theta$ (°)
<b>step.111a</b>	bridge-step	-1.53	2.09	2.12	1.46	15.2
<b>step.111b</b>	bridge-step-terrace	-1.34	2.18	2.22	1.45	12.8
<b>step.111c</b>	gauche-atop-step	-1.22	2.07	<b>3.02</b>	1.45	51.4
<b>step.111d</b>	trans-atop-step	-1.16	2.04	<b>3.02</b>	1.48	28.4
<b>step.111e</b>	bridge-terrace	-1.15	2.15	2.16	1.46	0.6
<b>step.111f</b>	trans-atop-terrace	-1.09	2.09	<b>3.07</b>	1.47	27.8
<b>step.111g</b>	gauche-atop-terrace	-1.06	2.12	<b>3.06</b>	1.44	27.6

#### 4.3.3.2. Adsorption at the adatoms on (111)

The fcc site on the Cu(111) surface is the energetically preferred location for the adatom, and we have therefore investigated the adsorption of  $N_2H_4$  near this adatom site in a number of different starting configurations. The description of the optimised geometries and the adsorption characteristics for the range of structures studied are given in **Table 4.5**, whereas **Figure 4.6** shows the lowest-energy adsorption configurations of the gauche and trans conformers of  $N_2H_4$  on the fcc-adatom. The strongest adsorption, releasing an energy of 1.26 eV/ $N_2H_4$ , is obtained when the molecule bridges between the Cu-adatom and a surface copper atom at Cu–N distances of 2.08 and 2.16 Å respectively. The molecule is tilted to the surface at an angle of 23.6 ° and the N–N bond is rotated with an angle of 17.4 ° from gauche towards the eclipsed conformer (**Figure. 4.6.fcc.111a**).

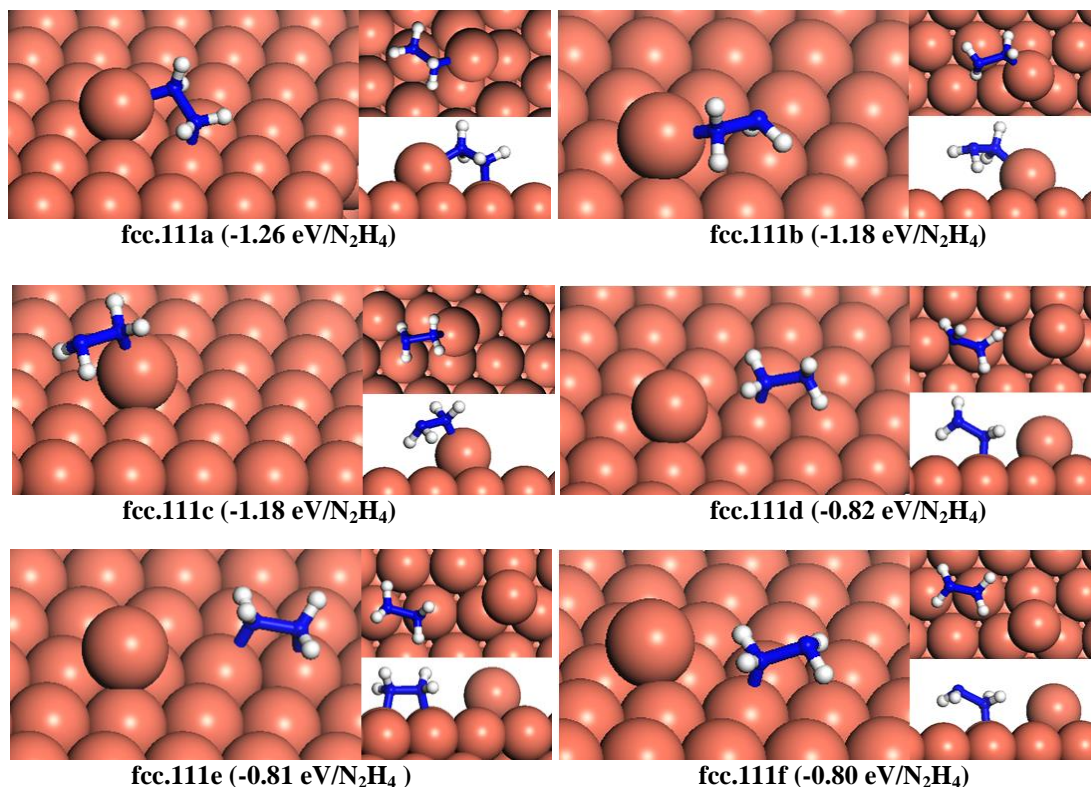


**Figure 4.6.** The lowest-energy configurations of adsorption of  $\text{N}_2\text{H}_4$  on fcc-adatom Cu(111) surface.

**Table 4.5.** Geometries and adsorption energies for the relaxed  $\text{N}_2\text{H}_4$  adsorbed structures on the fcc-adatom Cu (111) surface. The angle between the N–N bond and the surface plane is  $\Theta$ , the N–N bond length in the gas phase is 1.44 Å. (Bold numbers indicate a nitrogen atom is bound to the adatom).

Label	Geometry	$E_{ads}$ (eV/ $\text{N}_2\text{H}_4$ )	N–Cu (Å)	N–Cu (Å)	N–N (Å)	$\Theta$ (°)
<b>fcc.111a</b>	bridge-adatom-surface atom	-1.26	<b>2.08</b>	2.16	1.45	23.6
<b>fcc.111b</b>	gauche-atop-adatom	-1.18	<b>2.02</b>	2.92	1.46	0.5
<b>fcc.111c</b>	trans-atop-adatom	-1.18	<b>1.99</b>	2.91	1.48	10.9
<b>fcc.111d</b>	gauche-atop-surface atom	-0.82	2.09	3.01	1.44	29.3
<b>fcc.111e</b>	bridge-surface atoms	-0.81	2.16	2.17	2.17	0.3
<b>fcc.111f</b>	trans-atop-surface atom	-0.80	2.07	3.08	1.47	26.9

Two slightly less favourable locations for the molecule are atop the adatom bonded through one N atom and releasing 1.18 eV/ $\text{N}_2\text{H}_4$  for both gauche and trans conformers (**Figure. 4.6.fcc.111b, c**). We have also studied the structures where the

gauche molecule is bound through both nitrogen atoms to the surface atoms next to the adatom (**Figure 4.6.fcc.111e**) or where a single N atom of  $N_2H_4$  in gauche and trans conformations interacts with the surface far from the Cu-adatom (**Figure 4.6.fcc.111d, f**). These turn out to be local minima with adsorption energies in the range of -0.80 to -0.82 eV/ $N_2H_4$ , *i.e.* similar to the adsorption energy on the perfect surface indicating the local effect of the adatom. They are also significantly weaker than those for the molecule adsorbed at the adatom, either through bridging or atop modes. The defects thus provide stronger adsorption sites than the planar surface.

#### 4.3.3.3. Adsorption at the vacancies on (111)

Finally, we have investigated the adsorption of  $N_2H_4$  at the Cu vacancies on the (111) surface. The lowest-energy structures are schematically shown in **Figure 4.7**, with geometric and energetic details summarized in **Table 4.6**. The strongest adsorption, releasing an energy of 1.20 eV/ $N_2H_4$ , is found for a configuration where the molecule bridges between two copper atoms next to the vacancy at Cu–N distances of 2.09 and 2.13 Å and inclined to the surface by an angle of 12.5 ° (**Figure 4.7.vacant.111a**). In this adsorption structure,  $N_2H_4$  rotates around the N–N bond with a torsional angle of 29.9 ° from gauche to eclipsed conformer.

Two local minima were found for the molecule adsorbed atop the atom next to the vacancy with different orientations of the gauche and trans conformers (**Figure 4.7.vacant.111b, c**) and adsorption energies of -0.94 and -0.93 eV/ $N_2H_4$  respectively.

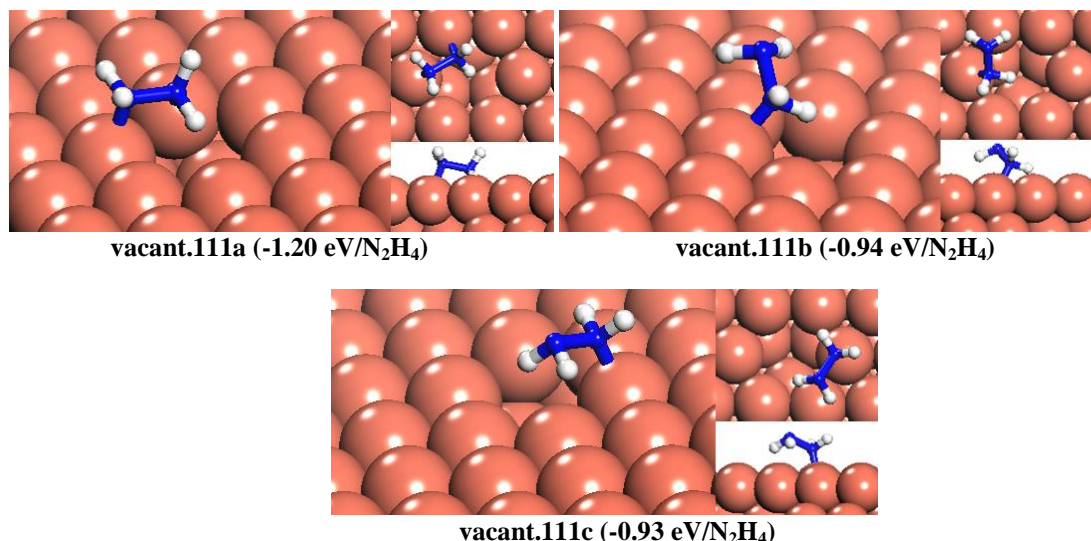


**Figure 4.7.** The lowest-energy configurations for adsorption of N<sub>2</sub>H<sub>4</sub> on vacant Cu(111) surface.

**Table 4.6.** Geometries and adsorption energies for the lowest-energy N<sub>2</sub>H<sub>4</sub> adsorbed structures on the vacant Cu(111) surface. The angle between the N–N bond and the surface plane is  $\Theta$ , the N–N bond length in the gas phase is 1.44 Å. (Bold numbers indicate a non-bonding nitrogen atom).

Label	Geometry	$E_{ads}$ (eV/N <sub>2</sub> H <sub>4</sub> )	N–Cu (Å)	N–Cu (Å)	N–N (Å)	$\Theta$ (°)
<b>vacant.111a</b>	bridge	-1.20	2.09	2.13	1.45	12.5
<b>vacant.111b</b>	gauche-atop	-0.94	2.07	<b>2.97</b>	1.47	32.9
<b>vacant.111c</b>	trans-atop	-0.93	2.06	<b>3.01</b>	1.47	24.4

### 4.3.4. N<sub>2</sub>H<sub>4</sub> adsorption at the Cu(100) surfaces

#### 4.3.4.1. Adsorption at the stepped (100)

**Figure 4.8** and **Table 4.7** show the properties of the three lowest-energy adsorption structures on the stepped Cu(100) surface. We found two adsorption configurations, where the hydrazine adsorbs in the gauche configuration on the step atoms, both releasing the same adsorption energy (-1.29 eV/N<sub>2</sub>H<sub>4</sub>) (**Figures 4.8.step.100a, b**), which is, however, weaker by 0.24 eV/N<sub>2</sub>H<sub>4</sub> than observed on the stepped (111) surface.

A third configuration is found from an initial structure with the hydrazine in the gauche conformer aligned perpendicular to the plane. Upon optimization, the molecule adsorbs with one N on top of a terrace Cu atom (**Figure 4.8.step.100c**), releasing an energy of 1.17 eV/N<sub>2</sub>H<sub>4</sub>.

We found a number of weaker adsorption structures (step.100d-g), which are summarized in **Table 4.7**.

When the molecule adsorbed atop of a Cu atom on the step edge (step.100e), it is less strongly bound by 0.11 eV/N<sub>2</sub>H<sub>4</sub> than when it is located atop a copper atom on the terrace (step.100c), in contrast to the results for the stepped (111) surface. As the (100) surface is already relatively unstable itself, the step edges on this surface are not necessarily more reactive than the terrace.

**Table 4.7.** Geometries and adsorption energies ( $E_{ads}$ ) of the relaxed N<sub>2</sub>H<sub>4</sub> adsorbed structures on the stepped Cu(100) surface. The angle between the N–N bond and the surface plane is  $\Theta$ , the N–N bond length in the gas phase is 1.44 Å. (Bold numbers indicate a non-bonding nitrogen atom).

Label	Geometry	$E_{ads}$ (eV/N <sub>2</sub> H <sub>4</sub> )	N–Cu (Å)	N–Cu (Å)	N–N (Å)	$\Theta$ (°)
<b>step.100a</b>	bridge-step	-1.29	2.12	2.12	1.46	15.73
<b>step.100b</b>	bridge-step	-1.29	2.10	2.16	1.45	11.93
<b>step.100c</b>	gauche-atop-terrace	-1.17	2.08	<b>3.04</b>	1.45	28.08
<b>step.100d</b>	bridge-terrace	-1.14	2.11	2.20	1.45	8.07
<b>step.100e</b>	gauche-atop-step	-1.06	2.04	<b>2.94</b>	1.45	35.21
<b>step.100f</b>	trans-atop-terrace	-1.05	2.05	<b>2.98</b>	1.47	40.73
<b>step.100g</b>	gauche-atop-terrace	-1.05	2.08	<b>2.96</b>	1.44	38.57

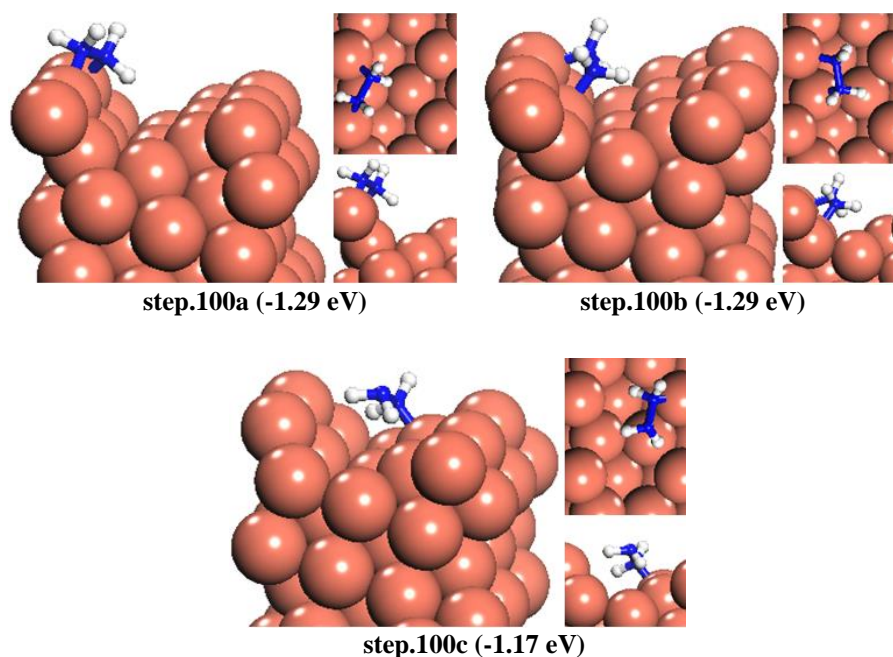


**Figure 4.8.** The lowest-energy configurations for adsorption of  $\text{N}_2\text{H}_4$  on the stepped Cu(100) surface. (Adsorption energies are given in parenthesis).

#### 4.3.4.2. Adsorption at the adatoms on (100)

As **Table 4.2** shows, the hollow-adatom Cu(100) surface provides the most stable adatom site on the surface, and we have therefore investigated adsorption of hydrazine on this surface from a number of different starting configurations. The lowest-energy adsorption structures are shown in **Figure 4.9** with the adsorption geometries and energetics listed in **Table 4.8**.

The most stable geometry is obtained with hydrazine in the gauche conformation, with one nitrogen atom at a position slightly displaced from the top site of the Cu-adatom (**Figure 4.9.adatom.100a**) and the N–N bond almost parallel to the surface. This adsorption releases  $1.18 \text{ eV}/\text{N}_2\text{H}_4$ , the same amount when the molecule binds to the surface Cu atoms nearby the adatom (**Figure 4.9.adatom.100b**), where hydrazine is lying flat with a torsion of  $31.68^\circ$  from the gauche conformation towards the eclipsed conformer. This adsorption structure is similar to that of the molecule

bridging in gauche conformation to the perfect (100) surface, releasing very similar binding energies. This result is in contrast to the (111) surface, where the adsorption on the adatom is stronger and it shows that the introduction of an adatom on the (100) surface does not have as prominent an effect on the hydrazine adsorption as on the (111).

**Table 4.8.** Geometries and adsorption energies ( $E_{ads}$ ) of the relaxed  $N_2H_4$  adsorbed structures on the adatom Cu(100) surface. The angle between the N–N bond and the surface plane is  $\Theta$ , the N–N bond length in the gas phase is 1.44 Å. (Bold numbers indicate a nitrogen atom is bound to the adatom).

Label	Geometry	$E_{ads}$ (eV/ $N_2H_4$ )	N–Cu (Å)	N–Cu (Å)	N–N (Å)	$\Theta$ (°)
<b>adatom.100a</b>	gauche-atop-adatom	-1.18	<b>2.07</b>	3.01	1.46	8.15
<b>adatom.100b</b>	bridge-surface atoms	-1.18	2.10	2.11	1.45	0.20
<b>adatom.100c</b>	bridge-adatom-surface atom	-1.12	<b>2.19</b>	2.19	1.46	16.75
<b>adatom.100d</b>	bridge-adatom-surface atom	-1.06	<b>2.13</b>	2.15	1.45	25.6
<b>adatom.100e</b>	trans-atop-surface atom	-1.07	2.05	3.02	1.41	27.42
<b>adatom.100f</b>	gauche-atop-surface atom	-1.04	2.08	3.02	1.45	24.81

**Figure 4.9** shows both adatom.100c and adatom.100d configurations where hydrazine binds to the adatom on the surface. Whilst hydrazine in adatom.100d is bound more closely to the copper atoms (N–Cu distance of 2.13 Å), with a rotation of 22.6° from the gauche conformation, the adatom-100c (N–Cu distance of 2.19 Å) is energetically more favourable, being only rotated 3.5° towards the eclipsed conformer. Hydrazine also adsorbs atop the surface copper atom through only one nitrogen atom, without bridging, in either trans or gauche conformer (adatom.100e, f).

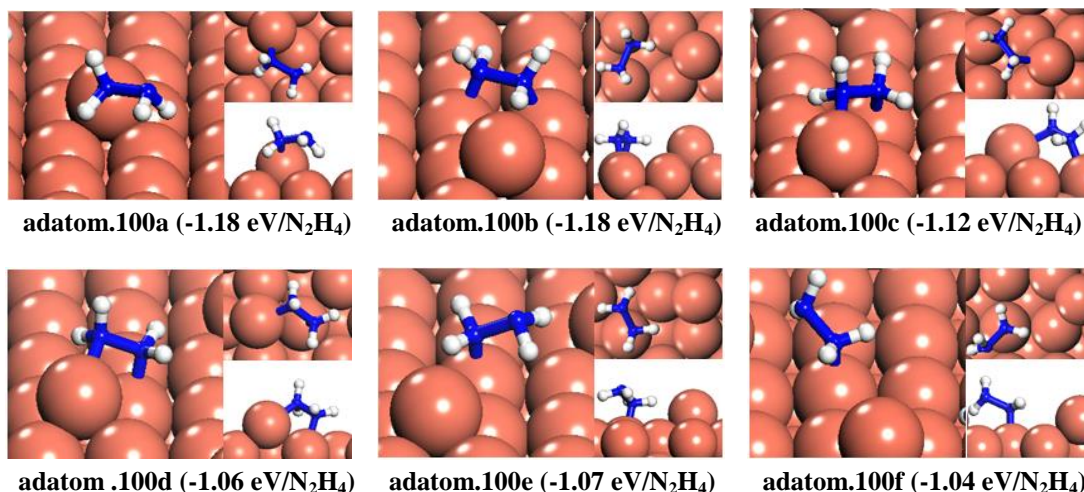


**Figure 4.9.** Surface geometry of the lowest-energy configurations for adsorption of N<sub>2</sub>H<sub>4</sub> on the adatom Cu(100) surface. (Adsorption energies are given in parenthesis).

#### 4.3.4.3. Adsorption at the vacancies on (100)

Finally, we have investigated the adsorption of N<sub>2</sub>H<sub>4</sub> at Cu vacancies on the (100) surface. The lowest-energy structures are schematically shown in **Figure 4.10**, with geometric and energetic details summarized in **Table 4.9**. In the strongest adsorption configuration, releasing an energy of 1.23 eV/N<sub>2</sub>H<sub>4</sub>, the molecule in the gauche conformation interacts through only one nitrogen with the surface Cu next to the vacancy, with a Cu–N distance of 2.07 Å, and inclined to the surface by an angle of 41.53 ° (**Figure 4.10.vacant.100a**). The adsorption structure of hydrazine bridging two Cu atoms next to the vacancy, with an adsorption energy of -1.19 eV/N<sub>2</sub>H<sub>4</sub> (**Figure 4.10.vacant.100b**), is weaker than the vacant.100a configuration but comparable to the same structure on the Cu(111) surface. A local minimum was found for the molecule adsorbed in the trans conformation on top of the atom next to the vacancy (**Figure 4.10.vacant.100c**), releasing an adsorption energy of 1.15 eV/N<sub>2</sub>H<sub>4</sub>.

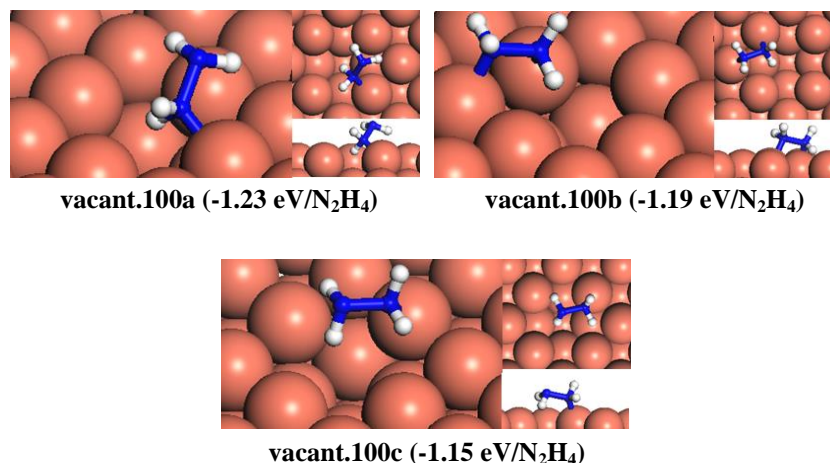


**Figure 4.10.** The lowest-energy configurations for adsorption of N<sub>2</sub>H<sub>4</sub> on the Cu(100) vacancy surface. (Adsorption energies are given in parenthesis).

**Table 4.9.** Geometries and adsorption energies ( $E_{ads}$ ) of the relaxed N<sub>2</sub>H<sub>4</sub> adsorbed structures on the Cu(100) vacancy surface. The angle between the N–N bond and the surface plane is  $\Theta$ , the N–N bond length in the gas phase is 1.44 Å. (Bold numbers indicate a non-bonding nitrogen atom.)

Label	Geometry	$E_{ads}$ (eV/N <sub>2</sub> H <sub>4</sub> )	N–Cu (Å)	N–Cu (Å)	N–N (Å)	$\Theta$ (°)
<b>vacant.100a</b>	gauche-atop	-1.23	2.07	<b>3.06</b>	1.45	41.53
<b>vacant.100b</b>	bridge	-1.19	2.07	2.14	1.45	12.21
<b>vacant.100c</b>	trans-atop	-1.15	2.05	<b>3.04</b>	1.47	11.24

### 4.3.5. N<sub>2</sub>H<sub>4</sub> adsorption at the Cu(110) surfaces

#### 4.3.5.1. Adsorption at the stepped (110)

The representative lowest-energy structures for the N<sub>2</sub>H<sub>4</sub> adsorption on the stepped (110) surface are shown in **Figure 4.11** with structural and energetics details listed in **Table 4.10**.

We found the strongest adsorption on the stepped Cu(110) when N<sub>2</sub>H<sub>4</sub> bridges between two copper atoms, one on the step and another on the terrace, with an adsorption energy of -1.60 eV/N<sub>2</sub>H<sub>4</sub> (**Figure 4.11.step.110a**) and Cu–N distances of 2.04 Å and 2.07 Å. The channels between rows of atoms accommodate the hydrogen

atoms much better, resulting in a torsional rotation of only 3.5 ° around the N–N bond towards the eclipsed conformation. The combination of these effects, and the lower coordination of the uppermost surface atoms on the stepped Cu(110) surface, results in the strongest adsorption found on any atomic step on the copper surfaces.

Bridging along the step edge is the second most favourable adsorption structure with adsorption energy of -1.58 eV/N<sub>2</sub>H<sub>4</sub> (**Figure 4.11.step.110b**). The bridging configurations near the step (*e.g.* step.110c) are less stable with varying adsorption energies, depending either on how far the molecule is located from the step edge or in which direction it bridges. The adsorption becomes more endothermic as N<sub>2</sub>H<sub>4</sub> moves away from the step edge or if the N<sub>2</sub>H<sub>4</sub> geometry is stretched on the long-bridge. Adsorption of hydrazine through only one nitrogen atom leads to weaker binding to the surface.

**Table 4.10.** Geometries and adsorption energies ( $E_{ads}$ ) of the relaxed N<sub>2</sub>H<sub>4</sub> adsorbed structures on the stepped Cu(110) surface. The angle between the N–N bond and the surface plane is  $\Theta$ , the N–N bond length in the gas phase is 1.44 Å. (Bold numbers indicate a non-bonding nitrogen atom.)

Label	Geometry	$E_{ads}$ (eV/N <sub>2</sub> H <sub>4</sub> )	N–Cu (Å)	N–Cu (Å)	N–N (Å)	$\Theta$ (°)
<b>step.110a</b>	bridge-step-terrace	-1.60	2.04	2.07	1.46	52.06
<b>step.110b</b>	bridge-step	-1.58	2.06	2.08	1.47	29.87
<b>step.110c</b>	bridge-terrace	-1.31	2.08	2.09	1.45	3.56
<b>step.110d</b>	bridge-terrace	-1.28	2.11	2.13	1.45	4.66
<b>step.110e</b>	bridge-terrace	-1.27	2.08	2.10	1.45	2.35
<b>step.110f</b>	bridge-terrace	-1.26	2.10	2.13	1.45	2.44
<b>step.110g</b>	gauche-atop-step	-1.18	2.02	<b>2.92</b>	1.45	20.56
<b>step.110h</b>	gauche-atop-terrace	-1.07	2.06	<b>2.96</b>	1.45	23.39
<b>step.110i</b>	trans-atop-terrace	-0.97	2.03	<b>2.97</b>	1.48	34.05

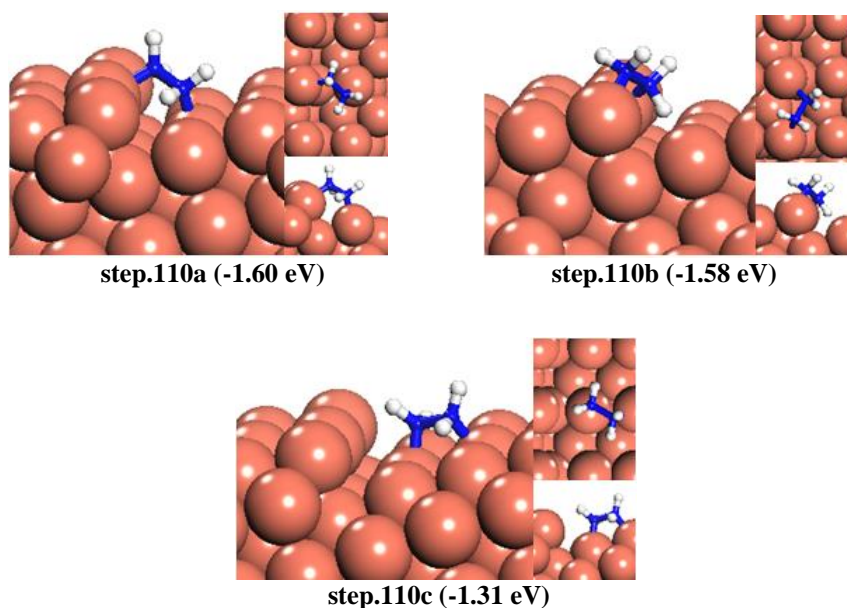


**Figure 4.11.** The lowest-energy configurations of adsorption of  $\text{N}_2\text{H}_4$  on the stepped Cu(110) surface. (Adsorption energies are given in parenthesis).

#### 4.3.5.2. Adsorption at the adatoms on (110)

We have studied adsorption of hydrazine in a number of different positions on the four-fold hollow-adatom (110) surface, which, as shown in **Table 4.2**, is the most stable adatom position on the (110) surface. We found the strongest adsorption when the molecule bridges only surface atoms, stronger even than adsorption involving the adatom (**Figure 4.12.adatom.110a**). This strong binding is due to the space between rows of Cu atoms, which allows a favourable adsorption geometry with an adsorption energy of  $-1.40 \text{ eV}/\text{N}_2\text{H}_4$ . When the molecule bridges along the long-bridge (**Figure 4.12.adatom.110b**), the Cu–N distances are lengthened to 2.13 and 2.17 Å, and this configuration releases an adsorption energy of  $1.28 \text{ eV}/\text{N}_2\text{H}_4$ .

As shown in **Table 4.11**, similar to the adsorption on the (100) surface, bridging from the adatom to a surface atom remote from the adatom (**Figure**

**4.12.adatom.110c**) is preferred over bridging to the closest copper atom (**Figure 4.12.adatom.110d**).

**Table 4.11.** Geometries and adsorption energies ( $E_{ads}$ ) of the relaxed  $N_2H_4$  adsorbed structures on the adatom Cu(110) surface. The angle between the N–N bond and the surface plane is  $\Theta$ , the N–N bond length in the gas phase is 1.44 Å. (Bold numbers indicate a nitrogen atom is bound to the adatom).

Label	Geometry	$E_{ads}$ (eV/ $N_2H_4$ )	N–Cu (Å)	N–Cu (Å)	N–N (Å)	$\Theta$ (°)
<b>adatom.110a</b>	bridge-surface atoms	-1.40	2.09	2.10	1.45	0.30
<b>adatom.110b</b>	bridge-surface atoms	-1.28	2.13	2.17	1.45	1.20
<b>adatom.110c</b>	bridge-adatom-surface atom	-1.22	<b>2.19</b>	2.16	1.46	22.41
<b>adatom.110d</b>	bridge-adatom-surface atom	-1.18	<b>2.12</b>	2.11	1.45	21.94
<b>adatom.110e</b>	gauche-atop-surface atom	-1.12	2.06	2.99	1.45	38.37
<b>adatom.110f</b>	trans-atop-surface atom	-1.05	2.03	3.04	1.47	50.73
<b>adatom.110g</b>	gauche-atop-adatom	-0.96	<b>2.05</b>	3.01	1.45	48.53
<b>adatom.110h</b>	trans-atop-adatom	-0.96	<b>2.02</b>	3.02	1.48	47.48

**Figure 4.12** also shows the adsorption structures where  $N_2H_4$  adsorbs through a single nitrogen atom, atop either a surface copper atom (adatom.110e, f) or an adatom (adatom.110g, h). As **Table 4.11** shows, binding to the top site is stronger than to the adatom. Adsorption of hydrazine in either gauche or trans conformation on the adatom releases 0.96 eV/ $N_2H_4$ , while adsorption of  $N_2H_4$  on a surface copper atom in the gauche conformation is more favourable than in the trans conformation by 0.07 eV/ $N_2H_4$ .

We found that the bridging site between the adatom and a surface atom is the preferred position for the molecule on the (111) surface, but in the strongest adsorption structures on the adatom (100) and (110) surfaces, hydrazine prefers to

bridge between surface atoms without involving the adatom, because these surfaces already contain low-coordinated atoms in the defect-free planes.

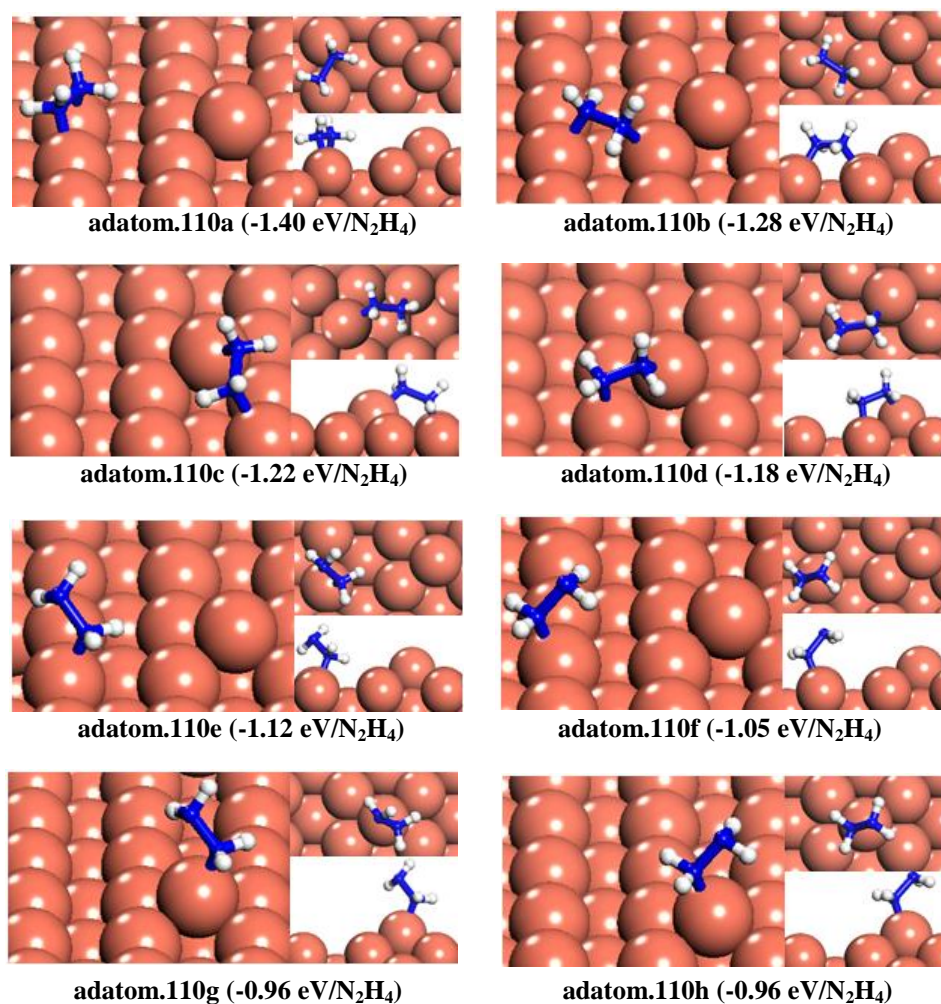


**Figure 4.12.** The lowest-energy configurations for adsorption of  $\text{N}_2\text{H}_4$  on the adatom Cu(110) surface. (Adsorption energies are given in parenthesis).

#### 4.3.5.3. Adsorption at the vacancies on (110)

The lowest-energy structures are schematically shown in **Figure 4.13**, with geometric and energetic details summarized in **Table 4.12**. We found the strongest adsorption on the Cu(110) surface with vacancy, releasing an energy of 1.35 eV/ $\text{N}_2\text{H}_4$ , when the molecule in the trans conformation interacts through only one nitrogen with a surface atom next to the vacancy at a Cu–N distance of 2.02 Å

(**Figure 4.13.vacant.110a**). The channels between rows next to the vacancy accommodate  $\text{N}_2\text{H}_4$  very well, leading to strong binding to the surface.

**Table 4.12.** Geometries and adsorption energies ( $E_{ads}$ ) of the relaxed  $\text{N}_2\text{H}_4$  adsorbed structures on the Cu(110) vacancy surface. The angle between the N–N bond and the surface plane is  $\Theta$ , the N–N bond length in the gas phase is 1.44 Å. (Bold numbers indicate a non-bonding nitrogen atom).

Label	Geometry	$E_{ads}$ (eV/ $\text{N}_2\text{H}_4$ )	N–Cu (Å)	N–Cu (Å)	N–N (Å)	$\Theta$ (°)
<b>vacant.110a</b>	trans-atop	-1.35	2.02	<b>2.95</b>	1.48	0.7
<b>vacant.110b</b>	bridge	-1.32	2.13	2.16	1.45	1.1
<b>vacant.110c</b>	gauche-atop	-1.29	2.04	<b>2.96</b>	1.45	2.5

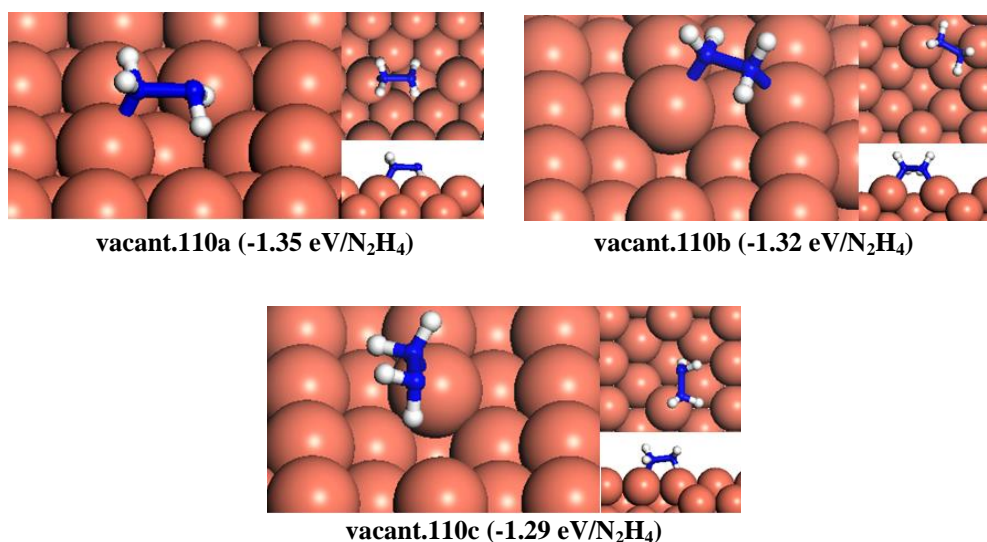


**Figure 4.13.** The lowest-energy configurations for adsorption of  $\text{N}_2\text{H}_4$  on the Cu(110) vacancy surface. (Adsorption energies are given in parenthesis).

We identified two other structures close in energy, where hydrazine bridges between two atoms next to the vacancy, with an adsorption energy of  $-1.32$  eV/ $\text{N}_2\text{H}_4$  (**Figure 4.13.vacant.110b**), similar to the molecule adsorbing on top of the atom next to the vacancy in a gauche conformation (**Figure 4.13.vacant.110c**),  $E_{ads} = -1.29$  eV/ $\text{N}_2\text{H}_4$ .

### 4.3.6. Electronic structure analysis

#### 4.3.6.1. Calculation of core level binding energy shifts

Identification of adsorption structures helps to understand the mechanism of surface chemical reactions. X-ray photoelectron spectroscopy (XPS) is one of the most highly used spectroscopies to identify the electronic and geometric structures of solid surfaces with adsorbed molecules. First-principles DFT calculations of the core-level binding energies shifts (CLS) are able to reveal the microscopic details of the various surface reactions, where it is hard to assign peaks for complicated structures on XPS, due to existing a number of adsorption sites with different coordinations. In this section, we have calculated the CLS for the N(1s) states upon N<sub>2</sub>H<sub>4</sub> adsorption at DFT level for deep understanding of the N<sub>2</sub>H<sub>4</sub> adsorption process on the copper surfaces and helping to interpret XPS peaks.

The core-level binding energy is the energy required to remove a core electron from the atom of interest. At DFT level, the binding energy of core electrons ( $E_{CL}$ ) is calculated as the energy difference between two separate calculations (Lizzit *et al.*, 2001; Kohler and Kresse, 2004) as per equation (4.5). The first calculation is a standard DFT calculation in which the number of core electrons corresponds to the unexcited ground state ( $E(n_c)$ ). In the second calculation one electron is removed from the core of one particular atom and added to the valence or conduction band ( $E(n_c-1)$ ). A total energy is then obtained via minimization of electronic configuration in the presence of the core-hole.

$$E_{CL} = E(n_c - 1) - E(n_c) \quad (4.5)$$

Core-level binding energy shifts ( $E_{CLS}$ ) are the changes in binding of specific core electrons ( $E_{CL}$ ) of atoms of interest compared to reference atoms, which are typically located in a different environment, equation (4.6):

$$E_{CLS} = E_{CL} - E_{CL}^{ref} \quad (4.6)$$

$E_{CLS}$  can be compared to the experimentally determined value, which is sensitive to the local environment. This calculation provides a unique way to gain detailed knowledge of adsorption sites and structures in a direct relation with experimental measurements. The chemical bonds are formed by orbital hybridization and often with charge transfer. In the case of molecular adsorption, the formation of a bond depends on the active site and their coordination leading to variations in  $E_{CL}$  for both adsorbates and substrates, which can be measured by X-ray photoelectron spectroscopy (XPS) and calculated computationally. To illustrate this, we present a CLS calculation for the most favorable adsorption structures on each Cu(111) surface. In **Table 4.13**, we summarize the calculated CLS for N(1s) of both N atoms in  $N_2H_4$  on the perfect, stepped, adatom and partially vacant Cu(111) surfaces. We obtained the biggest CLS for the geometries where the molecule bridges through both nitrogen atoms. As **Figure 4.14** shows, for weaker adsorption through one nitrogen, we found a shift to lower binding energies due to a major charge transfer from the Cu to that particular N in the  $N_2H_4$  molecule. These results contrast to the experimental work by Littrell and colleagues (Littrell and Tatarchuk, 1986) where they used in situ XPS to obtain a CLS of -6.1 eV for adsorption of  $N_2H_4$  on copper at  $6 \times 10^{-4}$  Torr and 295 K. This significant difference between calculated and measured CLS for N(1s) was also seen in NO adsorption on the Pt(111) surface (Zeng *et al.*, 2010; Zeng *et al.*, 2009), where calculated CLS for N(1s) is  $\sim -0.7$  eV, which is

quantitatively in line with our results. They did a comprehensive investigation and revealed the sensitivity of the CLS versus the tilted angle and the distance between molecule and surface indicating that the discrepancy between DFT and experiment results may come from the thermal vibration and rotation of adsorbed molecules. XPS measurements at low temperatures therefore could be helpful.

**Table 4.13.** Core-level binding energy shifts ( $E_{CLS}$ ) for both N(1s) for atoms of  $N_2H_4$  on the strongest adsorption structures on the perfect, stepped, adatom and vacant Cu(111) surfaces.

Structure	Geometry	$E_{ads}$ (eV)	$E_{CLS}$ (eV)
flat.111a	bridge	-0.85	-0.45, -0.44
flat.111c	gauche-atop	-0.81	-1.48, -0.92
step.111a	bridge-step	-1.53	-0.32, 0.09
step.111c	gauche-atop-step	-1.22	-1.31, -0.90
adatom.111a	bridge-adatom-surface atom	-1.26	-0.47, -0.20
adatom.111d	gauche-atop-surface atom	-0.82	-1.50, -1.04
vacant.111a	bridge	-1.20	-0.55, -0.36
vacant.111c	trans-atop	-0.93	-1.73, -0.76

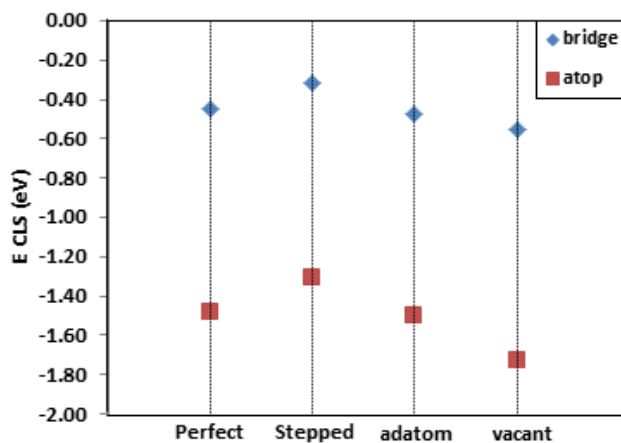


**Figure 4.14.** Core-level binding energy shifts ( $E_{CLS}$ ) for N(1s) of  $N_2H_4$  in the strongest adsorption structures on the perfect, stepped, adatom and vacancy Cu(111) surfaces.

#### 4.3.6.2. Morphology

The equilibrium morphology of a crystal is determined by the surface energy and the related growth rate of the various surfaces and provides a measure of the relative stabilities of the surfaces. Wulff's Theorem (Wulff, 1901) states that a polar plot of surface energy versus orientation of normal vectors would give the crystal morphology based on the approach of Gibbs (Gibbs, 1928), who proposed that under thermodynamic control the equilibrium form of a crystal should possess minimal total surface free energy for a given volume. Lattice dynamics simulations have shown that the contribution of the excess entropy term to the surface free energy is small compared to the enthalpy term, as the differences between the entropies of the bulk and the surface are small and, hence, for solid surfaces the surface energy is a close approximation for the surface free energy (Mkhonto and de Leeuw, 2002). Thus, the surface energies can be assumed to determine the equilibrium morphology of the crystal. This approach has been employed in the calculation of the effect of surface adsorbates on the thermodynamic morphologies of many different materials, *e.g.* oxides, carbonates, phosphates and sulphides (Mkhonto and de Leeuw, 2002; de Leeuw and Parker, 1999; de Leeuw and Cooper, 2007; Santos-Carballal *et al.*, 2014; Devey *et al.*, 2008; de Leeuw and Parker, 1998), where good agreement was obtained with experiment. We have therefore used the same approach here to obtain the morphologies of the copper particles and investigate the effect of hydrazine adsorption on the expression of the different surfaces in the resulting morphologies. Wulff crystal morphologies were calculated from the surface energies of the perfect and defect-containing copper surfaces listed in **Table 4.2**. The calculated cuboctahedron morphology deriving from the surface energies of the perfect, adatom and vacancy surfaces, represented in **Figure 4.15.a** shows that the (111) surface is

highly prominent, but that the (100) and (110) planes are also expressed. It also indicates that the introduction of point defects on the surfaces does not change the morphology. However, the addition of an extended defect, such as steps on the surfaces (**Figure 4.15.b**), does affect the crystal shape; in the extreme case, where all surfaces are considered to contain high step densities, the (110) surface disappears from the Cu morphology due to its relatively high surface energy.

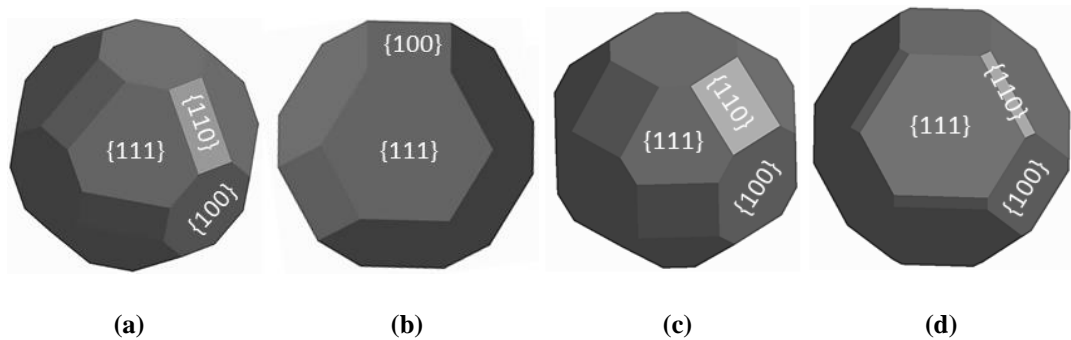


**Figure 4.15.** Calculated crystal morphology of copper before hydrazine adsorption: (a) perfect, adatom and vacancy, (b) step crystals; and after hydrazine adsorption: (c) perfect, adatom and vacancy, (d) step crystals.

We have also obtained the morphology of Cu particles after adsorption of  $N_2H_4$  on the surfaces, using equation (4.7);

$$\gamma_r = \frac{E_{slab+N_2H_4} - [nE_{bulk} + E_{N_2H_4}]}{A} - \frac{E_{slab}^{unrelaxed} - nE_{bulk}}{2A} \quad (4.7)$$

Since the surface energies change as an effect of hydrazine adsorption, the morphology is altered. Due to a decrease in the surface energy, and therefore increase in the stability of the (110) surface upon hydrazine adsorption, the particles' morphology shows an increase in (110) surface area (**Figures 4.15.c, d**). We should note, however, that these results are based on the adsorption of only one  $N_2H_4$  molecule on the Cu surfaces, whereas increasing the hydrazine coverage on the surfaces may conceivably lead to further expression of the (110) surface in the

morphology. These results are in agreement with previous experiments which showed that  $N_2H_4$  stabilizes the surfaces as a capping agent during Cu nanoparticle synthesis, thereby modifying the nanoparticles' shapes and sizes (Lisiecki, 2005).

#### 4.3.6.3. Density of states

We have obtained the electronic density of states (DOS) (**Figures 4.16 – 4.18**) to investigate if the electronic structures of the N p-orbitals of the two nitrogen atoms in hydrazine remain identical or become different upon adsorption, depending on how the  $N_2H_4$  molecules interact to the surface, *i.e.* through both nitrogens or through only a single nitrogen atom. The symmetry of the bridging configurations is shown by the identical electronic structure of the N p-orbitals. However, the local electronic density of states projections (LDOS) on the N p-band of the adatom-111 (**Figure 4.16**), adatom and vacant-100 (**Figure 4.17**) and vacant-110 (**Figure 4.18**) surfaces show a shift to lower energies for the nitrogen atom closer to the surface. This shift can also be seen on the stepped (110) (**Figure 4.18**) for the N atom interacting with the Cu atom on the step edge.

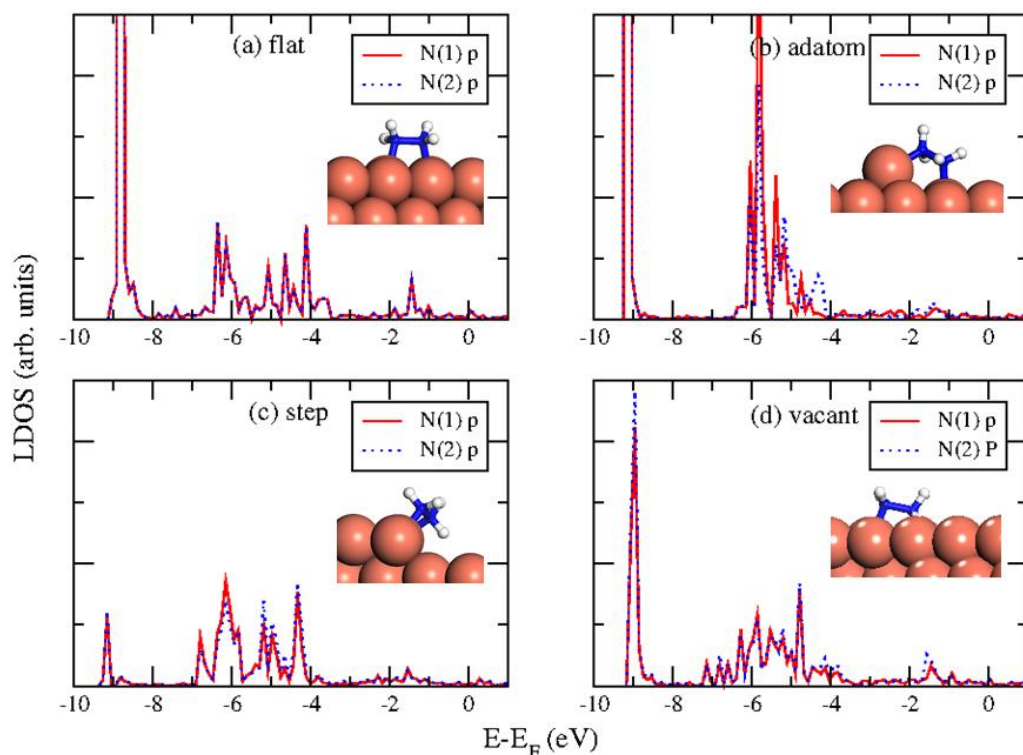


**Figure 4.16.** Site-projected electronic LDOS of the lowest-energy adsorbed structures on each perfect and defective (111) surface for nitrogen p-band. N(1) is the nitrogen closest to the surface and N(2) is the second nitrogen atom of  $N_2H_4$ .

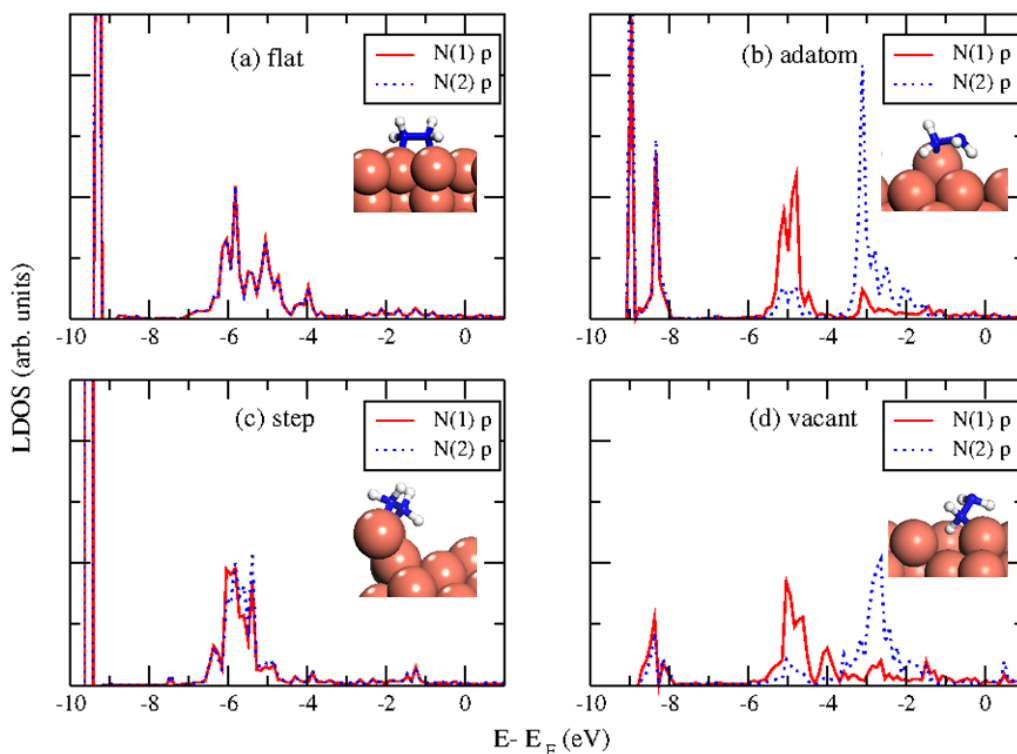


**Figure 4.17.** Site-projected electronic LDOS of the lowest-energy adsorbed structures on each perfect and defective (100) surface for nitrogen p-band. N(1) is the nitrogen closest to the surface and N(2) is the second nitrogen atom of  $N_2H_4$ .

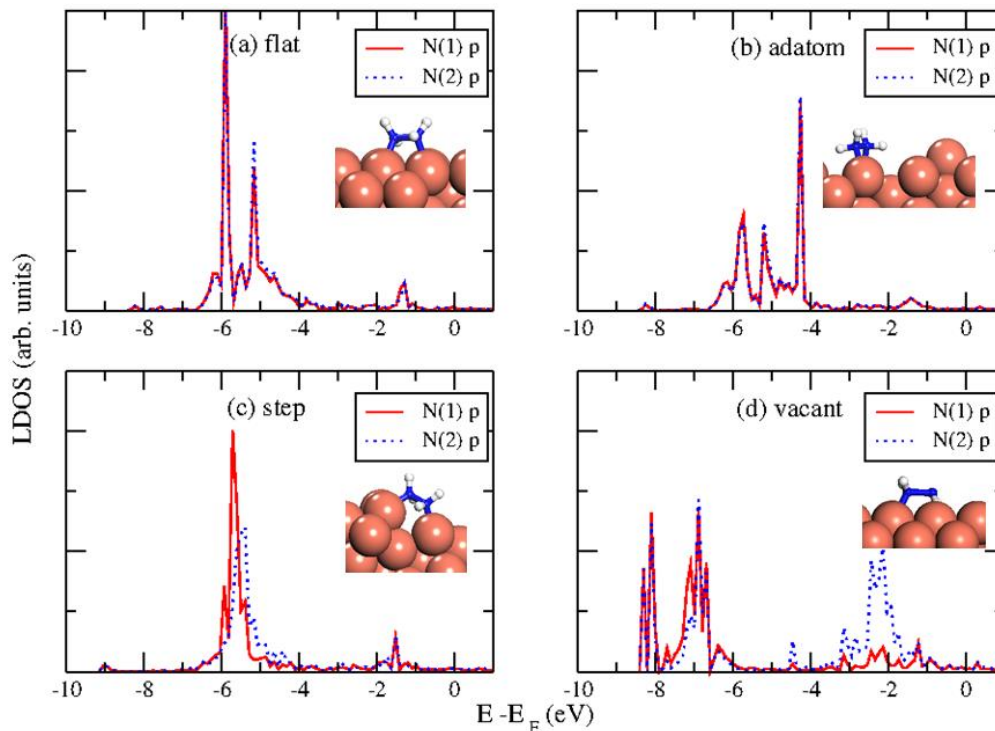


**Figure 4.18.** Site-projected electronic LDOS of the lowest-energy adsorbed structures on each perfect and defective (110) surface for nitrogen p-band. N(1) is the nitrogen closest to the surface and N(2) is the second nitrogen atom of  $N_2H_4$ .

#### 4.3.6.4. Charge density analysis

In order to characterize the bond between  $N_2H_4$  and the Cu surfaces, we have carried out an analysis of the electron density, where the charge density difference was obtained by subtracting from the charge density of the total adsorbate system, the sum of the charge densities of the molecule and the clean surface in the same geometry, equation (4.8):

$$\rho_{transfer} = \rho_{surf+mol} - (\rho_{surf} + \rho_{mol}) \quad (4.8)$$

**Figures 4.19 – 4.21** show the induced charge density with an isovalue of  $\pm 0.02 \text{ e}/\text{\AA}^3$  on each surface upon  $N_2H_4$  adsorption. It indicates the transferred charge densities which on the perfect Cu surfaces originate primarily from the Cu atoms in the

uppermost layer, whereas on the Cu step, adatom and partially vacant surfaces, the charge is transferred mainly from the unsaturated Cu atoms.

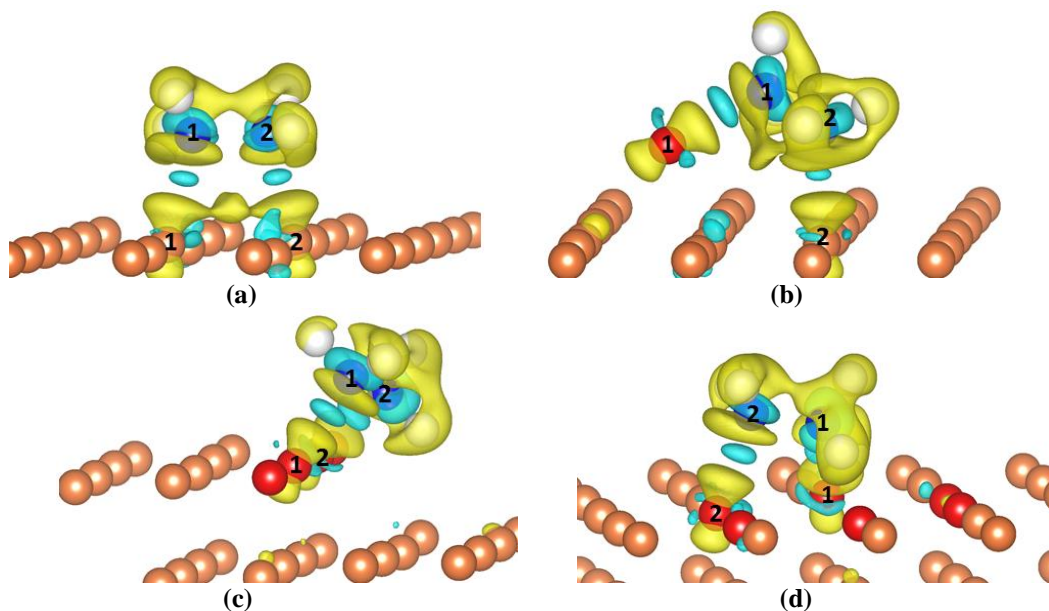


**Figure 4.19.** Induced charge density presentation of the adsorption of  $\text{N}_2\text{H}_4$  molecule on (a) perfect, (b) adatom, (c) step and (d) vacant Cu(111) surfaces by an isosurface of  $\pm 0.02 \text{ e}/\text{\AA}^3$ , where yellow and blue denote lost and gain of electron density. Low-coordinated atoms are shown in red.

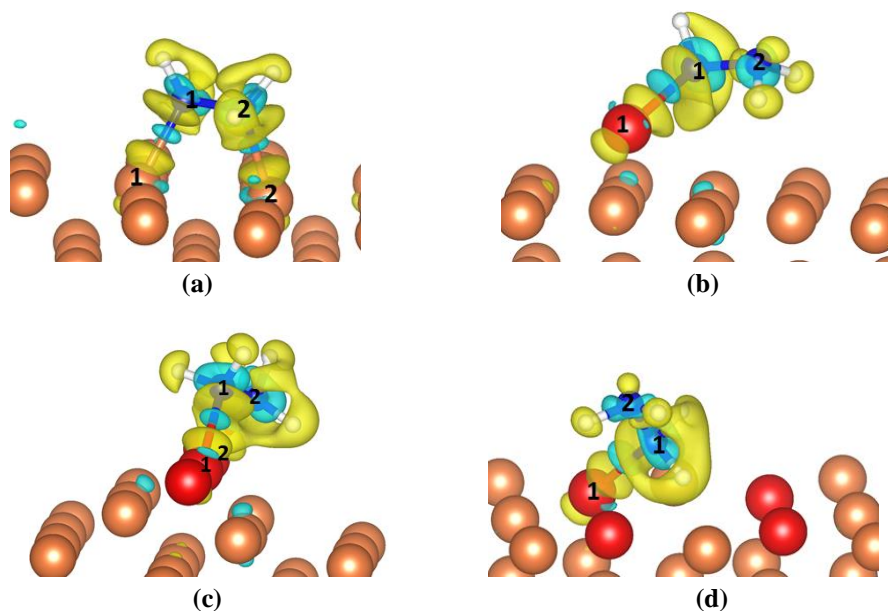


**Figure 4.20.** Induced charge density presentation of the adsorption of  $\text{N}_2\text{H}_4$  molecule on (a) perfect, (b) adatom, (c) step and (d) vacant Cu(100) surfaces by an isosurface of  $\pm 0.02 \text{ e}/\text{\AA}^3$ , where yellow and blue denote lost and gain of electron density. Low-coordinated atoms are shown in red.

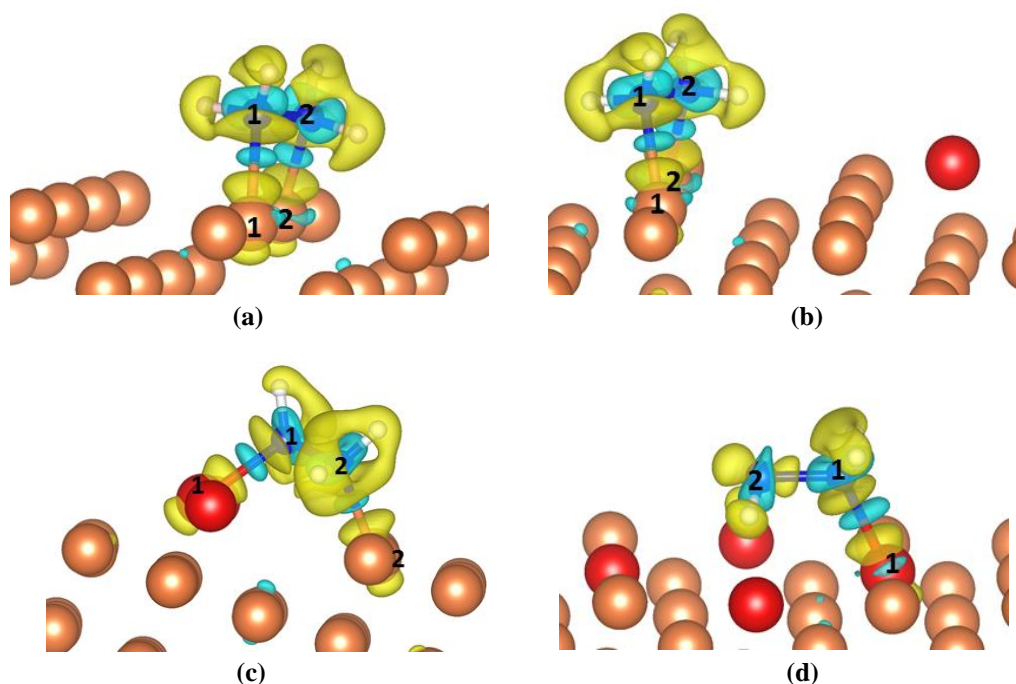


**Figure 4.21.** Induced charge density presentation of the adsorption of  $\text{N}_2\text{H}_4$  molecule on (a) perfect, (b) adatom, (c) step and (d) vacant Cu(110) surfaces by an isosurface of  $\pm 0.02 \text{ e}/\text{\AA}^3$ , where yellow and blue denote lost and gain of electron density. Low-coordinated atoms are shown in red.

In order to analyze the observed N p-band shift in the atop hydrazine adsorption structures and identify any changes in the charges of the adsorbed molecule compared to hydrazine in the gas phase, we have carried out Bader (Bader *et al.*, 1987) charge analyses implemented in the Henkelman algorithm (Henkelman *et al.*, 2006). The charge analysis in **Tables 4.14 – 4.16** show that on those structures where hydrazine interacts through only one atom to the surface, the N atom interacting with the surface is more negatively charged compared with the non-interacting N. This charge distribution is in agreement with the DOS, where there is a larger shift in energy of the p-bands of the interacting N atom, whereas in the bridging configurations both N atoms of hydrazine have practically the same charge. On all investigated Cu surfaces, the resulting net charge transfer between the  $\text{N}_2\text{H}_4$  and surface is very small (less than  $0.1 \text{ e}^-/\text{N}$ ) suggesting only a local charge redistribution

within the  $N_2H_4/Cu$  systems, where the observed distortion of the molecule indicates electronic rearrangement upon adsorption, suggesting a chemical interaction between the molecule and the surface and covalent character of the Cu–N bond.

We found no trend between the amount of charge transferred and the calculated adsorption energies of  $N_2H_4$  at the different Cu surfaces, which indicates that the variation in strength of  $N_2H_4$  binding may be an effect of the coordination of the interacting surface Cu atoms. In order to clarify this suggestion, we have analysed the adsorption energy per N atom in relation to the coordination number (CN) of the interacting Cu atoms on all Cu surfaces in the next section.

**Table 4.14.** Atomic charges of adsorbed hydrazine and the interacting surface Cu atoms on different Cu(111) surfaces. The atomic charges of gas-phase hydrazine are also reported.

system	N1 (e <sup>-</sup> )	N2 (e <sup>-</sup> )	H1 (e <sup>-</sup> )	H2 (e <sup>-</sup> )	H3 (e <sup>-</sup> )	H4 (e <sup>-</sup> )	Cu1 (e <sup>-</sup> )	Cu2 (e <sup>-</sup> )
flat	-0.79	-0.75	0.41	0.41	0.45	0.41	0.12	0.12
step	-0.77	-0.77	0.43	0.40	0.43	0.42	0.13	0.13
adatom	-0.79	-0.75	0.42	0.39	0.43	0.43	0.18	0.14
vacant	-0.79	-0.78	0.42	0.42	0.43	0.42	0.13	0.13
gas-phase hydrazine	-0.73	-0.73	0.37	0.36	0.37	0.36		

**Table 4.15.** Atomic charges of adsorbed hydrazine and the interacting surface Cu atoms on different Cu(100) surfaces. The atomic charges of gas-phase hydrazine are also reported.

system	N1 (e <sup>-</sup> )	N2 (e <sup>-</sup> )	H1 (e <sup>-</sup> )	H2 (e <sup>-</sup> )	H3 (e <sup>-</sup> )	H4 (e <sup>-</sup> )	Cu1 (e <sup>-</sup> )	Cu2 (e <sup>-</sup> )
flat	-0.79	-0.78	0.4	0.41	0.42	0.4	0.13	0.13
step	-0.78	-0.78	0.43	0.41	0.44	0.4	0.11	0.11
adatom	-0.81	-0.72	0.36	0.42	0.41	0.38	-0.03	
vacant	-0.81	-0.75	0.4	0.41	0.4	0.38	0.18	
gas-phase hydrazine	-0.73	-0.73	0.37	0.36	0.37	0.36		

**Table 4.16.** Atomic charges of adsorbed hydrazine and the interacting surface Cu atoms on different Cu(110) surfaces. The atomic charges of gas-phase hydrazine are also reported.

system	N1 (e <sup>-</sup> )	N2 (e <sup>-</sup> )	H1 (e <sup>-</sup> )	H2 (e <sup>-</sup> )	H3 (e <sup>-</sup> )	H4 (e <sup>-</sup> )	Cu1 (e <sup>-</sup> )	Cu2 (e <sup>-</sup> )
flat	-0.79	-0.79	0.43	0.41	0.44	0.41	0.15	0.16
step	-0.78	-0.75	0.42	0.4	0.41	0.38	0.14	0.14
adatom	-0.79	-0.77	0.42	0.41	0.43	0.41	0.15	0.14
vacant	-0.81	-0.72	0.36	0.42	0.44	0.38	0.19	
gas-phase hydrazine	-0.73	-0.73	0.37	0.36	0.37	0.36		

#### 4.3.6.5. Coordination Number

It is clear that the hydrazine molecule adsorbs more strongly on the perfect (110) surface compared to the perfect (100) and (111) Cu surfaces. The Cu atoms in the perfect (110) surface have a coordination number (CN) of 7, while the perfect (100) surface atoms are 8-fold coordinated, showing a weaker N<sub>2</sub>H<sub>4</sub> adsorption, with the weakest adsorption taking place on the perfect (111) surface where the CN is 9; This trend is in line with other theoretical studies (Daff *et al.*, 2009; Daff and de Leeuw, 2012). Although the low-coordinated atoms on the perfect (110) allow the molecule to bind strongly to the surface, the introduction of defects can also provide sites for strong adsorption on the more stable (111) and (100) surfaces.

In order to clarify the effect of CN on the adsorption energy, we have analysed the adsorption energy per Cu–N bond with respect to the coordination number of the interacting Cu atoms. Within this approximation, where hydrazine interacts through both N atoms to surface Cu atoms with the same CN, because the N atoms of the hydrazine molecule in that case have the same LDOS and charge, the binding energy per Cu–N bond is obtained by halving their respective total adsorption energies. In the structures where the two N atoms bind to surface Cu atoms with different CNs and where one Cu has the same CN as on flat surface, we assume that the energy per

Cu–N bond is obtained by the difference between the total adsorption energy of hydrazine at the surface and the adsorption energy per Cu–N bond on the flat surface. However, the calculation of the adsorption energies per interacting N atom is difficult on the (100) adatom and vacancy-containing surfaces, where hydrazine interacts through a single N atom to the surface, because, in principle, we cannot calculate the contribution of the non-bonding N atom to the total adsorption energy. On these surfaces, we have therefore used the second lowest-energy structures, where hydrazine interacts through both N atoms, which enables us to calculate the adsorption energy per Cu–N bond for all surfaces. A plot of the adsorption energy per Cu–N bond as a function of the CN of the interacting Cu is shown in **Figure 4.22.a**, from which it is evident that creating defects with lower CN sites leads to stronger binding. Interestingly, the same CN leads to practically the same  $E_{ads}$  on different surfaces, to within 0.1 eV, independent of the adsorption site.

It has been shown that the d-band center model of chemisorption, developed by Hammer and Nørskov (Hammer and Norskov, 1995; Greeley *et al.*, 2002), can predict the trend in adsorption energies of various adsorbates on metal surfaces. In general, the closest the energy of the d-band center of the site to the Fermi level, the stronger the binding of the adsorbate to the surface. In the present study, we have found a trend of d-band center as a function of CN of interacting Cu surface atom, presented in **Figure 4.22.b**. The linear-trend line indicates a direct relationship between CN and the d-band center of the metal atom. This linear relationship allows us to predict future adsorption affinities based on the CN alone, without the need to calculate the electronic structure of the metallic surface projected on a particular interacting site.

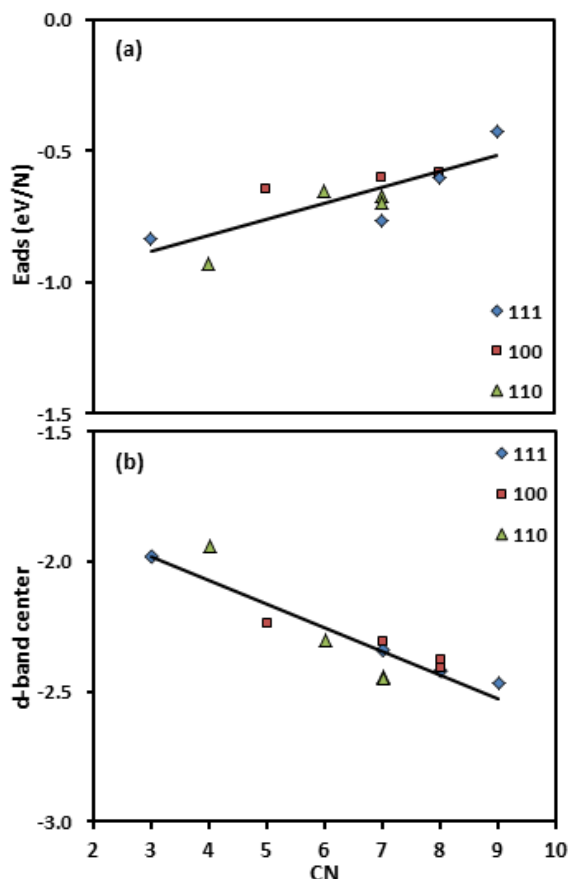


**Figure 4.22.** (a) adsorption energy per N interaction, (b) d-band centre of interacting Cu atoms as a function of coordination number (CN) of interacting Cu atoms, for the lowest-energy adsorption structures on the perfect and defective Cu(111), (100) and (110) surfaces, except on the adatom (100) and vacancy surfaces, where we used the second lowest-energy adsorption structures (see text). The linear trend-lines in the plots fit the equation (a)  $y = -0.09x - 1.71$ ,  $R^2 = 0.84$  and (b)  $y = 0.0605x - 1.0648$ ,  $R^2 = 0.68$ .

## 4.4. Conclusions

We have used DFT-D2 calculations to investigate the adsorption of hydrazine on the defect-containing (111), (100) and (110) surfaces of copper. The creation of defects in the form of steps, Cu-adatoms and vacancies provides lower-coordinated Cu sites, allowing stronger hydrazine adsorption than that on the perfect surfaces. The presence of an extended edge of low-coordinated surface atoms in the form of a step on the (110) surface results in the strongest binding of hydrazine to any of the copper surfaces. The effect of the introduction of defects is more important on the more

stable surfaces, *i.e.* while the presence of a step on the (111) surface almost doubles the strength of adsorption compared to the planar surface, the increase in binding strength to the stepped (100) and (110) surfaces is only 1.10 and 1.19 times that of the binding on the flat (100) and (110) surfaces, respectively. However, adsorption of hydrazine to the stepped (110) surface remains the strongest.

The preferred geometry for hydrazine adsorption on any of the perfect and defective (110) and (100) surfaces is through the molecule bridging two surface copper atoms through both N atoms, except on the (100) adatom, and the (100) and (110) vacancy-containing surfaces, where a structure with only one N on a top site is preferred, with the hydrazine in gauche and trans conformations respectively. A shift occurs of the N p-orbital towards lower energies for those N atoms of hydrazine that are closer to the surface, where they gain more charge.

The thermodynamic morphology of the Cu nano-crystal can be affected by the presence of defects and further changes upon hydrazine adsorption. A linear trend for hydrazine adsorption as a function of CN, as well as for the site d-band electronic structure, indicates that lower CN atoms provide sites with d-band centres closer to the Fermi level, which allows stronger binding. The linear trend lines offer a predictive route to match adsorption strength to CN and d-band centre.

## *Chapter 5: Hydrazine network on the Cu(111) surface*

### **Abstract**

We have used first-principles calculations, including a correction for the dispersive forces (DFT-D2), to investigate the arrangement of hydrazine ( $\text{N}_2\text{H}_4$ ) molecules upon adsorption on the Cu(111) surface, showing that surface-molecule interactions affect the process most. Our calculations provide insight into the interplay between lateral adsorbate-adsorbate and vertical adsorbate-substrate interactions. We found that main contributors to the assembly of the hydrazine layers are the binding interactions between the adsorbates and the substrate. The dispersion forces are predominant in both vertical and lateral interactions, whereas hydrogen-bonding is least important and organisation of the  $\text{N}_2\text{H}_4$  monolayers is therefore primarily due to the long-range interactions. Optimised geometries for several hydrazine conformations were found to be coverage-dependent. The electronic properties such as charge density and density of states have been calculated for different hydrazine coverages, which indicate that no charge transfer occurs between molecules. Scanning tunnelling microscopy images were simulated, where the observed protrusions arise from the trans conformers. We also found that the hydrazine coverage affects the Cu(111) surface energy and further investigation of other Cu facets is needed to determine the  $\text{N}_2\text{H}_4$  coverage effect on the nanoparticles' morphology. Finally, we have simulated the temperature programmed desorption of different coverages of hydrazine from the Cu(111) giving a desorption peak between 150 and 200 K.

## 5.1. Introduction

The assembly of organic molecules on solid surfaces is finding increasing applications in nanoscience, due to the ease of preparation and their power to control surface chemical and physical properties. The driving forces that induce the formation of highly ordered assembled molecular structures on the substrate are the adsorbate-adsorbate and the adsorbate-substrate interactions. The molecular orientation during the assembly process may be governed by long-range binding forces such as hydrogen-bonding, dipole-dipole, van der Waals (vdW) and electrostatic interactions which act at a molecular level. Owing to the directional nature of these interactions, especially hydrogen-bonding, they may be used as control tools in the design of assembled monolayers (Mali *et al.*, 2012). A fundamental understanding of these interactions will help to better control the structure and properties of these systems (Thanthiriwatte *et al.*, 2011). Density functional theory (DFT) is a suitable technique to investigate the assembly process at the atomic level and the electronic structures of the systems at different coverages of molecules, as successfully shown on a number of substrates (Irrera *et al.*, 2013a; Kim *et al.*, 2008; Kuhnle, 2009; Mura *et al.*, 2010; Smerieri *et al.*, 2010; Tranca *et al.*, 2013).

Molecular assembly of adsorbates may also be applied in the synthesis of well-defined nanoparticles for specific applications. Understanding the nanoparticle production process helps us to generate particles with specific sizes, morphologies and desired properties for particular applications. Reverse micelle-based synthesis, for instance, has achieved much in the way of controlling the size and shape of copper nanoparticles, although the underlying processes are still not fully

understood. Many factors affect the size and shape of nanoparticles and one important factor is the concentration of the reducing-capping agent, *e.g.* hydrazine ( $\text{N}_2\text{H}_4$ ), which experiment has shown has a strong effect on the nanoparticle morphology (Lisiecki, 2005; Filankembo *et al.*, 2003; Kitchens *et al.*, 2003; Lisiecki and Pileni, 1993; Salzemann *et al.*, 2004b; Tanori and Pileni, 1995; Tanori and Pileni, 1997). Thus, understanding the molecular adsorption of  $\text{N}_2\text{H}_4$  on the dominant Cu(111) surface at different coverages may help identify measures to control the growth direction and design of copper and other metal nanoparticles.

In this Chapter we have applied electronic structure calculations based on the Density Functional Theory (DFT), with additional semi-empirical terms to take into account essential dispersion interactions, to investigate the interactions between hydrazine molecules. We have investigated the systems with different concentrations of hydrazine, forming a network layer at the molecular level, to provide insight into the interplay between lateral adsorbate-adsorbate and vertical adsorbate-substrate interactions, and to deduce the effect of the concentration of hydrazine on the copper crystal shape. The application of a full monolayer allows us to mimic the hydrazine assembly and understand the intermolecular interactions. We have also modelled scanning tunnelling microscopy (STM) images for future comparison with experiment.

## 5.2. Computational methods

The calculations in this Chapter were done using the Vienna Ab-initio Simulation Package (VASP) (Kresse and Furthmuller, 1996b; Kresse and Furthmuller, 1996a), which allows calculations based on the density functional theory (DFT) (Kresse and Hafner, 1993; Kresse and Hafner, 1994; Kresse and Furthmuller, 1996a; Kresse and

Furthmuller, 1996b). To improve the description of the long-range interactions, we have employed the DFT-D2 (Grimme, 2006; Grimme, 2004) method of Grimme, which has been showed to make important contributions to the surface-molecule interactions (Tafreshi *et al.*, 2014b; Tafreshi *et al.*, 2014a; Irrera *et al.*, 2013a; Dzade *et al.*, 2013). For the detailed methodology employed in this Chapter, please refer to Chapter 3.

Following our work in the previous Chapters, we have used a slab model of four atomic layers, in which the three uppermost layers were free to relax during the optimization, while the bottom layer was kept frozen at the optimized bulk positions. The slab used is a  $3 \times 3$  supercell from the full unit cell,  $p(6 \times 6)$ , containing 36 atoms per layer (144 Cu atoms/unit cell) and exposing an area of  $198.8 \text{ \AA}^2$ , which cell size enables us to investigate a realistic hydrazine network.

We started building an overlayer of hydrazine molecules from a single hydrazine on the planar Cu(111), as investigated in Chapter 3 (Tafreshi *et al.*, 2014b), and increasing to two, three, four, five, six and nine molecules per cell, resulting in a wide range of coverages: from 0.50 to 4.53 molecules/nm<sup>2</sup>. We carried out a relaxation of the geometry after each addition.

The adsorption energy ( $E_{ads}$ ) per molecule was calculated as the difference between the total energy of the optimised substrate-adsorbate system ( $E_{slab+nmol}$ ) and the sum of the energy of the relaxed clean surface ( $E_{slab}$ ) and  $n$  times the energy of an isolated N<sub>2</sub>H<sub>4</sub> ( $E_{mol}$ ) in the gauche conformation, which is the most stable hydrazine conformer in the gas phase;  $n$  is the number of hydrazine molecules, equation (5.1):

$$E_{ads} = [E_{slab+nmol} - (E_{slab} + n.E_{mol})] / n \quad (5.1)$$

The binding and cohesion energies per molecule have also been calculated to discuss the interplay between transversal ( $E_{bind}$ ) and lateral interaction ( $E_{cohe}$ ) (Bader, 1990), which are defined as:

$$E_{bind} = \frac{E_{slab+nmol} - (E_{slab}^* + E_{nmol})}{n} \quad (5.2)$$

$$E_{cohe} = [E_{nmol} - nE_{mol}] / n \quad (5.3)$$

Where,  $E_{nmol}$  is the energy of the hydrazine network in the vacuum and  $E_{slab}^*$  is the energy of the copper surface, both with the same geometry as found in the adsorbate-substrate calculation (denoted by the asterisk). Within this definition, negative  $E_{ads}$ ,  $E_{bind}$  and  $E_{cohe}$  values mean a release of energy during the process. The Bader population analysis as implemented by the Henkelman algorithm (Henkelman *et al.*, 2006) is also used to clarify the nature of the binding between molecules and the surface.

The scanning tunnelling microscopy (STM) images were simulated using the Tersoff-Hamann formalism (Tersoff and Hamann, 1985), in which tunnelling currents are proportional to the local density of states (LDOS) of the surface over a range that corresponds from the Fermi energy ( $E_F$ ) to the bias. We integrated our DFT-based partial charge density from -1.5 eV to  $E_F$  using Hive (Vanpoucke and Brocks, 2008).

### 5.3. Results and discussions

An isolated hydrazine molecule prefers to adsorb parallel to Cu(111) in a gauche conformation, but rotated towards the eclipsed conformation, interacting through

both nitrogen atoms with Cu–N distances of 2.16 and 2.17 Å, as shown in **Table 5.1**. This structure with the calculated adsorption energy of -0.85 eV/N<sub>2</sub>H<sub>4</sub> and a long-range interaction energy contribution of -0.61 eV/N<sub>2</sub>H<sub>4</sub> is shown in **Figure 5.1**. As we have shown in the Chapter 3, the dispersion correction enhances the hydrazine adsorption on the Cu(111) surface and increases the adsorption energy, while it changes the preferred orientation of the molecule from the atop geometry obtained by pure DFT (Daff and de Leeuw, 2012) to a bridging adsorption configuration by using dispersion-corrected DFT-D2.

We have modelled several hydrazine configurations to produce the hydrazine assembly. We started from two molecules and identified the lowest-energy configuration, followed by a further increase in the coverage through addition of another molecule onto the surface and exploration of the different orientations under the new coverage. The hydrazine network was grown in this way until full monolayer coverage was obtained. The lowest-energy structures are shown in **Figures 5.1 – 5.3**. We have reported the geometric details in **Table 5.1** and the adsorption, binding, and cohesion energies for each system, as well as the dispersion contributions to the energies, in **Table 5.2**.

### 5.3.1. Adsorption Structures of hydrazine molecules on Cu(111)

First, we investigated the relative orientation between two molecules in the supercell, as shown in **Figure 5.1**. We positioned different hydrazine conformers, including gauche, trans and eclipsed conformers, onto the surface, providing several choices for pairing of the N<sub>2</sub>H<sub>4</sub> molecules. We found three low-energy configurations with only small differences in the adsorption energies,  $\Delta E_{ads}^{2(A)-2(B)} = -0.06$  eV and  $\Delta E_{ads}^{2(A)-2(C)} = -0.03$  eV, as shown in **Table 5.2**. Structure 2(A) has one hydrazine in

the gauche and its neighbouring molecule in the trans conformation. In structure 2(B) one hydrazine is in the gauche conformation, adsorbing through one N atop a Cu atom, while the other molecule rotates towards the eclipsed conformation, thereby enabling the molecule to bridge through both N atoms to the surface. In the third structure, 2(C), both molecules are in the gauche conformation and, like structure 2(A), they adsorb on the surface through one N atom.

Configuration 2(A) binds most strongly, due to the higher contribution of the dispersion interaction (**Table 5.2**). Although there is negligible difference in charge transfer (CT) from the hydrazine clusters to the surface,  $\Delta(\text{CT})^{2(\text{A})-2(\text{B})} = -0.02 e^-$  and  $\Delta(\text{CT})^{2(\text{A})-2(\text{C})} = +0.03 e^-$ , the molecules in structure 2(A) are closer to the surface. The structure of the trans conformer makes it feasible to form H-bonds with nitrogen atoms of the neighbouring gauche conformer and enables molecules to interact by lateral interactions. Structure 2(A) is stabilised by the dispersive forces which contribute half of the adsorption energy. Since in structure 2(B) the hydrazine assembly has become bound covalently to the surface through three bonds, compared to two bonds in 2(A) and 2(C), it leads to more charge transfer ( $+0.19 e^-$ ) and a larger binding energy to the surface ( $-1.19 eV$ ), the largest of the calculated structures (**Table 5.2**). However, the longer distance and weaker interaction between the molecules results in a smaller adsorption energy. Owing to the closer distance between the molecules in structure 2(C), this has the highest cohesion energy, although the repulsion between the hydrogens of the two gauche conformers decreases the adsorption energy.

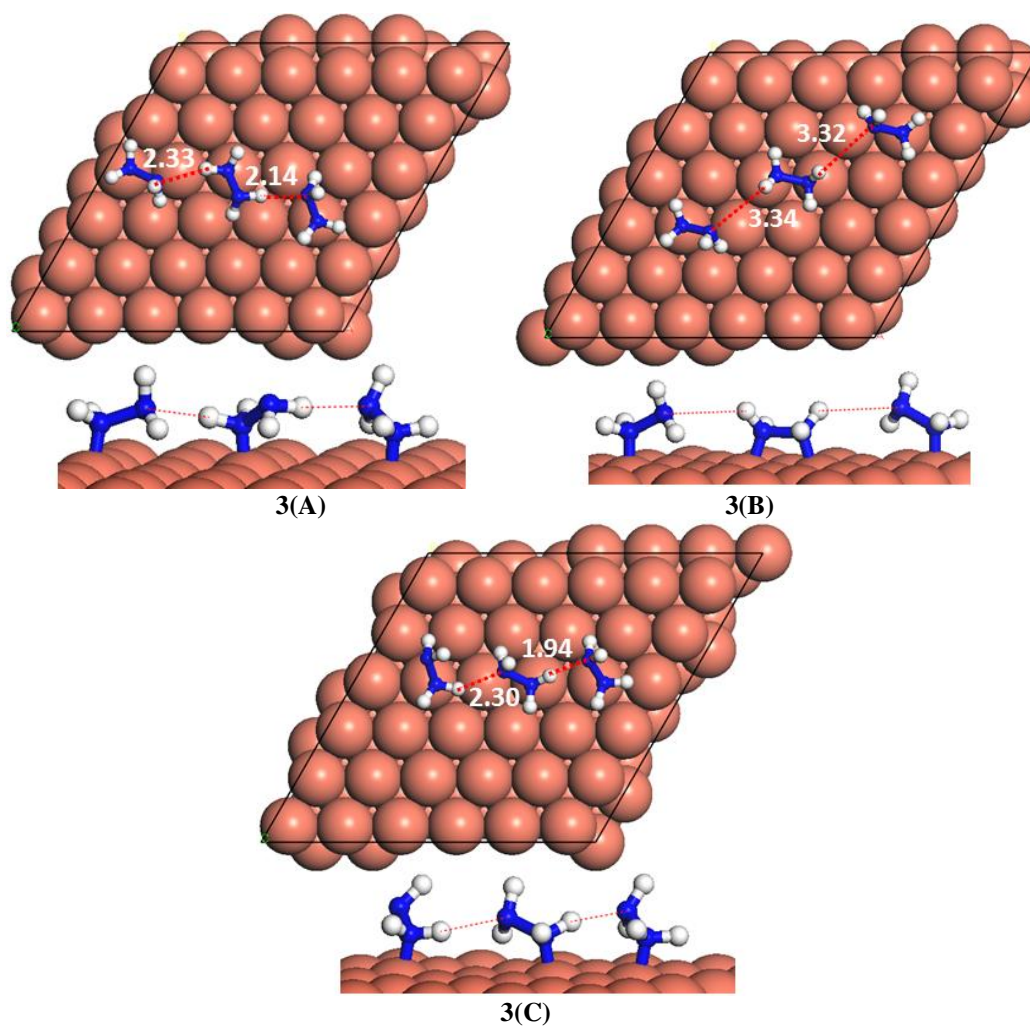


We next increased the coverage by adding a third molecule to the previous three configurations, where the most stable networks formed are indicated as 3(A), 3(B) and 3(C) in **Figure 5.2**. In the 3(A) network, which is grown from the optimized 2(A) geometry, the adsorption energy decreases to  $E_{ads} = -1.10$  eV through addition of another gauche hydrazine, which forms an H-bond between one of the nitrogen atoms and one of the H atoms of the trans conformer. The charge transfer from the molecules to the surfaces is also the largest of these three configurations (**Table 5.1**), making this the most stable structure at this coverage.

Configuration 3(B) grown from 2(B), decreases the adsorption energy to -1.03 eV compared to 3(A),  $\Delta E_{ads}^{3(A)-3(B)} = -0.07$  eV. In this case, one of the hydrazine molecules bridges through both nitrogen atoms to the surface, whereas the others, in gauche conformation, bind only by one nitrogen to the copper atoms, allowing the formation of hydrogen bonds through their N to hydrogen atoms of the ‘bridging’ hydrazine in the middle. Structure 3(C) grows from 2(C), with all hydrazine molecules in gauche conformation and interacting through only one nitrogen atom to the surface, releasing a smaller adsorption energy of  $E_{ads} = 1.01$  eV, *i.e.* -0.09 eV less favourable than configuration 3(A). The energy difference is related to the smaller charge transfer from the molecules to the surface (shown in **Table 5.1**). The 3(C) has the highest cohesion energy among the calculated configurations,  $E_{cohe} = -0.10$  eV, which is due to the short distance between the molecules and therefore stronger H-bonds.

**Table 5.2.** Adsorption ( $E_{ads}$ ), binding ( $E_{bind}$ ) and cohesion ( $E_{cohe}$ ) energies. Long-range interaction energy contributions to these energies are also reported with vdW superscript.

No. hydrazine (types)	$E_{ads}$ (eV/N <sub>2</sub> H <sub>4</sub> )	$E_{ads}^{vdW}$ (eV/N <sub>2</sub> H <sub>4</sub> )	$E_{bind}$ (eV/N <sub>2</sub> H <sub>4</sub> )	$E_{bind}^{vdW}$ (eV/N <sub>2</sub> H <sub>4</sub> )	$E_{cohe}$ (eV/N <sub>2</sub> H <sub>4</sub> )	$E_{cohe}^{vdW}$ (eV/N <sub>2</sub> H <sub>4</sub> )	No. hydrogen bonds
2(A)	-1.12	-0.57	-1.14	-0.53	-0.02	-0.02	1
2(B)	-1.06	-0.50	-1.19	-0.54	0.06	-0.01	1
2(C)	-1.09	-0.45	-1.10	-0.51	-0.04	-0.03	1
3(A)	-1.10	-0.55	-1.10	-0.51	-0.04	-0.03	2
3(B)	-1.03	-0.56	-1.15	-0.53	0.06	-0.01	2
3(C)	-1.01	-0.59	-0.97	-0.52	-0.10	-0.04	2
4	-1.07	-0.57	-1.06	-0.52	-0.05	-0.04	3
5	-1.06	-0.57	-1.05	-0.52	-0.05	-0.04	4
6	-1.01	-0.52	-1.00	-0.48	-0.05	-0.04	4
9	-0.95	-0.58	-0.92	-0.52	-0.07	-0.05	6

**Figure 5.2.** Assembly of hydrazine configurations 3(A), 3(B) and 3(C) for three molecules on the Cu(111) surface. The hydrogen-bond distances are indicated and labelled in Å. (N = blue, H = white, Cu = orange).

Based on the lowest-energy structure found for the  $[\text{N}_2\text{H}_4]_n$  assembly by three molecules ( $n=3$ ), we increased the coverage by adding one and two extra molecules to this network. **Figure 5.3** shows the lowest-energy assemblies of  $[\text{N}_2\text{H}_4]_n$  clusters ( $n=4, 5$ ), with three and four H-bonds respectively. The calculated energies for these structures, (**Table 5.2**), show that the clusters are energetically degenerate ( $\Delta E_{ads}^{4-5} = -0.01$  eV), indicating that the extra H-bond in the structure does not contribute much to the stability of the structure and confirming that the hydrazine assembly is mostly due to dispersion forces.

The lowest-energy  $[\text{N}_2\text{H}_4]_6$  assembly on the surface is shown in **Figure 5.3** with an adsorption energy of  $E_{ads} = -1.01$  eV, *i.e.* the same adsorption energy as 3(C). It is grown from 3(A) and consists of two trans structures in the centre, neighboured by four gauche conformers, with all the molecules binding to the surface through one N atom. Although there are four H atoms oriented towards the N of a neighbouring molecule, the calculated cohesion energy ( $E_{cohe} = -0.05$  eV) varies little and is of a similar magnitude compared to the other hydrazine assemblies with fewer hydrogen-bonds, which is due to the relatively long and weak hydrogen-bonds between molecules.

By adding three more hydrazine molecules and increasing the coverage to nine molecules ( $4.53$  molecules/nm<sup>2</sup>), aimed at attaining full coverage, we found the lowest-energy configuration with an adsorption energy of  $E_{ads} = -0.95$  eV/N<sub>2</sub>H<sub>4</sub> and dispersion contribution of  $E_{ads}^{vdW} = -0.58$  eV/N<sub>2</sub>H<sub>4</sub>, represented in **Figure 5.3**. Together with  $E_{cohe} = -0.07$  eV/N<sub>2</sub>H<sub>4</sub> and  $E_{bind} = -0.92$  eV/N<sub>2</sub>H<sub>4</sub>, these results indicate that the binding of the N<sub>2</sub>H<sub>4</sub> molecule to the Cu surface is the main contributor to the stabilization of the hydrazine network, owing to the covalent character of the

interaction of all molecules with the surface (Chapter 4). Dispersion forces make up almost half of the adsorption and binding energies, showing that the dispersive forces are also essential in the description of the hydrazine organization. The high contribution of dispersion forces to the small cohesion energies indicate that van der Waals forces are the main interaction between molecules, whereas hydrogen-bonding is only a weak factor in the formation of the hydrazine assemblies, because of the relatively long distances between molecules.

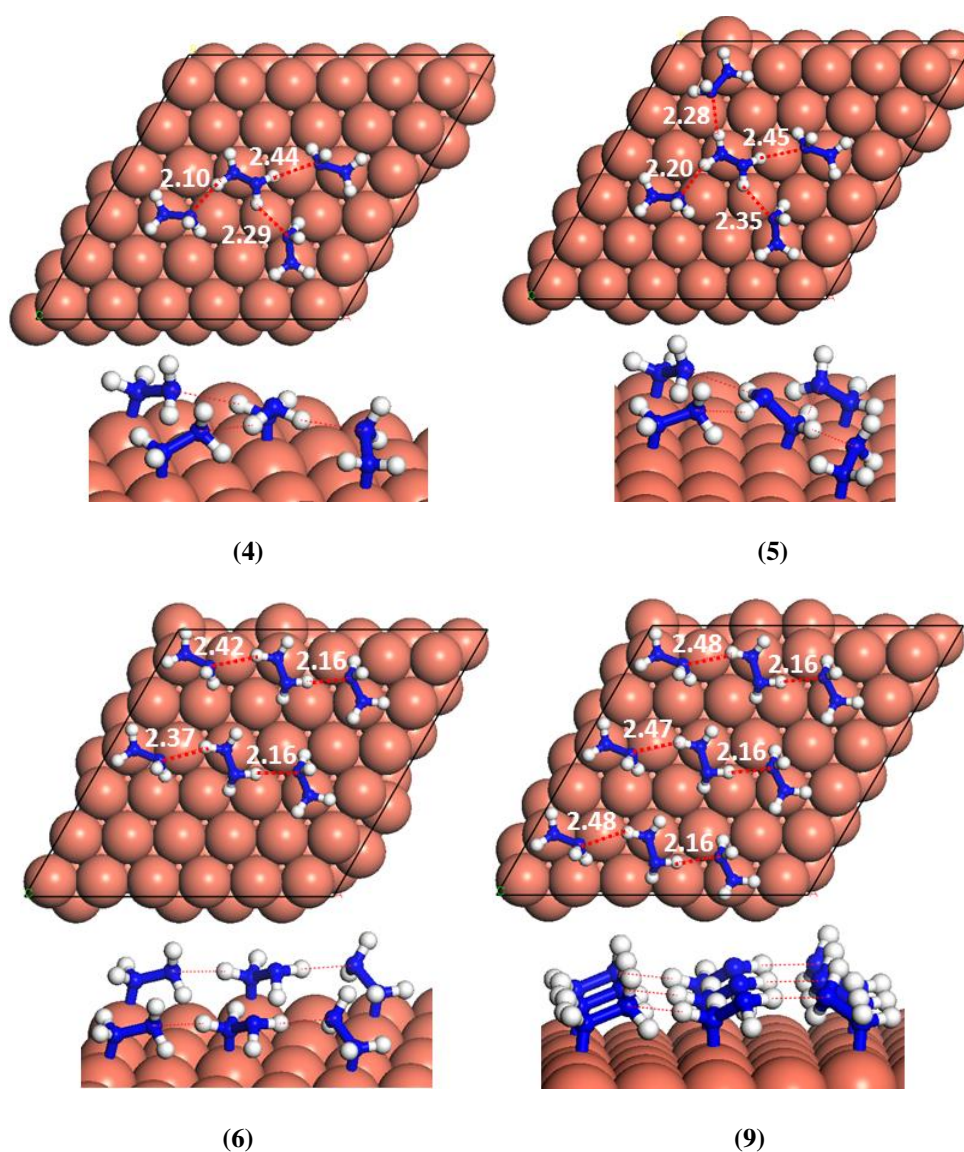


**Figure 5.3.** Self-assembly of hydrazine for four, five, six and nine molecules on the Cu(111) surface. The hydrogen-bond distances are indicated and labelled in Å. (N = blue, H = white, Cu = orange).

### 5.3.2. Electronic structure characterization

We have calculated the charge density differences for hydrazine on the Cu(111) surfaces by subtracting the individual electron densities of the molecular cluster and the surface, both calculated in the geometry of the combined system, from the density of the total system, see **Figure 5.4**. Yellow and blue regions correspond to positive and negative electronic charge modifications, respectively, between Cu substrate and molecules. The charge density difference has been calculated for two different coverages of hydrazine on the Cu(111), *i.e.* with 5 and 9 molecules. The electronic density rearrangement takes place individually, with negligible polarization of the molecular electron clouds, which is quite similar to the single molecule adsorption. This electronic behaviour matches the energetics, showing that the molecule-surface interactions (binding energy) contribute most to the hydrazine assembly.

We also derived the topographical STM images, providing information about the spatial distribution of the valence band states in the vicinity of the Fermi energy ( $E_F$ ), from the optimised structures of the different coverages composed of 5 and 9 hydrazine molecules. The positions of the atomic species adsorbed on a surface can be affected (Irrera *et al.*, 2013a) in low temperature experimental STM, where they do not show the real space images of single molecules and small clusters on surfaces (Hodgson and Haq, 2009; Henderson, 2002) for several reasons, such as high mobility of the molecules during adsorption resulting in immediate formation of larger clusters and error in cluster assignment. Moreover, tip interactions can perturb the image by vibrational excitation (Gawronski *et al.*, 2005) or restructuring (Gawronski *et al.*, 2008) and dissociating adsorbed molecules (Morgenstern and

Rieder, 2002). However, simulated STM images do not suffer from any external perturbations.

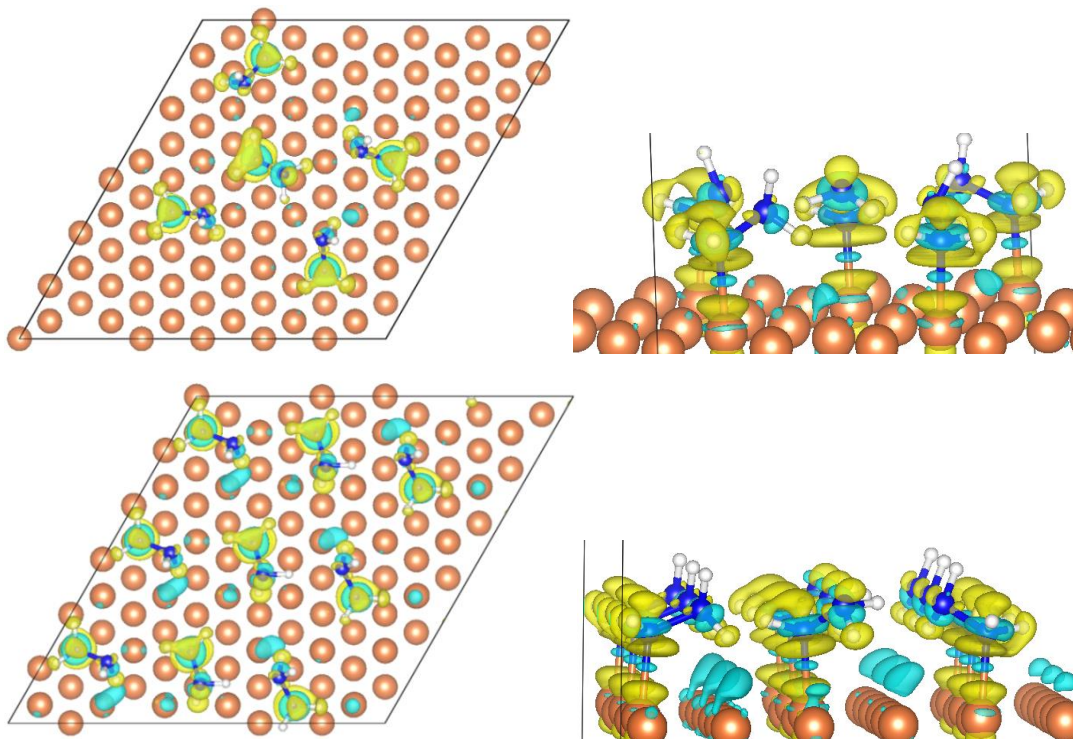


**Figure 5.4.** Top and side views of the charge density difference induced by deposition of 5 and 9 hydrazine molecules on Cu(111). The isosurface was set to  $\pm 0.02 \text{ e}/\text{\AA}^3$ , where yellow and blue denote loss and gain of electron density respectively.

We have tested different potentials with respect to the Fermi level energy and concluded that a bias of -1.50 eV is enough to provide a clear STM image. **Figure 5.5** shows the STM images at a density of  $8 \times 10^{-5} \text{ e}/\text{\AA}^3$  and distance of 1.7 Å for the hydrazine assembly composed of 5 molecules and for full coverage with 9 molecules at a density of  $2 \times 10^{-4} \text{ e}/\text{\AA}^3$ , where the tip is at 1.4 Å from the highest atom. The insets in **Figure 5.5** clearly show the trans and gauche conformers that determine the STM images. As there is no experimental STM to compare with, our simulated STM for the hydrazine networks on Cu(111) are at the moment a good reference for future experiment.

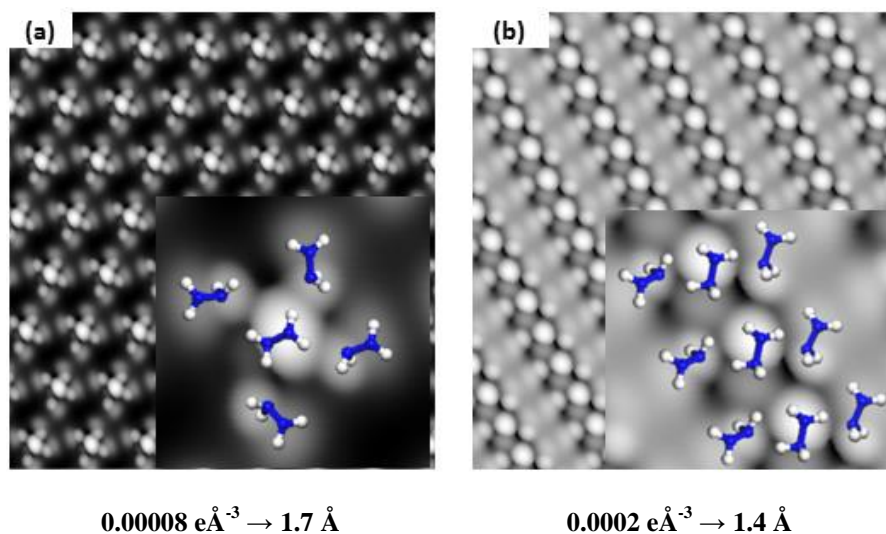


**Figure 5.5.** Simulated STM images of the hydrazine network with a) 5 and b) 9 hydrazine molecules at a simulated bias of -1.5 V. Insets show enlargement of the STM images. Densities and tip distances are also indicated. (N = blue, H = white).

The density of states (DOS) in **Figure 5.6** explains some features of the STM owing to its relationship to the partial charges. The negligible appearance of DOS of hydrogen atoms in the energy range  $[-1.5 - 0]$  eV explains why they are not observed at that bias in the STM images. The N atoms of the trans conformers show more and sharper peaks than the gauche structures in the energy range of  $[-1.5 - 0]$  eV, which explains why the protrusions from N atoms of trans conformers are more intensive in the STM image.

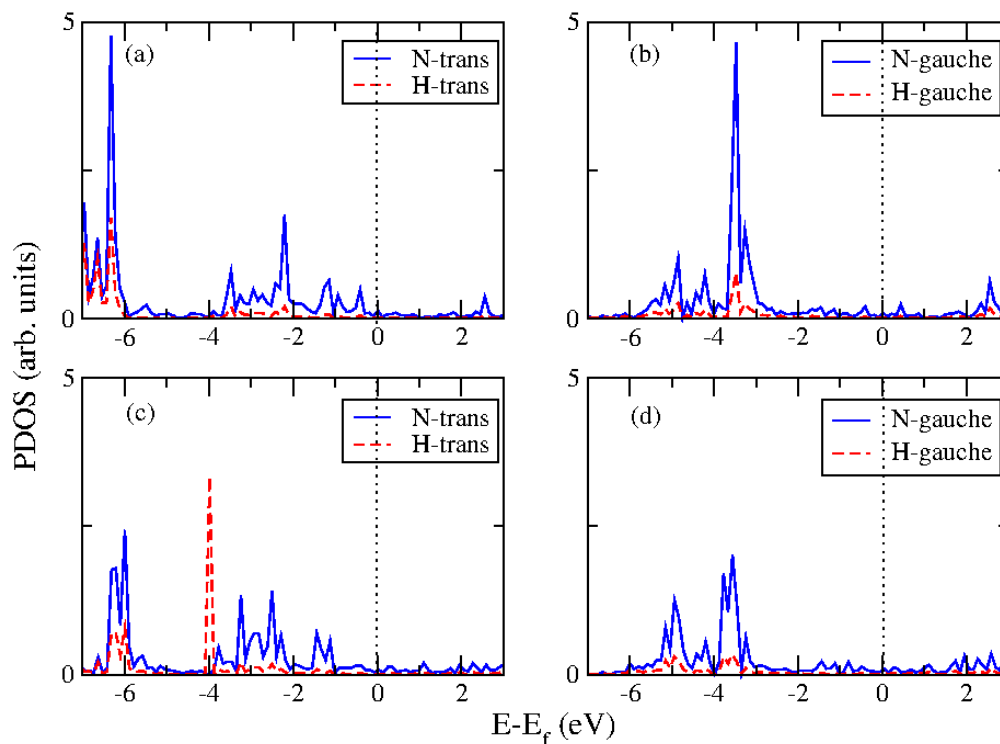


**Figure 5.6.** The average PDOS of N and H atoms of trans and gauche conformations of  $N_2H_4$  corresponding to  $[N_2H_4]_5$  cluster in (a) and (b); and the full coverage  $[N_2H_4]_9$  cluster in (c) and (d) on the Cu(111) surface.  $E = 0$  eV corresponds to the Fermi level.

In order to clarify the effect of the hydrazine coverage on the binding and cohesion energies, we have analysed these energies for each structure in relation to the number of molecules in the assembled layer. A linear trend is presented in **Figure 5.7**, indicating that while the cohesion energy remains almost constant with increasing number of molecules, the adsorption energy as well as binding energy between assembled hydrazine layer and the surface becomes less. This trend confirms that the molecule-molecule interactions are weak and the hydrazine network is led by the binding energy, which contributes more to the adsorption energy than the cohesion energy.

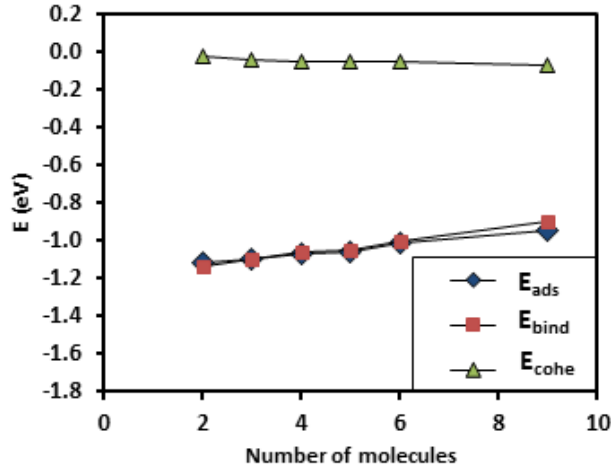


**Figure 5.7.** Adsorption ( $E_{ads}$ ), binding ( $E_{bind}$ ) and cohesion ( $E_{cohe}$ ) energies of the lowest-energy adsorption structures as a function of the number of hydrazine molecules.

Since according to the Wulff's Theorem (Wulff, 1901) the surface energies can be assumed to determine the equilibrium morphology of the crystal and the experimental study by Lisiecki (Lisiecki, 2005) showed that controlling the hydrazine concentration is a key parameter enabling the size and shape control of copper nanoparticles, we have calculated the relaxed surface energy ( $\gamma$ ) of the Cu(111) surface for the lowest-energy adsorption configurations at different hydrazine coverages using the equation (5.4) to investigate how increasing hydrazine coverage affects the morphology of Cu nanoparticles.

$$\gamma_r = \frac{E_{slab+Nmol} - [nE_{bulk} + NE_{mol}]}{A} - \frac{E_{slab}^{unrelaxed} - nE_{bulk}}{2A} \quad (5.4)$$

Where  $E_{slab+Nmol}$  is the total energy of the optimised substrate-adsorbate system and  $E_{mol}$  is the energy of an isolated  $N_2H_4$  in the gauche conformation, which is the most stable hydrazine conformer in the gas phase and  $N$  is the number of hydrazine molecules,  $E_{slab}^{unrelaxed}$  is the total energy of the unrelaxed slab prior to surface geometry optimization,  $E_{bulk}$  is the energy of the primitive cell containing one Cu

atom,  $n$  is the number of atoms in the slab and  $A$  is the surface area of one side of the slab.

**Figure 5.8** shows the variation of the Cu(111) surface energy as a function of  $N_2H_4$  coverage. Since increasing the number of hydrazine molecules results in decreasing the surface energy, Cu(111) will increase its area ratio with respect to the other surfaces changing the particles' morphology. However to predict the copper nanoparticles' morphology changes as a function of hydrazine coverage, other surfaces with lower coordination have to be studied under different  $N_2H_4$  coverages.

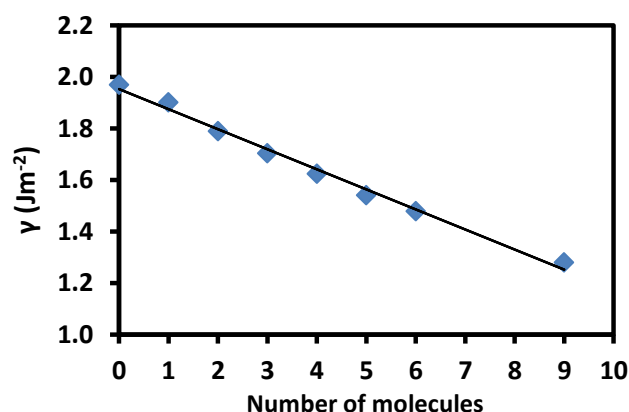


**Figure 5.8.** Surface energy ( $\gamma$ ) of the Cu(111) surface for the lowest-energy adsorption structures as a function of the number of molecules. The linear trend-lines in the plots fit the equation  $y = -0.0779x + 1.9534$ ,  $R^2 = 0.99$ .

### 5.3.3. Temperature programmed desorption

In order to extrapolate the electronic structure results to real conditions we have simulated the temperature programmed desorption (TPD) of  $N_2H_4$  from the Cu(111) surface, considering pre-adsorbed  $N_2H_4$  molecules with different coverages to mimic an experimental reactor with a high pumping speed to avoid re-adsorption of the

$N_2H_4$  molecule. The energy interaction is coverage dependent, as derived from our results for coverages between 0.06 and 0.25 ML  $N_2H_4$  coverage, a monolayer (ML) is defined as the number of molecules divided by the number of Cu atoms on the surface.

The  $N_2H_4$  pressure and coverage as a function of time with the rate constant of  $k$  are derived from the following set of differential equations:

$$\frac{dP_{N_2H_4}}{dt} = k\theta_{N_2H_4} \quad (5.5)$$

$$\frac{d\theta_{N_2H_4}}{dt} = -k\theta_{N_2H_4} \quad (5.6)$$

Where  $\theta$  is the coverage in ML and  $t$  is the time.

In the heterogeneous catalytic system, the constant rate of desorption process is computed using transition-state theory by Eyring (Eyring, 1935) and Evans and Polanyi (Evans and Polanyi, 1935), as follows;

$$k = A_0 \exp\left(\frac{-E_a}{k_B T}\right) = \frac{k_B T}{h} \frac{q_{TS}}{q_{IS}} \exp\left(\frac{-E_a}{k_B T}\right) \quad (5.7)$$

Where  $h$  is the Plank constant,  $k_B$  is the Boltzmann constant,  $T$  is the temperature,  $A_0$  is the pre-exponential factor,  $E_a$  is the desorption energy and;  $q_{IS}$  and  $q_{TS}$  are the partition functions of reactants and transition states, respectively. The partition function  $q_{IS}$  includes all the vibrational modes, while  $q_{TS}$  is the partition function for the transition state, where the only degree of freedom the molecule has is vibrational, from which the vibration between the molecule and the surface representing the reaction coordinate has been excluded. The values of the  $N_2H_4$

desorption rate constant and pre-exponential factor at 150 and 300 K are reported in **Table 5.3**.

**Figure 5.9** shows the simulated TPD spectra of molecular  $\text{N}_2\text{H}_4$  on the Cu(111) surface, where the derivative of the  $\text{N}_2\text{H}_4$  partial pressure with respect to the temperature results in a peak showing the temperature at which the  $\text{N}_2\text{H}_4$  pressure reaches its maximum. Since experimental reports show that hydrazine starts to decompose at around 300 K (Alhaydari *et al.*, 1985), we have considered a temperature range between 100 and 300 K to investigate  $\text{N}_2\text{H}_4$  desorption, without involving hydrazine reactions on the Cu surface. A heating rate of 1 K/min was applied, measuring the pressure every second. From **Figure 5.9** it is clear that  $\text{N}_2\text{H}_4$  desorption takes place between 150 and 200 K from the Cu(111) surface. Similar desorption temperatures have been reported for hydrazine on rhodium (Prasad and Gland, 1991a) and  $\text{Ir}_n/\text{Al}_2\text{O}_3$  (Lee *et al.*, 2005) surfaces.

**Table 5.3.** Calculated pre-exponential factors ( $A_0$ ) and desorption rate constants ( $k$ ) for  $\text{N}_2\text{H}_4$  from Cu(111) at 150 and 300 K are reported.

	$A_0$ ( $\text{s}^{-1}$ )		$k$ ( $\text{s}^{-1}$ )	
	150 K	300 K	150 K	300 K
$\text{N}_2\text{H}_4$ (ads) $\rightarrow$ $\text{N}_2\text{H}_4$ (g)	$8.39 \times 10^{11}$	$2.31 \times 10^{11}$	$4.14 \times 10^{-5}$	$5.68 \times 10^7$

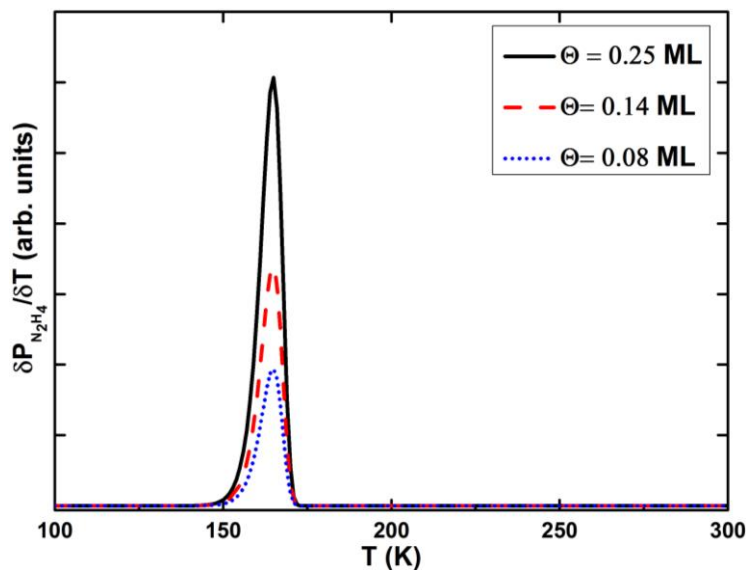


**Figure 5.9.** Simulated TPD curves for  $N_2H_4$  desorption from Cu(111) surface for a reaction time of 1 s and heating rate of 1 K/min at different initial coverages.

## 5.4. Conclusions

We have presented a theoretical study using DFT-D2 of the assembly of hydrazine networks adsorbed on the Cu(111) surface. Our results show that the molecule-molecule interactions are very weak and arise mostly from dispersive forces. We conclude that binding of the  $N_2H_4$  molecules with the Cu surface, plus dispersive forces between adsorbate and surface are the main interactions driving the assembled adsorbate networks, although the cohesion energies between the molecules, arising primarily from long-range interactions, also affect the arrangement of the molecules in the surface overlayer. The relatively large dispersion contributions to the cohesion energies indicate that the molecule-molecule interactions arise mostly from vdW forces and that hydrogen-bonding is the smallest contributory factor in the hydrazine assembly. Our charge density difference calculations show that the molecule and substrate share electrons, while no charge transfer was observed between molecules. The STM images for the two hydrazine networks composed of five and nine

molecules were calculated, where the observed protrusions arise from the trans conformers. We have also investigated the surface energy as a function of hydrazine concentration, indicating that variation in the hydrazine coverage on the Cu(111) affects significantly the shapes of the copper nanoparticles, and further investigation of other Cu facets of the nanoparticles is therefore required to obtain the effect of hydrazine coverage on their surface energies. Temperature programmed desorption of hydrazine from the Cu(111) surface was simulated for different hydrazine coverages, showing a desorption peak between 150 and 200 K.

## *Chapter 6: Hydrazine decomposition mechanism on the planar and stepped Cu(111) surfaces*

### **Abstract**

We have investigated the adsorption of hydrazine ( $\text{N}_2\text{H}_4$ ) and its reactivity on the terraces and steps of Cu(111) surfaces by first-principles calculations in order to gain insight into the hydrazine decomposition mechanism. We have investigated different possibilities for the N–N and N–H bond cleavage for the intermediate states by analysing the reaction and barrier energies of each elementary step. We have found that hydrazine dehydrogenation via N–H bond scission is neither energetically nor kinetically favourable on the flat and stepped surfaces, but hydrazine prefers to form  $\text{NH}_2$  via N–N bond decoupling on the Cu(111) with an activation energy below 1 eV. The  $\text{NH}_2$  molecule reacts fairly easily with co-adsorbed  $\text{NH}_2$  to form  $\text{NH}_3$  as well as with  $\text{N}_2\text{H}_x$  ( $x=1-4$ ) by abstracting hydrogen to produce  $\text{NH}_3$  and  $\text{N}_2$  molecules on both the flat and stepped surfaces. We also found that all intermediates except NNH prefer N–N bond breaking as the most likely dissociation pathway, where the produced amide and imide intermediates can be hydrogenated to form  $\text{NH}_3$  in the presence of hydrogen. NNH is the only intermediate, that prefers to dissociate via a highly exothermic N–H bond breaking process to produce an  $\text{N}_2$  molecule after overcoming a small barrier energy. We also studied production of  $\text{H}_2$  by recombination of hydrogen ad-atoms, which considering the activation energies is particularly favoured under conditions of moderate temperatures. Our results agree well with experiments suggesting that  $\text{N}_2\text{H}_4$  adsorbs dissociatively on copper above ~

300 K leading to N<sub>2</sub>, NH<sub>3</sub> and H<sub>2</sub>. In general, the lower coordination of the steps is found to lead to higher reactivity than on the flat Cu(111) surface. Furthermore, the calculations show that the influence of step edge atoms is very different for the intra- and inter-molecular dehydrogenation mechanisms. It also increases the barrier of N–N decoupling of all the existing species in the reaction.

## 6.1. Introduction

Hydrogen has received much attention over the last decades as an energy resource (Dutta, 2014; Schlapbach and Zuttel, 2001), for instance, in the Proton Exchange Membrane (PEM) fuel cells which are one of the new carbon-free technologies for power generators. However, finding materials with a high storage capacity of hydrogen at room temperature is difficult and much effort is spent on developing new materials or employing organic and inorganic compounds for onboard hydrogen generation. Hydrazine (N<sub>2</sub>H<sub>4</sub>) with a hydrogen content of 12.5 wt % is a good hydrogen source for PEM fuel cells and since it is liquid at temperatures ranging from 2°C to 114°C, it is ideal for portable applications, for example for its current use in space vehicles or satellites (Zheng *et al.*, 2005; Schmidt, 2001; Pakdehi *et al.*, 2014). Although hydrazine is a toxic substance, its decomposition products, N<sub>2</sub>, H<sub>2</sub> and NH<sub>3</sub> are non-poisonous and carbon-free (Zheng *et al.*, 2005). Its decomposition over catalysts at room temperature is exothermic without the need for external energy. Hydrazine is also used in a monopropellant thruster to control and adjust the orbits and altitudes of spacecrafts and satellites (Mary *et al.*, 1999; Schmidt, 2001), which is based on the production of larger volumes of N<sub>2</sub>, H<sub>2</sub> and NH<sub>3</sub> gases from the decomposition of a relatively small volume of liquid hydrazine. The most important catalyst used for this reaction is Ir/Al<sub>2</sub>O<sub>3</sub> with a high loading of iridium (20–40%)

(Mary *et al.*, 1999; Balcon *et al.*, 2000; Schmidt, 2001; Contour and Pannetie.G, 1972). However, due to the high price and limited resources of iridium, scientists are seeking to develop new, cheaper, active and readily available alternative catalysts for N<sub>2</sub>H<sub>4</sub> decomposition.

We aim to investigate at the molecular level the catalytic activity of Cu towards N<sub>2</sub>H<sub>4</sub> decomposition to understand the thermodynamics and kinetics of the elementary steps, and to evaluate if copper-based catalysts, which are much cheaper than iridium, could be used for hydrazine decomposition. Experimental studies have revealed that adsorption of N<sub>2</sub>H<sub>4</sub> on copper at relatively low temperatures is likely to be reversible and non-dissociative up to ~ 300 K, above which the hydrazine decomposes and generates the gaseous products NH<sub>3</sub>, N<sub>2</sub> and H<sub>2</sub> (Matloob and Roberts, 1977; Alhaydari *et al.*, 1985). There are two typical reactions for hydrazine decomposition;



and



The competition between the two decomposition reactions is influenced by the catalyst and the reaction conditions. A few comprehensive computational studies have been performed on the mechanism of hydrazine decomposition on transition metal surfaces, *e.g.* the density functional theory (DFT) study of hydrazine decomposition on the Ir(111) surface (Zhang *et al.*, 2011), which showed that N–N bond cleavage of hydrazine is more easily accomplished than that of the N–H bond, and the NH<sub>2</sub> radicals can abstract hydrogen atoms one by one from N<sub>2</sub>H<sub>4</sub> resulting in

the formation of  $N_2$  and  $NH_3$  molecules. On Fe(211) (McKay *et al.*, 2011), the dehydrogenation and nitrogen decoupling are competitive routes, with  $NH_2$  and N being the dominant surface intermediates at mild temperatures, leading to gas-phase  $N_2$  and  $NH_3$  at higher temperatures. A DFT study of the dissociative adsorption of  $N_2H_4$ , by breaking of the hydrazine N–N bond, on low-index planar copper surfaces with and without Cu adatoms, showed that dissociative adsorption is thermodynamically strongly favoured over molecular sorption (Daff and de Leeuw, 2012). In this study, we have used improved DFT methodology, including long range interaction corrections to model more accurately the van der Waals forces and analyse the thermodynamics and kinetics of the complete dissociation reaction.

Beside the more stable perfect and planar surfaces, defects and steps are common surface features. Previous experimental and theoretical results have suggested that low-coordinated sites show higher catalytic activity and can influence the overall surface chemistry (Norskov *et al.*, 2002; Liu and Hu, 2003; Zubkov *et al.*, 2003; Gambardella *et al.*, 2001; Ciobica and van Santen, 2002; de Leeuw and Purton, 2001; Parker *et al.*, 1999). Dahl. *et al.* (Dahl *et al.*, 1999) showed that the energy barrier for  $N_2$  dissociation is more than 1 eV lower on the Ru(0001) step edge than on the terraces. On the same surface, Zambelli *et al.* (Zambelli *et al.*, 1996) have reported that the step edges are the active sites for NO dissociation. Xu and Mavrikakis showed that the tensile strain at steps substantially facilitates the  $O_2$  activation on gold surfaces (Xu and Mavrikakis, 2003b), although the effect of steps on  $O_2$  dissociation on Cu surfaces is not expected to be as pronounced as in other gas-metal systems (Xu and Mavrikakis, 2003a). The results for CO dissociation on Ni surface indicates that the energy barriers for CO dissociation strongly favour reactions occurring near surface steps (Li *et al.*, 2004). Fu and Somorjai (Fu and Somorjai,

1992) were able to provide evidence of enhanced interaction of CO<sub>2</sub> on Cu steps, which results in the sensitivity of the methanol synthesis process to copper surface structures. Some studies have shown that the effect of step edge atoms is very different for the different reaction pathways. For example, Vang *et al.* in their study on ethylene dissociation on flat and stepped Ni(111) found that on the steps the barrier for C–C bond breaking is lowered significantly more than the barrier for dehydrogenation.

Following our investigation of the adsorption of molecular hydrazine on realistic Cu surfaces in the previous Chapters, here we have carried out density functional theory calculations including dispersive interactions (Grimme, 2004; Grimme, 2006), to characterize the most favourable adsorption sites, geometries and energies of the N<sub>2</sub>H<sub>4</sub> decomposition intermediates. We have suggested and analysed three different decomposition mechanisms, including dehydrogenation via intra- and inter-molecular pathways and N–N bond cleavage on both flat and stepped Cu(111) surfaces.

## 6.2. Computational methods

We have carried out electronic structure calculations using DFT-D2 method of Grimme (Grimme, 2004; Grimme, 2006) as implemented in the Vienna Ab initio Simulation Package (VASP) (Kresse and Furthmuller, 1996b; Kresse and Furthmuller, 1996a; Kresse and Hafner, 1993; Kresse and Hafner, 1994) to improve the description of the long-range interaction. For the detailed methodology employed in this Chapter, please refer to Chapter 3.

The flat and stepped slabs were modelled with a  $2 \times 2$  and  $3 \times 2$  supercell from the full unit cell,  $p(4 \times 4)$  and  $p(6 \times 4)$  where the adsorbate and the top three layers out of four and four layers out of five layers of the flat and stepped slabs, were allowed to relax during structural optimisation, in line with previous studies (Koitz *et al.*, 2013; Gajdos and Hafner, 2005). A  $5 \times 5 \times 1$  and  $3 \times 5 \times 1$  Monkhorst-Pack grid (Monkhorst and Pack, 1976) of  $\mathbf{k}$ -points was used to sample the Brillouin zone for flat and stepped surfaces respectively.

We have calculated the adsorption energies of the intermediates from the hydrazine decomposition process relative to the hydrazine molecule in the gas-phase:

$$E_{ads}(N_y H_x) = (E_{N_y H_x}^{surf} + (4 - x)E_H^{surf} + (2 - y)E_N^{surf}) - (((4 - x) + (2 - y) + 1))E^{surf} + E_{N_2 H_4}^{gas} \quad (6.3)$$

Where  $E_{N_y H_x}^{surf}$  is the total energy of the  $N_y H_x$  species adsorbed on a relaxed surface and  $E_H^{surf}$  and  $E_N^{surf}$  are the energies of an isolated H- and N-atom adsorbed somewhere else on the relaxed surface, at a non-interactive distance.  $E^{surf}$  and  $E_{N_2 H_4}^{gas}$  are the energies of the naked surface and isolated gas-phase hydrazine respectively.

Within this definition, a negative  $E_{ads}$  value means a release of energy during adsorption. A combination of two varieties of the nudged elastic band (NEB) method (Mills and Jonsson, 1994; Mills *et al.*, 1995) and the improved dimer method (IDM) (Heyden *et al.*, 2005) were used to identify transition state (TS) structures, which we verified by a single imaginary frequency associated with the reaction coordinate. The reaction energy ( $E_r$ ) was obtained from the difference in energy between final and initial states and a negative  $E_r$  hence indicates an exothermic process. The forward

and reverse activation barriers ( $E_a$ ) were defined as the energy difference between the TS and the initial state or final state, respectively.

### 6.3. Results

We have first created the perfect Cu(111) surface, which is the close-packed plane of the fcc structure (**Figure 6.1.a**) and is the most stable copper surface (Daff *et al.*, 2009). The surface Cu atoms are arranged in a hexagonal lattice with a separation of 2.52 Å between nearest neighbour atoms. The stepped Cu(111) surface has been studied to investigate the presence of an extended edge of low-coordinated atoms on the N<sub>2</sub>H<sub>4</sub> dissociation behaviour (shown in **Figure 6.1.b**). Each unit cell in the stepped slab was offset by one atomic layer with respect to the next cell (de Leeuw *et al.*, 2000; de Leeuw and Nelson, 2003; de Leeuw *et al.*, 2004).

The three major conformations of hydrazine in the gas-phase are gauche, trans and eclipsed (**Figure 6.2**), where the gauche conformer is the lowest-energy structure. The trans and eclipsed conformations are 0.13 and 0.36 eV higher in energy, respectively, than the gauche conformation. We have identified the strongest adsorption geometries by placing the different intermediates at a variety of positions on the planar and stepped Cu(111) surfaces. Adsorption energies and structural parameters for various intermediate species in their most stable configurations on the flat and stepped Cu(111) are presented in **Table 6.1** and **Figure 6.3**. We note that because of the lower coordination of the stepped surface atoms, all intermediates are more stable on the step than on the terrace sites.

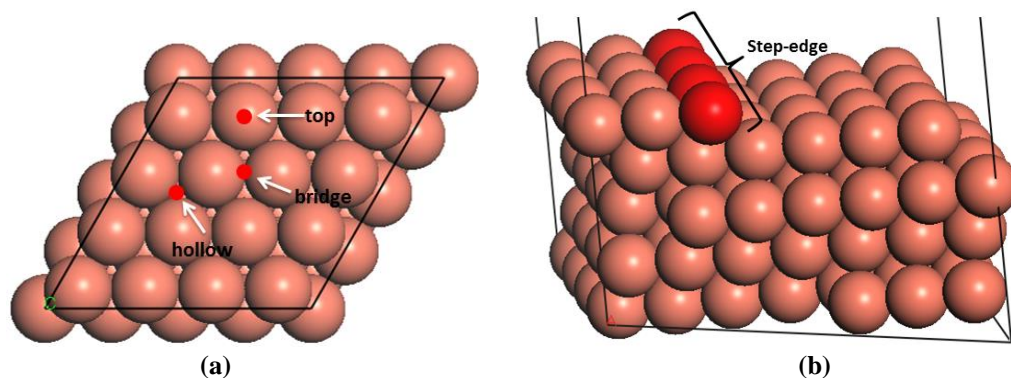


**Figure 6.1.** The simulation cells and surface geometry of different sites used in the calculations of (a) perfect (top view) and (b) stepped (side view) surfaces. Note that low-coordinated atoms in the stepped surface are shaded darker.

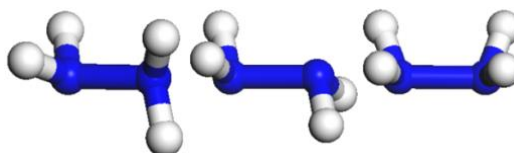


**Figure 6.2.** Representation of the  $\text{N}_2\text{H}_4$  conformations, from left to right: gauche, trans and eclipsed.

**Table 6.1.** Adsorption energies ( $E_{ads}$ ) and average geometric parameters of the most favourable adsorption structures of different  $\text{N}_2\text{H}_4$  decomposition intermediates on the flat and stepped Cu(111) surface. Adsorption energies are relative to the gas-phase hydrazine; bold numbers show the adsorption energies relative to the species in their gas-phase:  $\text{NH}_3$ ,  $\text{N}_2$  and  $\text{H}_2$ .

adsorbate	$E_{ads}$	$E_{ads}$	Cu–N	Cu–N	N–N	N–N	N–H	N–H
	(eV), flat	(eV), step	(Å), flat	(Å), step	(Å), flat	(Å), step	(Å), flat	(Å), step
$\text{N}_2\text{H}_4$	-0.98	-1.53	2.178	2.104	1.452	1.455	1.026	1.028
$\text{N}_2\text{H}_3$	-0.85	-1.21	2.023	2.033	1.455	1.462	1.024	1.027
<b>NHNH</b>	-0.10	-0.68	1.966	1.922	1.359	1.308	1.027	1.030
<b>NNH<sub>2</sub></b>	-0.18	-0.66	1.946	1.904	1.345	1.299	1.019	1.028
<b>NNH</b>	0.37	-0.39	1.971	1.938	1.240	1.237	1.041	1.042
<b>NH<sub>3</sub></b>	<b>-0.81</b>	<b>-1.06</b>	2.092	2.072	–	–	1.023	1.025
<b>NH<sub>2</sub></b>	-0.13	-1.42	1.982	1.942	–	–	1.021	1.022
<b>NH</b>	0.38	-0.58	1.898	1.566	–	–	1.022	1.023
<b>N<sub>2</sub></b>	<b>-0.15</b>	<b>-0.39</b>	1.985	1.931	1.121	1.123	–	–
<b>H<sub>2</sub></b>	<b>-0.10</b>	<b>-0.12</b>	–	–	–	–	–	–
<b>N</b>	<b>1.32</b>	<b>0.87</b>	1.838	2.002	–	–	–	–
<b>H</b>	<b>-0.28</b>	<b>-0.36</b>	–	–	–	–	–	–

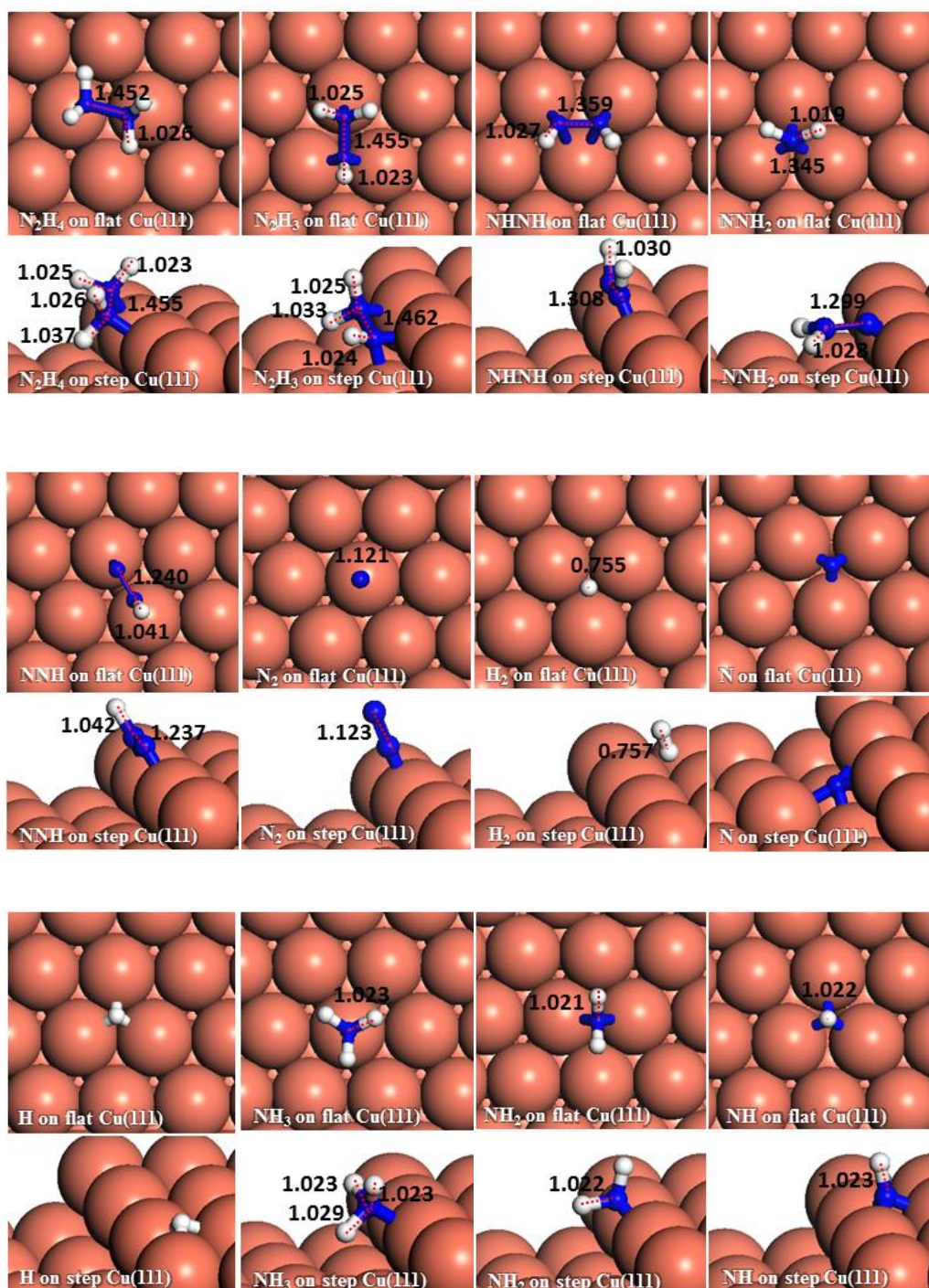


**Figure 6.3.** Surface geometries of the most preferred adsorption configurations of the various intermediates on the flat (top-view) and stepped (side-view) Cu(111) surfaces with their N–N and N–H bond distances in Å.

### 6.3.1. Adsorption on the planar and stepped Cu(111)

**N<sub>2</sub>H<sub>4</sub>.** We placed different N<sub>2</sub>H<sub>4</sub> conformers (**Figure 6.2**) in a number of non-equivalent initial configurations on the planar and stepped Cu(111) surface in order to identify the mode of strongest adsorption. The preferred N<sub>2</sub>H<sub>4</sub> adsorption structures on the flat and stepped Cu(111) surfaces are in the gauche conformation, releasing an  $E_{ads}$  of 0.98 and 1.53 eV/N<sub>2</sub>H<sub>4</sub> respectively. While it binds through both nitrogen atoms to the flat surface with Cu–N distances of 2.178 Å, it prefers to bridge to the copper step edge atoms with shorter Cu–N distances of 2.104 Å. Hydrazine adsorbs almost parallel to both the flat and stepped surfaces, elongating the N–N bond to 1.452 and 1.455 Å respectively, compared to a length of 1.438 Å in the gas-phase. These configurations are a result of N–N bond rotation from gauche towards the eclipsed conformer with a torsional angle of 39.6 ° and 34.6 ° on the flat and stepped surfaces respectively.

**N<sub>2</sub>H<sub>3</sub>.** As the first product of dehydrogenation, the most stable adsorption structure for the N<sub>2</sub>H<sub>3</sub> conformer is the NHHN<sub>2</sub> structure, which has different binding geometries on the flat versus the stepped Cu(111) surfaces: on the terrace, it prefers the hollow site with the NH-end closer to the surface, bridging two surface Cu atoms with Cu–N bond lengths of ~ 2.0 Å, whereas the NH<sub>2</sub> part has a Cu–N bond length of 2.070 Å. On the step, it binds on the edge atoms with its NH-end inclined to the lower terrace, with Cu–N distance of 2.078 Å. The N–N bond on the step edge elongates to 1.462 Å compared to 1.455 Å on the terrace. While the energy of N<sub>2</sub>H<sub>3</sub> adsorption on the terrace is -0.85 eV relative to gas-phase hydrazine, it adsorbs more strongly to the step edge by 0.36 eV.

**N<sub>2</sub>H<sub>2</sub>.** The next intermediate is N<sub>2</sub>H<sub>2</sub>, which has two different conformers: NHNH, with one hydrogen atom at each nitrogen or NNH<sub>2</sub>, where both hydrogen atoms are located on the same nitrogen. While the latter one adsorbs perpendicularly on the terrace with the lower N atom in a three-fold hollow site ( $E_{ads} = -0.18$  eV), it prefers to bridge through the N on the step edge, lying parallel to the lower terrace with a larger adsorption energy of -0.66 eV. The adsorption of the NHNH structure on the terrace releases only 0.10 eV when it adsorbs through both nitrogen atoms in an hcp site parallel to the surface. NHNH bridges on the Cu step edges more strongly, releasing an energy of 0.68 eV.

**N<sub>2</sub>H.** The adsorption geometries of N<sub>2</sub>H are identical on both terrace and step surfaces, adsorbing on a bridge site through both nitrogen atoms parallel to the surface. While this process is endothermic ( $E_{ads} = 0.37$  eV) on the terrace, the adsorption on the step edge is exothermic, releasing an energy of 0.39 eV. The N–N bond lengths on terrace and step edge are 1.240 and 1.237 Å respectively, *i.e.* elongated compared to the 1.150 Å of the N<sub>2</sub>H molecule in the gas-phase (Pople and Curtiss, 1991).

**N<sub>2</sub>.** We investigated the N<sub>2</sub> molecule adsorption at different sites on the surface and found that N<sub>2</sub> adsorbs on a top site on both terrace or step edge, with the molecule's axis perpendicular to the surface at Cu–N distances of 1.985 and 1.931 Å respectively. The N<sub>2</sub> adsorption energy with respect to gas-phase nitrogen is -0.15 and -0.39 eV on the flat and step surfaces respectively. It shows that nitrogen adsorption on the Cu surfaces is weak and it could easily desorb by increasing the temperature. The N–N bond length is 1.121 and 1.123 Å on the terrace and step edge respectively (experimental bond length 1.098 Å in the gas-phase (Huber, 1979)). In

other sites,  $\text{N}_2$  interacts more weakly and the molecule moves away to  $\sim 3 \text{ \AA}$  from the surface.

**N.** Nitrogen atom adsorbs on a three-fold hollow site on the terrace and on a four-fold site at the foot of the step edge, both endothermically requiring 1.32 and 0.87 eV on the terrace and step edge, respectively, relative to gas-phase  $\text{N}_2$ . This preference by N for a three-fold adsorption site on Cu(111) was also found in previous work (Wang *et al.*, 2005).

**$\text{NH}_3$ .** The adsorption geometry of ammonia is identical on both the flat and stepped Cu surfaces with preference for a top site, with Cu–N bond lengths of 2.092 and 2.072  $\text{Å}$  on the flat and stepped surfaces respectively. Theoretical studies have shown that strong electrostatic contributions (Biemolt *et al.*, 1992a) and the Pauli repulsion of the lone-pair orbital of  $\text{NH}_3$  by the copper 3d electrons (Biemolt *et al.*, 1992b) directs the  $\text{NH}_3$  towards one-fold adsorption on the copper surfaces. The  $\text{NH}_3$  adsorption is exothermic with energies of -0.81 and -1.06 eV relative to gas-phase  $\text{NH}_3$  on the terrace and step edge, respectively. These results show that the ammonia molecule adsorbs relatively strongly to the Cu surface and its desorption would be endothermic.

**$\text{NH}_2$ .** The presence of low-coordinated Cu atoms stabilizes the  $\text{NH}_2$  intermediates more than any other species, by increasing the  $\text{NH}_2$  adsorption energy from -0.13 to -1.42 eV, while the adsorption geometry remains the same on both terrace and step edge with  $\text{NH}_2$  bridging between Cu surface atoms. The Cu–N bond and N–H bond lengths are 1.982  $\text{Å}$  and 1.021  $\text{Å}$  on the terrace and 1.942  $\text{Å}$  and 1.022  $\text{Å}$  on step edge, which are slightly shorter than the experimentally reported N–H bond in the gas-phase (1.024  $\text{Å}$ ) (Lide, 1996).

**NH.** The adsorption of imide is endothermic by 0.38 eV on the flat Cu(111) surface, while on the stepped Cu(111) surface it is exothermic by 0.58 eV. The adsorption geometry for NH is identical on both terrace and step edge, where it adsorbs on a three-fold hollow site, with a Cu–N bond length of 1.566 Å on the step edge compared to 1.898 Å on the flat surface.

**H<sub>2</sub>.** The hydrogen molecule releases an energy of 0.10 eV relative to gas-phase hydrogen, when it is perpendicularly adsorbed on the fcc site of the terrace, with an H–H bond length of 0.755 Å (experimental bond length 0.741 Å in gas-phase (Huber, 1979; Lide, 1996)). The adsorption on the step edge does not change the H<sub>2</sub> geometry on the Cu(111) surface, but makes it slightly more exothermic ( $E_{ads} = -0.12$  eV) relative to gas-phase hydrogen. As such, hydrogen is physisorbed to the Cu surfaces at a distance of  $\sim 2.80$  Å, indicating that it should easily desorb from the surface.

**H.** For the hydrogen atom, similar to the nitrogen atom, the three-fold hollow site is the preferred site at low coverage. The hydrogen adsorption on both the flat and stepped surfaces is exothermic relative to gas-phase hydrogen, by 0.28 and 0.36 eV, respectively.

### **6.3.2. N<sub>2</sub>H<sub>x</sub> (x=1-4) decomposition pathways on the planar and stepped Cu(111)**

#### **6.3.2.1. N<sub>2</sub>H<sub>4</sub> dissociation and dehydrogenation**

**Table 6.2** summarizes the energetics of the different reaction pathways on both planar and stepped Cu(111) surfaces. We started from the most stable geometry of hydrazine, where hydrazine bridges through both nitrogen atoms to the Cu surface

atoms. The pathways for hydrazine N–N bond breaking on both flat and stepped surfaces, leading to  $\text{NH}_2$  intermediates, are shown in **Figure 6.4.a**. The reaction is exothermic (0.87 eV) on the flat surface with an energy barrier of 0.86 eV. The presence of low-coordinated atoms in the step make the N–N bond breaking process more exothermic, releasing an energy of 1.66 eV, although the energy barrier is increased by 0.04 eV. This indicates that although a stepped surface favours the N–N bond breaking thermodynamically, it does not modify the kinetics of the reaction.

Dehydrogenation of  $\text{N}_2\text{H}_4$  was also investigated (**Figure 6.4.b**). The energy barrier for this path on the flat surface is 1.55 eV and the process is endothermic by 0.31 eV. The activation energy on the stepped surface decreases to 1.11 eV, but the process becomes less favourable thermodynamically ( $E_r = 0.74$  eV).

These results indicate that on the Cu(111) with or without surface steps, the N–N bond cleavage of hydrazine is energetically and kinetically preferred over its dehydrogenation which is in line with a previous experimental study showing that N–H bond breaking needs more energy than N–N breaking (Block and Schulzek.G, 1973). From the charge density calculations in Chapter 4, which shows the induced charge density on the Cu(111) surface upon  $\text{N}_2\text{H}_4$  adsorption, it can be observed that more charge is accumulated between the N and H atoms of hydrazine than between the two N atoms, which agrees well with these energetic results.

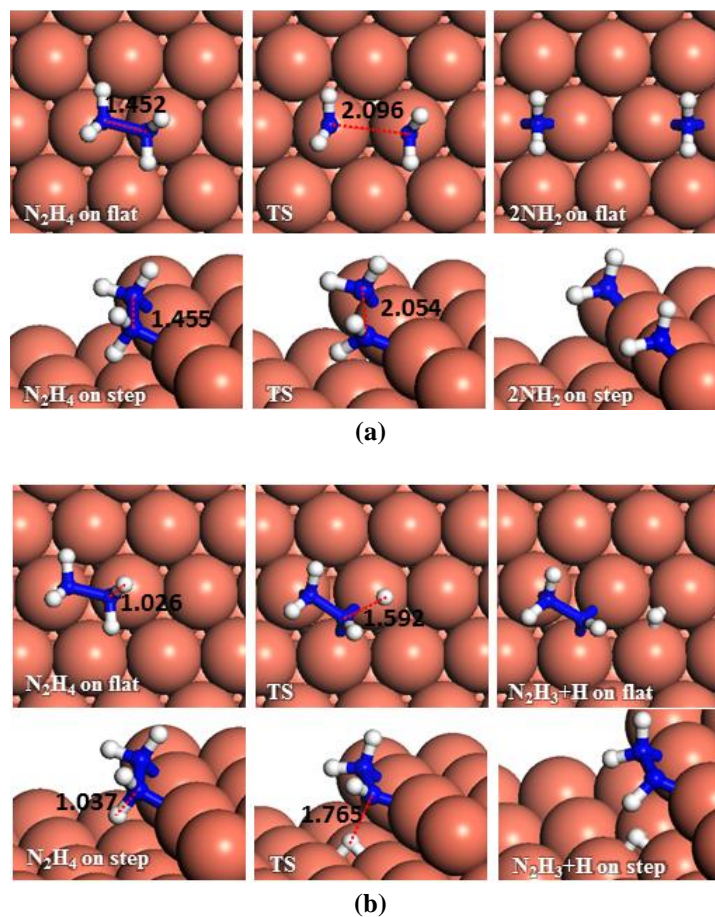


**Figure 6.4.** Schematic representation of the initial, transition and final states for  $\text{N}_2\text{H}_4$  dissociation pathways on the flat (top-view) and stepped (side-view) Cu(111) surfaces via (a) N–N, (b) N–H breaking. Bond lengths are given in Å.

### 6.3.2.2. $\text{N}_2\text{H}_3$ dissociation and dehydrogenation

The  $\text{N}_2\text{H}_3$  decomposition may proceed by N–N or N–H breaking. Initial, transition and final states for the N–N scission are represented in **Figure 6.5.a** leading to NH and  $\text{NH}_2$ . While this process has an activation barrier of 1.06 eV and the reaction is exothermic by 0.30 eV on the flat surface, the barrier increases by 0.21 eV but the reaction becomes more exothermic (0.76 eV) on the stepped surface.

There are two distinct pathways for dehydrogenation of  $\text{N}_2\text{H}_3$ , respectively shown in **Figures 6.5.b, c**. The one leading to  $\text{NNH}_2$  and an H atom has a barrier and reaction energy of 1.53 and 0.74 eV, respectively, on the flat surface, and 1.77 and 0.75 eV on

the step. The alternative dehydrogenation pathway leads to NHNH and H as products. The barrier for this endothermic process ( $E_r = 0.84$  eV) is 1.61 eV on the flat surface, while the step decreases the barrier to 1.56 eV although it is still endothermic ( $E_r = 0.69$  eV).

Although NHNH and NNH<sub>2</sub> are products of the dehydrogenation of N<sub>2</sub>H<sub>3</sub> on Cu(111) surface, the N–N bond breaking of N<sub>2</sub>H<sub>3</sub> is energetically more favourable. Our results indicate that low-coordinated atoms make the N–N decoupling of N<sub>2</sub>H<sub>3</sub> more feasible thermodynamically, although they do not affect the kinetics.

**Table 6.2.** Calculated reaction ( $E_r$ ) and barrier ( $E_a$ ) energies for the forward and reverse reaction pathways considered. Note that (\*) indicates adsorbed state. The  $E_r$  of the adsorption and desorption processes are the corresponding  $E_{ads}$  which for each species were calculated relative to them in the gas-phase.

	Reactions	Flat			Step		
		$E_r$ (eV)	$E_a$ forward (eV)	$E_a$ reverse (eV)	$E_r$ (eV)	$E_a$ forward (eV)	$E_a$ reverse (eV)
<b>Adsorption-Desorption</b>							
<b>R1</b>	$N_2H_4 \leftrightarrow N_2H_4^*$	-0.98	–	–	-1.53	–	–
<b>R2</b>	$NH_3^* \leftrightarrow NH_3$	0.81	–	–	1.06	–	–
<b>R3</b>	$N_2^* \leftrightarrow N_2$	0.15	–	–	0.39	–	–
<b>R4</b>	$H_2^* \leftrightarrow H_2$	0.10	–	–	0.12	–	–
<b><math>N_2H_4</math> Dissociation</b>							
<b>R5</b>	$N_2H_4^* \leftrightarrow 2NH_2^*$	-0.87	0.86	1.73	-1.66	0.90	2.56
<b>R6</b>	$N_2H_4^* \leftrightarrow N_2H_3^* + H^*$	0.31	1.55	1.24	0.74	1.11	0.37
<b><math>N_2H_3</math> Dissociation</b>							
<b>R7</b>	$N_2H_3^* \leftrightarrow NH_2^* + NH^*$	-0.30	1.06	1.36	-0.76	1.27	2.03
<b>R8</b>	$N_2H_3^* \leftrightarrow NNH_2^* + H^*$	0.74	1.53	0.79	0.75	1.77	1.02
<b>R9</b>	$N_2H_3^* \leftrightarrow NHNH^* + H^*$	0.84	1.61	0.77	0.69	1.56	0.87
<b><math>N_2H_2</math> Dissociation</b>							
<b>R10</b>	$NNH_2^* \leftrightarrow NH_2^* + N^*$	0.13	1.42	1.29	0.18	1.52	1.34
<b>R11</b>	$NHNH^* \leftrightarrow 2NH^*$	-0.34	0.85	1.19	-0.76	0.93	1.69
<b>R12</b>	$NNH_2^* \leftrightarrow NNH^* + H^*$	0.58	1.35	0.77	0.86	0.89	0.03
<b>R13</b>	$NHNH^* \leftrightarrow NNH^* + H^*$	0.60	1.68	1.08	0.43	1.39	0.96
<b>NNH Dissociation</b>							
<b>R14</b>	$NNH^* \leftrightarrow NH^* + N^*$	0.16	1.47	1.31	-0.41	1.89	2.3

<b>R15</b>	$\text{NNH}^* \leftrightarrow \text{N}_2^* + \text{H}^*$	-1.5	0.37	1.87	-1.11	0.62	1.73
<b>N<sub>2</sub> Dissociation</b>							
<b>R16</b>	$\text{N}_2^* \leftrightarrow 2\text{N}^*$	3.22	4.78	1.56	1.96	6.02	4.06
<b>H–H Coupling</b>							
<b>R17</b>	$2\text{H}^* \leftrightarrow \text{H}_2^*$	0.43	1.08	0.65	0.81	1.28	0.47
<b>NH<sub>x</sub>(x=1-3) Dehydrogenation</b>							
<b>R18</b>	$\text{NH}_3^* \leftrightarrow \text{NH}_2^* + \text{H}^*$	0.74	1.63	0.89	0.67	1.59	0.92
<b>R19</b>	$\text{NH}_2^* \leftrightarrow \text{NH}^* + \text{H}^*$	0.67	1.59	0.92	1.06	1.81	0.75
<b>R20</b>	$\text{NH}^* \leftrightarrow \text{N}^* + \text{H}^*$	1.46	1.97	0.51	1.36	2.07	0.71
<b>Interaction of NH<sub>2</sub> molecules</b>							
<b>R21</b>	$2\text{NH}_2^* \leftrightarrow \text{NH}^* + \text{NH}_3^*$	-0.05	0.55	0.6	0.37	2.05	1.68
<b>Interaction of NH<sub>2</sub> with N<sub>2</sub>H<sub>x</sub> (x=1–4)</b>							
<b>R22</b>	$\text{N}_2\text{H}_4^* + \text{NH}_2^* \leftrightarrow \text{N}_2\text{H}_3^* + \text{NH}_3^*$	-0.35	0.59	0.94	-0.22	0.03	0.25
<b>R23</b>	$\text{N}_2\text{H}_3^* + \text{NH}_2^* \leftrightarrow \text{NHNH}^* + \text{NH}_3^*$	0.11	0.80	0.69	-0.01	0.64	0.65
<b>R24</b>	$\text{N}_2\text{H}_3^* + \text{NH}_2^* \leftrightarrow \text{NNH}_2^* + \text{NH}_3^*$	-0.12	0.70	0.82	-0.06	0.67	0.73
<b>R25</b>	$\text{NNH}_2^* + \text{NH}_2^* \leftrightarrow \text{NNH}^* + \text{NH}_3^*$	0.15	0.44	0.29	-0.47	0.15	0.62
<b>R26</b>	$\text{NHNH}^* + \text{NH}_2^* \leftrightarrow \text{NNH}^* + \text{NH}_3^*$	-0.26	0.36	0.62	0.01	1.00	0.99
<b>R27</b>	$\text{NNH}^* + \text{NH}_2^* \leftrightarrow \text{N}_2^* + \text{NH}_3^*$	-2.13	0.14	2.29	-1.60	0.57	2.17

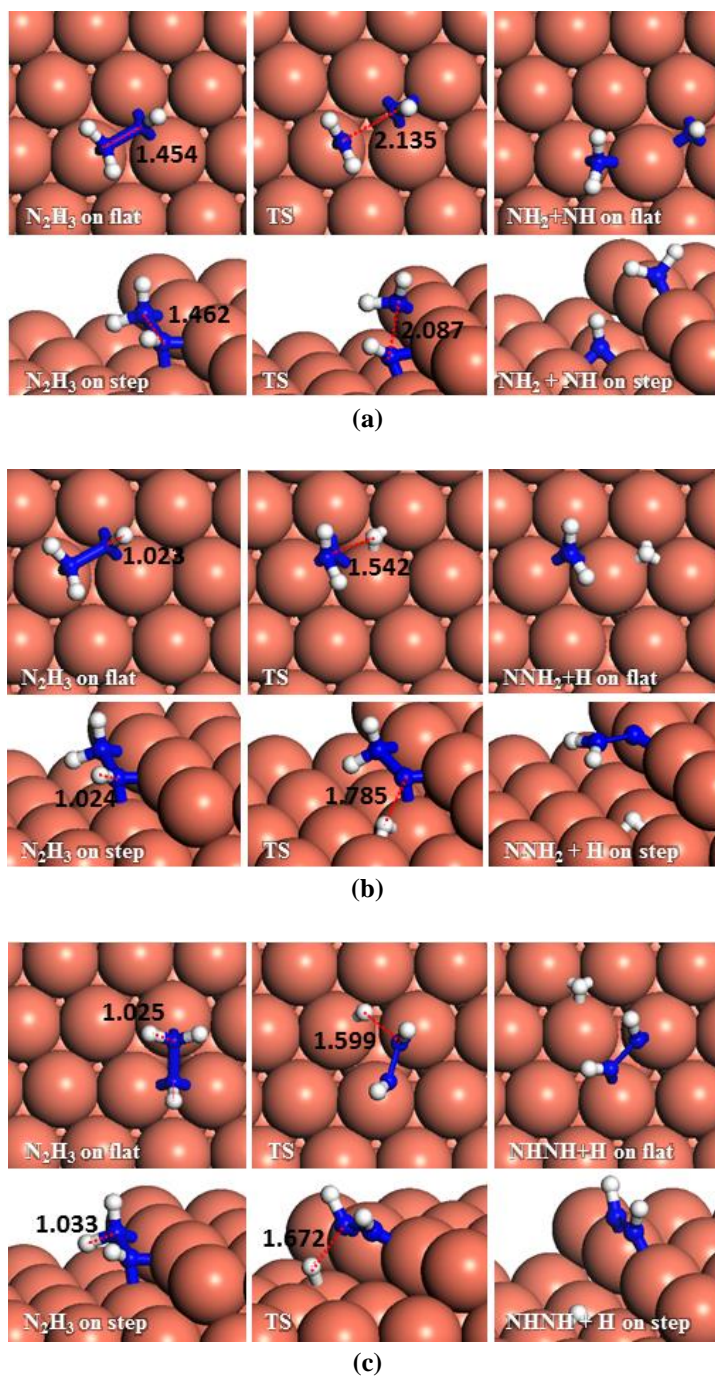


**Figure 6.5.** Schematic representation of the initial, transition and final states for  $\text{N}_2\text{H}_3$  dissociation pathways on the flat (top-view) and stepped (side-view) Cu(111) surfaces via (a) N–N, (b) and (c) N–H breaking. Bond lengths are given in Å.

### 6.3.2.3. $\text{N}_2\text{H}_2$ dissociation and dehydrogenation

We have studied the processes of N–N and N–H breaking of two  $\text{N}_2\text{H}_2$  conformations:  $\text{NNH}_2$  and  $\text{NHNH}$ . The pathway for N–N bond breaking of the  $\text{NNH}_2$  intermediate, yielding  $\text{NH}_2$  and N, see **Figure 6.6.a**, has an activation barrier and reaction energy of 1.42 and +0.13 eV respectively. When the stepped surface is considered the N–N breaking barrier increases by 0.1 eV and the process is 0.05 eV more endothermic compared to the terrace. The dehydrogenation process of  $\text{NNH}_2$  leads to  $\text{NNH}$  and an H atom (**Figure 6.6.b**). For this process on the flat surface, the required energy is 1.35 eV and the products are 0.58 eV higher in energy than the reactants. On the stepped surface, the barrier energy decreases to 0.89 eV but the process is more endothermic by 0.28 eV.

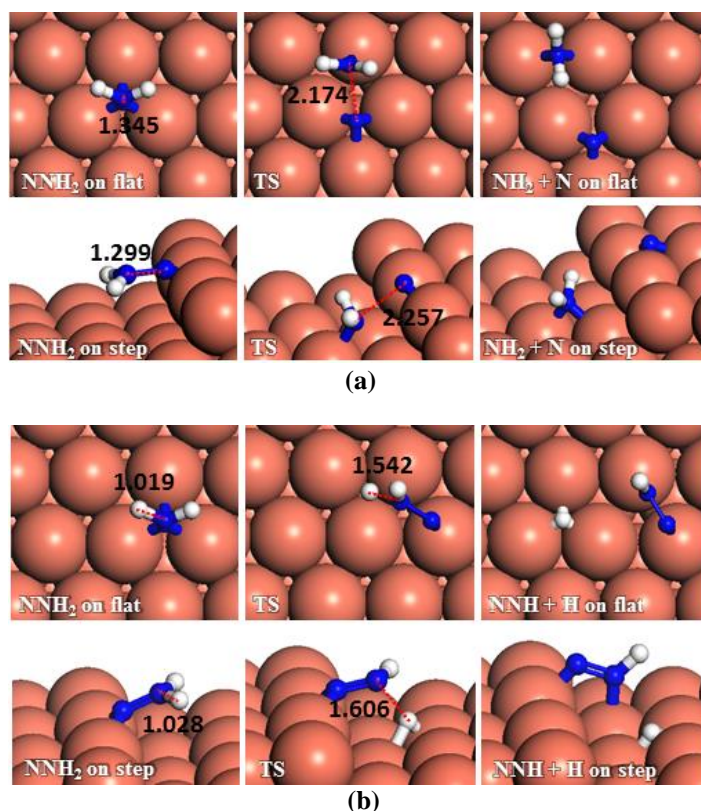


**Figure 6.6.** Schematic representation of the initial, transition and final states for  $\text{NNH}_2$  dissociation pathways on the flat (top-view) and stepped (side-view) Cu(111) surfaces via (a) N–N, and (b) N–H breaking. Bond lengths are given in Å.

As to N–N bond breaking of NHNH (**Figure 6.7.a**), while the reaction barrier is 0.85 eV and the reaction is exothermic by -0.34 eV on the flat surface, these values increase to 0.93 and -0.76 eV respectively on the atomic step system. However, the dehydrogenation of NHNH resulting in NNH and an H species has a barrier of 1.68 eV and is endothermic by 0.60 eV on the flat surface (Figure 6.7.b). The lower coordination of the steps decreases both the barrier and the reaction energy to 1.39 and 0.43 eV respectively. Thus, the production of NH molecules via N–N bond breaking of NHNH is more favourable than other dissociation mechanisms of  $N_2H_2$  from both a thermodynamic and kinetic point of view.

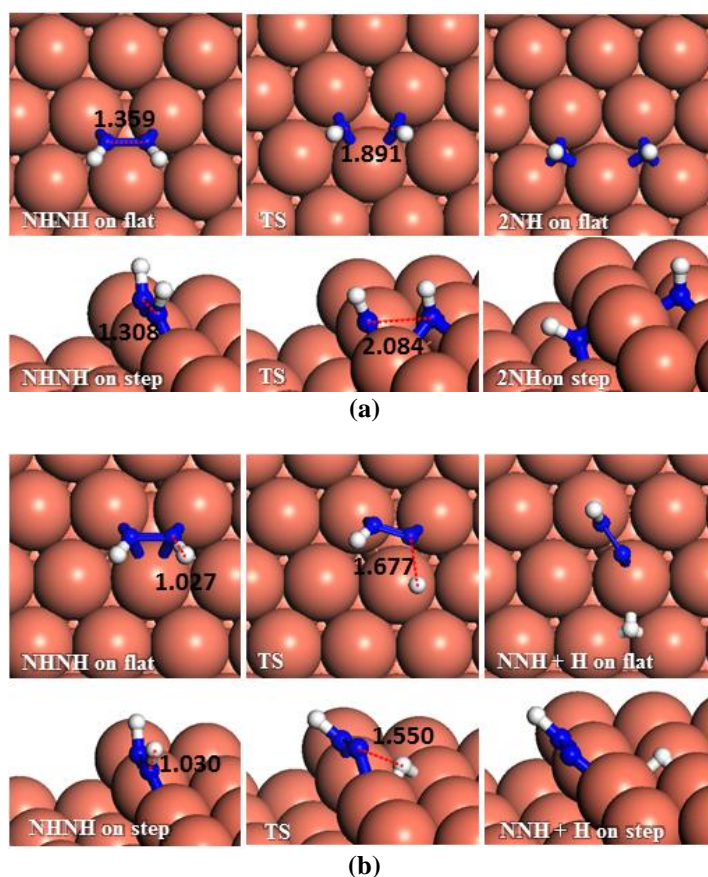


**Figure 6.7.** Schematic representation of the initial, transition and final states for NHNH dissociation pathways on the flat (top-view) and stepped (side-view) Cu(111) surfaces via (a) N–N, and (b) N–H breaking. Bond lengths are given in Å.

#### 6.3.2.4. NNH dissociation and dehydrogenation

Schematic representation of the NNH dissociation on the Cu(111) terrace is shown in **Figure 6.8.a**, where breaking the N–N bond leads to NH and N. The process has to overcome an energy barrier of 1.47 eV and it is slightly endothermic ( $E_r = 0.16$  eV). The step edge makes the process more favourable thermodynamically with an exothermic reaction energy of -0.41 eV, but the energy barrier increases to 1.89 eV, making it therefore less feasible kinetically. The dehydrogenation reaction of NNH, which completes the dehydrogenation process of N<sub>2</sub>H<sub>4</sub>, is represented in **Figure 6.8.b**. This reaction pathway has energy barriers of 0.37 and 0.62 eV and is highly exothermic by -1.5 eV and -1.11 eV on terrace and step edge, respectively, which therefore becomes the most feasible intra-molecular dehydrogenation reaction of any intermediate on the Cu(111) surface.

#### 6.3.2.5. N<sub>2</sub> dissociation

We have also considered the reaction pathway for N–N decoupling in the N<sub>2</sub> molecule on Cu(111) surfaces (**Figure 6.9**). As expected, due to the molecule's strong interatomic bond, the process is highly unaffordable with energy barriers of 4.78 eV on the terrace and 6.02 eV on the step edge. The process is also highly endothermic ( $E_r = 3.22$  eV) on the terrace, although the step reduces the endothermic reaction energy to 1.96 eV.

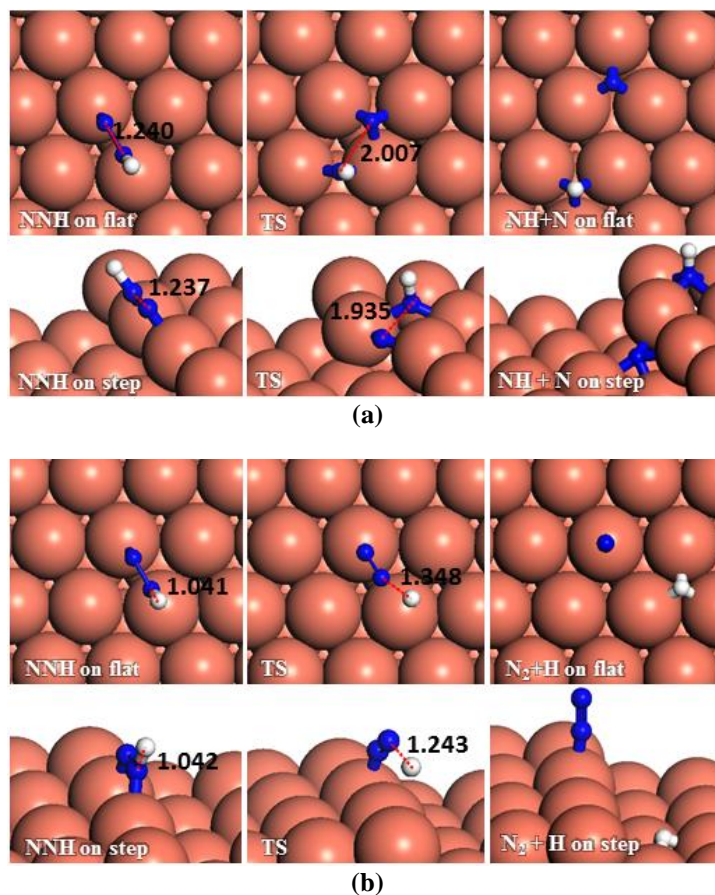


**Figure 6.8.** Schematic representation of the initial, transition and final states for NNH dissociation pathways on the flat (top-view) and stepped (side-view) Cu(111) surfaces via (a) N-N, (b) N-H breaking. Bond lengths are given in Å.

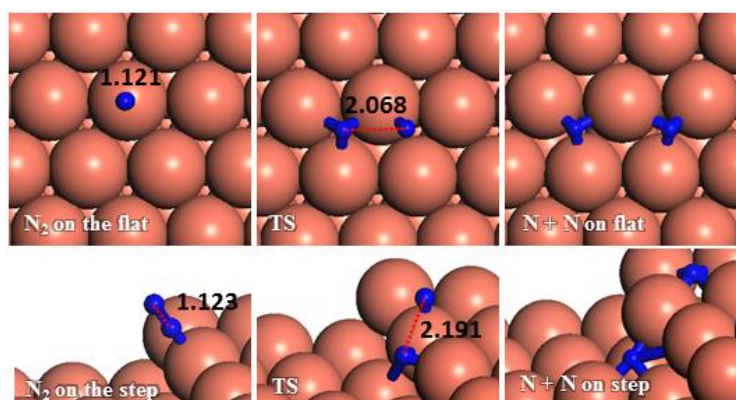


**Figure 6.9.** Schematic representation of the initial, transition and final states for N<sub>2</sub> dissociation pathways on the flat (top-view) and stepped (side-view) Cu(111) surfaces. Bond lengths are given in Å.

### 6.3.2.6. $\text{NH}_x$ (x=1-3) dehydrogenation

We have also investigated the consecutive dehydrogenation of ammonia, see **Figure 6.10.a**. The barrier and the endothermic reaction energy associated with the first N–H bond breaking process are 1.63 eV and 0.74 eV respectively on the flat surface, *i.e.* slightly higher than the barrier of 1.59 eV and a reaction energy of 0.67 eV on the step. The exothermic reverse (hydrogenation) reaction is more likely to happen with energy barriers of 0.89 and 0.92 eV on the terrace and step respectively. The dehydrogenation of  $\text{NH}_2$  (**Figure 6.10.b**) and further dehydrogenation of  $\text{NH}$  (**Figure 6.10.c**) are also unlikely to succeed based on their associated high barrier energies, *i.e.* 1.59 and 1.97 eV on the flat surface and 1.81 and 2.07 on the stepped surface, respectively. The DFT calculated barrier energies for the dehydrogenation of  $\text{NH}_3$ ,  $\text{NH}_2$  and  $\text{NH}$  to form  $\text{HCN}$  on Pt(111) are smaller than our results, *i.e.* 1.39, 1.30 and 1.40 eV respectively (Gomez-Diaz and Lopez, 2011), although not significantly.

The reverse process, hydrogenation of  $\text{NH}$  has activation energies of 0.92 and 0.75 eV on the terrace and step, respectively. The hydrogenation of  $\text{N}$  is energetically favourable ( $E_r = -1.46$  and  $-1.36$  eV) leading to  $\text{NH}$  via energy barriers of only 0.51 and 0.71 eV on the flat and stepped surfaces, respectively. These energies show that the Cu surface could be a good catalyst for ammonia synthesis compared to the Ru(0001) surface, where the calculated barriers for hydrogenation of  $\text{N}$ ,  $\text{NH}$  and  $\text{NH}_2$  were found to be more than 1.2 and 1.1 eV on terraces and steps, respectively (Logadottir and Norskov, 2003; Honkala *et al.*, 2005).

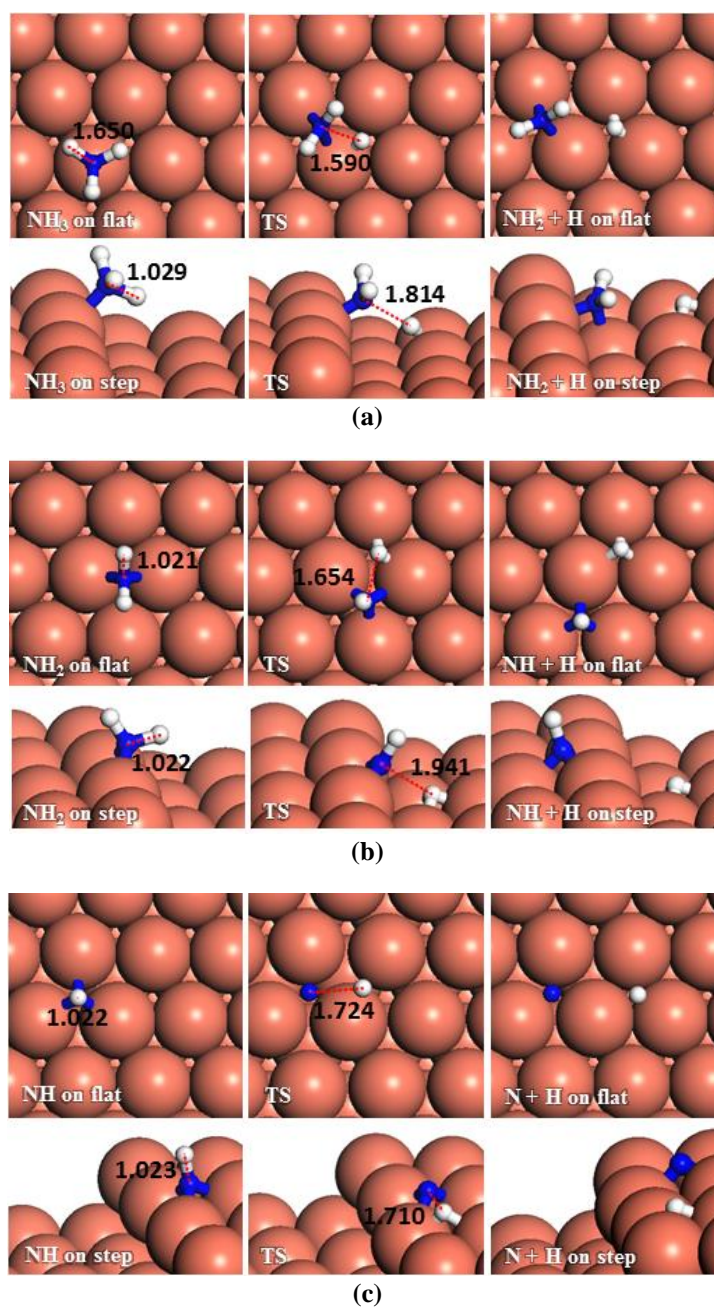


**Figure 6.10.** Schematic representation of the initial, transition and final states for (a)  $\text{NH}_3$ , (b)  $\text{NH}_2$  and (c)  $\text{NH}$  dehydrogenation pathways on the flat (top-view) and stepped (side-view) Cu(111) surfaces. Bond lengths are given in Å.

### 6.3.2.7. H–H coupling

We have also considered another secondary process, the pathways for H–H coupling, see **Figure 6.11**. As **Table 6.2** shows, combining two hydrogen atoms on the stepped

surface exhibits higher barrier and endothermic reaction energies of 1.28 and 0.81 eV than on the flat surface,  $E_a = 1.08$  and  $E_r = 0.43$  eV. The reverse reaction, the exothermic  $H_2$  dissociation reaction, has energy barriers of 0.65 and 0.47 eV on the terrace and stepped surfaces, respectively, indicating that  $H_2$  should adsorb dissociatively on Cu surfaces and the presence of step edge makes this process more likely to proceed, due to the stabilisation provided by the low-coordinated atoms, where the electronic structure is different than that for the terrace atoms (Tafreshi *et al.*, 2014b; Tafreshi *et al.*, 2014a).

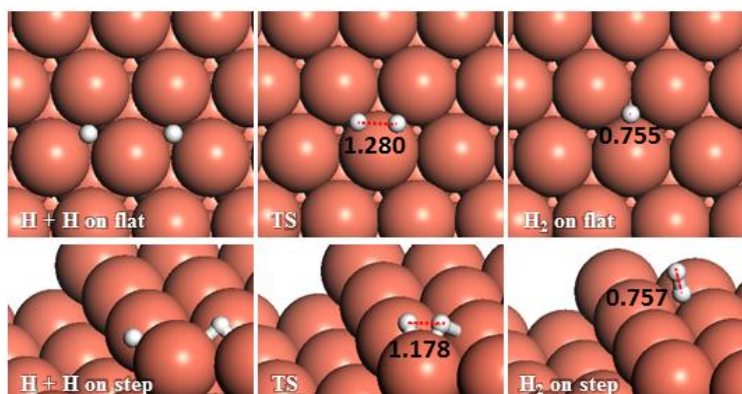


**Figure 6.11.** Schematic representation of the initial, transition and final states for H–H coupling pathways on the flat (top-view) and stepped (side-view) Cu(111) surfaces. Bond lengths are given in Å.

### 6.3.2.8. Inter-molecular dehydrogenation pathways

Having investigated the barriers for both N–N and N–H bond scission of the different possible intermediates of  $N_2H_4$  dissociation, it is evident that breaking the hydrazine N–N bond and producing  $NH_2$  fragments is the most likely process to occur on both the flat and stepped Cu(111) surfaces. Furthermore, the dehydrogenation of  $NH_2$  is unfavourable to proceed at low temperatures due to the high energy of the transition states. We have therefore investigated other pathways involving the  $NH_2$  groups. There are two possibilities:  $NH_2$  can either react with another  $N_2H_x$  ( $x=1-4$ )

intermediate subtracting a hydrogen, or react with another  $\text{NH}_2$  from hydrazine decomposition.

#### 6.3.2.8.1. $\text{N}_2\text{H}_x$ ( $x=1-4$ ) dehydrogenation by $\text{NH}_2$

The intermediate  $\text{NH}_2$  may interact with hydrazine or other decomposition intermediates, and the pathways for subsequent dehydrogenation steps are shown in **Figure 6.12**.

In the first suggested process (**Figure 6.12.a**),  $\text{NH}_2$  interacts with  $\text{N}_2\text{H}_4$  and abstracts one of its H atoms leading to  $\text{N}_2\text{H}_3$  and  $\text{NH}_3$ . The energy barrier for this process is 0.59 eV on the flat surface, but it decreases to only 0.03 eV on the stepped surface, and releases energies of 0.35 and 0.22 eV, respectively. This step therefore could proceed fairly easily on both the flat and stepped Cu(111) surfaces.

In the second process, represented in **Figures 6.12.b, c**, the  $\text{NH}_2$  molecule subtracts a hydrogen from  $\text{N}_2\text{H}_3$  leading to  $\text{NNH}_2$  or  $\text{NHNH}$ . If  $\text{NNH}_2$  is formed, the process requires overcoming a barrier of 0.70 eV, but the products are 0.12 eV more favourable than the reactants on the flat surface. The presence of steps on the surface leads to  $\text{NNH}_2$  via a slightly lower barrier ( $E_a = 0.67$  eV), but releasing only 0.06 eV. The alternative pathway, leading to  $\text{NHNH}$ , has barriers of 0.80 and 0.64 eV on the terrace and step, respectively, while the process is endothermic by 0.11 eV on the terrace and practically in thermodynamic equilibrium ( $E_r = -0.01$  eV) on the stepped surface.

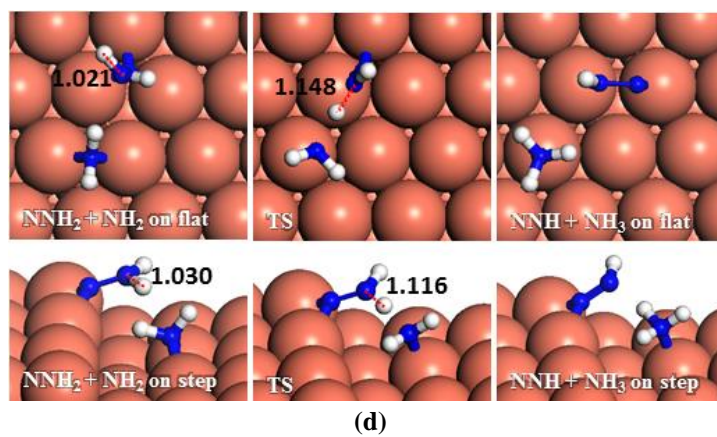
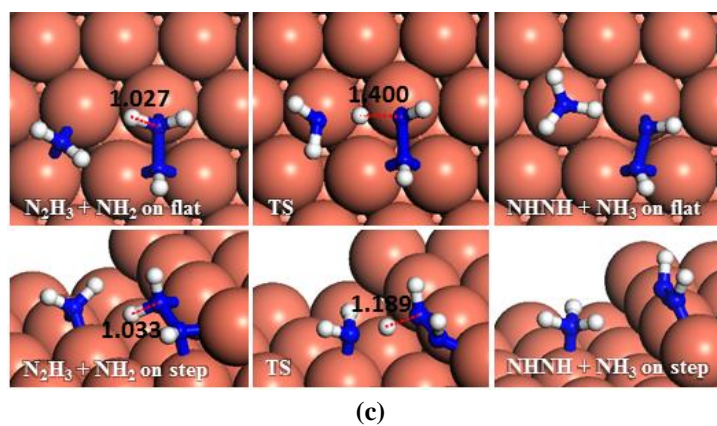
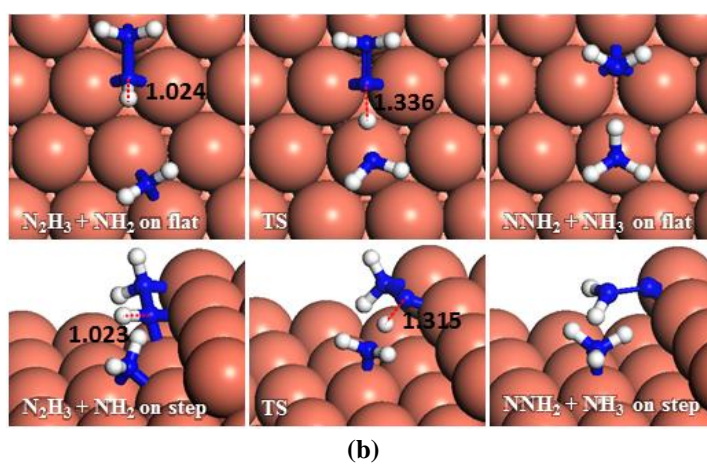
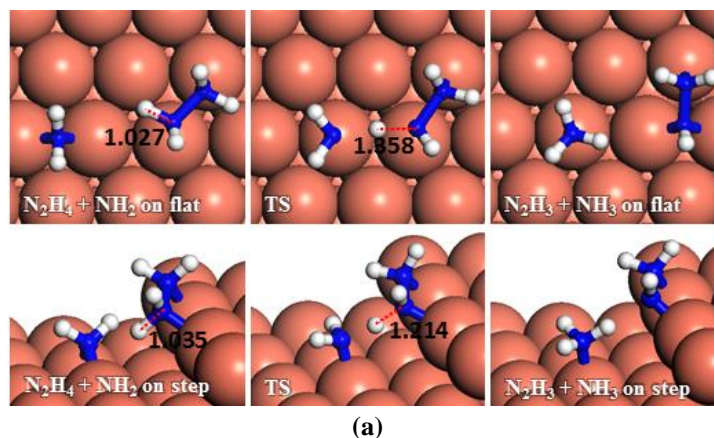
In the next dehydrogenation pathway (**Figures 6.12.d, e**),  $\text{NH}_2$  reacts with either the  $\text{NNH}_2$  or  $\text{NHNH}$  structure, leading to the formation of  $\text{NNH}$ . The dehydrogenation process starting with  $\text{NNH}_2$  is endothermic by 0.15 eV with an energy barrier of 0.44

eV on the terrace, while on the stepped surface it has a barrier of only 0.15 eV and an exothermic reaction energy of 0.47 eV. However, the interaction between NHHH and NH<sub>2</sub> is exothermic by 0.26 with a barrier of only 0.36 eV on the flat surface that increases by 0.64 eV for a thermodynamically equilibrated reaction on the stepped surface ( $E_a = 1.00$  and  $E_r = 0.01$  eV). The reaction between NH<sub>2</sub> and NHHH is therefore likely to succeed on the flat surface, although the reaction between NNH<sub>2</sub> and NH<sub>2</sub> is more feasible on the stepped surface.

In the last dehydrogenation process, the reaction between NH<sub>2</sub> and NNH yields N<sub>2</sub> and NH<sub>3</sub> (**Figure 6.12.f**). This reaction is highly exothermic releasing energies of 2.13 and 1.60 eV on the flat and stepped surfaces, respectively which may be used for the desorption of N<sub>2</sub> and NH<sub>3</sub>, which requires energies of 0.15 and 0.81 eV on the flat and 0.39 and 1.06 eV on the stepped surfaces, respectively.

#### 6.3.2.8.2. Interaction of NH<sub>2</sub> molecules

The NH<sub>2</sub> molecules, *i.e.* produced by hydrazine N–N bond scission, may also react together leading to NH and NH<sub>3</sub>, see **Figure 6.13**. The calculated energy barrier for this reaction is only 0.55 eV and the products are practically in thermodynamic equilibrium with the reactants ( $E_r = -0.05$  eV) on the flat surface. Although this process is therefore feasible on the flat Cu(111) surface, it is rather difficult to succeed on the stepped surface, due to a high barrier energy of 2.05 eV ( $E_r = 0.37$  eV).



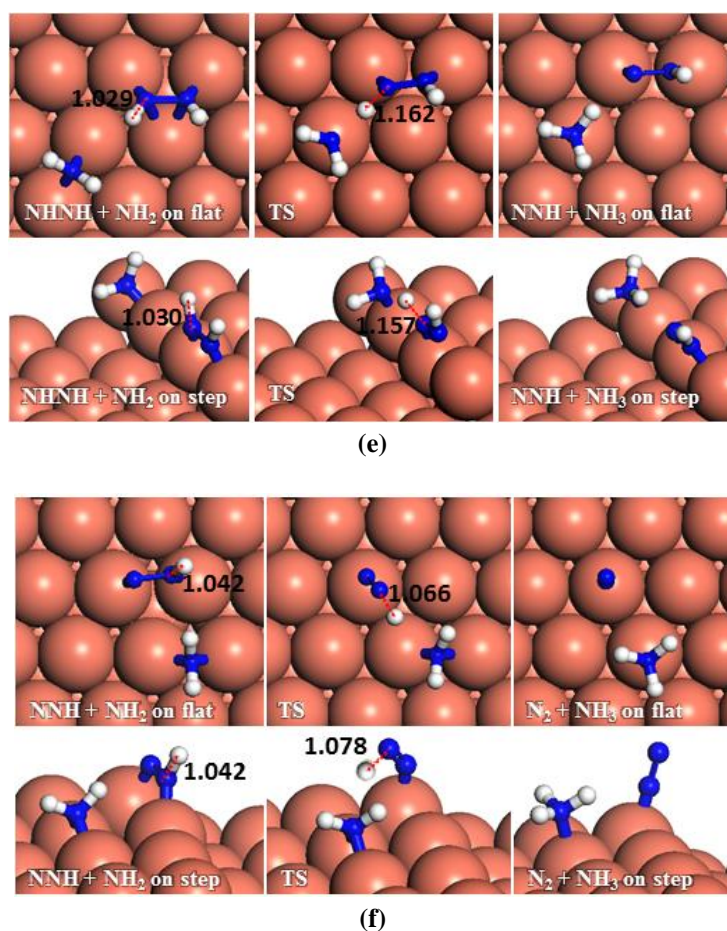


**Figure 6.12.** Schematic representation of the initial, transition and final states for dehydrogenation pathways on the flat (top-view) and stepped (side-view) Cu(111) via  $\text{NH}_2$  attacking to (a)  $\text{N}_2\text{H}_4$ , (b) and (c)  $\text{N}_2\text{H}_3$ , (d)  $\text{NNH}_2$ , (e)  $\text{NHNH}$  and (f)  $\text{NNH}$ . Bond lengths are given in Å.

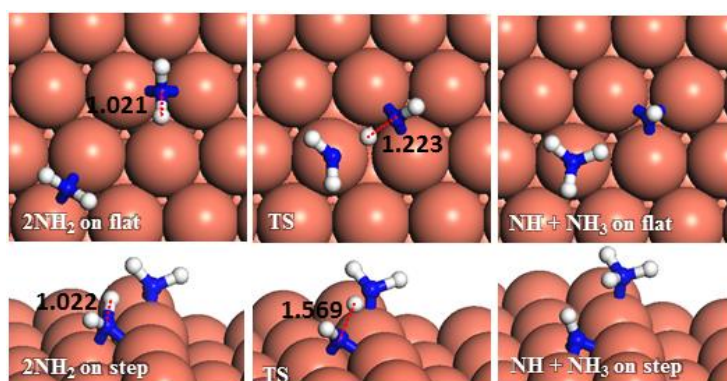


**Figure 6.13.** Schematic representation of the initial, transition and final states for dehydrogenation pathway via  $\text{NH}_2$  attacking  $\text{NH}_2$  on the flat (top-view) and stepped (side-view) Cu(111) surfaces. Bond lengths are given in Å.

## 6.4. Discussions

The most stable adsorption structures of the intermediates dehydrogenation showed that their order of stability on the surface with respect to the hydrazine is  $N_2H_4 > N_2H_3 > N_2H_2 > N_2H$ , indicating that more oxidised intermediates are less stable on the Cu surfaces. The same trend is found for the N–N average bond lengths, showing that dehydrogenation results in shorter and stronger N–N bond and less stable intermediates on the surface.

We summarised the energy profiles of the reaction mechanism in **Figures 6.14 – 6.16**. The plot in **Figure 6.14** contains the different pathways for intra-molecular dehydrogenation, whereas the  $N_2H_4$  decomposition via N–N scission and further dehydrogenation reactions are shown in **Figure 6.15**, and **Figure 6.16** summarises the inter-molecular dehydrogenation pathway.

The  $N_2H_4$  dehydrogenation,  $N_2H_4^* \rightarrow N_2H_3^* + H^*$  and subsequent ones are unlikely to occur under moderate conditions, owing to the high reaction barriers, see **Table 6.2** and **Figure 6.14**. The rate-determining step for the  $N_2H_4$  intra-molecular dehydrogenation mechanism is  $NHNH^* \rightarrow NNH^* + H^*$  on the flat surface with an energy barrier of 1.68 eV, and  $N_2H_3^* \rightarrow NNH_2^* + H^*$  on the stepped surface with activation barrier of 1.77 eV. It is therefore unlikely that a large amount of  $N_2$  is produced via this intra-molecular dehydrogenation pathway. Overall, from the investigation of N–H bond scission of all species on the surface, NNH is the only fragment which is easily dehydrogenated to the  $N_2$  molecule, with barriers of only 0.37 and 0.62 eV on the flat and stepped surfaces, respectively, and a relatively exothermic reaction ( $E_r \sim 1.3$  eV). These results also suggest that at moderate temperatures the recombination of produced H atoms will lead to the formation of

H<sub>2</sub>; this reaction has activation energies of ~ 1.1 eV on the flat and stepped surfaces and the products desorb easily from the surface.

From investigation of N–N bond scission in any intermediate on the surface, we found that the N–N decoupling in N<sub>2</sub>H<sub>4</sub> (N<sub>2</sub>H<sub>4</sub>\* → 2NH<sub>2</sub>\*), see **Table 6.2** and **Figure 6.15**, is the predominant mechanism, leading to amide intermediate production in agreement with experiment (Block and Schulzek.G, 1973). The exothermic decomposition of N<sub>2</sub>H<sub>3</sub> and NHHH fragments via N–N decoupling also have low activation energies compared to the other intermediates on the flat and stepped surfaces.

The production of NH<sub>3</sub> takes place from the exothermic reaction of NH<sub>2</sub> radicals on the flat surface by an activation energy of only 0.55 eV. Further NH<sub>3</sub> production from the interaction of N<sub>2</sub>H<sub>x</sub> (x=1–4) and NH<sub>2</sub> is also possible, resulting in the production of N<sub>2</sub>; all these steps have barrier energies below 1 eV on either the flat or stepped surfaces, see **Table 6.2** and **Figure 6.16**. The rate-determining step for the inter-molecular dehydrogenation via NH<sub>2</sub> is the reaction N<sub>2</sub>H<sub>3</sub>\* + NH<sub>2</sub>\* → NHHH\* + NH<sub>3</sub>\* which has an activation energy of 0.80 eV on the flat surface, while on the stepped surfaces NHHH\* + NH<sub>2</sub>\* → NNH\* + NH<sub>3</sub>\* has a barrier of 1.00 eV where it is the rate-determining step. The N<sub>2</sub> molecule produced from one single hydrazine molecule via an inter-molecular dehydrogenation mechanism, **Figure 6.16**, is in agreement with experimental reports where the N<sub>2</sub>H<sub>4</sub> remains stable during the dissociation process (Maurel and Menezo, 1978; Block and Schulzek.G, 1973).

Thus we may conclude that the NH<sub>2</sub> radical governs the N<sub>2</sub>H<sub>4</sub> dissociation, which agrees well with experimental and theoretical studies about the role of NH<sub>2</sub> in the hydrazine decomposition (Aika *et al.*, 1970; Konnov and De Ruyck, 2001). The

released energies from the exothermic reactions provide enough energy for the evolution of  $\text{NH}_3$ ,  $\text{N}_2$  and  $\text{H}_2$  gases from the surface. Experimental works also revealed that the decomposition of hydrazine on copper films occurs above 300 K with gaseous products of  $\text{NH}_3$ ,  $\text{N}_2$  and some  $\text{H}_2$  (Alhaydari *et al.*, 1985), which is consistent with the mechanism in **Figure 6.16**.

Furthermore, the calculations showed the influence of low-coordinated atoms on the different  $\text{N}_2\text{H}_4$  decomposition pathways, *i.e.* at the step edges. These surface atoms stabilise some intermediates more than others along the different pathways, although there is no clear trend in the activation energies except to increase the N–N decoupling barriers of the intermediates in the presence of step edge atoms.

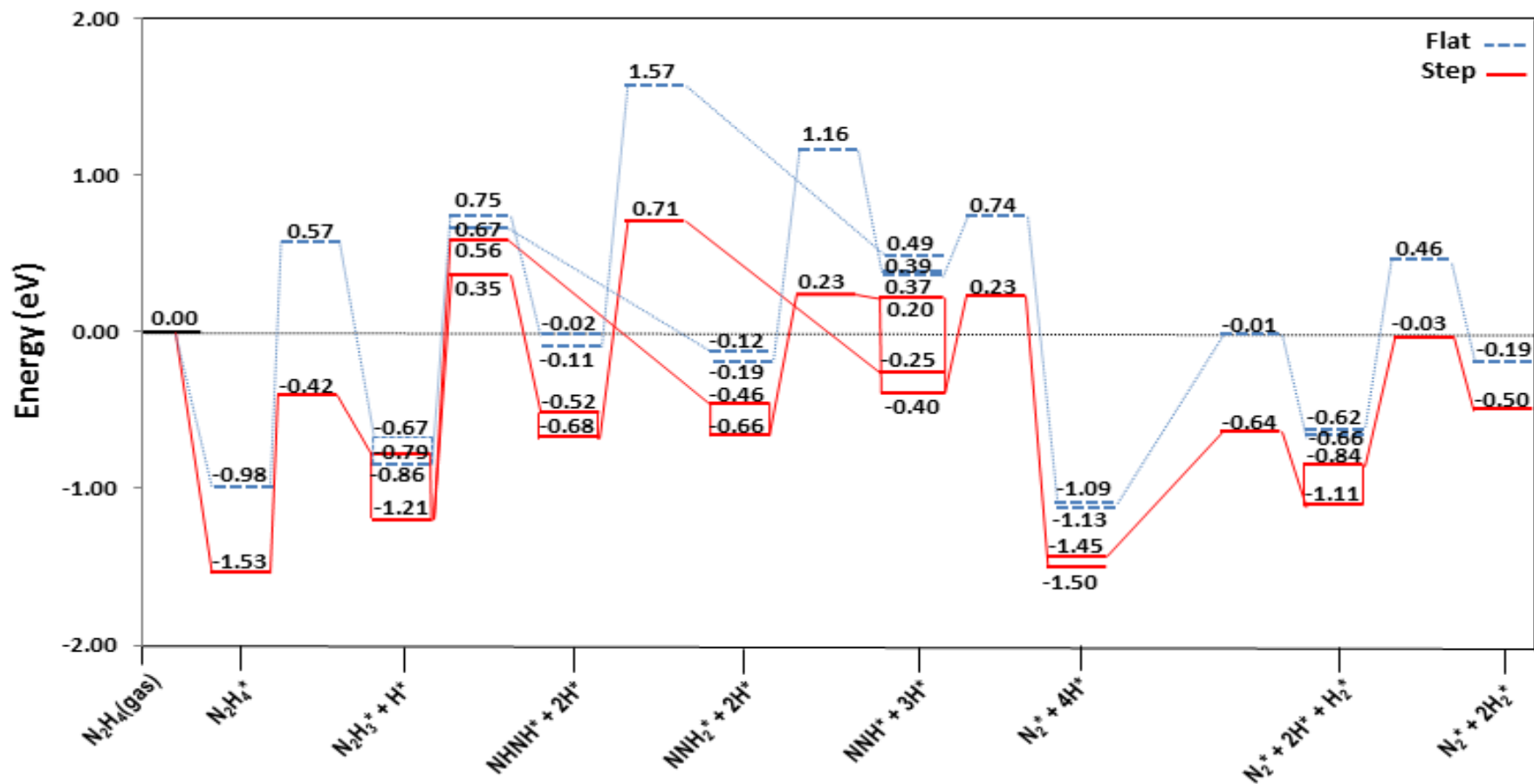


**Figure 6.14.** Reaction profiles for dissociation of  $N_2H_4$  via intra-molecular dehydrogenation mechanism on the flat (---) and stepped (—) Cu(111) surfaces. Energies are relative to the energy of the gas-phase hydrazine (in eV). Note that we have considered the diffusion of intermediates to their most stable adsorption sites on the surface as a barrier-less pathway.

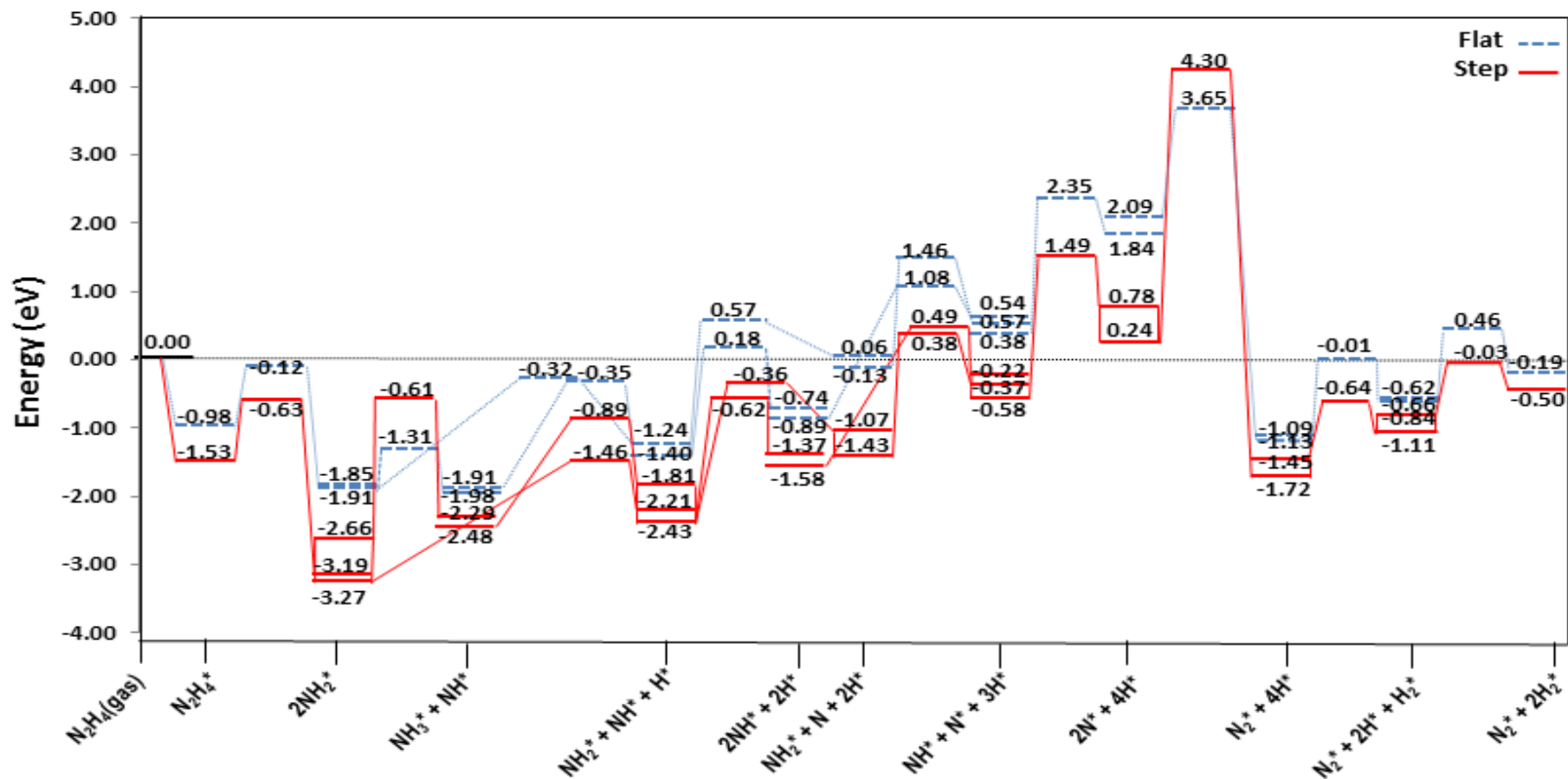


**Figure 6.15.** Reaction profiles for dissociation of  $N_2H_4$  via N–N bond breaking and subsequent dehydrogenation pathways on the flat (---) and stepped (—) Cu(111) surfaces. Energies are relative to the energy of the gas-phase hydrazine (in eV). Note that we have considered the diffusion of intermediates to their most stable adsorption sites as a barrier-less pathway.

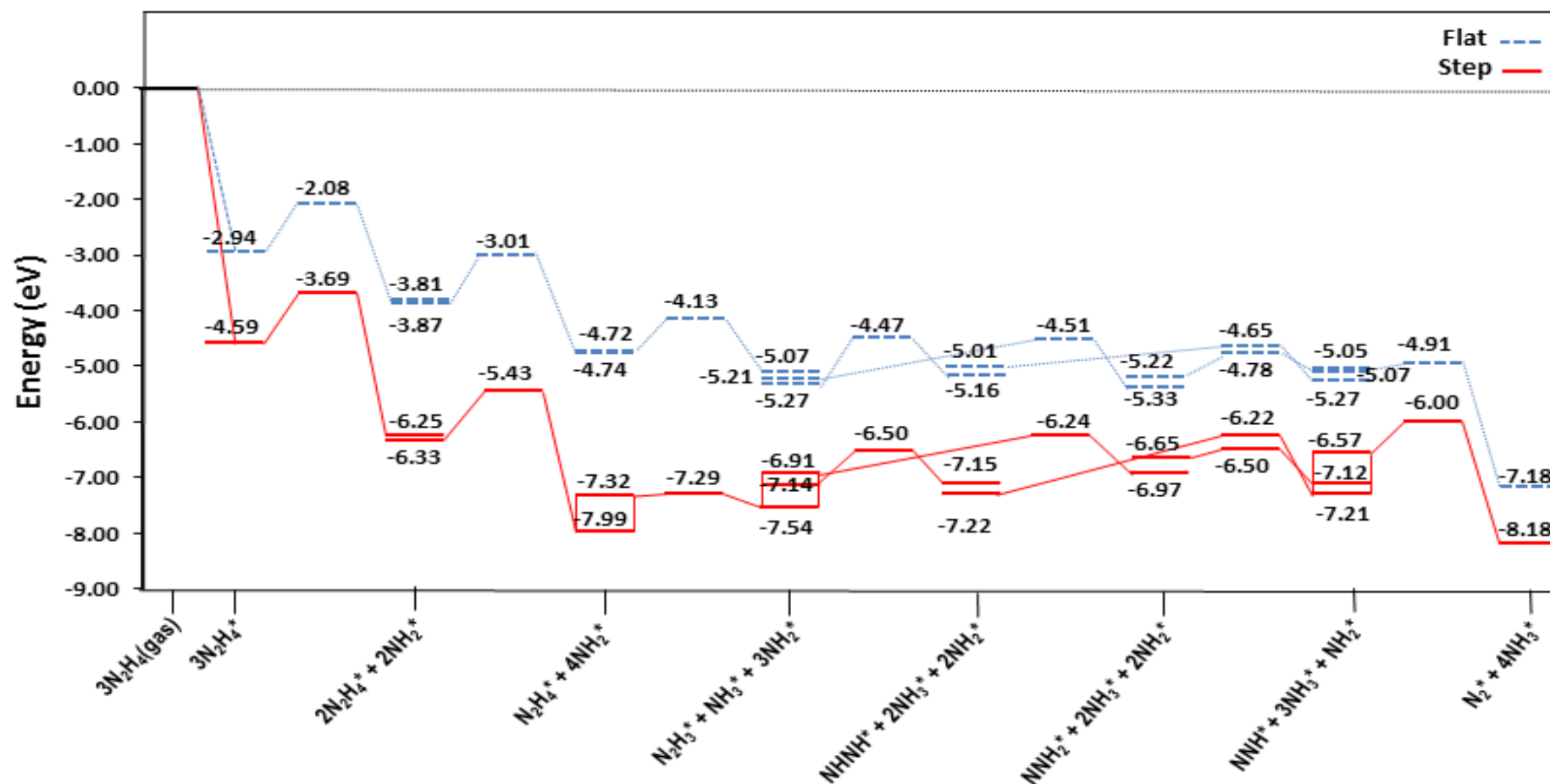


**Figure 6.16.** Reaction profiles for dissociation of  $\text{N}_2\text{H}_4$  via inter-molecular dehydrogenation via  $\text{NH}_2$  on the flat (---) and stepped (—) Cu(111) surfaces. Energies are relative to the energy of the gas-phase hydrazine (in eV). Note that we have considered the diffusion of inter-mediate to their most stable adsorption sites on the surface as a barrier-less pathway.

## 6.5. Conclusions

We have employed DFT level calculations with long-range interaction corrections to carry out a systematic study of the  $\text{N}_2\text{H}_4$  decomposition mechanisms on the flat and stepped Cu(111) surfaces. We have identified the most stable adsorption sites for all intermediates along the different mechanisms of N–H and N–N bond scission. We have found that  $\text{N}_2\text{H}_4$  dehydrogenation is kinetically an unlikely process on both flat and stepped Cu(111) surfaces due to high barrier energies. However, N–N decoupling is energetically feasible, leading to  $\text{NH}_2$  intermediates. The inter-molecular dehydrogenation reaction is the predominant mechanism between either  $\text{NH}_2$  fragments on the flat surface, or  $\text{NH}_2$  and  $\text{N}_2\text{H}_x$  ( $x=1-4$ ) intermediates on the flat or stepped surfaces, leading to the formation of  $\text{N}_2$  and  $\text{NH}_3$ , as shown in **Figure 6.16**. This process is highly exothermic, releasing  $\sim 2.50$  eV per hydrazine molecule, which agrees well with the use of  $\text{N}_2\text{H}_4$  as a rocket fuel. Meanwhile the amide and imide intermediates are hydrogenated to  $\text{NH}_3$  in the presence of hydrogen, which competes with the recombination of H atoms leading to  $\text{H}_2$  molecules. We also found that, while the introduction of low-coordinated atoms, as on the step edge on the surface, increases the barrier of N–N decoupling along the reaction, it has different effects on the barriers of intra- and inter-molecular dehydrogenation mechanisms.

## ***Chapter 7: Microkinetic simulation of hydrazine dissociation on the Cu(111) surface***

### **Abstract**

The investigation by microkinetic simulations provides detailed information about the hydrazine ( $\text{N}_2\text{H}_4$ ) decomposition reaction on the Cu(111) surface. In the microkinetic model, we have considered 52 elementary reactions derived from density functional theory calculations, where the energetic terms of all steady states were corrected with reference to the working temperature. The spectra of the simulated temperature programmed reactions (TPR) showed how the pre-adsorbed  $\text{N}_2\text{H}_4$  coverage and heating rate affect the evolution of products, including  $\text{NH}_3$ ,  $\text{N}_2$  and  $\text{H}_2$ . The batch reactor simulations revealed that  $\text{NH}_3$  and  $\text{N}_2$  are the dominant products, while the  $\text{H}_2$  yield is minor, *i.e.* the highest  $\text{H}_2$  selectivity obtained in the simulation at 350 K is 5.38 %, compared to 81.92 % and 36.27 % of  $\text{NH}_3$  and  $\text{N}_2$  respectively. Adsorbed intermediates such as  $\text{N}_2\text{H}_3$  and  $\text{NH}$  are species with longer residence time on the surface during  $\text{N}_2\text{H}_4$  decomposition in the batch reactor simulation, in the 190 – 265 and 270 – 370 K temperature ranges, respectively.

## 7.1. Introduction

Microkinetic simulations are convenient tools to approach a catalytic process from the atomic level to reactor conditions. In recent years, there has been increasing interest in the development of microkinetic models for various industrially relevant processes such as ammonia synthesis (Stoltze, 1987; Honkala *et al.*, 2005; Hellman *et al.*, 2006; Hellman *et al.*, 2009), oxidation (Wang *et al.*, 2014; Novell-Leruth *et al.*, 2008), and decomposition (Rasim *et al.*, 2010; Hellman *et al.*, 2009), methanol synthesis (Askgaard *et al.*, 1995) and decomposition (Greeley and Mavrikakis, 2004; Kandoi *et al.*, 2006; Gokhale *et al.*, 2004), ethylene oxidation (Stegelmann *et al.*, 2004) and water gas shift reaction (Gokhale *et al.*, 2008; Grabow *et al.*, 2008; Madon *et al.*, 2011). To construct a reliable microkinetic model, it is necessary to investigate all the relevant processes involved, such as adsorption, desorption, and surface reactions. Density functional theory (DFT) is commonly used to determine the energy profile along the reaction pathway that will be employed in the microkinetic modelling (Roldán *et al.*, 2010; Dzade *et al.*, 2013).

Hydrazine ( $\text{N}_2\text{H}_4$ ) decomposition by heterogeneous catalysis is one of the most widely employed techniques for ammonia synthesis and the production of hydrogen in industrial processes such as the proton exchange membrane fuel cell (PEMFC) due to its hydrogen content of 12.5 wt%. Moreover, since hydrazine is liquid under mild conditions and its decomposition over catalysts at room temperature is exothermic without the need for added energy, it is ideal for portable applications such as space vehicles or satellites (Zheng *et al.*, 2005; Schmidt, 2001; Pakdehi *et al.*, 2014; Block and Schulzek.G, 1973; Grunze, 1979). Hydrazine is also used in a monopropellant thruster to control and adjust the orbits and altitudes of spacecrafts

and satellites, based on the production of much larger volumes of nitrogen, hydrogen and ammonia gases (Mary *et al.*, 1999; Schmidt, 2001). The most important catalyst used in the hydrazine decomposition reaction is Ir/Al<sub>2</sub>O<sub>3</sub> with a very high loading of iridium (20–40 %) (Mary *et al.*, 1999; Balcon *et al.*, 2000; Schmidt, 2001; Contour and Pannetie.G, 1972). However, owing to the high price and limited resources of iridium, considerable research has been focused on the development of cheaper, active and readily available alternative catalysts for hydrazine decomposition. Al-Haydari *et al.* showed that hydrazine molecules adsorb molecularly on a Cu film at 243 K with 20% of the adsorption reversible; further dissociative adsorption continues above 303 K producing mainly NH<sub>3</sub> with N<sub>2</sub> and H<sub>2</sub> gaseous products (Alhaydari *et al.*, 1985).

We have successfully investigated the dissociative adsorption of hydrazine (N<sub>2</sub>H<sub>4</sub>) on the planar and stepped Cu(111) surfaces by first-principles calculations in Chapter 6. The thermodynamic and kinetic potential energy surface (PES) show that intermolecular dehydrogenation of hydrazine to yield NH<sub>3</sub> and N<sub>2</sub> is the favoured route among the explored reaction pathways. Based on the reactions investigated in Chapter 6 (Tafreshi *et al.*, 2015a), we have established a microkinetic model to simulate a batch reactor where hydrazine is in contact with the planar Cu(111) surface, where we have used 52 elementary reactions including adsorption, desorption and reactions on the surface. We have also evaluated the effect of temperature, initial N<sub>2</sub>H<sub>4</sub> coverage and heating rate on a temperature programmed reaction (TPR), as well as the selectivity towards the formation of NH<sub>3</sub>, N<sub>2</sub> and H<sub>2</sub>.

## 7.2. Computational methods

In the heterogeneous catalytic system, the constant rate of each surface elementary step is commonly computed using the transition-state theory (TST) approximations of Eyring (Eyring, 1935) and Evans and Polanyi (Evans and Polanyi, 1935). Although TST is widely applicable and provides a useful description of the chemical reactions rates, it has limitations, especially in reactions with a low energy barrier, as according to the quantum mechanics particles can tunnel across the barrier even though their energy is considerably less than the energy needed to go over the barrier (Sholl and Steckel, 2009). TST also fails in its description of reactions at high temperature, where the motion of molecules becomes more complex and collisions may lead to transition states far away from the lowest-energy saddle point on the potential energy surface (Pineda and Schwartz, 2006). TST assumes that each intermediate is long-lived in each elementary step to reach a Boltzmann distribution of energy, and it thus fails in situations where intermediates are very short-lived (Anslyn and Dougherty, 2006). TST also assumes that the transition states can evolve only to products, while in some cases they may return to the reactants. However, this theory still remains very useful in calculating the thermodynamic properties of the transition state and reaction rates.

Based on the mechanisms investigated in Chapter 6 (Tafreshi *et al.*, 2015a) on the decomposition of  $\text{N}_2\text{H}_4$  on the Cu(111) surface, the microkinetic model constitutes of the 52 reactions summarized in **Table 7.2**. In this model, we have ignored the lateral adsorbate–adsorbate interactions in accord with our study in Chapter 5 (Tafreshi *et al.*, 2015b). Surface diffusion is also neglected, assuming that the reaction energy barrier of diffusion is much smaller than any other barrier in the decomposition

process. As for some species in our model, the active sites cannot be easily defined; we have considered an active site as a hexagonal site made up from 7 Cu atoms where the reactants and products in every elementary step occupy only one site on the surface. Consequently, the coverage of free sites,  $\theta_*(t)$ , is defined by:

$$\theta_*(t) = 1 - \sum_i^n \theta_i(t) \quad (7.1)$$

Upon defining the rate equations, we have used Mathematica (Wolfram Research, 2012) to solve the differential equations set, which describes the relationship between the species coverages and time.

All the thermodynamic and kinetic parameters were extracted from calculations in Chapter 6 based on the density functional theory (DFT) using the VASP code (Kresse and Furthmuller, 1996b; Kresse and Furthmuller, 1996a; Kresse and Hafner, 1993; Kresse and Hafner, 1994) where the Cu(111) surface was modelled by four-layers slab with an area of 88.37 Å<sup>2</sup> in a 2×2 supercell. The adsorbate and three top most surface layers were allowed to relax during structural optimisation. A 5×5×1 Monkhorst-Pack grid (Monkhorst and Pack, 1976) of **k**- points was used to sample the Brillouin zone. For the detailed methodology employed in this Chapter, please refer to Chapter 3.

Spin polarization has been tested and found to be unimportant. All the optimised structures were verified to be located at the local minima on the potential energy surface (PES) by the vibration analysis. A combination of two varieties of the nudged elastic band (NEB) method (Mills and Jonsson, 1994; Mills *et al.*, 1995) and the improved dimer method (IDM) (Heyden *et al.*, 2005) were used to identify

transition state (TS) structures which we verified by a single imaginary frequency associated with the reaction coordinate.

We have calculated the adsorption ( $E_{ads}$ ) and desorption ( $E_{des} = -E_{ads}$ ) energies for the species using the equation (7.2);

$$E_{ads} = E_{molecule}^{surf} - (E^{surf} + E_{molecule}^{gas}) \quad (7.2)$$

Where  $E_{molecule}^{surf}$  is the total energy of the species adsorbed on a relaxed Cu(111) surface and  $E^{surf}$  and  $E_{molecule}^{gas}$  are the energies of the naked surface and isolated gas-phase molecule, respectively. Within this definition, a negative  $E_{ads}$  value means release of energy during adsorption. The reaction energies ( $E_r$ ) were estimated by the difference in energy between the final and initial states; hence, a negative  $E_r$  indicates an exothermic process. The forward activation barriers ( $E_a$ ) were defined as the energy difference between the transition state (TS) and the initial state. The accuracy in determining  $E_{ads}$ ,  $E_r$  and  $E_a$ , is further improved by correcting the static DFT electronic energy using the zero point energies. The zero point energy (ZPE) accounts for the vibrational energy that exists even at 0 K and is calculated as  $ZPE = \sum \frac{1}{2} h \nu_i$  where  $\nu_i$  corresponds to the vibrational modes of the species. To obtain more accurate results, we have also taken into account the temperature dependence of the energy. Thus, the free Gibbs energy,  $G$ , as a temperature function for each different system in a temperature range can be calculated using the global partition function,  $Q$ , and several relevant physical parameters such as entropy ( $S$ ), specific heat at constant pressure ( $C_p$ ) and enthalpy ( $H$ ) derived by the following equations (Kuhn *et al.*, 2009; Chorkendorff and Niemantsverdriet, 2007);

$$S = k_B \ln Q + k_B T \left( \frac{\partial \ln Q}{\partial T} \right)_V \quad (7.3)$$

$$C_p = T \left[ \frac{\partial S}{\partial T} \right] \quad (7.4)$$

$$H = E_{DFT} + E_{(S=0, T=0, ZPE)} + \int_0^T C_p \delta T \quad (7.5)$$

$$G = H - TS \quad (7.6)$$

The thermodynamic properties of the intermediates on the surface or in the gas phase were calculated using the above equations. **Figure 7.1** shows both the calculated and NIST database (Chase *et al.*, 1998) thermodynamic properties of NH<sub>3</sub> in the gas phase while the free energy of N<sub>2</sub>, H<sub>2</sub> in the gas phase is shown in **Figure 7.2**. **Table 7.1** contains the relative error of the derived properties compared with the extracted datas from Shomate equations in the NIST database (Chase *et al.*, 1998).

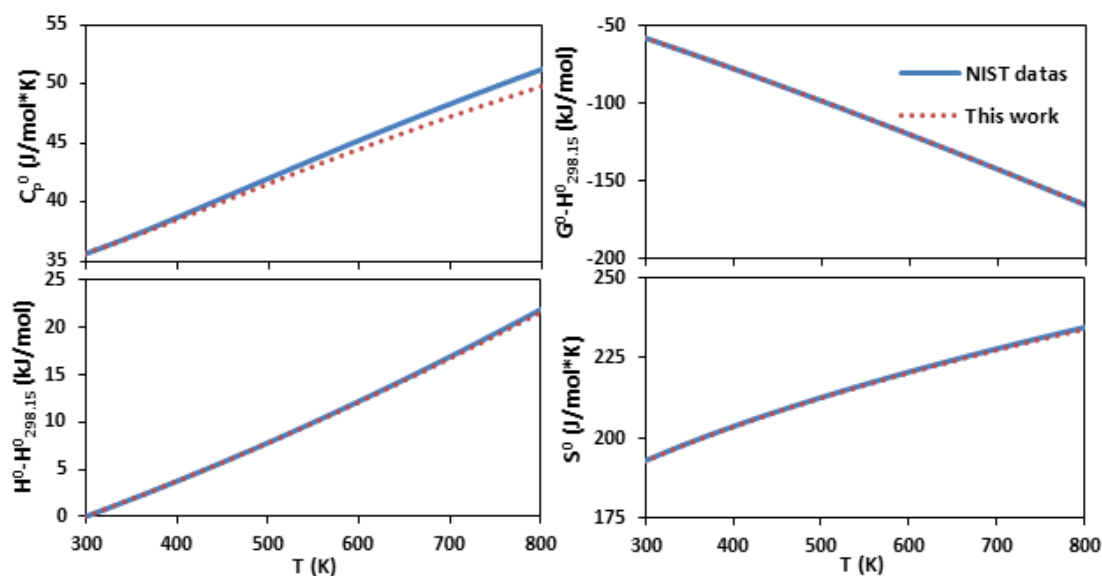


**Figure 7.1.** Calculated thermodynamic properties of NH<sub>3</sub> in the gas phase compared with the NIST database (Chase *et al.*, 1998).

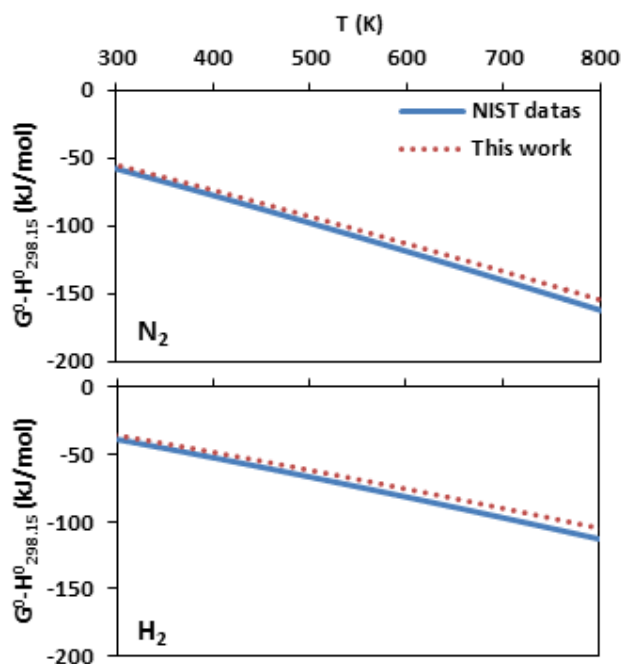


**Figure 7.2.** Calculated thermodynamic properties of  $N_2$  and  $H_2$  in the gas phase compared with NIST database (Chase *et al.*, 1998).

**Table 7.1.** Relative errors (in %) of the calculated thermodynamic properties of  $NH_3$ ,  $N_2$  and  $H_2$  in the gas phase compared with the NIST database (Chase *et al.*, 1998).

	$(Cp^0_{cal.} - Cp^0_{NIST}) / Cp^0_{NIST} * 100$	$(S^0_{cal.} - S^0_{NIST}) / S^0_{NIST} * 100$	$(H^0_{cal.} - H^0_{NIST}) / H^0_{NIST} * 100$	$(G^0_{cal.} - G^0_{NIST}) / G^0_{NIST} * 100$
$NH_3$	-1.37	-0.13	-0.76	-0.08
$N_2$	-0.48	-4.55	-0.30	-4.82
$H_2$	-0.61	-6.76	-0.42	-7.33

### 7.3. Results and discussions

The 52 elementary steps for hydrazine decomposition summarised in **Table 7.2** include adsorption and desorption of reactants and products, N–N decoupling, dehydrogenation of  $N_2H_x$  ( $x=1-4$ ) and  $NH_x$  ( $x=1-3$ ) and inter-molecular interaction on the surface. We have also included in **Table 7.2** the reaction ( $E_r^{ZPE}$ ) and barrier ( $E_a^{ZPE}$ ) energies corrected with zero point energy, the pre-exponential factors ( $A_0$ ), and the reaction rate constants ( $k$ ) of each elementary step at 300 and 650 K. From the variation of the reaction rate constants with temperature, we can conclude which step has the limiting rate and the least favourable reaction for each mechanism. We

have represented the reaction rate constants as a function of temperature in **Figure 7.3**. The adsorption sticking coefficients ( $S_0$ ) of  $N_2H_4$ ,  $NH_3$ ,  $N_2$  and  $H_2$  on the Cu(111) surface at 300 and 650 K are also provided, in **Table 7.3**, where similar results have been reported for  $NH_3$  on Ru(0001) (Danielson *et al.*, 1978),  $N_2$  on Fe(100) and Fe (111) (Bozso *et al.*, 1977) and  $H_2$  on low-index Cu surfaces (Anger *et al.*, 1989).

We have calculated two different microkinetic models. In the first part of our work, we have modelled a temperature programmed reaction (TPR) where any gas is pumped out to the detector, avoiding its re-adsorption. In the second section, we have explored the catalytic activity of copper surfaces towards  $N_2H_4$  dissociation in a batch reactor under different conditions, starting from a situation where the naked Cu surface is in contact with a given pressure of  $N_2H_4$ .

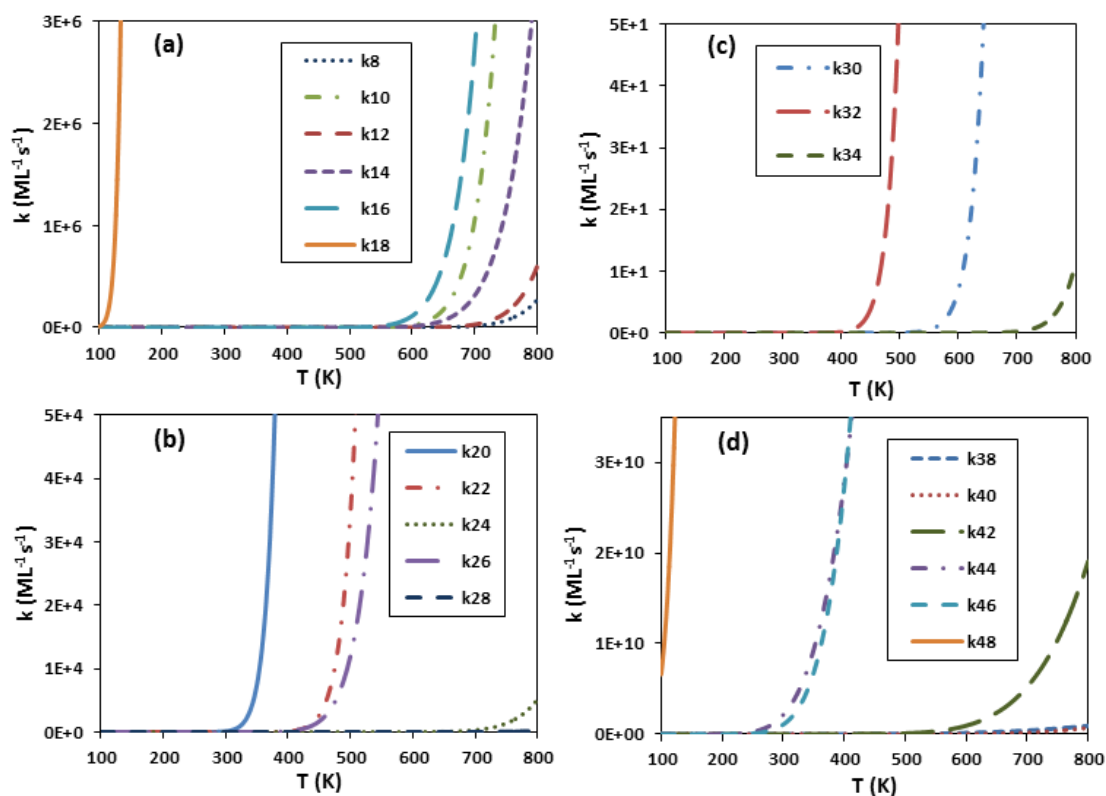


**Figure 7.3.** Calculated reaction rate constants ( $k$ ) as a function of temperature ( $T$ ) for reactions of, (a)  $N_2H_x$  ( $x=1-4$ ) dehydrogenation, (b)  $N_2H_x$  ( $x=1-4$ ) N–N decoupling, (c)  $NH_x$  ( $x=1-3$ ) dehydrogenation and, (d) interaction of  $NH_2$  with  $N_2H_x$  ( $x=1-4$ ) mechanisms.

### 7.3.1. Temperature programmed reaction simulation

The first part of the microkinetic simulation started from the  $N_2H_4$  molecule pre-adsorbed on the Cu surface without molecular hydrazine in the gas phase and excluding the adsorption steps (R0, R3, R5, R7).

The rate equations of the elementary reactions and corresponding differential equations are listed in the Appendix.

**Table 7.2.** Calculated ZPE corrected reaction ( $E_r^{ZPE}$ ) and barrier ( $E_a^{ZPE}$ ) energies for the reaction pathways considered. The pre-exponential factors ( $A_0$ ) and reaction rate constants ( $k$ ) at 300 and 650 K are also included. The  $E_r^{ZPE}$  of the adsorption and desorption processes are the corresponding  $E_{ads}^{ZPE}$  and  $E_{des}^{ZPE}$  which for each species were calculated relative to them in the gas-phase. Note that “\*” and (X\*) indicate a free site and the adsorbed specie on the surface respectively. The units of  $A_0$  and  $k$  for first order and second order reactions are  $s^{-1}$  and  $ML^{-1}s^{-1}$  respectively.

	Reactions	$E_r^{ZPE}$ (eV)	$E_a^{ZPE}$ (eV)	$A_0$ 300 K	$A_0$ 650 K	$k$ 300 K	$k$ 650 K
<b>Adsorption-Desorption</b>							
<b>R0</b>	$N_2H_4 + * \rightarrow N_2H_4^*$	-0.94	—	$1.04 \times 10^4$	$7.06 \times 10^3$	$1.21 \times 10^{-2}$	$4.91 \times 10^{-4}$
<b>R1</b>	$N_2H_4^* \rightarrow N_2H_4 + *$	0.94	—	$2.31 \times 10^{11}$	$1.75 \times 10^{10}$	$5.33 \times 10^4$	$2.71 \times 10^{11}$
<b>R2</b>	$NH_3^* \rightarrow NH_3 + *$	0.78	—	$4.98 \times 10^{11}$	$9.19 \times 10^{10}$	$2.01 \times 10^8$	$9.10 \times 10^{11}$
<b>R3</b>	$NH_3 + * \rightarrow NH_3^*$	-0.78	—	$1.43 \times 10^4$	$9.69 \times 10^3$	2.68	$7.15 \times 10^{-2}$
<b>R4</b>	$N_2^* \rightarrow N_2 + *$	0.11	—	$6.72 \times 10^{10}$	$6.93 \times 10^9$	$8.26 \times 10^{12}$	$8.10 \times 10^{13}$
<b>R5</b>	$N_2 + * \rightarrow N_2^*$	-0.11	—	$1.11 \times 10^4$	$7.55 \times 10^3$	$6.10 \times 10^{-1}$	$8.83 \times 10^{-2}$
<b>R6</b>	$H^* + H^* \rightarrow H_2 + *$	0.45	—	$5.81 \times 10^{12}$	$6.01 \times 10^{12}$	$1.04 \times 10^8$	$1.02 \times 10^{14}$
<b>R7</b>	$H_2 + * \rightarrow H^* + H^*$	-0.45	—	$4.16 \times 10^4$	$2.82 \times 10^4$	$9.83 \times 10^2$	$1.42 \times 10^2$
<b><math>N_2H_x</math> (x=1-4) Dehydrogenation</b>							
<b>R8</b>	$N_2H_4^* \rightarrow N_2H_3^* + H^*$	0.16	1.30	$8.33 \times 10^{12}$	$2.14 \times 10^{13}$	$1.30 \times 10^{-9}$	$2.54 \times 10^3$
<b>R9</b>	$N_2H_3^* + H^* \rightarrow N_2H_4^*$	-0.16	1.14	$3.12 \times 10^{13}$	$1.06 \times 10^{14}$	$6.13 \times 10^{-6}$	$9.15 \times 10^5$
<b>R10</b>	$N_2H_3^* \rightarrow NNH_2^* + H^*$	0.55	1.26	$2.54 \times 10^{13}$	$1.14 \times 10^{14}$	$8.37 \times 10^{-8}$	$1.78 \times 10^5$
<b>R11</b>	$NNH_2^* + H^* \rightarrow N_2H_3^*$	-0.55	0.71	$1.45 \times 10^{13}$	$6.00 \times 10^{13}$	$1.23 \times 10^7$	$2.84 \times 10^{11}$
<b>R12</b>	$N_2H_3^* \rightarrow NHH^* + H^*$	0.64	1.35	$1.47 \times 10^{13}$	$4.26 \times 10^{13}$	$7.84 \times 10^{-10}$	$4.75 \times 10^3$
<b>R13</b>	$NHH^* + H^* \rightarrow N_2H_3^*$	-0.64	0.71	$5.52 \times 10^{12}$	$9.61 \times 10^{12}$	4.74	$1.95 \times 10^7$
<b>R14</b>	$NNH_2^* \rightarrow NNH^* + H^*$	0.45	1.12	$9.77 \times 10^{12}$	$2.12 \times 10^{13}$	$2.46 \times 10^{-6}$	$7.04 \times 10^4$
<b>R15</b>	$NNH^* + H^* \rightarrow NNH_2^*$	-0.45	0.67	$1.81 \times 10^{13}$	$6.00 \times 10^{13}$	$8.64 \times 10^4$	$2.35 \times 10^{10}$
<b>R16</b>	$NHH^* \rightarrow NNH^* + H^*$	0.46	1.47	$2.03 \times 10^{13}$	$4.88 \times 10^{13}$	$3.3 \times 10^{-5}$	$6.33 \times 10^5$
<b>R17</b>	$NNH^* + H^* \rightarrow NHH^*$	-0.46	1.01	$1.75 \times 10^{13}$	$4.51 \times 10^{13}$	$8.12 \times 10^3$	$4.60 \times 10^9$
<b>R18</b>	$NNH^* \rightarrow N_2^* + H^*$	-1.62	0.17	$1.54 \times 10^{13}$	$4.16 \times 10^{13}$	$4.64 \times 10^{10}$	$5.81 \times 10^{12}$
<b>R19</b>	$N_2^* + H^* \rightarrow NNH^*$	1.62	1.79	$2.13 \times 10^{12}$	$3.51 \times 10^{12}$	$9.17 \times 10^{-19}$	$1.44 \times 10^{-2}$
<b><math>N_2H_x</math> (x=1-4) N-N Decoupling</b>							
<b>R20</b>	$N_2H_4^* \rightarrow NH_2^* + NH_2^*$	-0.98	0.69	$1.68 \times 10^{13}$	$5.74 \times 10^{13}$	$1.22 \times 10^2$	$1.11 \times 10^9$
<b>R21</b>	$NH_2^* + NH_2^* \rightarrow N_2H_4^*$	0.98	1.67	$3.72 \times 10^{13}$	$8.93 \times 10^{13}$	$1.90 \times 10^{-14}$	$6.54 \times 10^1$

<b>R22</b>	$\text{N}_2\text{H}_3^* \rightarrow \text{NH}_2^* + \text{NH}^*$	-0.39	0.90	$1.10 \times 10^{13}$	$3.54 \times 10^{13}$	$9.1 \times 10^{-3}$	$7.86 \times 10^6$
<b>R23</b>	$\text{NH}_2^* + \text{NH}^* \rightarrow \text{N}_2\text{H}_3^*$	0.39	1.29	$1.17 \times 10^{13}$	$2.59 \times 10^{13}$	$3.68 \times 10^{-9}$	$4.40 \times 10^3$
<b>R24</b>	$\text{NNH}_2^* \rightarrow \text{NH}_2^* + \text{N}^*$	0.12	1.35	$2.87 \times 10^{12}$	$4.42 \times 10^{12}$	$3.58 \times 10^{-11}$	$5.54 \times 10^1$
<b>R25</b>	$\text{NH}_2^* + \text{N}^* \rightarrow \text{NNH}_2^*$	-0.12	1.23	$1.40 \times 10^{13}$	$3.64 \times 10^{13}$	$1.07 \times 10^{-7}$	$3.48 \times 10^4$
<b>R26</b>	$\text{NHNH}^* \rightarrow \text{NH}^* + \text{NH}^*$	-0.38	0.79	$2.42 \times 10^{12}$	$3.05 \times 10^{12}$	$9.97 \times 10^{-2}$	$7.09 \times 10^5$
<b>R27</b>	$\text{NH}^* + \text{NH}^* \rightarrow \text{NHNH}^*$	0.38	1.17	$8.86 \times 10^{12}$	$1.43 \times 10^{13}$	$6.14 \times 10^{-7}$	$1.86 \times 10^4$
<b>R28</b>	$\text{NNH}^* \rightarrow \text{NH}^* + \text{N}^*$	0.15	1.42	$1.47 \times 10^{12}$	$1.62 \times 10^{12}$	$4.48 \times 10^{-13}$	1.83
<b>R29</b>	$\text{NH}^* + \text{N}^* \rightarrow \text{NNH}^*$	-0.15	1.27	$7.53 \times 10^{12}$	$1.28 \times 10^{13}$	$4.08 \times 10^{-9}$	$1.69 \times 10^3$
<b>NH<sub>x</sub> (x=1-3) Dehydrogenation</b>							
<b>R30</b>	$\text{NH}_3^* \rightarrow \text{NH}_2^* + \text{H}^*$	0.60	1.41	$3.26 \times 10^{12}$	$9.05 \times 10^{12}$	$3.27 \times 10^{-12}$	$6.85 \times 10^1$
<b>R31</b>	$\text{NH}_2^* + \text{H}^* \rightarrow \text{NH}_3^*$	-0.60	0.81	$1.04 \times 10^{13}$	$2.57 \times 10^{13}$	$6.00 \times 10^{-1}$	$2.99 \times 10^7$
<b>R32</b>	$\text{NH}_2^* \rightarrow \text{NH}^* + \text{H}^*$	0.56	1.40	$3.12 \times 10^{12}$	$4.64 \times 10^{12}$	$6.60 \times 10^{-6}$	$1.52 \times 10^4$
<b>R33</b>	$\text{NH}^* + \text{H}^* \rightarrow \text{NH}_2^*$	-0.56	0.84	$1.08 \times 10^{13}$	$2.99 \times 10^{13}$	$2.14 \times 10^{-1}$	$2.43 \times 10^7$
<b>R34</b>	$\text{NH}^* \rightarrow \text{N}^* + \text{H}^*$	1.34	1.79	$6.31 \times 10^{12}$	$1.22 \times 10^{13}$	$5.16 \times 10^{-20}$	$1.70 \times 10^{-2}$
<b>R35</b>	$\text{N}^* + \text{H}^* \rightarrow \text{NH}^*$	-1.34	0.45	$6.89 \times 10^{12}$	$1.44 \times 10^{13}$	$2.62 \times 10^3$	$6.53 \times 10^8$
<b>Interaction of NH<sub>2</sub> molecules</b>							
<b>R36</b>	$2\text{NH}_2^* \rightarrow \text{NH}^* + \text{NH}_3^*$	0.00	0.45	$1.54 \times 10^{13}$	$2.58 \times 10^{13}$	$1.08 \times 10^7$	$4.69 \times 10^{10}$
<b>R37</b>	$\text{NH}^* + \text{NH}_3^* \rightarrow 2\text{NH}_2^*$	0.00	0.45	$1.19 \times 10^{13}$	$2.88 \times 10^{13}$	$6.20 \times 10^5$	$1.97 \times 10^{10}$
<b>Interaction of NH<sub>2</sub> with N<sub>2</sub>H<sub>x</sub> (x=1-4)</b>							
<b>R38</b>	$\text{N}_2\text{H}_4^* + \text{NH}_2^* \rightarrow \text{N}_2\text{H}_3^* + \text{NH}_3^*$	-0.36	0.42	$2.42 \times 10^{12}$	$2.73 \times 10^{12}$	$4.81 \times 10^4$	$2.38 \times 10^8$
<b>R39</b>	$\text{N}_2\text{H}_3^* + \text{NH}_3^* \rightarrow \text{N}_2\text{H}_4^* + \text{NH}_2^*$	0.36	0.78	$2.72 \times 10^{12}$	$4.52 \times 10^{12}$	$3.17 \times 10^{-2}$	$8.22 \times 10^5$
<b>R40</b>	$\text{N}_2\text{H}_3^* + \text{NH}_2^* \rightarrow \text{NHNH}^* + \text{NH}_3^*$	0.08	0.64	$5.64 \times 10^{12}$	$9.39 \times 10^{12}$	$1.10 \times 10^2$	$7.79 \times 10^7$
<b>R41</b>	$\text{NHNH}^* + \text{NH}_3^* \rightarrow \text{N}_2\text{H}_3^* + \text{NH}_2^*$	-0.08	0.56	$1.04 \times 10^{12}$	$8.98 \times 10^{11}$	$3.73 \times 10^1$	$2.06 \times 10^6$
<b>R42</b>	$\text{N}_2\text{H}_3^* + \text{NH}_2^* \rightarrow \text{NNH}_2^* + \text{NH}_3^*$	-0.13	0.53	$1.37 \times 10^{13}$	$3.14 \times 10^{13}$	$5.58 \times 10^3$	$2.35 \times 10^9$
<b>R43</b>	$\text{NNH}_2^* + \text{NH}_3^* \rightarrow \text{N}_2\text{H}_3^* + \text{NH}_2^*$	0.13	0.66	$1.98 \times 10^{12}$	$2.46 \times 10^{12}$	5.18	$3.44 \times 10^6$
<b>R44</b>	$\text{NHNH}^* + \text{NH}_2^* \rightarrow \text{NNH}^* + \text{NH}_3^*$	-0.23	0.25	$1.53 \times 10^{13}$	$2.39 \times 10^{13}$	$2.11 \times 10^9$	$4.60 \times 10^{11}$
<b>R45</b>	$\text{NNH}^* + \text{NH}_3^* \rightarrow \text{NHNH}^* + \text{NH}_2^*$	0.23	0.48	$4.44 \times 10^{12}$	$5.50 \times 10^{12}$	$2.41 \times 10^4$	$4.00 \times 10^8$
<b>R46</b>	$\text{NNH}_2^* + \text{NH}_2^* \rightarrow \text{NNH}^* + \text{NH}_3^*$	0.12	0.30	$2.55 \times 10^{13}$	$5.38 \times 10^{13}$	$1.05 \times 10^9$	$1.06 \times 10^{12}$
<b>R47</b>	$\text{NNH}^* + \text{NH}_3^* \rightarrow \text{NNH}_2^* + \text{NH}_2^*$	-0.12	0.18	$7.72 \times 10^{12}$	$1.60 \times 10^{13}$	$1.21 \times 10^{10}$	$8.63 \times 10^{11}$
<b>R48</b>	$\text{NNH}^* + \text{NH}_2^* \rightarrow \text{N}_2^* + \text{NH}_3^*$	-2.09	0.08	$1.60 \times 10^{13}$	$3.11 \times 10^{13}$	$4.38 \times 10^{12}$	$2.54 \times 10^{13}$
<b>R49</b>	$\text{N}_2^* + \text{NH}_3^* \rightarrow \text{NNH}^* + \text{NH}_2^*$	2.09	2.17	$1.00 \times 10^{12}$	$1.43 \times 10^{12}$	$1.25 \times 10^{-25}$	$3.26 \times 10^{-6}$
<b>N<sub>2</sub> Dissociation</b>							
<b>R50</b>	$\text{N}_2^* \rightarrow \text{N}^* + \text{N}^*$	3.20	4.69	$6.71 \times 10^{11}$	$7.03 \times 10^{11}$	$1.09 \times 10^{-68}$	$1.53 \times 10^{-26}$
<b>R51</b>	$\text{N}^* + \text{N}^* \rightarrow \text{N}_2^*$	-3.20	1.49	$3.01 \times 10^{13}$	$9.02 \times 10^{13}$	$1.08 \times 10^{-11}$	$1.51 \times 10^3$

**Table 7.3.** Calculated sticking coefficients ( $S_0$ ) of  $N_2H_4$ ,  $NH_3$ ,  $N_2$  and  $H_2$  adsorption on Cu(111) surface at 300 and 650 K. Note that “\*” and (X\*) indicate a free site and the adsorbed species on the surface, respectively.

Reactions	$S_0$ This work, 300 K	$S_0$ This work, 650 K	$S_0$ Other works
<b>R0</b> $N_2H_4 + * \rightarrow N_2H_4^*$	$1.17 \times 10^{-6}$	$6.96 \times 10^{-8}$	—
<b>R3</b> $NH_3 + * \rightarrow NH_3^*$	$1.88 \times 10^{-4}$	$7.38 \times 10^{-6}$	$\leq 2 \times 10^{-4}$ , 300 – 500 K <sup>A</sup>
<b>R5</b> $N_2 + * \rightarrow N_2^*$	$5.5 \times 10^{-5}$	$1.2 \times 10^{-5}$	$1.0 \times 10^{-6} - 1.0 \times 10^{-7}$ , 500 K <sup>B</sup>
<b>R7</b> $H_2 + * \rightarrow 2H^*$	$2.36 \times 10^{-2}$	$5.03 \times 10^{-3}$	$1.0 \times 10^{-5} - 5.0 \times 10^{-2}$ , 190 K <sup>C</sup>

<sup>A</sup> (Danielson *et al.*, 1978)

<sup>B</sup> (Bozso *et al.*, 1977)

<sup>C</sup> (Anger *et al.*, 1989)

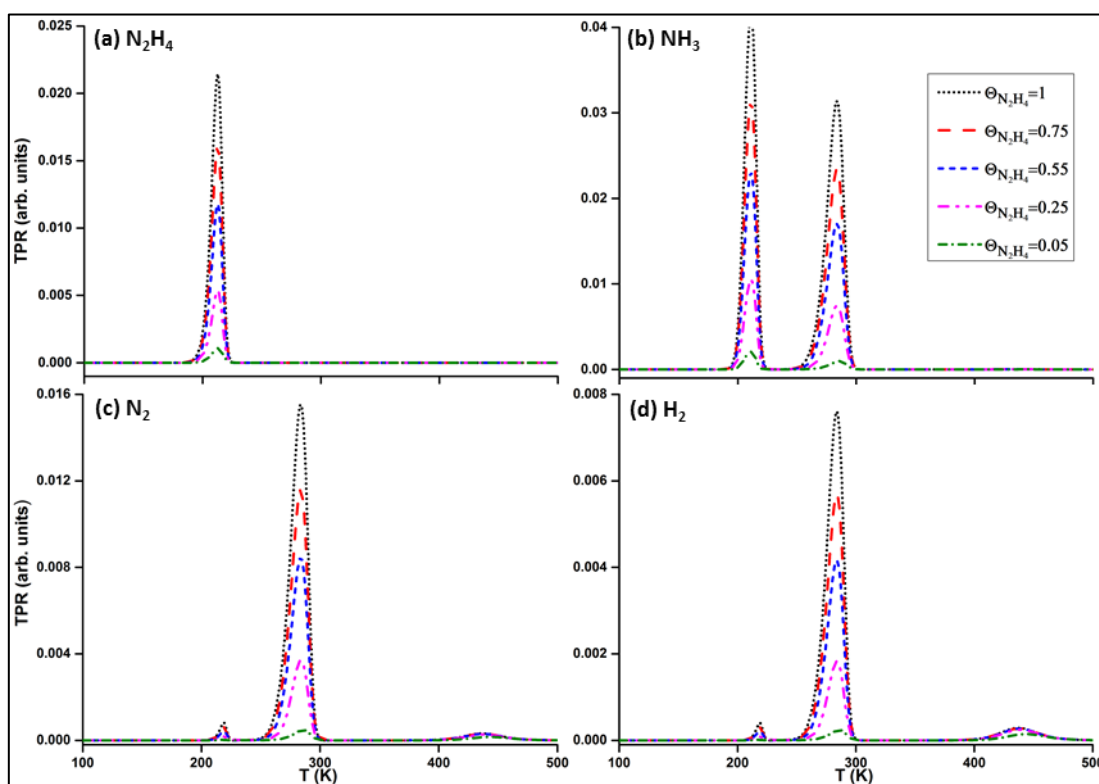


**Figure 7.4.** Simulated TPR spectra for  $N_2H_4$ ,  $NH_3$ ,  $N_2$  and  $H_2$  desorption from Cu(111) surface starting from adsorbed  $N_2H_4$  at different initial coverages at a reaction time of 1s with a 1K/min heating rate.

**Figure 7.4** shows the simulated TPR spectra of  $N_2H_4$ ,  $NH_3$ ,  $N_2$  and  $H_2$  gases from different initial  $N_2H_4$  coverages. The TPR plots show desorption of species from the surface as the temperature increases. The desorption peaks therefore show the

temperature at which the molecules has the highest desorption rate. As **Figure 7.4** shows, different initial  $\text{N}_2\text{H}_4$  coverages do not change the temperature of the maximum desorption rate. **Figure 7.4** in conjunction with **Figure 7.5** relates the pressures of desorbed gases and the coverages of the most abundant species on the surface, *i.e.*  $\text{N}_2\text{H}_4$ ,  $\text{N}_2\text{H}_3$  and  $\text{NH}_3$ , as a function of temperature. **Figure 7.4.a** indicates that  $\text{N}_2\text{H}_4$  desorption takes place at around 213 K, similarly to the desorption peak on a Rh foil surface (Prasad and Gland, 1991a). As **Figure 7.5.b** shows  $\text{N}_2\text{H}_4$  disappears completely from the surface at around 220 K by desorbing or converting to such species as  $\text{N}_2\text{H}_3$  and  $\text{NH}_3$ , which desorbs quickly from the surface ( $k_2 \sim 10^8 \text{ s}^{-1}$ ). The high amount of  $\text{N}_2\text{H}_3$  on the surface between 200 – 300 K (**Figure 7.5.b**) and desorbed  $\text{NH}_3$  from the surface, *i.e.* the first peak of  $\text{NH}_3$  TPR at 211 K (**Figure 7.4.b**), indicate that an inter-molecular dehydrogenation mechanism is taking place. It produces  $\text{NH}_2$  from N–N decoupling of another  $\text{N}_2\text{H}_4$  interacting with  $\text{N}_2\text{H}_4$  molecule (R38) which, at this low temperature, is feasible from kinetic and thermodynamic points of view. This reaction is the most favoured step in the temperature range of 200 – 265 K where the  $\text{N}_2\text{H}_3$  coverage increases. However, at higher temperatures, the  $\text{N}_2\text{H}_3$  coverage decreases by reacting with  $\text{NH}_2$  intermediates, losing hydrogen atoms (R40, R42, R44, R46 and R48) and resulting in the formation of other species, *i.e.* the  $\text{NH}_3$  peak at 284 K (**Figure 7.4.b**).

The  $\text{N}_2$  and  $\text{H}_2$  have three desorption peaks, two smaller peaks at around 219 and 440 K and a maximum desorption peak at 284 K. The  $\text{N}_2$  and  $\text{H}_2$  desorption peaks at ~ 219 K are due to the recombination of H and N ad-atoms on the surface produced by decomposition of intermediates. The maximum  $\text{N}_2$  and  $\text{H}_2$  desorption peaks at around 284 K, which appear at the same temperature as the second  $\text{NH}_3$  desorption peak, are due to reactions of inter-molecular dehydrogenation, resulting in

production of NNH and reaction between NNH and  $\text{NH}_2$  (R48) as well as NNH decomposition (R18). The smaller peaks at higher temperature correspond to the recombination of atomic H and N following the decomposition reactions of NH to N and H on the surface (R34). NH is stable on the surface until 450 K, as shown in **Figure 7.5.b**, in line with other studies of hydrazine dissociation on Ni (Gland *et al.*, 1985), Rh (Prasad and Gland, 1991b).

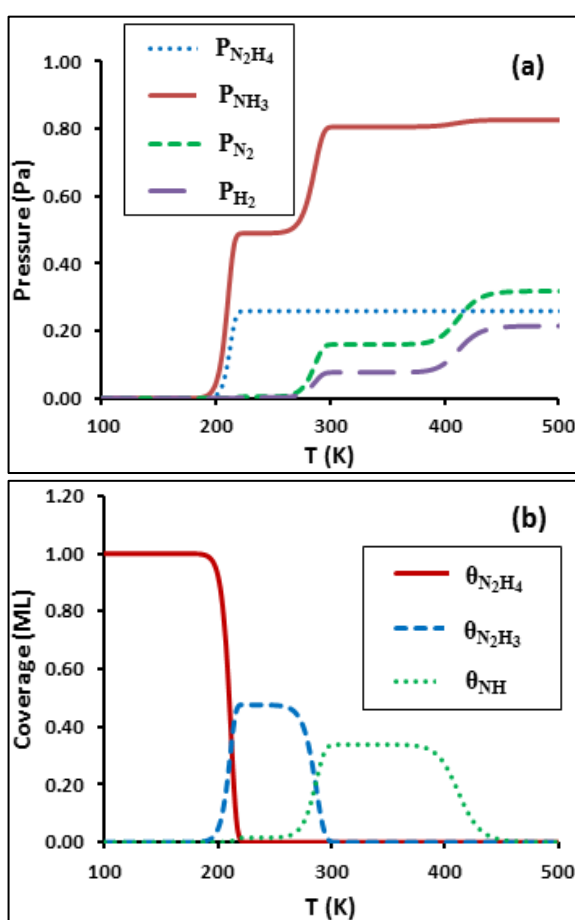


**Figure 7.5.** (a) The partial pressure of desorbed  $\text{N}_2\text{H}_4$ ,  $\text{NH}_3$ ,  $\text{N}_2$  and  $\text{H}_2$  gases and (b) surface coverage of  $\text{N}_2\text{H}_4$ ,  $\text{N}_2\text{H}_3$  and NH as a function of temperature with an initial  $\text{N}_2\text{H}_4$  full coverage in the TPR simulation at a reaction time of 1s with a 1K/min heating rate.

**Figure 7.6** reports the spectra of gases produced during the TPR, at an initial condition of a full coverage of  $\text{N}_2\text{H}_4$ , for a temperature range from 100 to 600 K and with three heating rates of 1, 5 and 8 K/min. As the heating rate increases, so does

the temperature at which the desorption rate is at the maximum (peak temperature), whereas the intensity of the peak increases as well, in agreement with an experimental TPD study of hydrazine decomposition on an  $\text{Al}_2\text{O}_3$ -supported Ir catalyst (Falconer and Wise, 1976). These changes, peak temperature and intensity, are related to a sudden variation of the pressures and the derivative slope. The higher the heating rate, the more abrupt are the changes in pressure and the higher the slope of  $\frac{\delta P}{\delta T}$ . Note the abrupt desorption of  $\text{N}_2\text{H}_4$  reduces the time for further reaction on the surface to produce  $\text{NH}_3$ ,  $\text{N}_2$  and  $\text{H}_2$ , indicating that a slower heating rate helps to increase the yield of  $\text{NH}_3$ ,  $\text{N}_2$  and  $\text{H}_2$ , **Figure 7.7**.

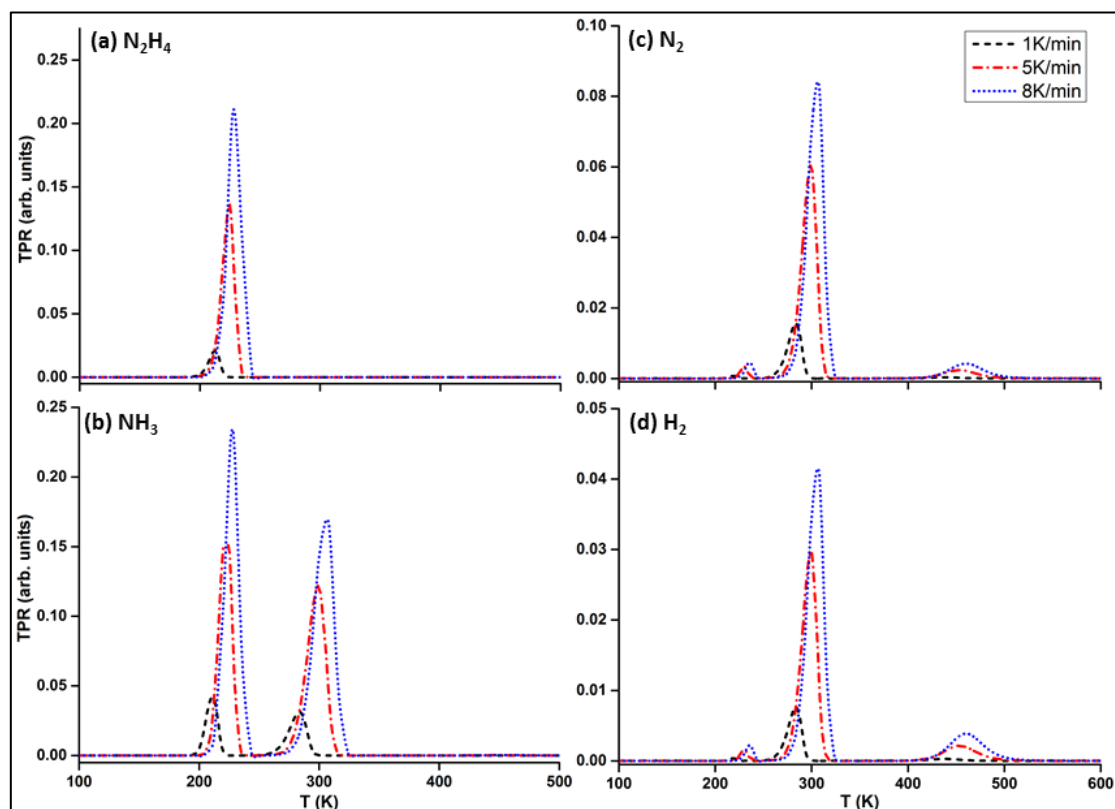


**Figure 7.6.** Simulated TPR curves for  $\text{N}_2\text{H}_4$ ,  $\text{NH}_3$ ,  $\text{N}_2$  and  $\text{H}_2$  desorption from Cu(111) surface starting from an initial  $\text{N}_2\text{H}_4$  coverage of 1 ML (full coverage) at reaction time of 1s for different heating rates.

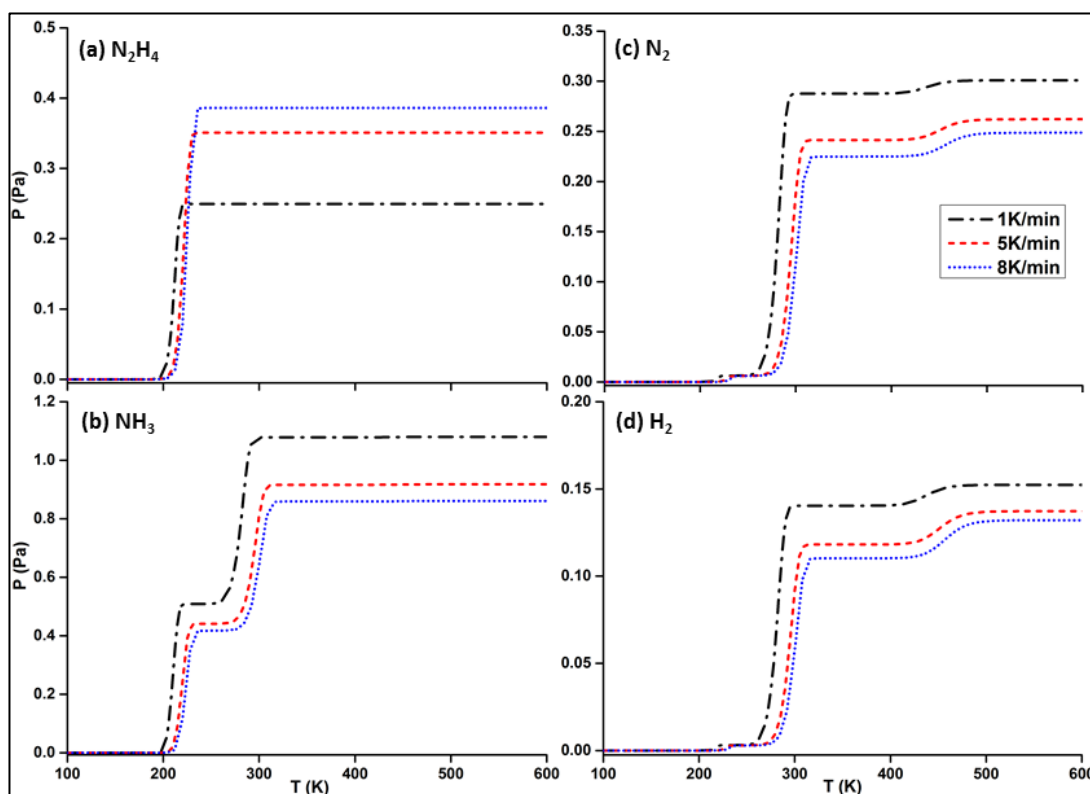


**Figure 7.7.**  $\text{N}_2\text{H}_4$ ,  $\text{NH}_3$ ,  $\text{N}_2$  and  $\text{H}_2$  evolution from Cu(111) surface as a function of temperature for an initial  $\text{N}_2\text{H}_4$  coverage of 1 ML (full coverage) in the TPR simulation at reaction time of 1s for different heating rates.

The composition of the reaction gas at different temperatures as a result of the hydrazine interacting with the Cu(111) surface is given in **Table 7.4** and is in agreement with the experimental report by Al-Haydari *et al.* (Alhaydari *et al.*, 1985).  $\text{NH}_3$  is the main and  $\text{H}_2$  is the least present gaseous product of the hydrazine decomposition. According to experiment, the temperature at which hydrazine starts to decompose is 303 K when  $\text{NH}_3$ ,  $\text{N}_2$  and some  $\text{H}_2$  desorb from the Cu film. In our simulation, as shown in **Figure 7.6**, hydrazine starts to decompose at around 190 K, when the first  $\text{NH}_3$  can be observed, while  $\text{N}_2$  and  $\text{H}_2$  desorb at higher temperature of 219 K. This discrepancy between experiment and simulation may be due to the adsorption of gases in liquid hydrazine, as well as the use of an experimental Cu film without well-defined Cu surfaces, which will include defects. Our previous works in

the Chapters 3 and 4 have shown that the introduction of defects on the surface provides more favourable sites for stronger hydrazine adsorption, resulting in higher temperatures for decomposition and desorption (Tafreshi *et al.*, 2014b; Tafreshi *et al.*, 2014a). Moreover, the heating rate and the reaction time of the experimental study were not reported.

**Table 7.4.** Percentage of composition of gaseous products throughout the hydrazine decomposition on Cu(111) surface from an initial  $N_2H_4$  full coverage in the TPR simulation at a reaction time of 1s with a 1K/min heating rate at different temperatures in comparison with experimental reports (Alhaydari *et al.*, 1985).

T (K)	NH <sub>3</sub> (%)		N <sub>2</sub> (%)		H <sub>2</sub> (%)	
	This work	Ref. <sup>A</sup>	This work	Ref. <sup>A</sup>	This work	Ref. <sup>A</sup>
<b>303</b>	77.28	75.60	15.33	18.75	7.38	5.62
<b>333</b>	77.28	72.63	15.34	22.93	7.39	4.58
<b>363</b>	77.23	69.49	15.36	27.23	7.41	3.25
<b>393</b>	75.25	69.56	16.37	27.34	8.38	3.10

<sup>A</sup>(Alhaydari *et al.*, 1985)

### 7.3.2. Batch reactor simulation

The microkinetic simulation of a batch reactor, discussed in this section, considers all elementary steps in **Table 7.2** and starts from a situation where the naked Cu surface is exposed to  $N_2H_4$  gas. We have carried out the microkinetic simulations of hydrazine decomposition at a small initial  $N_2H_4$  pressure of 6 Pa in the temperature range of 100 – 800 K. The corresponding differential equations are listed in the Appendix.

We have represented the pressure of  $N_2H_4$ ,  $NH_3$ ,  $N_2$  and  $H_2$  as a function of the temperature and the reaction time in 3D plots (**Figure 7.8**). They show that at 100 K  $N_2H_4$  adsorbs very quickly, in less than 1s, on the surface, which fully covered by  $N_2H_4$  molecules. The decomposition of the  $N_2H_4$  molecules on the surface starts at around 200 K and the  $N_2H_4$  molecules still in the gas phase can occupy the resulting

empty sites on the surface.  $\text{N}_2\text{H}_4$  pressure reaches an equilibrium state at around 300 K, when its pressure decreases below 0.1 Pa. The  $\text{NH}_3$  starts to desorb from the Cu(111) surface at around 200 K, while  $\text{N}_2$  and  $\text{H}_2$  appear in the gas phase at the higher temperature of 220 K.  $\text{NH}_3$  and  $\text{N}_2$  desorption reach equilibrium at around 300 K, with pressures of 7.5 and 2.1 Pa respectively, and any increase in the temperature does not further affect their desorption. The  $\text{H}_2$  pressure increases with increasing temperature up to 300 K (0.38 Pa), then decreases to 0.33 Pa at 370 K, where it reaches equilibrium.

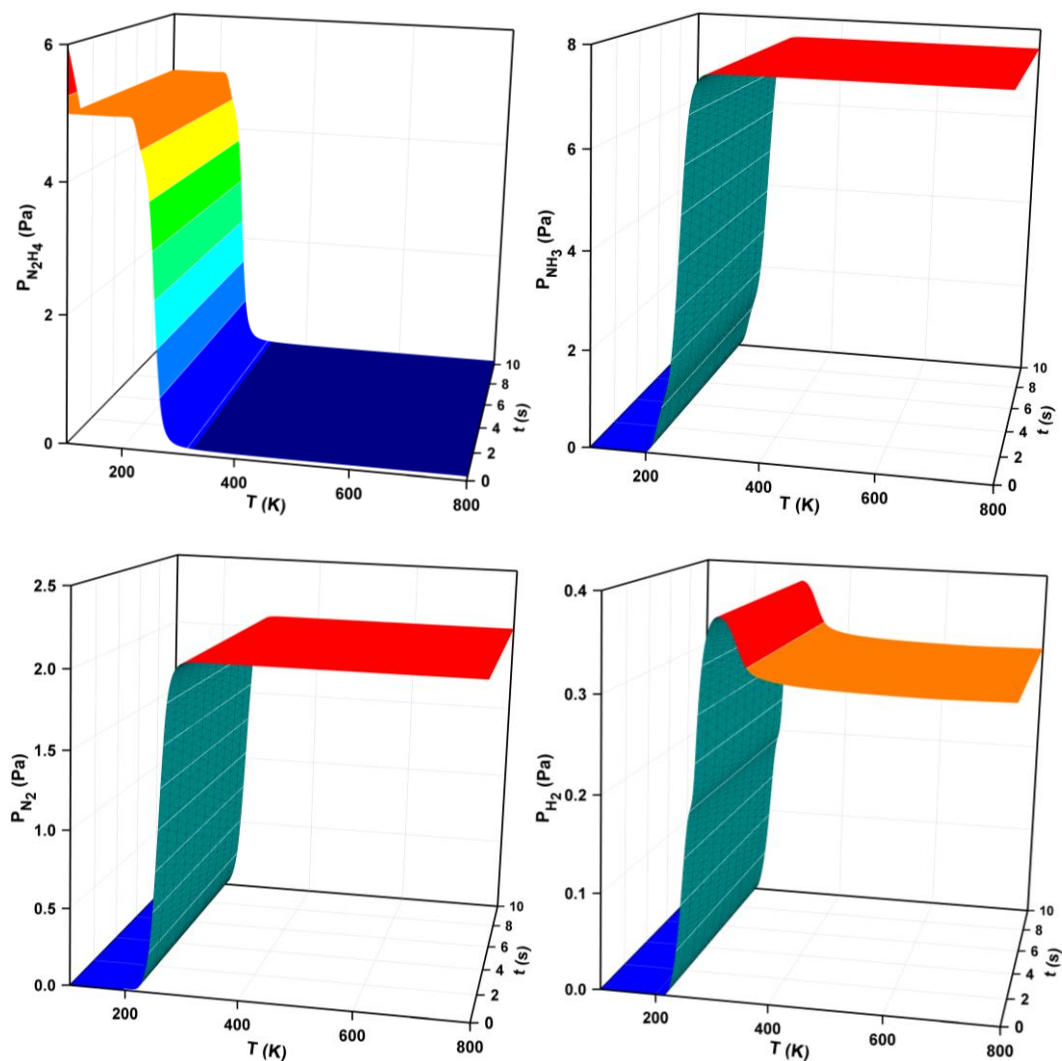


**Figure 7.8.**  $N_2H_4$ ,  $NH_3$ ,  $N_2$  and  $H_2$  evolution from Cu(111) surface as a function of temperature and time for an initial  $N_2H_4$  pressure of 6 Pa with a 1K/min heating rate in the batch reactor simulation.

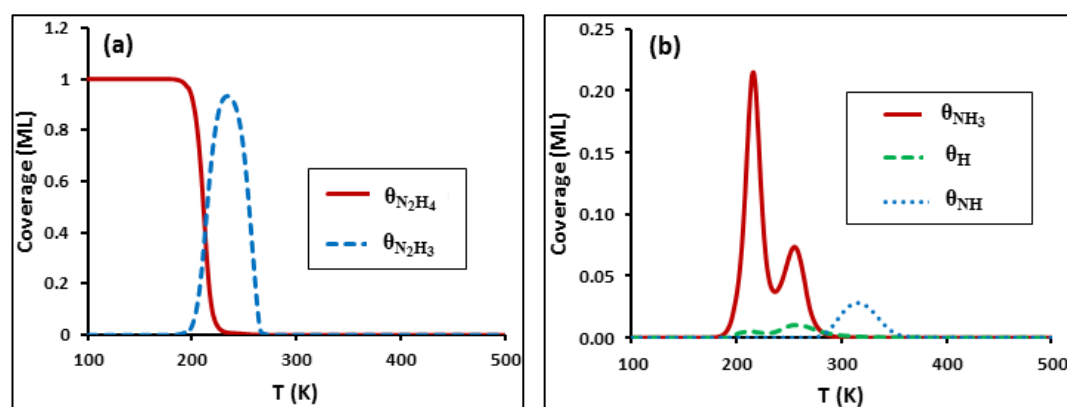


**Figure 7.9.** The surface coverage of (a)  $N_2H_4$  and  $N_2H_3$ , (b)  $NH_3$ , H and NH as a function of temperature with an initial  $N_2H_4$  pressure of 6 Pa, in the batch reactor simulation at a reaction time of 1s with a 1K/min heating rate.

To understand the  $\text{N}_2\text{H}_4$  overall decomposition mechanisms, the coverage of some intermediates is plotted in **Figure 7.9** showing how the coverages of  $\text{N}_2\text{H}_4$ ,  $\text{N}_2\text{H}_3$ ,  $\text{NH}_3$ , H and NH change with temperature at a reaction time of 1s after the surface was covered fully with adsorbed  $\text{N}_2\text{H}_4$ .

The observed trends for the coverages of  $\text{N}_2\text{H}_4$ ,  $\text{N}_2\text{H}_3$  and NH in the batch reactor simulation are the same as those in the TPR simulation, although the coverages of the species are different owing to the quick adsorption of  $\text{N}_2\text{H}_4$  on the naked Cu surface. The hydrazine N–N decoupling (R20) is again the most preferred reaction among the ones studied due to a lower energy barrier. The produced  $\text{NH}_2$  intermediate attacks another intact hydrazine molecule and subtracts one of its hydrogens, resulting in the production of  $\text{NH}_3$  and  $\text{N}_2\text{H}_3$  molecules on the Cu(111) surface (R38), which is an exothermic reaction ( $E_r = -0.36$  eV) with low energy barrier of 0.42 eV. **Figure 7.9.a** shows that as soon as the coverage of  $\text{N}_2\text{H}_4$  molecules on the surface starts to decrease, the coverage of the  $\text{N}_2\text{H}_3$  intermediates starts to increase until all  $\text{N}_2\text{H}_4$  is converted to  $\text{N}_2\text{H}_3$  and  $\text{NH}_3$  at 230 K when, almost the entire surface is covered with  $\text{N}_2\text{H}_3$  and some  $\text{NH}_3$  molecules, which desorb quickly from the surface.  $\text{N}_2\text{H}_3$  is stable on the surface in the temperature range of 190 – 265 K. The coverage of  $\text{NH}_3$ , **Figure 7.9.b**, starts to decrease when the temperature reaches 215 K and  $\text{NH}_3$  has obtained enough energy to desorb from the surface. The  $\text{NH}_2$  present on the surface, obtained from the  $\text{H}_2\text{N}-\text{NH}_2$  band breaking, attacks  $\text{N}_2\text{H}_3$  (R40 and R42) in a mechanism of inter-molecular dehydrogenation, resulting in a decrease in the  $\text{N}_2\text{H}_3$  coverage at around 230 K, also leading to other species on the surface.

The existence of H atoms on the surface in the temperature range of 200 – 350 K (**Figure 7.9.b**) indicates the dehydrogenation of species in this temperature range

with reaction energy barriers higher than 1.2 eV (R8, R10, R12, R14 and R16). The production of NH from the dehydrogenation of NH<sub>3</sub> and NH<sub>2</sub> on the surface (R30 and R32) takes place at temperatures higher than 270 K, because of an even higher energy barrier of 1.40 eV, which results in the observed NH peak in **Figure 7.9.b** centred at 315 K. From here, the NH coverage starts to decrease via decomposition to N and H atoms on the surface, (R34) with an energy barrier of 1.79 eV. The fact that NH is stable during hydrazine decomposition in the temperature range of 270 – 370 K is in line with the experimental work by Gland *et al.*, where they showed that NH is stable during hydrazine decomposition on the Ni(111) surface in the 285 to 365 K temperature range (Gland *et al.*, 1985), as well as on Ru (Rauscher *et al.*, 1993), Rh (Prasad and Gland, 1991b; Daniel and White, 1986), Ir (Wood and Wise, 1975b), W (Cosser and Tompkins, 1971a) and Mo (Contaminard and Tompkins, 1971) surfaces.

The associative desorption of H atoms, produced by dehydrogenation, results in the peak centred at ~ 300 K, shown in **Figure 7.8**. The highly endothermic reaction between N<sub>2</sub> and H on the surface (R19), with an energy barrier of 1.79 eV, could only occur at high temperatures, and leads to a decrease of H<sub>2</sub> pressure at around 300 K, shown in **Figure 7.8**, due to dissociative adsorption of H<sub>2</sub> in order to provide enough H atoms on the surface.

We have also examined the N<sub>2</sub>H<sub>4</sub> conversion and NH<sub>3</sub>, N<sub>2</sub> and H<sub>2</sub> selectivities at a fixed temperature of 350 K as a function of initial N<sub>2</sub>H<sub>4</sub> pressure, varied from 10<sup>-6</sup> to 100 Pa, shown in **Figure 7.10.a**. The system reaches the highest NH<sub>3</sub> selectivity of 81.92 % for an initial N<sub>2</sub>H<sub>4</sub> pressure of 0.1 Pa, the N<sub>2</sub> selectivity reaches its maximum (36.27 %) at  $P_{N_2H_4} = 100\text{Pa}$ , and the maximum H<sub>2</sub> selectivity (5.38 %)

occurs for an initial  $N_2H_4$  pressure of 0.001 Pa.  $N_2H_4$  conversion is complete for  $P_{N_2H_4} \leq 10$  Pa.

**Figure 7.10.b** plots the  $N_2H_4$  conversion and  $NH_3$ ,  $N_2$  and  $H_2$  selectivities with temperature in an initial  $N_2H_4$  pressure of 6 Pa. The  $N_2H_4$  conversion reaches its maximum at  $\sim 330$  K (98.5%), while  $NH_3$ ,  $N_2$  and  $H_2$  selectivities converge to 64.5 %, 35.1 % and 2.63 % respectively at around 265 K.

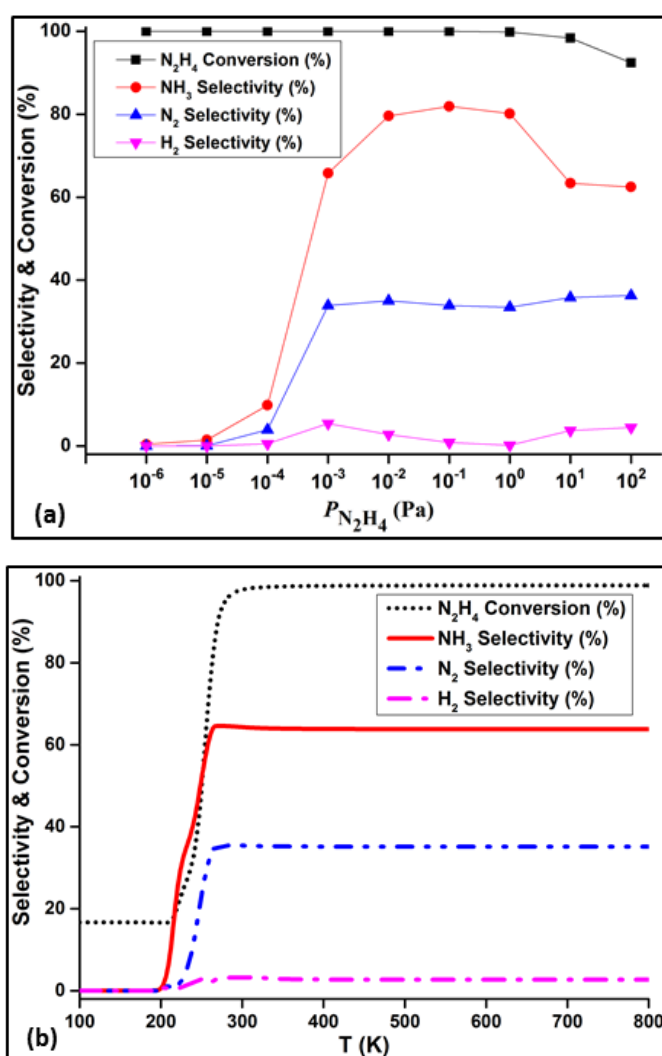


**Figure 7.10.**  $N_2H_4$  conversion and  $NH_3$ ,  $N_2$  and  $H_2$  selectivities as a function of (a) initial  $N_2H_4$  pressure at 350 K, (b) temperature with an initial  $N_2H_4$  pressure of 6 Pa in the batch reactor simulation at a reaction time of 1s with a 1K/min heating rate.

## 7.4. Conclusions

A microkinetic model based on density functional theory calculations was established, taking into account adsorption, desorption and reaction processes of all the reactants, intermediates and products, to simulate  $\text{N}_2\text{H}_4$  decomposition on the Cu(111) surface. Two simulation models have been considered; the first model started from a situation of pre-adsorbed  $\text{N}_2\text{H}_4$  and considered a constant removal of gases from the reactor, *i.e.* simulating TPR spectra. In the second model we have considered a naked Cu(111) surface in contact with  $\text{N}_2\text{H}_4$ , where all the gaseous products from the  $\text{N}_2\text{H}_4$  decomposition are allowed to adsorb and desorb freely until the system reaches equilibrium in the batch reactor. The simulated TPR shows that gas desorption peaks depend on the heating rate and initial  $\text{N}_2\text{H}_4$  coverage. The simulations of the batch reactor show that  $\text{NH}_3$  and  $\text{N}_2$  are the major gaseous products, in agreement with experiment. The coverage of intermediates with temperature shows that  $\text{N}_2\text{H}_3$  and  $\text{NH}$  are the most stable intermediates on the surface during  $\text{N}_2\text{H}_4$  decomposition in the batch reactor simulation in the 190 – 265 and 270 – 370 K temperature ranges, respectively. Temperature and initial  $\text{N}_2\text{H}_4$  pressures affect the  $\text{N}_2\text{H}_4$  conversion and  $\text{NH}_3$ ,  $\text{N}_2$  and  $\text{H}_2$  selectivities. The highest  $\text{NH}_3$ ,  $\text{N}_2$  and  $\text{H}_2$  selectivities obtained in the simulation at 350 K are 81.92 %, 36.27 % and 5.38 %, respectively, and in the simulation with an initial  $\text{N}_2\text{H}_4$  pressure of 6 Pa, the  $\text{N}_2\text{H}_4$  conversion converges to 98.5 % at 330 K while  $\text{NH}_3$ ,  $\text{N}_2$  and  $\text{H}_2$  selectivities reach convergence of 64.5 %, 35.1 % and 2.63 %, respectively, at 265 K. This study, whose findings are in line with available experiment shows that microkinetic simulation is an effective tool to predict the conditions for the production of ammonia, nitrogen and hydrogen gases from the heterogeneous catalytic

decomposition of hydrazine on Cu surfaces. This method can now be further rolled out to alternative systems.

## *Chapter 8: Conclusions and future works*

In this thesis, we have presented a comprehensive computational study of the structure of low-index Cu surfaces, the subsequent molecular adsorption of single hydrazine on the perfect and defective Cu surfaces, the formation of a hydrazine network on Cu surfaces, as well as thermodynamic and microkinetic investigations of hydrazine dissociation mechanisms on the Cu surfaces, using first principles methods based on the density functional theory.

In the first part of this thesis, we have modelled the interaction of a single hydrazine molecule with perfect Cu(111), (100) and (110) surfaces using a dispersion corrected density functional theory (DFT-D2) method. Energy minimization calculations of the hydrazine adsorption on Cu show that the hydrazine molecule interacts more strongly with the (110) surface, bridging through both N atoms to the surface, while the (111) surface offers the weakest adsorption to the molecule. The van der Waals interactions are found to play an important role in stabilizing the hydrazine molecule at the surface, which leads to stronger bonds between Cu and N atoms, thereby inclining the molecule to the surface in bridging modes. In future studies, it would be worth using other dispersion corrected DFT methods like DFT-D3 which is the latest dispersion method by Grimme to evaluate how this affects the hydrazine–Cu system compared with the DFT-D2 results.

We have studied the geometries of three types of defects including adatom, vacancies and steps on the Cu(111), (100) and (110) surfaces. Subsequent hydrazine adsorption on these surfaces shows that the strongest adsorption energy is found on the stepped

(110) surface where atoms with lower coordination numbers (CN) provide sites with d-band centres closer to the Fermi level, which allows stronger binding. Our calculations reveal that although the (110) surface contains a number of low-coordinated atoms that enhance the surface-molecule interactions, the addition of defects on the more stable (111) and (100) surfaces provides sites that enable hydrazine binding to almost the same extent. The cooperative adsorption of water and hydrazine at perfect and defective copper surfaces is worth investigating in future studies.

Our results from the study of the assembly of hydrazine networks adsorbed on the Cu(111) surface show that the binding of the molecules to the surface is the main interaction driving the network formation, arising mostly from long-range interactions. The results also revealed that vdW forces are the largest contributors to the molecule-molecule interactions, compared with hydrogen-bonding interactions which have the least contribution. Charge density difference calculations showed that the molecule and substrate share electrons, while no charge transfer was observed between molecules. We have also investigated the surface energy as a function of hydrazine concentration, indicating that variation in the hydrazine coverage on the Cu(111) affects the shapes of the copper nanoparticles through Cu(111), and further investigation of other Cu facets of the nanoparticles is therefore required to obtain the effect of hydrazine coverage on Cu nanoparticles' morphology. Temperature programmed desorption (TPD) of hydrazine from the Cu(111) surface was simulated for different hydrazine coverages, showing a desorption peak between 150 and 200 K, which is comparable to similar studies of the desorption temperatures for hydrazine at other surfaces.

The results from the study of the  $\text{N}_2\text{H}_4$  decomposition mechanisms on the flat and stepped Cu(111) surfaces reveal that  $\text{N}_2\text{H}_4$  dehydrogenation is kinetically an unlikely process to occur on either flat or stepped Cu(111) surfaces, but that N–N decoupling is energetically feasible, leading to  $\text{NH}_2$  intermediates. The inter-molecular dehydrogenation reaction is the predominant mechanism between either  $\text{NH}_2$  fragments on the flat surface, or  $\text{NH}_2$  and  $\text{N}_2\text{H}_x$  ( $x=1-4$ ) intermediates on both the flat and stepped surfaces, leading to the formation of  $\text{N}_2$  and  $\text{NH}_3$ . The produced amide and imide intermediates are hydrogenated to  $\text{NH}_3$  in the presence of hydrogen, which competes with the recombination of H atoms leading to  $\text{H}_2$  molecules. We also found that, while the introduction of low-coordinated atoms *e.g.* on the step edge on the surface, increases the barrier of N–N decoupling along the reaction pathway, it has different effects on the barriers of the reactions of intra- and inter-molecular dehydrogenation mechanisms. Future theoretical extensions to this work could include investigation of other possible reactions and mechanisms of hydrazine decomposition on Cu surfaces.

A microkinetic study was carried out taking into account adsorption, desorption and reaction processes of all the reactants, intermediates and products in simulations to predict the conditions for the production of ammonia, nitrogen and hydrogen gases from the heterogeneous catalytic decomposition of hydrazine on Cu surfaces under both temperature programmed reaction (TPR) and batch reactor conditions. The simulated TPR showed that gas desorption peaks depend on the heating rate and initial  $\text{N}_2\text{H}_4$  coverage. The simulations of the batch reactor showed that  $\text{NH}_3$  and  $\text{N}_2$  are the major gaseous products, in agreement with experiment. The coverage of intermediates with respect to temperature showed that  $\text{N}_2\text{H}_3$  and  $\text{NH}$  are the most stable intermediates on the surface during  $\text{N}_2\text{H}_4$  decomposition. Temperature and

initial  $\text{N}_2\text{H}_4$  pressures affect the  $\text{N}_2\text{H}_4$  conversion and  $\text{NH}_3$ ,  $\text{N}_2$  and  $\text{H}_2$  selectivities. In future work, microkinetics modelling of defective Cu surfaces could be investigated in order to evaluate the effect of the presence of defects on the conditions required for the production of  $\text{NH}_3$ ,  $\text{N}_2$  and  $\text{H}_2$  gases from the catalytic decomposition of hydrazine on Cu. The interesting catalytic activities of Cu towards hydrazine should stimulate experimental efforts to explore the potential of Cu for applications in environmental catalysis.

# Appendix

The following are the rate equations of the elementary reactions applied in the simulations of hydrazine decomposition on the Cu(111) surface.

$$r_0(t) = \frac{A}{\sqrt{2\pi m_{N_2H_4} k_B T}} \frac{q_0^{TS}}{q_0^{IS}} e^{-\frac{E_0^a}{k_B T}} P_{N_2H_4}(t) \theta_*(t)$$

$$r_1(t) = \frac{k_B T}{h} \frac{q_1^{TS}}{q_1^{IS}} e^{-\frac{E_1^a}{k_B T}} \theta_{N_2H_4}(t)$$

$$r_2(t) = \frac{k_B T}{h} \frac{q_2^{TS}}{q_2^{IS}} e^{-\frac{E_2^a}{k_B T}} \theta_{NH_3}(t)$$

$$r_3(t) = \frac{A}{\sqrt{2\pi m_{NH_3} k_B T}} \frac{q_3^{TS}}{q_3^{IS}} e^{-\frac{E_3^a}{k_B T}} P_{NH_3}(t) \theta_*(t)$$

$$r_4(t) = \frac{k_B T}{h} \frac{q_4^{TS}}{q_4^{IS}} e^{-\frac{E_4^a}{k_B T}} \theta_{N_2}(t)$$

$$r_5(t) = \frac{A}{\sqrt{2\pi m_{N_2} k_B T}} \frac{q_5^{TS}}{q_5^{IS}} e^{-\frac{E_5^a}{k_B T}} P_{N_2}(t) \theta_*(t)$$

$$r_6(t) = \frac{k_B T}{h} \frac{q_6^{TS}}{q_6^{IS}} e^{-\frac{E_6^a}{k_B T}} \theta_H^2(t)$$

$$r_7(t) = \frac{A}{\sqrt{2\pi m_{H_2} k_B T}} \frac{q_7^{TS}}{q_7^{IS}} e^{-\frac{E_7^a}{k_B T}} P_{H_2}(t) \theta_*(t)$$

$$r_8(t) = \frac{k_B T}{h} \frac{q_8^{TS}}{q_8^{IS}} e^{-\frac{E_8^a}{k_B T}} \theta_{N_2H_4}(t)$$

$$r_9(t) = \frac{k_B T}{h} \frac{q_9^{TS}}{q_9^{IS}} e^{-\frac{E_9^a}{k_B T}} \theta_{N_2H_3}(t) \theta_H(t)$$

$$r_{10}(t) = \frac{k_B T}{h} \frac{q_{10}^{TS}}{q_{10}^{IS}} e^{-\frac{E_{10}^a}{k_B T}} \theta_{N_2H_3}(t)$$

$$r_{11}(t) = \frac{k_B T}{h} \frac{q_{11}^{TS}}{q_{11}^{IS}} e^{-\frac{E_{11}^a}{k_B T}} \theta_{NNH_2}(t) \theta_H(t)$$

$$r_{12}(t) = \frac{k_B T}{h} \frac{q_{12}^{TS}}{q_{12}^{IS}} e^{-\frac{E_{12}^a}{k_B T}} \theta_{N_2H_3}(t)$$

$$r_{13}(t) = \frac{k_B T}{h} \frac{q_{13}^{TS}}{q_{13}^{IS}} e^{-\frac{E_{13}^a}{k_B T}} \theta_{NHNH}(t) \theta_H(t)$$

$$r_{14}(t) = \frac{k_B T}{h} \frac{q_{14}^{TS}}{q_{14}^{IS}} e^{-\frac{E_{14}^a}{k_B T}} \theta_{NNH_2}(t)$$

$$r_{15}(t) = \frac{k_B T}{h} \frac{q_{15}^{TS}}{q_{15}^{IS}} e^{-\frac{E_{15}^a}{k_B T}} \theta_{NNH}(t) \theta_H(t)$$

$$r_{16}(t) = \frac{k_B T}{h} \frac{q_{16}^{TS}}{q_{16}^{IS}} e^{-\frac{E_{16}^a}{k_B T}} \theta_{NHNH}(t)$$

$$r_{17}(t) = \frac{k_B T}{h} \frac{q_{17}^{TS}}{q_{17}^{IS}} e^{-\frac{E_{17}^a}{k_B T}} \theta_{NNH}(t) \theta_H(t)$$

$$r_{18}(t) = \frac{k_B T}{h} \frac{q_{18}^{TS}}{q_{18}^{IS}} e^{-\frac{E_{18}^a}{k_B T}} \theta_{NNH}(t)$$

$$r_{19}(t) = \frac{k_B T}{h} \frac{q_{19}^{TS}}{q_{19}^{IS}} e^{-\frac{E_{19}^a}{k_B T}} \theta_{N_2}(t) \theta_H(t)$$

$$r_{20}(t) = \frac{k_B T}{h} \frac{q_{20}^{TS}}{q_{20}^{IS}} e^{-\frac{E_{20}^a}{k_B T}} \theta_{N_2H_4}(t)$$

$$r_{21}(t) = \frac{k_B T}{h} \frac{q_{21}^{TS}}{q_{21}^{IS}} e^{-\frac{E_{21}^a}{k_B T}} \theta_{NH_2}^2(t)$$

$$r_{22}(t) = \frac{k_B T}{h} \frac{q_{22}^{TS}}{q_{22}^{IS}} e^{-\frac{E_{22}^a}{k_B T}} \theta_{N_2H_3}(t)$$

$$r_{23}(t) = \frac{k_B T}{h} \frac{q_{23}^{TS}}{q_{23}^{IS}} e^{-\frac{E_{23}^a}{k_B T}} \theta_{NH_2}(t) \theta_{NH}(t)$$

$$r_{24}(t) = \frac{k_B T}{h} \frac{q_{24}^{TS}}{q_{24}^{IS}} e^{-\frac{E_{24}^a}{k_B T}} \theta_{NNH_2}(t)$$

$$r_{25}(t) = \frac{k_B T}{h} \frac{q_{25}^{TS}}{q_{25}^{IS}} e^{-\frac{E_{25}^a}{k_B T}} \theta_{NH_2}(t) \theta_N(t)$$

$$r_{26}(t) = \frac{k_B T}{h} \frac{q_{26}^{TS}}{q_{26}^{IS}} e^{-\frac{E_{26}^a}{k_B T}} \theta_{NHNH}(t)$$

$$r_{27}(t) = \frac{k_B T}{h} \frac{q_{27}^{TS}}{q_{27}^{IS}} e^{-\frac{E_{27}^a}{k_B T}} \theta_{NH}^2(t)$$

$$r_{28}(t) = \frac{k_B T}{h} \frac{q_{28}^{TS}}{q_{28}^{IS}} e^{-\frac{E_{28}^a}{k_B T}} \theta_{NNH}(t)$$

$$r_{29}(t) = \frac{k_B T}{h} \frac{q_{29}^{TS}}{q_{29}^{IS}} e^{-\frac{E_{29}^a}{k_B T}} \theta_{NH}(t) \theta_N(t)$$

$$r_{30}(t) = \frac{k_B T}{h} \frac{q_{30}^{TS}}{q_{30}^{IS}} e^{-\frac{E_{30}^a}{k_B T}} \theta_{NH_3}(t)$$

$$r_{31}(t) = \frac{k_B T}{h} \frac{q_{31}^{TS}}{q_{31}^{IS}} e^{-\frac{E_{31}^a}{k_B T}} \theta_{NH_2}(t) \theta_H(t)$$

$$r_{32}(t) = \frac{k_B T}{h} \frac{q_{32}^{TS}}{q_{32}^{IS}} e^{-\frac{E_{32}^a}{k_B T}} \theta_{NH_2}(t)$$

$$r_{33}(t) = \frac{k_B T}{h} \frac{q_{33}^{TS}}{q_{33}^{IS}} e^{-\frac{E_{33}^a}{k_B T}} \theta_{NH}(t) \theta_H(t)$$

$$r_{34}(t) = \frac{k_B T}{h} \frac{q_{34}^{TS}}{q_{34}^{IS}} e^{-\frac{E_{34}^a}{k_B T}} \theta_{NH}(t)$$

$$r_{35}(t) = \frac{k_B T}{h} \frac{q_{35}^{TS}}{q_{35}^{IS}} e^{-\frac{E_{35}^a}{k_B T}} \theta_N(t) \theta_H(t)$$

$$r_{36}(t) = \frac{k_B T}{h} \frac{q_{36}^{TS}}{q_{36}^{IS}} e^{-\frac{E_{36}^a}{k_B T}} \theta_{NH_2}^2(t)$$

$$r_{37}(t) = \frac{k_B T}{h} \frac{q_{37}^{TS}}{q_{37}^{IS}} e^{-\frac{E_{37}^a}{k_B T}} \theta_{NH}(t) \theta_{NH_3}(t)$$

$$r_{38}(t) = \frac{k_B T}{h} \frac{q_{38}^{TS}}{q_{38}^{IS}} e^{-\frac{E_{38}^a}{k_B T}} \theta_{N_2H_4}(t) \theta_{NH_2}(t)$$

$$r_{39}(t) = \frac{k_B T}{h} \frac{q_{39}^{TS}}{q_{39}^{IS}} e^{-\frac{E_{39}^a}{k_B T}} \theta_{N_2H_3}(t) \theta_{NH_3}(t)$$

$$r_{40}(t) = \frac{k_B T}{h} \frac{q_{40}^{TS}}{q_{40}^{IS}} e^{-\frac{E_{40}^a}{k_B T}} \theta_{N_2H_3}(t) \theta_{NH_2}(t)$$

$$r_{41}(t) = \frac{k_B T}{h} \frac{q_{41}^{TS}}{q_{41}^{IS}} e^{-\frac{E_{41}^a}{k_B T}} \theta_{NHNH}(t) \theta_{NH_3}(t)$$

$$r_{42}(t) = \frac{k_B T}{h} \frac{q_{42}^{TS}}{q_{42}^{IS}} e^{-\frac{E_{42}^a}{k_B T}} \theta_{N_2H_3}(t) \theta_{NH_2}(t)$$

$$r_{43}(t) = \frac{k_B T}{h} \frac{q_{43}^{TS}}{q_{43}^{IS}} e^{-\frac{E_{43}^a}{k_B T}} \theta_{NNH_2}(t) \theta_{NH_3}(t)$$

$$r_{44}(t) = \frac{k_B T}{h} \frac{q_{44}^{TS}}{q_{44}^{IS}} e^{-\frac{E_{44}^a}{k_B T}} \theta_{NHNH}(t) \theta_{NH_2}(t)$$

$$r_{45}(t) = \frac{k_B T}{h} \frac{q_{45}^{TS}}{q_{45}^{IS}} e^{-\frac{E_{45}^a}{k_B T}} \theta_{NNH}(t) \theta_{NH_3}(t)$$

$$r_{46}(t) = \frac{k_B T}{h} \frac{q_{46}^{TS}}{q_{46}^{IS}} e^{-\frac{E_{46}^a}{k_B T}} \theta_{NNH_2}(t) \theta_{NH_2}(t)$$

$$r_{47}(t) = \frac{k_B T}{h} \frac{q_{47}^{TS}}{q_{47}^{IS}} e^{-\frac{E_{47}^a}{k_B T}} \theta_{NNH}(t) \theta_{NH_3}(t)$$

$$r_{48}(t) = \frac{k_B T}{h} \frac{q_{48}^{TS}}{q_{48}^{IS}} e^{-\frac{E_{48}^a}{k_B T}} \theta_{NNH}(t) \theta_{NH_2}(t)$$

$$r_{49}(t) = \frac{k_B T}{h} \frac{q_{49}^{TS}}{q_{49}^{IS}} e^{-\frac{E_{49}^a}{k_B T}} \theta_{N_2}(t) \theta_{NH_3}(t)$$

$$r_{50}(t) = \frac{k_B T}{h} \frac{q_{50}^{TS}}{q_{50}^{IS}} e^{-\frac{E_{50}^a}{k_B T}} \theta_{N_2}(t)$$

$$r_{51}(t) = \frac{k_B T}{h} \frac{q_{51}^{TS}}{q_{51}^{IS}} e^{-\frac{E_{51}^a}{k_B T}} \theta_N^2(t)$$

**Differential equations in the TPR simulation:**

$$\frac{dP_{N_2H_4}}{dt} = r_1$$

$$\frac{dP_{NH_3}}{dt} = r_2$$

$$\frac{dP_{N_2}}{dt} = r_4$$

$$\frac{dP_{H_2}}{dt} = r_6$$

$$\frac{d\theta_{N_2H_4}}{dt} = -r_1 + r_9 - r_8 + r_{21} - r_{20} + r_{39} - r_{38}$$

$$\frac{d\theta_{NH_3}}{dt} = -r_2 + r_{31} - r_{30} + r_{38} - r_{39} + r_{40} - r_{41} + r_{42} - r_{43} + r_{44} - r_{45} + r_{46} - r_{47} + r_{48} - r_{49}$$

$$\frac{d\theta_{N_2}}{dt} = -r_4 + r_{51} - r_{50} + r_{48} - r_{49} + r_{18} - r_{19}$$

$$\frac{d\theta_{N_2H_3}}{dt} = r_8 - r_9 + r_{11} - r_{10} + r_{13} - r_{12} + r_{23} - r_{22} + r_{38} - r_{39} + r_{41} - r_{40} + r_{43} - r_{42}$$

$$\frac{d\theta_{NNH_2}}{dt} = r_{10} - r_{11} + r_{15} - r_{14} + r_{25} - r_{24} + r_{42} - r_{43} + r_{47} - r_{46}$$

$$\frac{d\theta_{NHNH}}{dt} = r_{12} - r_{13} + r_{17} - r_{16} + r_{27} - r_{26} + r_{40} - r_{41} + r_{45} - r_{44}$$

$$\frac{d\theta_{NNH}}{dt} = r_{14} - r_{15} + r_{16} - r_{17} + r_{19} - r_{18} + r_{29} - r_{28} + r_{44} - r_{45} + r_{46} - r_{47} + r_{49} - r_{48}$$

$$\frac{d\theta_{NH_2}}{dt} = 2r_{20} - 2r_{21} + r_{22} - r_{23} + r_{24} - r_{25} + r_{30} - r_{31} + r_{33} - r_{32} + 2r_{37} - 2r_{36} + r_{39} - r_{38} + r_{41} - r_{40} + r_{43} - r_{42} + r_{45} - r_{44} + r_{47} - r_{46} + r_{49} - r_{48}$$

$$\frac{d\theta_{NH}}{dt} = r_{22} - r_{23} + 2r_{26} - 2r_{27} + r_{28} - r_{29} + r_{32} - r_{33} + r_{35} - r_{34} + r_{36} - r_{37}$$

$$\frac{d\theta_N}{dt} = r_{24} - r_{25} + r_{28} - r_{29} + r_{34} - r_{35} + 2r_{50} - 2r_{51}$$

$$\frac{d\theta_H}{dt} = -2r_6 + r_8 - r_9 + r_{10} - r_{11} + r_{12} - r_{13} + r_{14} - r_{15} + r_{16} - r_{17} + r_{18} - r_{19} + r_{30} - r_{31} + r_{32} - r_{33} + r_{34} - r_{35}$$

**Differential equations in the batch reactor simulation:**

$$\frac{dP_{N_2H_4}}{dt} = r_1 - r_0$$

$$\frac{dP_{NH_3}}{dt} = r_2 - r_3$$

$$\frac{dP_{N_2}}{dt} = r_4 - r_5$$

$$\frac{dP_{H_2}}{dt} = r_6 - r_7$$

$$\frac{d\theta_{N_2H_4}}{dt} = r_0 - r_1 + r_9 - r_8 + r_{21} - r_{20} + r_{39} - r_{38}$$

$$\frac{d\theta_{NH_3}}{dt} = r_3 - r_2 + r_{31} - r_{30} + r_{38} - r_{39} + r_{40} - r_{41} + r_{42} - r_{43} + r_{44} - r_{45} + r_{46} - r_{47} + r_{48} - r_{49}$$

$$\frac{d\theta_{N_2}}{dt} = r_5 - r_4 + r_{51} - r_{50} + r_{48} - r_{49} + r_{18} - r_{19}$$

$$\frac{d\theta_{N_2H_3}}{dt} = r_8 - r_9 + r_{11} - r_{10} + r_{13} - r_{12} + r_{23} - r_{22} + r_{38} - r_{39} + r_{41} - r_{40} + r_{43} - r_{42}$$

$$\frac{d\theta_{NNH_2}}{dt} = r_{10} - r_{11} + r_{15} - r_{14} + r_{25} - r_{24} + r_{42} - r_{43} + r_{47} - r_{46}$$

$$\frac{d\theta_{NHNH}}{dt} = r_{12} - r_{13} + r_{17} - r_{16} + r_{27} - r_{26} + r_{40} - r_{41} + r_{45} - r_{44}$$

$$\frac{d\theta_{NNH}}{dt} = r_{14} - r_{15} + r_{16} - r_{17} + r_{19} - r_{18} + r_{29} - r_{28} + r_{44} - r_{45} + r_{46} - r_{47} + r_{49} - r_{48}$$

$$\begin{aligned} \frac{d\theta_{NH_2}}{dt} &= 2r_{20} - 2r_{21} + r_{22} - r_{23} + r_{24} - r_{25} + r_{30} - r_{31} + r_{33} - r_{32} + 2r_{37} - 2r_{36} + r_{39} - r_{38} \\ &+ r_{41} - r_{40} + r_{43} - r_{42} + r_{45} - r_{44} + r_{47} - r_{46} + r_{49} - r_{48} \end{aligned}$$

$$\frac{d\theta_{NH}}{dt} = r_{22} - r_{23} + 2r_{26} - 2r_{27} + r_{28} - r_{29} + r_{32} - r_{33} + r_{35} - r_{34} + r_{36} - r_{37}$$

$$\frac{d\theta_N}{dt} = r_{24} - r_{25} + r_{28} - r_{29} + r_{34} - r_{35} + 2r_{50} - 2r_{51}$$

$$\begin{aligned} \frac{d\theta_H}{dt} &= 2r_7 - 2r_6 + r_8 - r_9 + r_{10} - r_{11} + r_{12} - r_{13} + r_{14} - r_{15} + r_{16} - r_{17} + r_{18} - r_{19} + r_{30} - r_{31} \\ &+ r_{32} - r_{33} + r_{34} - r_{35} \end{aligned}$$

## References

- AGUSTA, M.K., DAVID, M., NAKANISHI, H., and KASAI, H., 2010. Hydrazine (N<sub>2</sub>H<sub>4</sub>) adsorption on Ni(100) - Density functional theory investigation. *Surface Science*, 604, 245-251.
- AGUSTA, M.K., DINO, W.A., DAVID, M., NAKANISHI, H., and KASAI, H., 2011. Theoretical study of hydrazine adsorption on Pt(111): Anti or cis? *Surface Science*, 605, 1347-1353.
- AGUSTA, M.K., and KASAI, H., 2012. First principles investigations of hydrazine adsorption conformations on Ni(111) surface. *Surface Science*, 606, 766-771.
- AIKA, K.I., OHHATA, T., and OZAKI, A., 1970. Hydrogenolysis of Hydrazine over Metals. *Journal of Catalysis*, 19, 140.
- ALBERAS, D.J., KISS, J., LIU, Z.M., and WHITE, J.M., 1992. Surface-Chemistry of Hydrazine on Pt(111). *Surface Science*, 278, 51-61.
- ALHAYDARI, Y.K., SALEH, J.M., and MATLOOB, M.H., 1985. Adsorption and Decomposition of Hydrazine on Metal-Films of Iron, Nickel, and Copper. *Journal of Physical Chemistry*, 89, 3286-3290.
- ANDREW, M.R., GRESSLER, W.J., JOHNSON, J.K., SHORT, R.T., and WILLIAMS, K.R., 1972. Engineering aspects of hydrazine-air fuel-cell power systems. *J. Appl. Electrochem*, 2, 327.
- ANGER, G., WINKLER, A., and RENDULIC, K.D., 1989. Adsorption and Desorption-Kinetics in the Systems H-2/Cu(111), H-2/Cu(110) and H-2/Cu(100). *Surface Science*, 220, 1-17.
- ANSLYN, E.V., and DOUGHTERY, D.A., 2006. *Transition State Theory and Related Topics*, Modern Physical Organic Chemistry. University Science Books.
- ANYAOGU, K.C., FEDOROV, A.V., and NECKERS, D.C., 2008. Synthesis, characterization, and antifouling potential of functionalized copper nanoparticles. *Langmuir*, 24, 4340-4346.
- APPL, M., 2000. Ammonia. *Ullmann's Encyclopedia of Industrial Chemistry*. Wiley-VCH Verlag GmbH & Co. KGaA.
- ASKGAARD, T.S., NORSKOV, J.K., OVESEN, C.V., and STOLTZE, P., 1995. A Kinetic-Model of Methanol Synthesis. *Journal of Catalysis*, 156, 229-242.

## References

---

- ATHANASSIOU, E.K., GRASS, R.N., and STARK, W.J., 2006. Large-scale production of carbon-coated copper nanoparticles for sensor applications. *Nanotechnology*, 17, 1668-1673.
- ATHAWALE, A.A., KATRE, P.P., KUMAR, M., and MAJUMDAR, M.B., 2005. Synthesis of CTAB-IPA reduced copper nanoparticles. *Materials Chemistry and Physics*, 91, 507-512.
- ATODIRESEI, N., CACIUC, V., FRANKE, J.H., and BLUGEL, S., 2008. Role of the van der Waals interactions on the bonding mechanism of pyridine on Cu(110) and Ag(110) surface: First-principles study. *Physical Review B*, 78.
- AYRAULT, G., and EHRLICH, G., 1974. Surface Self-Diffusion on a Fcc Crystal - Atomic View. *Journal of Chemical Physics*, 60, 281-294.
- BADER, R.F.W., 1990. *Atoms in molecules : a quantum theory*, Oxford, Clarendon Press.
- BADER, R.F.W., CARROLL, M.T., CHEESEMAN, J.R., and CHANG, C., 1987. Properties of Atoms in Molecules - Atomic Volumes. *Journal of the American Chemical Society*, 109, 7968-7979.
- BAKER, C., PRADHAN, A., PAKSTIS, L., POCHAN, D.J., and SHAH, S.I., 2005. Synthesis and antibacterial properties of silver nanoparticles. *Journal of Nanoscience and Nanotechnology*, 5, 244-249.
- BALCON, S., MARY, S., KAPPENSTEIN, C., and GENGEMBRE, E., 2000. Monopropellant decomposition catalysts II. Sintering studies on Ir/Al<sub>2</sub>O<sub>3</sub> catalysts, influence of chloride anions. *Applied Catalysis a-General*, 196, 179-190.
- BENNICI, S., and GERVASINI, A., 2006. Catalytic activity of dispersed CuO phases towards nitrogen oxides (N<sub>2</sub>O, NO, and NO<sub>2</sub>). *Applied Catalysis B-Environmental*, 62, 336-344.
- BIEMOLT, W., DAVIES, P.R., JANSEN, A.P.J., and VANSANTEN, R.A., 1992a. The Adsorption Site of Ammonia at Copper Surfaces. *Catalysis Today*, 12, 427-432.
- BIEMOLT, W., VANDEKERKHOF, G.J.C.S., DAVIES, P.R., JANSEN, A.P.J., and VANSANTEN, R.A., 1992b. Chemisorption Theory of Ammonia on Copper. *Chemical Physics Letters*, 188, 477-486.
- BLOCH, F., 1928. Radiation absorpability in quantum mechanics. *Physikalische Zeitschrift*, 29, 58-66.

## References

---

- BLOCHL, P.E., 1994. Projector Augmented-Wave Method. *Physical Review B*, 50, 17953-17979.
- BLOCK, J., and SCHULZEK.G, 1973. Catalytic Decomposition of Nitrogen-15-Labeled Hydrazine on Mgo-Supported Iron. *Journal of Catalysis*, 30, 327-329.
- BLOMEN, L.J.M.J., and MUGERWA, M.N., 1993. *Fuel Cell Systems*.
- BORN, M., and OPPENHEIMER, R., 1927. Quantum theory of molecules. *Annalen Der Physik*, 84, 0457-0484.
- BOZSO, F., ERTL, G., GRUNZE, M., and WEISS, M., 1977. Interaction of Nitrogen with Iron Surfaces .1. Fe(100) and Fe(111). *Journal of Catalysis*, 49, 18-41.
- BRANDS, D.S., POELS, E.K., and BLIEK, A., 1999. Ester hydrogenolysis over promoted Cu/SiO<sub>2</sub> catalysts. *Applied Catalysis a-General*, 184, 279-289.
- BREEMAN, M., and BOERMA, D.O., 1992. Migration of Cu Adatoms on a Cu(100) Surface, Studied with Low-Energy Ion-Scattering (Leis). *Surface Science*, 269, 224-228.
- BU, Y., SHINN, D.W., and LIN, M.C., 1992. Adsorption and Thermal-Decomposition of N<sub>2</sub>h<sub>4</sub> and Ch<sub>3</sub>n<sub>2</sub>h<sub>3</sub> on Si(111)7x7. *Surface Science*, 276, 184-199.
- CARRETTE, L., FRIEDRICH, K.A., and STIMMING, U., 2000. Fuel cells: Principles, types, fuels, and applications. *Chemphyschem*, 1, 162-193.
- CHARY, K.V.R., SEELA, K.K., SAGAR, G.V., and SREEDHAR, B., 2004. Characterization and reactivity of niobia supported copper oxide catalysts. *Journal of Physical Chemistry B*, 108, 658-663.
- CHASE, M.W., NATIONAL INSTITUTE OF, S., and TECHNOLOGY, 1998. *NIST-JANAF thermochemical tables*, [Washington, D.C.]; Woodbury, N.Y., American Chemical Society ; American Institute of Physics for the National Institute of Standards and Technology.
- CHATTERJEE, A.K., SARKAR, R.K., CHATTOPADHYAY, A.P., AICH, P., CHAKRABORTY, R., and BASU, T., 2012. A simple robust method for synthesis of metallic copper nanoparticles of high antibacterial potency against E. coli. *Nanotechnology*, 23.
- CHEN, L., HU, G.Z., ZOU, G.J., SHAO, S.J., and WANG, X.L., 2009. Efficient anchorage of Pd nanoparticles on carbon nanotubes as a catalyst for hydrazine oxidation. *Electrochemistry Communications*, 11, 504-507.

- CHEN, L., ZHANG, D.J., CHEN, J.M., ZHOU, H.D., and WAN, H.Q., 2006. The use of CTAB to control the size of copper nanoparticles and the concentration of alkylthiols on their surfaces. *Materials Science and Engineering a-Structural Materials Properties Microstructure and Processing*, 415, 156-161.
- CHEN, T.Y., CHEN, S.F., SHEU, H.S., and YEH, C.S., 2002. Reactivity of laser-prepared copper nanoparticles: Oxidation of thiols to disulfides. *Journal of Physical Chemistry B*, 106, 9717-9722.
- CHORKENDORFF, I., and NIEMANTSVERDRIET, J.W., 2007. *Concepts of modern catalysis and kinetics*, Weinheim, Wiley-VCH.
- CHUNGPHILLIPS, A., and JEBBER, K.A., 1995. Ab-Initio Studies of Critical Conformations in Ethane, Methylamine, Methanol, Hydrazine, Hydroxylamine, and Hydrogen-Peroxide. *Journal of Chemical Physics*, 102, 7080-7087.
- CIOBICA, I.M., and VAN SANTEN, R.A., 2002. A DFT study of CH<sub>x</sub> chemisorption and transition states for C-H activation on the Ru(1120) surface. *Journal of Physical Chemistry B*, 106, 6200-6205.
- CIOFFI, N., TORSI, L., DITARANTO, N., TANTILLO, G., GHIBELLI, L., SABBATINI, L., BLEVE-ZACHEO, T., D'ALESSIO, M., ZAMBONIN, P.G., and TRAVERSA, E., 2005. Copper nanoparticle/polymer composites with antifungal and bacteriostatic properties. *Chemistry of Materials*, 17, 5255-5262.
- CONTAMINARD, R.C.A., and TOMPKINS, F.C., 1971. Heterogeneous decomposition of hydrazine on molybdenum films. *Transactions of the Faraday Society*, 67, 545-555.
- CONTOUR, J.P., and PANNETIE, G., 1972. Hydrazine Decomposition over a Supported Iridium Catalyst. *Journal of Catalysis*, 24, 434-&.
- COSSER, R.C., and TOMPKINS, F.C., 1971a. Heterogeneous decomposition of hydrazine on tungsten films. *Transactions of the Faraday Society*, 67, 526-544.
- COSSER, R.C., and TOMPKINS, F.C., 1971b. Heterogeneous Decomposition of Hydrazine on Tungsten Films. *Transactions of the Faraday Society*, 67, 526-&.
- CUI, Y., ZHAO, Y.Y., TIAN, Y., ZHANG, W., LU, X.Y., and JIANG, X.Y., 2012. The molecular mechanism of action of bactericidal gold nanoparticles on Escherichia coli. *Biomaterials*, 33, 2327-2333.
- DAFF, T.D., COSTA, D., LISIECKI, I., and DE LEEUW, N.H., 2009. Density Functional Theory Calculations of the Interaction of Hydrazine with Low-Index Copper Surfaces. *Journal of Physical Chemistry C*, 113, 15714-15722.

- DAFF, T.D., and DE LEEUW, N.H., 2012. A density functional theory investigation of the molecular and dissociative adsorption of hydrazine on defective copper surfaces. *Journal of Materials Chemistry*, 22, 23210-23220.
- DAHL, S., LOGADOTTIR, A., EGEBERG, R.C., LARSEN, J.H., CHORKENDORFF, I., TORNQVIST, E., and NORSKOV, J.K., 1999. Role of steps in N<sub>2</sub> activation on Ru(0001). *Physical Review Letters*, 83, 1814-1817.
- DANIEL, W.M., and WHITE, J.M., 1986. Hydrazine adsorption and the coadsorption of CO and D<sub>2</sub> with nitrogen atoms on Rh(100). *Surface Science*, 171, 289-302.
- DANIELSON, L.R., DRESSER, M.J., DONALDSON, E.E., and DICKINSON, J.T., 1978. Adsorption and Desorption of Ammonia, Hydrogen, and Nitrogen on Ruthenium (0001). *Surface Science*, 71, 599-614.
- DATTA, K.K.R., KULKARNI, C., and ESWARAMOORTHY, M., 2010. Aminoclay: a permselective matrix to stabilize copper nanoparticles. *Chemical Communications*, 46, 616-618.
- DAVIS, S.C., and KLABUNDE, K.J., 1982. Unsupported Small Metal Particles - Preparation, Reactivity, and Characterization. *Chemical Reviews*, 82, 153-208.
- DE LEEUW, N.H., and COOPER, T.G., 2007. Surface simulation studies of the hydration of white rust Fe(OH)<sub>2</sub>, goethite alpha-FeO(OH) and hematite alpha-Fe<sub>2</sub>O<sub>3</sub>. *Geochimica Et Cosmochimica Acta*, 71, 1655-1673.
- DE LEEUW, N.H., and NELSON, C.J., 2003. A computer modeling study of perfect and defective silver (111) surfaces. *Journal of Physical Chemistry B*, 107, 3528-3534.
- DE LEEUW, N.H., NELSON, C.J., CATLOW, C.R.A., SAUTET, P., and DONG, W., 2004. Density-functional theory calculations of the adsorption of Cl at perfect and defective Ag(111) surfaces. *Physical Review B*, 69.
- DE LEEUW, N.H., and PARKER, S.C., 1998. Surface structure and morphology of calcium carbonate polymorphs calcite, aragonite, and vaterite: An atomistic approach. *Journal of Physical Chemistry B*, 102, 2914-2922.
- DE LEEUW, N.H., and PARKER, S.C., 1999. Effect of chemisorption and physisorption of water on the surface structure and stability of alpha-alumina. *Journal of the American Ceramic Society*, 82, 3209-3216.
- DE LEEUW, N.H., PARKER, S.C., CATLOW, C.R.A., and PRICE, G.D., 2000. Proton-containing defects at forsterite {010} tilt grain boundaries and stepped surfaces. *American Mineralogist*, 85, 1143-1154.

- DE LEEUW, N.H., and PURTON, J.A., 2001. Density-functional theory calculations of the interaction of protons and water with low-coordinated surface sites of calcium oxide. *Physical Review B*, 63, 195417.
- DEMIRCI, U.B., 2007. Direct liquid-feed fuel cells: Thermodynamic and environmental concerns. *Journal of Power Sources*, 169, 239-246.
- DEVEY, A.J., GRAU-CRESPO, R., and DE LEEUW, N.H., 2008. Combined density functional theory and interatomic potential study of the bulk and surface structures and properties of the iron sulfide mackinawite (FeS). *Journal of Physical Chemistry C*, 112, 10960-10967.
- DHAS, N.A., RAJ, C.P., and GEDANKEN, A., 1998. Synthesis, characterization, and properties of metallic copper nanoparticles. *Chemistry of Materials*, 10, 1446-1452.
- DIAZ, G., PEREZ-HERNANDEZ, R., GOMEZ-CORTES, A., BENAÏSSA, M., MARISCAL, R., and FIERRO, J.L.G., 1999. CuO-SiO<sub>2</sub> sol-gel catalysts: Characterization and catalytic properties for NO reduction. *Journal of Catalysis*, 187, 1-14.
- DONG, B., HE, B.L., HUANG, J., GAO, G.Y., YANG, Z., and LI, H.L., 2008. High dispersion and electrocatalytic activity of Pd/titanium dioxide nanotubes catalysts for hydrazine oxidation. *Journal of Power Sources*, 175, 266-271.
- DOPHEIDE, R., SCHROTER, L., and ZACHARIAS, H., 1991. Adsorption and Decomposition of Hydrazine on Pd(100). *Surface Science*, 257, 86-96.
- DUTTA, S., 2014. A review on production, storage of hydrogen and its utilization as an energy resource. *Journal of Industrial and Engineering Chemistry*, 20, 1148-1156.
- DYER, C.K., 2002. Fuel cells for portable applications. *Journal of Power Sources*, 106, 31-34.
- DZADE, N.Y., ROLDAN, A., and DE LEEUW, N.H., 2013. Adsorption of methylamine on mackinawite (FES) surfaces: A density functional theory study. *Journal of Chemical Physics*, 139.
- EASTMAN, J.A., CHOI, S.U.S., LI, S., YU, W., and THOMPSON, L.J., 2001. Anomalous increase in effective thermal conductivities of ethylene glycol-based nanofluids containing copper nanoparticles. *Applied Physics Letters*, 78, 718-720.
- EL-SAYED, M.A., 2004. Small is different: Shape-, size-, and composition-dependent properties of some colloidal semiconductor nanocrystals. *ACCOUNTS OF CHEMICAL RESEARCH*, 37, 326-333.

- EREMEEV, S.V., LIPNITSKII, A.G., POTEKAEV, A.I., and CHULKOV, E.V., 1997. Diffusion activation energy of point defects at the surfaces of fcc metals. *Physics of Low-Dimensional Structures*, 3-4, 127-133.
- EVANS, M.G., and POLANYI, M., 1935. Some applications of the transition state method to the calculation of reaction velocities, especially in solution. *Transactions of the Faraday Society*, 31, 0875-0893.
- EYRING, H., 1935. The activated complex in chemical reactions. *Journal of Chemical Physics*, 3, 107-115.
- FAHLMAN, B.D., 2007. *Materials Chemistry*, Springer.
- FALCONER, J.L., and WISE, H., 1976. Temperature Programmed Desorption Spectroscopy of N<sub>2</sub>H<sub>4</sub> Decomposition on Al<sub>2</sub>O<sub>3</sub>-Supported Ir Catalyst. *Journal of Catalysis*, 43, 220-233.
- FEYNMAN, R.P., 1939. Forces in molecules. *Physical Review*, 56, 340-343.
- FILANKEMBO, A., GIORGIO, S., LISIECKI, I., and PILENI, M.P., 2003. Is the anion the major parameter in the shape control of nanocrystals? *Journal of Physical Chemistry B*, 107, 7492-7500.
- FILANKEMBO, A., and PILENI, M.P., 2000. Is the template of self-colloidal assemblies the only factor that controls nanocrystal shapes? *Journal of Physical Chemistry B*, 104, 5865-5868.
- FRIDMAN, V.Z., and DAVYDOV, A.A., 2000. Dehydrogenation of cyclohexanol on copper-containing catalysts I. The influence of the oxidation state of copper on the activity of copper sites. *Journal of Catalysis*, 195, 20-30.
- FU, S.S., and SOMORJAI, G.A., 1992. Interactions of O<sub>2</sub>, Co, Co<sub>2</sub>, and D<sub>2</sub> with the Stepped Cu(311) Crystal-Face - Comparison to Cu(110). *Surface Science*, 262, 68-76.
- GAJDOS, M., and HAFNER, J., 2005. CO adsorption on Cu(111) and Cu(001) surfaces: Improving site preference in DFT calculations. *Surface Science*, 590, 117-126.
- GAMBARDELLA, P., SLJIVANCANIN, Z., HAMMER, B., BLANC, M., KUHNKE, K., and KERN, K., 2001. Oxygen dissociation at Pt steps. *Physical Review Letters*, 87.

## References

---

- GAO, G.Y., GUO, D.J., WANG, C., and LI, H.L., 2007. Electrocrystallized Ag nanoparticle on functional multi-walled carbon nanotube surfaces for hydrazine oxidation. *Electrochemistry Communications*, 9, 1582-1586.
- GAWRONSKI, H., CARRASCO, J., MICHAELIDES, A., and MORGENSTERN, K., 2008. Manipulation and control of hydrogen bond dynamics in absorbed ice nanoclusters. *Physical Review Letters*, 101, 136102.
- GAWRONSKI, H., MORGENSTERN, K., and RIEDER, K.H., 2005. Electronic excitation of ice monomers on Au(111) by scanning tunneling microscopy - Vibrational spectra and induced processes. *European Physical Journal D*, 35, 349-353.
- GERMAIN, V., BRIOUDE, A., INGERT, D., and PILENI, M.P., 2005. Silver nanodisks: Size selection via centrifugation and optical properties. *Journal of Chemical Physics*, 122.
- GIBBS, J.W., 1928. *In collected works*, New York, Longman.
- GILL, P.E., MURRAY, W., and WRIGHT, M.H., 1981. *Practical Optimization*, London, Academic Press.
- GLAND, J.L., FISHER, G.B., and MITCHELL, G.E., 1985. Vibrational characterization of adsorbed NH on the Ni(111) surface. *Chemical Physics Letters*, 119, 89-92.
- GLASSTONE, S., LAIDLER, K.J., and EYRING, H., 1941. *The theory of rate processes; the kinetics of chemical reactions, viscosity, diffusion and electrochemical phenomena*, New York; London, McGraw-Hill Book Company, inc.
- GOKHALE, A.A., DUMESIC, J.A., and MAVRIKAKIS, M., 2008. On the mechanism of low-temperature water gas shift reaction on copper. *Journal of the American Chemical Society*, 130, 1402-1414.
- GOKHALE, A.A., KANDOI, S., GREELEY, J.P., MAVRIKAKIS, M., and DUMESIC, J.A., 2004. Molecular-level descriptions of surface chemistry in kinetic models using density functional theory. *Chemical Engineering Science*, 59, 4679-4691.
- GOMEZ-DIAZ, J., and LOPEZ, N., 2011. Mechanistic Switch between Oxidative (Andrussow) and Nonoxidative (Degussa) Formation of HCN on Pt(111) by Density Functional Theory. *Journal of Physical Chemistry C*, 115, 5667-5674.
- GORTE, R.J., PARK, S., VOHS, J.M., and WANG, C.H., 2000. Anodes for direct oxidation of dry hydrocarbons in a solid-oxide fuel cell. *Advanced Materials*, 12, 1465-1469.

## References

---

- GRABOW, L.C., GOKHALE, A.A., EVANS, S.T., DUMESIC, J.A., and MAVRIKAKIS, M., 2008. Mechanism of the water gas shift reaction on Pt: First principles, experiments, and microkinetic modeling. *Journal of Physical Chemistry C*, 112, 4608-4617.
- GRANOT, E., FILANOVSKY, B., PRESMAN, I., KURAS, I., and PATOLSKY, F., 2012. Hydrazine/air direct-liquid fuel cell based on nanostructured copper anodes. *Journal of Power Sources*, 204, 116-121.
- GREELEY, J., and MAVRIKAKIS, M., 2004. Competitive paths for methanol decomposition on Pt(111). *Journal of the American Chemical Society*, 126, 3910-3919.
- GREELEY, J., NORSKOV, J.K., and MAVRIKAKIS, M., 2002. Electronic structure and catalysis on metal surfaces. *Annual Review of Physical Chemistry*, 53, 319-348.
- GRIMME, S., 2004. Accurate description of van der Waals complexes by density functional theory including empirical corrections. *Journal of Computational Chemistry*, 25, 1463-1473.
- GRIMME, S., 2006. Semiempirical GGA-type density functional constructed with a long-range dispersion correction. *Journal of Computational Chemistry*, 27, 1787-1799.
- GRUNZE, M., 1979. Interaction of Hydrazine with an Fe(111) Surface. *Surface Science*, 81, 603-625.
- HAAS, I., SHANMUGAM, S., and GEDANKEN, A., 2006. Pulsed sonoelectrochemical synthesis of size-controlled copper nanoparticles stabilized by poly(*n*-vinylpyrrolidone). *Journal of Physical Chemistry B*, 110, 16947-16952.
- HAMANN, D.R., SCHLUTER, M., and CHIANG, C., 1979. Norm-Conserving Pseudopotentials. *Physical Review Letters*, 43, 1494-1497.
- HAMMER, B., and NORSKOV, J.K., 1995. Electronic factors determining the reactivity of metal surfaces. *Surface Science*, 343, 211-220.
- HANSEN, L., STOLTZE, P., JACOBSEN, K.W., and NORSKOV, J.K., 1991. Self-Diffusion on Copper Surfaces. *Physical Review B*, 44, 6523-6526.
- HARAM, S.K., MAHADESHWAR, A.R., and DIXIT, S.G., 1996. Synthesis and characterization of copper sulfide nanoparticles in Triton-X 100 water-in-oil microemulsions. *Journal of Physical Chemistry*, 100, 5868-5873.

## References

---

- HEATH, J.R., 1999. Nanoscale materials. *ACCOUNTS OF CHEMICAL RESEARCH*, 32, 388-388.
- HELLMAN, A., HONKALA, K., REMEDIAKIS, I.N., LOGADOTTIR, A., CARLSSON, A., DAHL, S., CHRISTENSEN, C.H., and NORSKOV, J.K., 2006. Insights into ammonia synthesis from first-principles. *Surface Science*, 600, 4264-4268.
- HELLMAN, A., HONKALA, K., REMEDIAKIS, I.N., LOGADOTTIR, A., CARLSSON, A., DAHL, S., CHRISTENSEN, C.H., and NORSKOV, J.K., 2009. Ammonia synthesis and decomposition on a Ru-based catalyst modeled by first-principles. *Surface Science*, 603, 1731-1739.
- HELLMANN, H., 1937. *Einführung in die quantenchemie*, Leipzig und Wien, F. Deuticke.
- HENDERSON, M.A., 2002. The interaction of water with solid surfaces: fundamental aspects revisited. *Surface Science Reports*, 46, 1-308.
- HENKELMAN, G., ARNALDSSON, A., and JONSSON, H., 2006. A fast and robust algorithm for Bader decomposition of charge density. *Computational Materials Science*, 36, 354-360.
- HENKELMAN, G., and JONSSON, H., 1999. A dimer method for finding saddle points on high dimensional potential surfaces using only first derivatives. *Journal of Chemical Physics*, 111, 7010-7022.
- HERMAN, R.G., KLIER, K., SIMMONS, G.W., FINN, B.P., BULKO, J.B., and KOBYLINSKI, T.P., 1979. Catalytic Synthesis of Methanol from Co-H<sub>2</sub>. I. Phase Composition, Electronic Properties, and Activities of the Cu-Zno-M<sub>2</sub>O<sub>3</sub> Catalysts. *Journal of Catalysis*, 56, 407-429.
- HEYDEN, A., BELL, A.T., and KEIL, F.J., 2005. Efficient methods for finding transition states in chemical reactions: Comparison of improved dimer method and partitioned rational function optimization method. *Journal of Chemical Physics*, 123.
- HODGSON, A., and HAQ, S., 2009. Water adsorption and the wetting of metal surfaces. *Surface Science Reports*, 64, 381-451.
- HOHENBERG, P., and KOHN, W., 1964. Inhomogeneous Electron Gas. *Physical Review B*, 136, B864-&.
- HONKALA, K., HELLMAN, A., REMEDIAKIS, I.N., LOGADOTTIR, A., CARLSSON, A., DAHL, S., CHRISTENSEN, C.H., and NORSKOV, J.K., 2005. Ammonia synthesis from first-principles calculations. *Science*, 307, 555-558.

## References

---

- HUANG, H.H., YAN, F.Q., KEK, Y.M., CHEW, C.H., XU, G.Q., JI, W., OH, P.S., and TANG, S.H., 1997. Synthesis, characterization, and nonlinear optical properties of copper nanoparticles. *Langmuir*, 13, 172-175.
- HUANG, S.X., RUFANEL, T.S., and GLAND, J.L., 1993. Diimide Formation on the Ni(100) Surface. *Surface Science*, 290, L673-L676.
- HUBER, K.P., G. HERZBERG, 1979. *Molecular Spectra and Molecular Structure: IV. Constants of Diatomic Molecules*, New York, Van Nostrand Reinhold Company.
- IRRERA, S., ROLDAN, A., PORTALONE, G., and DE LEEUW, N.H., 2013a. The Role of Hydrogen Bonding and Proton Transfer in the Formation of Uracil Networks on the Gold (100) Surface: A Density Functional Theory Approach. *Journal of Physical Chemistry C*, 117, 3949-3957.
- IRRERA, S., ROLDAN, A., PORTALONE, G., and DE LEEUW, N.H., 2013b. The Role of Hydrogen Bonding and Proton Transfer in the Formation of Uracil Networks on the Gold (100) Surface: A Density Functional Theory Approach. *The Journal of Physical Chemistry C*, 117, 3949-3957.
- JOHNSON, D.W., and ROBERTS, M.W., 1980. Adsorption of Hydrazine and Ammonia on Aluminum. *Journal of Electron Spectroscopy and Related Phenomena*, 19, 185-195.
- JONES, D.A., 1996. *Principles and Prevention of Corrosion* NJ, Prentice Hall Upper saddle River.
- JONES, G.W., MARCANO, J.M., NORSKOV, J.K., and VENABLES, J.A., 1990. Energies Controlling Nucleation and Growth-Processes - the Case of Ag/W(110). *Physical Review Letters*, 65, 3317-3320.
- JOSHI, S.S., PATIL, S.F., IYER, V., and MAHUMUNI, S., 1998. Radiation induced synthesis and characterization of copper nanoparticles. *Nanostructured Materials*, 10, 1135-1144.
- KANDOI, S., GREELEY, J., SANCHEZ-CASTILLO, M.A., EVANS, S.T., GOKHALE, A.A., DUMESIC, J.A., and MAVRIKAKIS, M., 2006. Prediction of experimental methanol decomposition rates on platinum from first principles. *Topics in Catalysis*, 37, 17-28.
- KANEKO, T., DERBYSHIRE, F., MAKINO, E., GRAY, D., and TAMURA, M., 2000. Coal Liquefaction. *Ullmann's Encyclopedia of Industrial Chemistry*. Wiley-VCH Verlag GmbH & Co. KGaA.

## References

---

- KARIM-NEZHAD, G., JAFARLOO, R., and DORRAJI, P.S., 2009. Copper (hydr)oxide modified copper electrode for electrocatalytic oxidation of hydrazine in alkaline media. *Electrochimica Acta*, 54, 5721-5726.
- KARIMI, M., TOMKOWSKI, T., VIDALI, G., and BIHAM, O., 1995. Diffusion of Cn on Cu Surfaces. *Physical Review B*, 52, 5364-5374.
- KASUYA, T., and KOJIMA, T., 1963. Internal Motions of Hydrazine. *Journal of the Physical Society of Japan*, 18, 364-&.
- KAURANEN, P.S., and SKOU, E., 1996. Mixed methanol oxidation oxygen reduction currents on a carbon supported Pt catalyst. *Journal of Electroanalytical Chemistry*, 408, 189-198.
- KIM, Y.S., KOO, J.Y., and KIM, H., 2008. Erratum: Interplay of Hydrogen-Bond and Coordinate Covalent-Bond Interactions in Self-Assembly of  $\{\mathrm{NH}\}_3$  Molecules on the Si(001) Surface [Phys. Rev. Lett. **100**, 256105 (2008)]. *Physical Review Letters*, 101, 256105.
- KITCHENS, C.L., MCLEOD, M.C., and ROBERTS, C.B., 2003. Solvent effects on the growth and steric stabilization of copper metallic nanoparticles in AOT reverse micelle systems. *Journal of Physical Chemistry B*, 107, 11331-11338.
- KNIEP, B.L., GIRGSDIES, F., and RESSLER, T., 2005. Effect of precipitate aging on the microstructural characteristics of Cu/ZnO catalysts for methanol steam reforming. *Journal of Catalysis*, 236, 34-44.
- KOBAYASHI, H., TAKEZAWA, N., and MINOCHI, C., 1981. Methanol-Reforming Reaction over Copper-Containing Catalysts - the Effects of Anions and Copper Loading in the Preparation of the Catalysts by Kneading Method. *Journal of Catalysis*, 69, 487-494.
- KOHLER, L., and KRESSE, G., 2004. Density functional study of CO on Rh(111). *Physical Review B*, 70.
- KOHN, W., and SHAM, L.J., 1965. Self-Consistent Equations Including Exchange and Correlation Effects. *Physical Review*, 140, 1133-&.
- KOITZ, R., SEITSONEN, A.P., IANNUZZI, M., and HUTTER, J., 2013. Structural and electronic properties of a large-scale Moire pattern of hexagonal boron nitride on Cu(111) studied with density functional theory. *Nanoscale*, 5, 5589-5595.
- KONNOV, A.A., and DE RUYCK, J., 2001. Kinetic modeling of the decomposition and flames of hydrazine. *Combustion and Flame*, 124, 106-126.

- KOOIJ, E.S., and POELSEMA, B., 2006. Shape and size effects in the optical properties of metallic nanorods. *Physical Chemistry Chemical Physics*, 8, 3349-3357.
- KRESSE, G., and FURTHMULLER, J., 1996a. Efficiency of ab-initio total energy calculations for metals and semiconductors using a plane-wave basis set. *Computational Materials Science*, 6, 15-50.
- KRESSE, G., and FURTHMULLER, J., 1996b. Efficient iterative schemes for ab initio total-energy calculations using a plane-wave basis set. *Physical Review B*, 54, 11169-11186.
- KRESSE, G., and HAFNER, J., 1993. Abinitio Molecular-Dynamics for Liquid-Metals. *Physical Review B*, 47, 558-561.
- KRESSE, G., and HAFNER, J., 1994. Ab-Initio Molecular-Dynamics Simulation of the Liquid-Metal Amorphous-Semiconductor Transition in Germanium. *Physical Review B*, 49, 14251-14269.
- KRESSE, G., and JOUBERT, D., 1999. From ultrasoft pseudopotentials to the projector augmented-wave method. *Physical Review B*, 59, 1758-1775.
- KRUK, T., SZCZEPANOWICZ, K., STEFAŃSKA, J., SOCHA, R.P., and WARSZYŃSKI, P., 2015. Synthesis and antimicrobial activity of monodisperse copper nanoparticles. *Colloids and Surfaces B: Biointerfaces*, 128, 17-22.
- KUHN, H., FÖRSTERLING, H.-D., and WALDECK, D.H., 2009. *Principles of physical chemistry*, Hoboken, N.J: John Wiley.
- KUHNLE, A., 2009. Self-assembly of organic molecules at metal surfaces. *Current Opinion in Colloid & Interface Science*, 14, 157-168.
- KURPICK, U., 2001. Self-diffusion on (100), (110), and (111) surfaces of Ni and Cu: A detailed study of prefactors and activation energies. *Physical Review B*, 64.
- KURPICK, U., KARA, A., and RAHMAN, T.S., 1997. Role of lattice vibrations in adatom diffusion. *Physical Review Letters*, 78, 1086-1089.
- KURPICK, U., and RAHMAN, T.S., 1999. The role of vibrational entropy in surface diffusion: adatoms and vacancies on Ag(100), Cu(100), and Ni(100). *Surface Science*, 427-28, 15-21.
- LAIDLER, K.J., 1987. *Chemical kinetics*, New York, Harper & Row.

## References

---

- LEE, S., FAN, C.Y., WU, T.P., and ANDERSON, S.L., 2005. Hydrazine decomposition over Ir-n/Al<sub>2</sub>O<sub>3</sub> model catalysts prepared by size-selected cluster deposition. *Journal of Physical Chemistry B*, 109, 381-388.
- LI, T., BHATIA, B., and SHOLL, D.S., 2004. First-principles study of C adsorption, O adsorption, and CO dissociation on flat and stepped Ni surfaces. *Journal of Chemical Physics*, 121, 10241-10249.
- LIDE, D.R., 1996. *CRC Handbook of Chemistry and Physics*, New York, CRC Press.
- LISIECKI, I., 2004. Size control of spherical metallic nanocrystals. *Colloids and Surfaces a-Physicochemical and Engineering Aspects*, 250, 499-507.
- LISIECKI, I., 2005. Size, shape, and structural control of metallic nanocrystals. *Journal of Physical Chemistry B*, 109, 12231-12244.
- LISIECKI, I., BJORLING, M., MOTTE, L., NINHAM, B., and PILENI, M.P., 1995. Synthesis of Copper Nanosize Particles in Anionic Reverse Micelles - Effect of the Addition of a Cationic Surfactant on the Size of the Crystallites. *Langmuir*, 11, 2385-2392.
- LISIECKI, I., and PILENI, M.P., 1993. Synthesis of Copper Metallic Clusters Using Reverse Micelles as Microreactors. *Journal of the American Chemical Society*, 115, 3887-3896.
- LITTRELL, D.M., and TATARCHUK, B.J., 1986. Hydrazine Reduction of Transition-Metal Oxides - In situ Characterization Using X-Ray Photoelectron-Spectroscopy. *Journal of Vacuum Science & Technology a-Vacuum Surfaces and Films*, 4, 1608-1612.
- LIU, C.L., COHEN, J.M., ADAMS, J.B., and VOTER, A.F., 1991. Eam Study of Surface Self-Diffusion of Single Adatoms of Fcc Metals Ni, Cu, Al, Ag, Au, Pd, and Pt. *Surface Science*, 253, 334-344.
- LIU, D.F., YANG, S.H., and LEE, S.T., 2008. Preparation of novel cuprous oxide-fullerene[60] core-shell nanowires and nanoparticles via a copper(I)-assisted fullerene-polymerization reaction. *Journal of Physical Chemistry C*, 112, 7110-7118.
- LIU, W.T., 2006. Nanoparticles and their biological and environmental applications. *Journal of Bioscience and Bioengineering*, 102, 1-7.
- LIU, Z.P., and HU, P., 2003. General rules for predicting where a catalytic reaction should occur on metal surfaces: A density functional theory study of C-H and C-O bond

## References

---

- breaking/making on flat, stepped, and kinked metal surfaces. *Journal of the American Chemical Society*, 125, 1958-1967.
- LIZZIT, S., BARALDI, A., GROSO, A., REUTER, K., GANDUGLIA-PIROVANO, M.V., STAMPL, C., SCHEFFLER, M., STICHLER, M., KELLER, C., WURTH, W., and MENZEL, D., 2001. Surface core-level shifts of clean and oxygen-covered Ru(0001). *Physical Review B*, 63.
- LOGADOTTIR, A., and NORSKOV, J.K., 2003. Ammonia synthesis over a Ru(0001) surface studied by density functional calculations. *Journal of Catalysis*, 220, 273-279.
- MADON, R.J., BRADEN, D., KANDOI, S., NAGEL, P., MAVRIKAKIS, M., and DUMESIC, J.A., 2011. Microkinetic analysis and mechanism of the water gas shift reaction over copper catalysts. *Journal of Catalysis*, 281, 1-11.
- MALI, K.S., ADISOEJOSO, J., GHIJSENS, E., DE CAT, I., and DE FEYTER, S., 2012. Exploring the Complexity of Supramolecular Interactions for Patterning at the Liquid-Solid Interface. *ACCOUNTS OF CHEMICAL RESEARCH*, 45, 1309-1320.
- MARCHI, A.J., FIERRO, J.L.G., SANTAMARIA, J., and MONZON, A., 1996. Dehydrogenation of isopropyl alcohol on a Cu/SiO<sub>2</sub> catalyst: A study of the activity evolution and reactivation of the catalyst. *Applied Catalysis a-General*, 142, 375-386.
- MARY, S., KAPPENSTEIN, C., BALCON, S., ROSSIGNOL, S., and GENGEMBRE, E., 1999. Monopropellant decomposition catalysts. I. Ageing of highly loaded Ir/Al<sub>2</sub>O<sub>3</sub> catalysts in oxygen and steam. Influence of chloride content. *Applied Catalysis a-General*, 182, 317-325.
- MATLOOB, M.H., and ROBERTS, M.W., 1977. Electron Spectroscopic Study of Nitrogen Species Adsorbed on Copper. *Journal of the Chemical Society-Faraday Transactions I*, 73, 1393-1405.
- MATSUI, I., 2005. Nanoparticles for electronic device applications: A brief review. *Journal of Chemical Engineering of Japan*, 38, 535-546.
- MATTER, P.H., BRADEN, D.J., and OZKAN, U.S., 2004. Steam reforming of methanol to H<sub>2</sub> over nonreduced Zr-containing CuO/ZnO catalysts. *Journal of Catalysis*, 223, 340-351.
- MAUREL, R., and MENEZO, J.C., 1978. Catalytic Decomposition of N-15-Labeled Hydrazine on Alumina-Supported Metals. *Journal of Catalysis*, 51, 293-295.

## References

---

- MCKAY, H.L., JENKINS, S.J., and WALES, D.J., 2011. Dissociative Chemisorption of Hydrazine on an Fe{211} Surface. *Journal of Physical Chemistry C*, 115, 17812-17828.
- MILEY, G.H., LUO, N., MATHER, J., BURTON, R., HAWKINS, G., GU, L.F., BYRD, E., GIMLIN, R., SHRESTHA, P.J., BENAVIDES, G., LAYSTROM, J., and CARROLL, D., 2007. Direct NaBH<sub>4</sub>/H<sub>2</sub>O<sub>2</sub> fuel cells. *Journal of Power Sources*, 165, 509-516.
- MILLS, G., and JONSSON, H., 1994. Quantum and Thermal Effects in H-2 Dissociative Adsorption - Evaluation of Free-Energy Barriers in Multidimensional Quantum-Systems. *Physical Review Letters*, 72, 1124-1127.
- MILLS, G., JONSSON, H., and SCHENTER, G.K., 1995. Reversible Work Transition-State Theory - Application to Dissociative Adsorption of Hydrogen. *Surface Science*, 324, 305-337.
- MINH, N.Q., 1993. Ceramic Fuel-Cells. *Journal of the American Ceramic Society*, 76, 563-588.
- MKHONTO, D., and DE LEEUW, N.H., 2002. A computer modelling study of the effect of water on the surface structure and morphology of fluorapatite: introducing a Ca-10(PO<sub>4</sub>)(6)F-2 potential model. *Journal of Materials Chemistry*, 12, 2633-2642.
- MONKHORST, H.J., and PACK, J.D., 1976. Special Points for Brillouin-Zone Integrations. *Physical Review B*, 13, 5188-5192.
- MONTALENTI, F., and FERRANDO, R., 1999. Jumps and concerted moves in Cu, Ag, and Au(110) adatom self-diffusion. *Physical Review B*, 59, 5881-5891.
- MORGENSTERN, K., and RIEDER, K.H., 2002. Dissociation of water molecules with the scanning tunnelling microscope. *Chemical Physics Letters*, 358, 250-256.
- MORONES, J.R., ELECHIGUERRA, J.L., CAMACHO, A., HOLT, K., KOURI, J.B., RAMIREZ, J.T., and YACAMAN, M.J., 2005. The bactericidal effect of silver nanoparticles. *Nanotechnology*, 16, 2346-2353.
- MURA, M., GULANS, A., THONHAUSER, T., and KANTOROVICH, L., 2010. Role of van der Waals interaction in forming molecule-metal junctions: flat organic molecules on the Au(111) surface. *Physical Chemistry Chemical Physics*, 12, 4759-4767.
- NORSKOV, J.K., BLIGAARD, T., LOGADOTTIR, A., BAHN, S., HANSEN, L.B., BOLLINGER, M., BENGAARD, H., HAMMER, B., SLJIVANCANIN, Z.,

## References

---

- MAVRIKAKIS, M., XU, Y., DAHL, S., and JACOBSEN, C.J.H., 2002. Universality in heterogeneous catalysis. *Journal of Catalysis*, 209, 275-278.
- NOVELL-LERUTH, G., RICART, J.M., and PEREZ-RAMIREZ, J., 2008. Pt(100)-catalyzed ammonia oxidation studied by DFT: Mechanism and microkinetics. *Journal of Physical Chemistry C*, 112, 13554-13562.
- PAKDEHI, S.G., SALIMI, M., and RASOOLZADEH, M., 2014. A review on decomposition of hydrazine and its kinetics as a novel approach for CO-free H<sub>2</sub> production. *Researches and Applications in Mechanical Engineering*, 3, 21-25.
- PARK, B.K., JEONG, S., KIM, D., MOON, J., LIM, S., and KIM, J.S., 2007. Synthesis and size control of monodisperse copper nanoparticles by polyol method. *Journal of Colloid and Interface Science*, 311, 417-424.
- PARK, P.W., and LEDFORD, J.S., 1998. The influence of surface structure on the catalytic activity of cerium promoted copper oxide catalysts on alumina: oxidation of carbon monoxide and methane. *Catalysis Letters*, 50, 41-48.
- PARK, S., GORTE, R.J., and VOHS, J.M., 2000. Applications of heterogeneous catalysis in the direct oxidation of hydrocarbons in a solid-oxide fuel cell. *Applied Catalysis a-General*, 200, 55-61.
- PARKER, S.C., DE LEEUW, N.H., HARRIS, D.J., HIGGINS, F.M., OLIVER, P.M., REDFERN, S.E., and WATSON, G.W., 1999. Atomistic simulation of oxide dislocations and interfaces. *Radiation Effects and Defects in Solids*, 151, 185-195.
- PARSONS, R., and VANDERNOOT, T., 1988. The Oxidation of Small Organic-Molecules - a Survey of Recent Fuel-Cell Related Research. *Journal of Electroanalytical Chemistry*, 257, 9-45.
- PERDEW, J.P., BURKE, K., and ERNZERHOF, M., 1996. Generalized gradient approximation made simple. *Physical Review Letters*, 77, 3865-3868.
- PERDEW, J.P., and WANG, Y., 1992. Accurate and Simple Analytic Representation of the Electron-Gas Correlation-Energy. *Physical Review B*, 45, 13244-13249.
- PILENI, M.P., 2001. Mesostructured fluids in oil-rich regions: Structural and templating approaches. *Langmuir*, 17, 7476-7486.
- PILENI, M.P., 2003. The role of soft colloidal templates in controlling the size and shape of inorganic nanocrystals. *Nature Materials*, 2, 145-150.

## References

---

- PINEDA, J., and SCHWARTZ, S.D., 2006. Protein dynamics and catalysis: the problems of transition state theory and the subtlety of dynamic control. *Philosophical Transactions of the Royal Society B: Biological Sciences*, 361, 1433-1438.
- PONCE, A.A., and KLABUNDE, K.J., 2005. Chemical and catalytic activity of copper nanoparticles prepared via metal vapor synthesis. *Journal of Molecular Catalysis a-Chemical*, 225, 1-6.
- POPLE, J.A., and CURTISS, L.A., 1991. The Energy of N<sub>2</sub>H<sub>2</sub> and Related-Compounds. *Journal of Chemical Physics*, 95, 4385-4388.
- PRASAD, J., and GLAND, J.L., 1991a. Hydrazine Decomposition on a Clean Rhodium Surface - a Temperature Programmed Reaction Spectroscopy Study. *Langmuir*, 7, 722-726.
- PRASAD, J., and GLAND, J.L., 1991b. Hydrazine decomposition on a clean rhodium surface: A temperature programmed reaction spectroscopy study. *Langmuir*, 7, 722-726.
- PRASAD, J., and GLAND, J.L., 1991c. The Selectivity of Hydrazine Oxidation on a Polycrystalline Rhodium Surface. *Surface Science*, 258, 67-74.
- RAMYADEVI, J., JEYASUBRAMANIAN, K., MARIKANI, A., RAJAKUMAR, G., and RAHUMAN, A.A., 2012. Synthesis and antimicrobial activity of copper nanoparticles. *Materials Letters*, 71, 114-116.
- RASIM, K., BOBETH, M., POMPE, W., and SERIANI, N., 2010. A microkinetic model of ammonia decomposition on a Pt overlayer on Au(111). *Journal of Molecular Catalysis a-Chemical*, 325, 15-24.
- RAUSCHER, H., KOSTOV, K.L., and MENZEL, D., 1993. Adsorption and Decomposition of Hydrazine on Ru(001). *Chemical Physics*, 177, 473-496.
- REN, G.G., HU, D.W., CHENG, E.W.C., VARGAS-REUS, M.A., REIP, P., and ALLAKER, R.P., 2009. Characterisation of copper oxide nanoparticles for antimicrobial applications. *International Journal of Antimicrobial Agents*, 33, 587-590.
- REN, X.M., WILSON, M.S., and GOTTESFELD, S., 1996. High performance direct methanol polymer electrolyte fuel cells. *Journal of the Electrochemical Society*, 143, L12-L15.
- RIEKE, R.D., WEHMEYER, R.M., WU, T.C., and EBERT, G.W., 1989. New Organocopper Reagents Prepared Utilizing Highly Reactive Copper. *Tetrahedron*, 45, 443-454.

- RIGGS, N.V., and RADOM, L., 1986. An Abinitio Investigation of the Equilibrium Structures of Hydrazine and of the Transition Structures Connecting Them. *Australian Journal of Chemistry*, 39, 1917-1928.
- ROLDÁN, A., NOVELL, G., RICART, J.M., and ILLAS, F., 2010. Theoretical Simulation of Temperature Programmed Desorption of Molecular Oxygen on Isolated Au Nanoparticles from Density Functional Calculations and Microkinetics Models. *The Journal of Physical Chemistry C*, 114, 5101-5106.
- RON, H., COHEN, H., MATLIS, S., RAPPAPORT, M., and RUBINSTEIN, I., 1998. Self-assembled monolayers on oxidized metals. 4. Superior n-alkanethiol monolayers on copper. *Journal of Physical Chemistry B*, 102, 9861-9869.
- ROSTOVSHCHIKOVA, T.N., SMIRNOV, V.V., KOZHEVIN, V.M., YAVSIN, D.A., ZABELIN, M.A., YASSIEVICH, I.N., and GUREVICH, S.A., 2005. New size effect in the catalysis by interacting copper nanoparticles. *Applied Catalysis a-General*, 296, 70-79.
- RUPARELIA, J.P., CHATTERIEE, A.K., DUTTAGUPTA, S.P., and MUKHERJI, S., 2008. Strain specificity in antimicrobial activity of silver and copper nanoparticles. *Acta Biomaterialia*, 4, 707-716.
- SALZEMANN, C., BRIOUDE, A., and PILENI, M.P., 2006. Tuning of copper nanocrystals optical properties with their shapes. *Journal of Physical Chemistry B*, 110, 7208-7212.
- SALZEMANN, C., LISIECKI, I., BRIOUDE, A., URBAN, J., and PILENI, M.P., 2004a. Collections of copper nanocrystals characterized by different sizes and shapes: Optical response of these nanoobjects. *Journal of Physical Chemistry B*, 108, 13242-13248.
- SALZEMANN, C., LISIECKI, L., URBAN, J., and PILENI, M.P., 2004b. Anisotropic copper nanocrystals synthesized in a supersaturated medium: Nanocrystal growth. *Langmuir*, 20, 11772-11777.
- SANTOS-CARBALLAL, D., ROLDAN, A., GRAU-CRESPO, R., and DE LEEUW, N.H., 2014. A DFT study of the structures, stabilities and redox behaviour of the major surfaces of magnetite Fe<sub>3</sub>O<sub>4</sub>. *Physical Chemistry Chemical Physics*, 16, 21082-21097.
- SCHLAPBACH, L., and ZUTTEL, A., 2001. Hydrogen-storage materials for mobile applications. *Nature*, 414, 353-358.

## References

---

- SCHMIDT, E.W., 2001. *Hydrazine and Its Derivatives: Preparation, Properties, Applications*, New York, Wiley.
- SCHRODINGER, E., 1926. An undulatory theory of the mechanics of atoms and molecules. *Physical Review*, 28, 1049-1070.
- SEROV, A., and KWAK, C., 2009a. Review of non-platinum anode catalysts for DMFC and PEMFC application. *Applied Catalysis B-Environmental*, 90, 313-320.
- SEROV, A., NEDOSEYKINA, T., SHVACHKO, O., and KWAK, C., 2010. Effect of precursor nature on the performance of palladium-cobalt electrocatalysts for direct methanol fuel cells. *Journal of Power Sources*, 195, 175-180.
- SEROV, A.A., CHO, S.Y., HAN, S., MIN, M., CHAI, G., NAM, K.H., and KWAK, C., 2007. Modification of palladium-based catalysts by chalcogenes for direct methanol fuel cells. *Electrochemistry Communications*, 9, 2041-2044.
- SEROV, A.A., and KWAK, C., 2009b. Synthesis, characterization and catalytic activity of RuFeSe/C as a cathode catalyst for low-temperature fuel cells. *Catalysis Communications*, 10, 1551-1554.
- SEROV, A.A., MIN, M., CHAI, G., HAN, S., KANG, S., and KWAK, C., 2008. Preparation, characterization, and high performance of RuSe/C for direct methanol fuel cells. *Journal of Power Sources*, 175, 175-182.
- SEROV, A.A., MIN, M., CHAI, G., HAN, S., SEO, S.J., PARK, Y., KIM, H., and KWAK, C., 2009. Electroreduction of oxygen over iron macrocyclic catalysts for DMFC applications. *Journal of Applied Electrochemistry*, 39, 1509-1516.
- SHEN, W.J., ICHIHASHI, Y., and MATSUMURA, Y., 2005. Low temperature methanol synthesis from carbon monoxide and hydrogen over ceria supported copper catalyst. *Applied Catalysis a-General*, 282, 221-226.
- SHEN, Y., XU, Q., GAO, H., and ZHU, N.N., 2009. Dendrimer-encapsulated Pd nanoparticles anchored on carbon nanotubes for electro-catalytic hydrazine oxidation. *Electrochemistry Communications*, 11, 1329-1332.
- SHOLL, D.S., and STECKEL, J.A., 2009. *Density functional theory : a practical introduction*, Hoboken, N.J., Wiley.
- SKRIVER, H.L., and ROSENGAARD, N.M., 1992. Surface energy and work function of elemental metals. *Physical Review B*, 46, 7157-7168.

## References

---

- SMERIERI, M., VATTUONE, L., COSTA, D., TIELENS, F., and SAVIO, L., 2010. Self-Assembly of (S)-Glutamic Acid on Ag(100): A Combined LT-STM and Ab Initio Investigation. *Langmuir*, 26, 7208-7215.
- SONDI, I., and SALOPEK-SONDI, B., 2004. Silver nanoparticles as antimicrobial agent: a case study on E-coli as a model for Gram-negative bacteria. *Journal of Colloid and Interface Science*, 275, 177-182.
- SPRINGER, T.E., ZAWODZINSKI, T.A., and GOTTESFELD, S., 1991. Polymer Electrolyte Fuel-Cell Model. *Journal of the Electrochemical Society*, 138, 2334-2342.
- STEGELMANN, C., SCHIODT, N.C., CAMPBELL, C.T., and STOLTZE, P., 2004. Microkinetic modeling of ethylene oxidation over silver. *Journal of Catalysis*, 221, 630-649.
- STOLTZE, P., 1987. Surface Science as the Basis for the Understanding of the Catalytic Synthesis of Ammonia. *Physica Scripta*, 36, 824-864.
- STRAUMAN.ME, and YU, L.S., 1969. Lattice Parameters, Densities, Expansion Coefficients and Perfection of Structure of Cu and of Cu-in Alpha Phase. *Acta Crystallographica Section a-Crystal Physics Diffraction Theoretical and General Crystallography*, A 25, 676-&.
- SU, X.D., ZHAO, J.Z., BALA, H., ZHU, Y.C., GAO, Y., MA, S.S., and WANG, Z.C., 2007. Fast synthesis of stable cubic copper nanocages in the aqueous phase. *Journal of Physical Chemistry C*, 111, 14689-14693.
- TAFRESHI, S.S., ROLDAN, A., and DE LEEUW, N.H., 2014a. Density Functional Theory Study of the Adsorption of Hydrazine on the Perfect and Defective Copper (100), (110), and (111) Surfaces. *The Journal of Physical Chemistry C*, 118, 26103-26114.
- TAFRESHI, S.S., ROLDAN, A., and DE LEEUW, N.H., 2015a. Density Functional Theory calculations of the hydrazine decomposition mechanism on the planar and stepped Cu(111) surfaces. *Physical Chemistry Chemical Physics*, 17, 21533-21546.
- TAFRESHI, S.S., ROLDAN, A., and DE LEEUW, N.H., 2015b. Hydrazine network on Cu(111) surface: A Density Functional Theory approach. *Surface Science*, 637-638, 140-148.
- TAFRESHI, S.S., ROLDAN, A., DZADE, N.Y., and DE LEEUW, N.H., 2014b. Adsorption of hydrazine on the perfect and defective copper (111) surface: A dispersion-corrected DFT study. *Surface Science*, 622, 1-8.

## References

---

- TAMURA, K., and KAHARA, T., 1976. Exhaust-Gas Compositions and Fuel Efficiencies of Hydrazine Air Fuel-Cells. *Journal of the Electrochemical Society*, 123, 776-780.
- TAN, C., WANG, F., LIU, J.J., ZHAO, Y.B., WANG, J.J., ZHANG, L.H., PARK, K.C., and ENDO, M., 2009. An easy route to prepare carbon black-silver hybrid catalysts for electro-catalytic oxidation of hydrazine. *Materials Letters*, 63, 969-971.
- TANG, Q.L., and CHEN, Z.X., 2007. Density functional slab model studies of water adsorption on flat and stepped Cu surfaces. *Surface Science*, 601, 954-964.
- TANG, X.L., ZHANG, B.C., LI, Y., XU, Y.D., XIN, Q., and SHEN, W.J., 2005. CuO/CeO<sub>2</sub> catalysts: Redox features and catalytic behaviors. *Applied Catalysis a-General*, 288, 116-125.
- TANORI, J., and PILENI, M.P., 1995. Change in the Shape of Copper Nanoparticles in Ordered Phases. *Advanced Materials*, 7, 862-864.
- TANORI, J., and PILENI, M.P., 1997. Control of the shape of copper metallic particles by using a colloidal system as template. *Langmuir*, 13, 639-646.
- TERSOFF, J., and HAMANN, D.R., 1985. Theory of the Scanning Tunneling Microscope. *Physical Review B*, 31, 805-813.
- THANTHIRIWATTE, K.S., HOHENSTEIN, E.G., BURNS, L.A., and SHERRILL, C.D., 2011. Assessment of the Performance of DFT and DFT-D Methods for Describing Distance Dependence of Hydrogen-Bonded Interactions. *Journal of Chemical Theory and Computation*, 7, 88-96.
- TILAKI, R.M., ZAD, A.I., and MAHDAVI, S.M., 2007. Size, composition and optical properties of copper nanoparticles prepared by laser ablation in liquids. *Applied Physics a-Materials Science & Processing*, 88, 415-419.
- TONG, D.G., ZENG, X.L., CHU, W., WANG, D., and WU, P., 2010. Preparation of monodispersed cobalt-boron spherical nanoparticles and their behavior during the catalytic decomposition of hydrous hydrazine. *Materials Research Bulletin*, 45, 442-447.
- TRANCA, I., SMERIERI, M., SAVIO, L., VATTUONE, L., COSTA, D., and TIELENS, F., 2013. Unraveling the Self-Assembly of the (S)-Glutamic Acid "Flower" Structure on Ag(100). *Langmuir*, 29, 7876-7884.
- VANDERBILT, D., 1990. Soft Self-Consistent Pseudopotentials in a Generalized Eigenvalue Formalism. *Physical Review B*, 41, 7892-7895.

## References

---

- VANDESCHEUR, F.T., VANDERLINDEN, B., MITTELMEIJERHAZELEGER, M.C., NAZLOOMIAN, J.G., and STAAL, L.H., 1994. Structure-Activity Relation and Ethane Formation in the Hydrogenolysis of Methyl Acetate on Silica-Supported Copper-Catalysts. *Applied Catalysis a-General*, 111, 63-77.
- VANPOUCKE, D.E.P., and BROCKS, G., 2008. Formation of Pt-induced Ge atomic nanowires on Pt/Ge(001): A density functional theory study. *Physical Review B*, 77, 241308.
- VITOS, L., RUBAN, A.V., SKRIVER, H.L., and KOLLAR, J., 1998. The surface energy of metals. *Surface Science*, 411, 186-202.
- VITULLI, G., BERNINI, M., BERTOZZI, S., PITZALIS, E., SALVADORI, P., COLUCCIA, S., and MARTRA, G., 2002. Nanoscale copper particles derived from solvated Cu atoms in the activation of molecular oxygen. *Chemistry of Materials*, 14, 1183-1186.
- VOLTER, J., and LIETZ, G., 1969. Catalytic Decomposition of Hydrazine Vapor on Chromium Manganese Iron Tungsten Rhenium and Osmium. *Zeitschrift Fur Anorganische Und Allgemeine Chemie*, 366, 191-&.
- WAGNER, M.L., and SCHMIDT, L.D., 1991. Adsorption and Decomposition of H<sub>2</sub>ncho, D<sub>2</sub>ncho, N<sub>2</sub>h<sub>4</sub>, and Nh<sub>3</sub> on Rh(111). *Surface Science*, 257, 113-128.
- WAIDHAS, M., DRENCKHAHN, W., PREIDEL, W., and LANDES, H., 1996. Direct-fuelled fuel cells. *Journal of Power Sources*, 61, 91-97.
- WANG, C.C., WU, J.Y., PHAM, T.L.M., and JIANG, J.C., 2014. Microkinetic Simulation of Ammonia Oxidation on the RuO<sub>2</sub>(110) Surface. *Acs Catalysis*, 4, 639-648.
- WANG, G.C., JIANG, L., PANG, X.Y., and NAKAMURA, J., 2005. Cluster and periodic DFT calculations: The adsorption of atomic nitrogen on M(111) (M = Cu, Ag, Au) surfaces. *Journal of Physical Chemistry B*, 109, 17943-17950.
- WANG, J.T., WASMUS, S., and SAVINELL, R.F., 1996. Real-time mass spectrometric study of the methanol crossover in a direct methanol fuel cell. *Journal of the Electrochemical Society*, 143, 1233-1239.
- WATSON, G.W., KELSEY, E.T., DELEEUW, N.H., HARRIS, D.J., and PARKER, S.C., 1996. Atomistic simulation of dislocations, surfaces and interfaces in MgO. *Journal of the Chemical Society-Faraday Transactions*, 92, 433-438.
- WEI, Y.H., CHEN, S., KOWALCZYK, B., HUDA, S., GRAY, T.P., and GRZYBOWSKI, B.A., 2010. Synthesis of Stable, Low-Dispersity Copper Nanoparticles and

## References

---

- Nanorods and Their Antifungal and Catalytic Properties. *Journal of Physical Chemistry C*, 114, 15612-15616.
- WILLIAMS, J.O., SCARSDALE, J.N., SCHAFER, L., and GEISE, H.J., 1981. Abinitio Studies of Structural Features Not Easily Amenable to Experiment .3. The Influence of Lone Pair Orbital Interactions on Molecular-Structure. *Theochem-Journal of Molecular Structure*, 1, 11-28.
- WOLFRAM RESEARCH, I., 2012. *Mathematica*, Champaign, Illinois, Wolfram Research, Inc.
- WOOD, B.J., and WISE, H., 1975a. Interaction of Hydrazine with Polycrystalline Iridium Foil. *Journal of Catalysis*, 39, 471-480.
- WOOD, B.J., and WISE, H., 1975b. The interaction of hydrazine with polycrystalline iridium foil. *Journal of Catalysis*, 39, 471-480.
- WULFF, G., 1901. On the question of speed of growth and dissolution of crystal surfaces. *Zeitschrift Fur Krystallographie Und Mineralogie*, 34, 449-530.
- XU, Y., and MAVRIKAKIS, M., 2003a. The adsorption and dissociation of O<sub>2</sub> molecular precursors on Cu: the effect of steps. *Surface Science*, 538, 219-232.
- XU, Y., and MAVRIKAKIS, M., 2003b. Adsorption and dissociation of O<sub>2</sub> on gold surfaces: Effect of steps and strain. *Journal of Physical Chemistry B*, 107, 9298-9307.
- YAMADA, K., ASAZAWA, K., YASUDA, K., IOROI, T., TANAKA, H., MIYAZAKI, Y., and KOBAYASHI, T., 2003. Investigation of PEM type direct hydrazine fuel cell. *Journal of Power Sources*, 115, 236-242.
- YAMAMOTO, O., 2000. Solid oxide fuel cells: fundamental aspects and prospects. *Electrochimica Acta*, 45, 2423-2435.
- YANG, G.W., GAO, G.Y., WANG, C., XU, C.L., and LI, H.L., 2008. Controllable deposition of Ag nanoparticles on carbon nanotubes as a catalyst for hydrazine oxidation. *Carbon*, 46, 747-752.
- YE, W.C., YANG, B., CAO, G.Y., DUAN, L., and WANG, C.M., 2008. Electrocatalytic oxidation of hydrazine compound on electroplated Pd/WO<sub>3</sub> film. *Thin Solid Films*, 516, 2957-2961.

## References

---

- YEH, M.S., YANG, Y.S., LEE, Y.P., LEE, H.F., YEH, Y.H., and YEH, C.S., 1999. Formation and characteristics of Cu colloids from CuO powder by laser irradiation in 2-propanol. *Journal of Physical Chemistry B*, 103, 6851-6857.
- YI, Q.F., LI, L., YU, W.Q., ZHOU, Z.H., and XU, G.R., 2008. A novel titanium-supported Ag/Ti electrode for the electro-oxidation of hydrazine. *Journal of Molecular Catalysis a-Chemical*, 295, 34-38.
- YILDIRIM, H., KARA, A., DURUKANOGLU, S., and RAHMAN, T.S., 2006. Calculated pre-exponential factors and energetics for adatom hopping on terraces and steps of Cu(100) and Cu(110). *Surface Science*, 600, 484-492.
- YOON, K.Y., BYEON, J.H., PARK, J.H., and HWANG, J., 2007. Susceptibility constants of Escherichia coli and Bacillus subtilis to silver and copper nanoparticles. *Science of the Total Environment*, 373, 572-575.
- ZAMBELLI, T., WINTTERLIN, J., TROST, J., and ERTL, G., 1996. Identification of the "active sites" of a surface-catalyzed reaction. *Science*, 273, 1688-1690.
- ZENG, Z.H., DA SILVA, J.L.F., DENG, H.Q., and LI, W.X., 2009. Density functional theory study of the energetics, electronic structure, and core-level shifts of NO adsorption on the Pt(111) surface. *Physical Review B*, 79.
- ZENG, Z.H., MA, X.F., DING, W.C., and LI, W.X., 2010. First-principles calculation of core-level binding energy shift in surface chemical processes. *Science China-Chemistry*, 53, 402-410.
- ZHANG, P.X., WANG, Y.G., HUANG, Y.Q., ZHANG, T., WU, G.S., and LI, J., 2011. Density functional theory investigations on the catalytic mechanisms of hydrazine decompositions on Ir(1 1 1). *Catalysis Today*, 165, 80-88.
- ZHAO, Y., ZHU, J.J., HONG, J.M., BIAN, N.S., and CHEN, H.Y., 2004. Microwave-induced polyol-process synthesis of copper and copper oxide nanocrystals with controllable morphology. *European Journal of Inorganic Chemistry*, 4072-4080.
- ZHENG, M.Y., CHENG, R.H., CHEN, X.W., LI, N., LI, L., WANG, X.D., and ZHANG, T., 2005. A novel approach for CO-free H<sub>2</sub> production via catalytic decomposition of hydrazine. *International Journal of Hydrogen Energy*, 30, 1081-1089.
- ZHOU, G.J., LU, M.K., and YANG, Z.S., 2006. Aqueous synthesis of copper nanocubes and bimetallic copper/palladium core-shell nanostructures. *Langmuir*, 22, 5900-5903.
- ZHOU, S.D., QIAN, C., and CHEN, X.Z., 2011. Comparative Theoretical Study of Adsorption and Dehydrogenation of Formic Acid, Hydrazine and Isopropanol on Pd(111) Surface. *Catalysis Letters*, 141, 726-734.

## References

---

- ZIEGLER, K.J., DOTY, R.C., JOHNSTON, K.P., and KORGEL, B.A., 2001. Synthesis of organic monolayer-stabilized copper nanocrystals in supercritical water. *Journal of the American Chemical Society*, 123, 7797-7803.
- ZUBKOV, T., MORGAN, G.A., YATES, J.T., KUHLERT, O., LISOWSKI, M., SCHILLINGER, R., FICK, D., and JANSCH, H.J., 2003. The effect of atomic steps on adsorption and desorption of CO on Ru(109). *Surface Science*, 526, 57-71.